

Optimization of design procedures and quality control for FRC

Doctoral thesis by:
Eduardo Galeote Moreno

Directed by:
Albert de la Fuente Antequera
Ana Blanco Álvarez

Doctoral programme:
Construction Engineering

Barcelona, December 2018



UNIVERSITAT POLITÈCNICA DE CATALUNYA
BARCELONATECH

Department of Civil and Environmental
Engineering

DOCTORAL THESIS

ACKNOWLEDGEMENTS – AGRADECIMIENTOS

Durante estos años he contado con el apoyo y la confianza de mis directores, Albert de la Fuente y Ana Blanco, a los que tengo que agradecer todo su trabajo, dedicación y entusiasmo por enseñar. Albert es inspiración y rebosa pasión en lo que hace y lo que se propone. Con él inicié el camino que me ha traído hasta aquí años antes de empezar el doctorado. Ana transmite motivación, mostrando siempre el lado más atento y amable para guiar en todo momento. Creo que ambos son todo un ejemplo que he tenido la fortuna de conocer durante este tiempo y, por ello, mi agradecimiento a ellos dos va mucho más allá de lo académico.

Quiero agradecer de forma especial a Sergio sus propuestas, la ayuda que ha prestado y todo lo que me ha enseñado. También a Antonio, Pau y Nacho su cercanía y contribuciones. *I would also like to thank Chris Goodier and Simon Austin for giving me the opportunity to stay at Loughborough University for six months. I really appreciate your kindness, the talks and discussions we used to have and all the advices I received from you.*

Las horas dedicadas a las campañas experimentales han sido una parte muy importante de esta tesis. Por ese motivo, quiero agradecer al personal del laboratorio todo el apoyo y la ayuda para sacar adelante mi trabajo. A Tomás por su enorme disposición a aportar ideas que mejoran y facilitan el trabajo. Y especialmente a Robert, Camilo y Jordi, siempre disponibles para ayudar con esa dosis de buen humor que hace que las horas en el laboratorio parezcan más cortas. También a Eva, por su atención y paciencia conmigo. Por otro lado, al Ministerio de Ciencia, Innovación y Universidades a través de la beca FPU13/04864, cuyo apoyo económico ha contribuido al desarrollo de esta tesis.

La tesis se hace infinitamente más llevadera cuando se está rodeado de compañeros y amigos con los que se comparten buenos momentos y dan su apoyo cuando la motivación decae. A Razmik, Andressa, Janill, Mylene y Jorge agradezco todas nuestras charlas, cafés interminables y bromas pesadas. Con Tai, Carlos y Tina empecé compartiendo el máster que me trajo la suerte de terminar haciendo el doctorado junto a ellos. A Francesco, Celia, Rubén, Fran, Stas, Amir, Débora, Luis, Renan y Liao por hacer del grupo un equipo en el que se respira el buen ambiente. Quiero agradecer también a Àlex su ayuda en la parte final de esta tesis. Gràcies a Anna per les llargues estones i xerrades explicant-nos les nostres alegries i les nostres misèries. Y más allá de la Universidad, agradecer a Miriam su confianza y comprensión siempre que lo he necesitado.

Por último, he querido dejar para el final de estos agradecimientos a las personas que en todo momento me han dado su apoyo incondicional para lograr mis objetivos. A mis padres, María y Eduardo, por el esfuerzo que siempre han hecho para que haya podido llegar hasta aquí y por ayudarme a levantarme cuando he caído. De ellos he aprendido la importancia del trabajo y la perseverancia para alcanzar cualquier meta. A mis hermanas, Nélica y Miriam, que me han animado y motivado para dar lo mejor de uno mismo. A María y Júlia, que son alegría y nos han unido si cabe aún más. A Jordi, por sus ánimos y por los momentos que también él ha hecho posibles.

ABSTRACT

Fibre reinforced concrete (FRC) presents objectively proven advantages in terms of post-cracking strength and manufacturing procedures. As a result, FRC with structural responsibility is increasingly being used in the construction industry. However, some concerns still remain regarding design and performance given the uncertainties concerning the effect of the distribution and orientation of the fibres. In this context, further research is required to improve current tools to characterize and design FRC structures.

The main topics addressed in this thesis are oriented to analyse the influence of fibres at the design stage, verify whether the constitutive models are representative and suitable to predict the response of real-scale elements and simplify FRC quality control. At the design stage, the influence of size effect on the bending tests used to determine the constitutive model has been analysed. Additionally, a model to estimate the residual strength of FRC based on the orientation of the fibres is proposed. Flexural tests on real-scale slabs reinforced with rebars and fibres have been analysed and compared to numerical simulations using the constitutive model of the Model Code 2010 (MC2010). Finally, a correlation based on the Barcelona test (BCN) is proposed as an alternative to the three-point bending test in quality control.

The first part of the study focuses on the pre-design stage of FRC. Standard and non-standard specimens were tested under a three-point bending test (3PBT) configuration to calculate the parameters defining the MC2010 constitutive model for FRC. The results revealed that the size effect in small non-standard specimens can be mitigated if, instead of the CMOD, the rotation of the sample is used as the reference parameter to determine the residual strengths associated to the constitutive law.

Subsequently, a model to estimate the post-cracking strength of FRC is presented. Given a degree of isotropy and a content of fibres, the model assigns a position and an orientation to each fibre. Assuming that only fibres contribute to the tensile strength after cracking, the pull-out load of all the fibres combined with the sectional equilibrium can be used to determine the post-cracking strength of FRC. The estimations of the post-cracking strength curves are able to reflect the influence of the specimen dimension as well as the content and the orientation of the fibres.

After the pre-design stage, real-scale slabs with different combinations of rebars and fibres were tested to analyse the influence of fibres on the flexural behaviour, cracking patterns and ductility. The experimental results were used to verify the predicted flexural response of the slabs simulated by means of sectional analyses and finite element methods based on the constitutive law of the MC2010. The simulations revealed a general overestimation of the flexural performance when compared to the experimental results.

The last part of the study aims to present an alternative method to optimize and streamline quality control of FRC based on a correlation between the 3PBT and the BCN. For this purpose, an experimental programme on mixes with different rheologies, compressive strengths and types and contents of fibres was conducted. The procedure to determine such a correlation is described while showing the importance of considering confidence intervals in the presence of results with high variability as in FRC.

RESUMEN

El hormigón reforzado con fibras (HRF) presenta ventajas objetivamente probadas en términos de resistencia residual y procesos de producción. En consecuencia, el HRF con responsabilidad estructural ha experimentado una creciente demanda en el sector de la construcción. No obstante, su uso aún suscita ciertas preocupaciones debidas esencialmente a la influencia de la distribución y la orientación de las fibras en la capacidad resistente. En este sentido, se hace necesario continuar investigando con el objeto de mejorar los métodos actuales de caracterización y diseño del HRF.

Los principales aspectos que se abordan en esta tesis están orientados a analizar la influencia de las fibras en la etapa de diseño, verificar la capacidad de los modelos constitutivos para predecir la respuesta estructural de elementos a escala real y simplificar el control de calidad del HRF. En la etapa de diseño, se ha estudiado la influencia del efecto escala en los ensayos de flexión destinados a obtener las ecuaciones constitutivas de HRF. Asimismo, se ha propuesto un modelo para estimar la resistencia residual del HRF basado en la orientación de las fibras. Por otro lado, se ha analizado el comportamiento a flexión de losas reforzadas con fibras y barras de acero, tras lo que se ha comparado los resultados experimentales de dichos ensayos con simulaciones numéricas basadas en las ecuaciones constitutivas descritas en el *Model Code 2010* (MC2010). Finalmente, se propone una correlación basada en el ensayo Barcelona (BCN) como alternativa al ensayo a flexión a tres puntos (3PBT) en la fase de control de calidad.

La primera parte del estudio se enfoca en la etapa de pre-diseño del HRF. Para ello, se han ensayado probetas prismáticas de distintos tamaños bajo una configuración de ensayo 3PBT para calcular los parámetros que definen la ecuación constitutiva del HRF según los criterios del MC2010. Los resultados muestran que el efecto escala puede verse reducido utilizando el giro, en lugar del CMOD, como parámetro de referencia para calcular las resistencias residuales asociadas a la ecuación constitutiva.

Posteriormente, se propone un modelo para estimar la resistencia residual del HRF. A partir de la isotropía y el contenido de fibras, se asigna a cada fibra una posición y una orientación determinada. Asimismo, el modelo asume que en estado fisurado únicamente las fibras contribuyen a la resistencia a tracción. De este modo, la contribución al arrancamiento de todas las fibras en combinación con el equilibrio seccional puede utilizarse para calcular la resistencia residual del HRF. De acuerdo con los resultados obtenidos, la resistencia residual calculada mediante el modelo es capaz de reflejar la influencia del tamaño de probeta, el contenido de fibras y su orientación.

Tras el estudio de la fase de pre-diseño, se ensayaron losas a escala real con diferentes combinaciones de HA y HRF con el objeto de analizar la influencia de las fibras en la respuesta a flexión, la aparición de fisuras y la ductilidad. Los resultados experimentales se utilizaron para verificar la idoneidad del modelo constitutivo del MC2010 cuando se utiliza para simular el comportamiento a flexión mediante análisis seccional y tridimensional mediante elementos finitos. Este estudio muestra que los resultados de las simulaciones presentan una sobreestimación generalizada de la respuesta a flexión de las losas en comparación con los resultados experimentales.

En la última parte se presenta un método alternativo para optimizar y agilizar el control de calidad del HRF. Dicha propuesta se basa en una correlación entre el ensayo 3PBT y el ensayo BCN. Para ello, se realizó una campaña experimental empleando hormigones con distintas reologías, resistencias a compresión y tipos y cuantías de fibras. El estudio describe

el proceso de obtención de la correlación y muestra la importancia del uso de intervalos de confianza frente a resultados que generalmente presentan una alta dispersión.

TABLE OF CONTENTS

1	INTRODUCTION.....	1
1.1	PROLOGUE.....	1
1.2	RESEARCH STRATEGY.....	2
1.3	OBJECTIVES.....	4
1.4	OUTLINE OF THE THESIS.....	5
2	STATE OF THE ART.....	9
2.1	INTRODUCTION.....	9
2.2	CHARACTERIZATION OF FRC.....	10
2.2.1	Experimental determination of the fibre orientation.....	10
2.2.2	Alternative tests to determine the mechanical properties of FRC.....	11
2.2.3	Constitutive FRC models based on alternative characterization tests.....	15
2.2.4	Implications on design and quality control.....	16
2.3	CHALLENGES OF STRUCTURAL DESIGN WITH FRC.....	18
2.3.1	Influence of size and geometry effects.....	18
2.3.2	Influence of fibre orientation.....	20
2.3.3	Partial safety factors.....	22
2.4	APPLICATION OF FRC IN STRUCTURES.....	22
2.4.1	Design strategies.....	23
2.4.2	Crack formation and control.....	25
2.5	CONCLUDING REMARKS.....	27
3	SIZE EFFECT ON PRISMATIC BEAMS TO OBTAIN FRC DESIGN PARAMATERS.....	29
3.1	INTRODUCTION.....	29
3.1.1	Objectives.....	30
3.1.2	Outline of the chapter.....	30
3.2	ANALYTICAL ASSESSMENT OF THE POST-CRACKING STRENGTH.....	31
3.2.1	Constitutive law for FRC.....	31
3.2.2	Approach to calculate the constitutive law for FRC.....	32
3.2.3	Analytical procedure.....	34
3.3	EXPERIMENTAL PROGRAMME.....	36
3.3.1	Materials and concrete mixes.....	36
3.3.2	Concrete production and specimens.....	38
3.4	ANALYSIS OF RESULTS.....	39

3.4.1	Compressive strength and modulus of elasticity.....	39
3.4.2	Flexural strength.....	40
3.4.3	Constitutive models	44
3.4.4	Sectional analysis.....	46
3.4.5	Neutral axis and stress distribution.....	48
3.5	CONCLUDING REMARKS	51
4	ISOTROPY-BASED ESTIMATION OF THE POST-CRACKING STRENGTH IN FRC...53	
4.1	INTRODUCTION	53
4.1.1	Objectives.....	54
4.1.2	Outline of the chapter	54
4.2	ISOTROPY-BASED DISTRIBUTION OF FIBRES.....	55
4.2.1	General description of the model.....	55
4.2.2	Critical section.....	56
4.2.3	Position and orientation of the fibres.....	57
4.2.4	Assumptions for the analysis of the model	60
4.3	STAGE I: ANALYSIS OF THE CROSS-SECTION	61
4.3.1	Number of fibres, distribution and orientation.....	61
4.3.2	Variability of results	67
4.4	STAGE II: ANALYSIS OF THE PULL-OUT STRENGTH	68
4.4.1	Inclination of the fibres	68
4.4.2	Embeddded length	71
4.5	STAGE III: ANALYSIS OF THE POST-CRACKING STRENGTH	72
4.5.1	Influence of the content of fibres	72
4.5.2	Influence of the geometry	72
4.5.3	Influence of the degree of isotropy.....	75
4.6	CONCLUDING REMARKS	76
5	DUCTILITY ASSESSMENT AND CHARACTERIZATION OF REAL-SCALE ISOSTATIC STRUCTURES.....77	
5.1	INTRODUCTION	77
5.1.1	Objectives.....	78
5.1.2	Outline of the chapter	78
5.2	DESIGN STRATEGY OF FRC ELEMENTS	78
5.3	EXPERIMENTAL PROGRAMME	81
5.3.1	Materials and concrete mix	81
5.3.2	Stage I. Characterization of the material.....	82

5.3.3	Stage II. Characterization of real-scale slabs.....	83
5.4	RESULTS OF STAGE I: MATERIALS.....	88
5.4.1	Air entrain, compressive strength and modulus of elasticity.....	88
5.4.2	Post-cracking strength.....	90
5.4.3	Ductility requirements of FRC.....	92
5.4.4	Tensile strength of steel rebars	93
5.5	RESULTS OF STAGE II: REAL-SCALE SLABS.....	94
5.5.1	Crack patterns	94
5.5.2	Crack width	96
5.5.3	Midspan deflection.....	97
5.5.4	Ductility assessment according to MC2010.....	99
5.5.5	Orientation of the fibres.....	101
5.5.6	Distribution of the fibres within the cross-section	104
5.6	CONCLUDING REMARKS	106
6	MODELLING THE FLEXURAL BEHAVIOUR OF REAL-SCALE ISOSTATIC SLABS..	109
6.1	INTRODUCTION	109
6.1.1	Objectives.....	110
6.1.2	Outline of the chapter	110
6.2	MODELLING STRATEGY	110
6.2.1	2D simulation: AES routine.....	111
6.2.2	3D simulation: Finite elements model (FEM)	111
6.2.3	Parameters for the simulation of the slabs	112
6.3	2D SIMULATION: PARAMETRIC STUDY OF THE CONSTITUTIVE MODEL.....	113
6.3.1	Reinforced concrete.....	114
6.3.2	Fibre reinforced concrete.....	115
6.3.3	Hybrid reinforced concrete	117
6.4	3D SIMULATION: PARAMETRIC STUDY OF THE CONSTITUTIVE MODEL.....	120
6.4.1	Reinforced concrete.....	120
6.4.2	Fibre reinforced concrete.....	122
6.4.3	Hybrid reinforced concrete	123
6.5	CONCLUDING REMARKS	125
7	CORRELATION BETWEEN THE BARCELONA TEST AND THE BENDING TEST TO OPTIMIZE QUALITY CONTROL.....	127
7.1	INTRODUCTION	127
7.1.1	Objectives.....	128

7.1.2	Outline of the chapter	129
7.2	EFFICIENCY OF QUALITY CONTROL.....	130
7.3	EXPERIMENTAL PROGRAMME	132
7.3.1	Materials and mixes.....	132
7.3.2	Specimens and test procedure	134
7.4	ANALYSIS AND COMPARISON OF THE RESULTS	136
7.4.1	Influence of the fibre type	136
7.4.2	Influence of the rheology.....	137
7.4.3	Influence of the type of cubic specimen	138
7.5	CORRELATIONS	140
7.5.1	Correlation depending on variables and test parameters	140
7.5.2	Proposal of correlation.....	141
7.5.3	Confidence intervals.....	142
7.5.4	Verification of the results	142
7.6	REAL CASE IMPLEMENTATION	143
7.6.1	Post-cracking strength.....	144
7.6.2	Correlation between tests	145
7.7	CONCLUDING REMARKS	146
8	CONCLUSIONS.....	149
8.1	GENERAL CONCLUSIONS	149
8.2	SPECIFIC CONCLUSIONS	150
8.3	FUTURE PERSPECTIVES.....	152
	REFERENCES.....	155
	PUBLICATIONS	169

LIST OF FIGURES

Figure 1.1 Number of publications on fibre reinforced concrete in Scopus.....	2
Figure 1.2 Topics defining the behaviour of FRC.....	3
Figure 1.3 Outline of the thesis.	6
Figure 2.1 Main topics addressed for the design of FRC.....	10
Figure 2.2 a) Barcelona test, b) DEWS (Nunes et al. 2017), c) SRDP (Conforti et al. 2018) and d) Montevideo test (Segura-Castillo et al. 2018b).	14
Figure 2.3 Variability of residual FRC strength according to five different tests (Conforti et al. 2018).....	17
Figure 2.4 Comparison of the size effect factor in the German code DBV and RILEM (Pujadas 2013).....	19
Figure 2.5 Distribution of fibres at the cross section (Alberti et al. 2016c) according to a) RILEM TC 162-TDF (Barr et al. 2003a) and b) Dupont (Dupont & Vandewalle 2005).	21
Figure 2.6 Fibre distribution in a vertical wall.....	21
Figure 2.7 Approach to determine the optimum content of fibres on structural elements.....	24
Figure 2.8 Typical F- δ curves for SFRC with different contents of fibres.....	25
Figure 2.9 a) Crushing test and b) crack pattern in SFRC.	25
Figure 2.10 a) Central loading configuration and b) crack pattern of the slab.....	26
Figure 2.11 Test setup and crack patterns of BBT segments (Caratelli et al. 2011).....	26
Figure 3.1 Constitutive law for FRC in tension.....	31
Figure 3.2 Failure mechanisms of the three-point bending test: a) FCO and b) ECO.....	33
Figure 3.3 Strain according to a) FCO and b) ECO.....	33
Figure 3.4 Schematic discretization of the cross-section and the linear distribution of strains and distribution of stresses.	34
Figure 3.5 Fundamental steps undertaken by a cracked section of FRC.	35
Figure 3.6 Flow chart of the analytical model.....	37
Figure 3.7 a) Conveyor belt for sand, b) nanosilica, c) pouring of concrete, d) spraying of curing layer.....	38
Figure 3.8 Prismatic specimens for three-point bending test.....	39
Figure 3.9 Average flexural stress in terms of strength-rotation.	41
Figure 3.10 Size effect on a) fLOP and b) maximum strength.....	42
Figure 3.11 Size effect on a) rotation capacity and b) CMOD at maximum residual strength.	43

Figure 3.12 Size effect on f_{ft} s and f_{ftu} according to FCO and ECO approaches.	46
Figure 3.13 Comparison between experimental and MC2010 results.	47
Figure 3.14 Stress distribution at the cross-section and relative neutral axis depth.....	49
Figure 3.15 Neutral axis depth according to a) CMOD and b) rotation.....	50
Figure 3.16 Neutral axis depth according to the content of fibres.....	50
Figure 3.17 Extended neutral axis depth-rotation according to the content of fibres.....	51
Figure 4.1 Models for the estimation of FRC flexural behaviour.	55
Figure 4.2 a) Failure mechanism and b) sectional forces.	56
Figure 4.3 Position and dimension of the critical section.....	57
Figure 4.4 Procedure for distributing the fibres in the concrete matrix.	58
Figure 4.5 a) Probability density function and b) cumulative normal distribution.....	59
Figure 4.6 a) Efficient dispersion of fibres and b) cluster of fibres in the cracked section..	62
Figure 4.7 Orientation numbers according to the degree of isotropy.	62
Figure 4.8 a) Ncs of the model according to η_x and b) comparison of Ncs of the model and Krenchel.....	63
Figure 4.9 Cumulative relative N_f according to orientation number η_x	64
Figure 4.10 Orientation profile of the fibres with a) ID1, b) ID2, c) ID3 and d) ID4.....	64
Figure 4.11 Theoretical distribution of the orientation number of the fibres in the cross-section.	65
Figure 4.12 Orientation numbers η_x , η_y and η_z vs. specimen dimension.....	66
Figure 4.13 Distribution profile of fibres.....	66
Figure 4.14 Variability of the orientation number.....	67
Figure 4.15 Variability of the number of fibres at the cracked section.....	68
Figure 4.16 a) Points of the pull-out law and b) pull-out force for different inclination angles.	69
Figure 4.17 Stages of fibre pull-out (Laranjeira et al. 2010a).	69
Figure 4.18 a) Debonding initiation, b) crack width at the end of debonding, c) final pull-out load and d) final crack width.	70
Figure 4.19 Influence of the embedded length for orientation angles a) $\theta = 30^\circ$ and b) $\theta = 60^\circ$	71
Figure 4.20 Influence of orientation angle and embedded length on the pull-out load at a) debonding initiation and b) fibre removal.....	71

Figure 4.21 Residual strength-CMOD curves for specimens of a) 150, b) 100 and c) 40 mm.	73
Figure 4.22 Comparison of the residual strength of three specimen dimensions.....	73
Figure 4.23 Residual strengths f_{R1} and f_{R3} according to the specimen dimension.	74
Figure 4.24 Relative number of fibres and variability at the cracked surface.	75
Figure 4.25 Influence of the degree of isotropy on a) f_{R1} and b) f_{R3}	75
Figure 5.1 M- χ diagram for sectional behaviour.....	80
Figure 5.2 Transient stages of the segments.....	80
Figure 5.3 Geometry of the slabs and reinforcement configuration.....	84
Figure 5.4 Pouring and vibration of the slabs.....	84
Figure 5.5 a) General configuration of the test and b) neoprene support.	85
Figure 5.6 Isostatic setup of the test and dimensions.	85
Figure 5.7 a) General configuration of the instrumentation, b) LVDT transducer, c) displacement transducers and d) laser.	86
Figure 5.8 a) Position of the cores, b) removal of hooks and c) drilling of cores.....	86
Figure 5.9 Detailed position of the cores in FRC slabs.	87
Figure 5.10 Analyser and cylindrical sensor.....	88
Figure 5.11 Measurement directions of inductance.....	88
Figure 5.12 a) Flexural residual strength and b) Barcelona test results.	92
Figure 5.13 Crack patterns in slabs under flexural test.....	94
Figure 5.14 Curves load-crack width for a) HRCS ₁ -25/1HE, HRCS ₁ -30/1HE, HRCS ₁ -20/2HE, HRCS ₁ -25/2HE and b) HRCS ₁ -25/1HE, HRCS ₂ -25/1HE.	96
Figure 5.15 Curves load-displacement for a) PCS and RCS, b) FRC, c) HRCS with fibres 1HE and d) HRCS with fibres 2HE.	98
Figure 5.16 Constitutive model for FRC.	100
Figure 5.17 M- χ diagrams of the slabs.....	100
Figure 5.18 a) Orientation number (η) profile in different directions and b) representation of η in polar coordinates.....	102
Figure 5.19 Isotropy, η , preferential orientation and main crack direction of the cores in FRCS slabs.....	103
Figure 5.20 Dimensions of the grid generated in the cross-section.....	105
Figure 5.21 Grid and number of fibres in the cracked cross-section of the slabs FRCS-20/2HE, FRCS-25/1HE and FRCS-30/1HE.	105

Figure 6.1 Distribution of strains and stresses of a concrete cross-section with fibres and steel rebars.....	111
Figure 6.2 Constitutive models for FRC and steel rebars in MC2010.	111
Figure 6.3 Boundary conditions and traditional reinforcement configuration.	112
Figure 6.4 Comparison between AES and experimental results of HRCS (Minelli et al. 2014).	113
Figure 6.5 Experimental, MC2010, plain concrete and calibrated P- δ curves of RCS ₁ and RCS ₂	114
Figure 6.6 Experimental, MC2010 and calibrated P- δ curves of FRCS-20/2HE, FRCS-25/1HE and FRCS-30/1HE.....	116
Figure 6.7 Comparison between the MC2010 and the calibrated constitutive laws of FRCS-20/2HE, FRCS-25/1HE and FRCS-30/1HE.	116
Figure 6.8 Experimental, MC2010 and calibrated P- δ curves of HRCS.	118
Figure 6.9 Comparison between the MC2010 and the calibrated constitutive laws of HRCS.	119
Figure 6.10 Experimental and calibrated P- δ curves of RCS ₁ and RCS ₂	120
Figure 6.11 Steel rebars load-carrying capacity in a) RCS ₁ and b) RCS ₂	121
Figure 6.12 Comparison of the experimental and calibrated simulation of FRCS-25/1HE and FRCS-30/1HE.	122
Figure 6.13 Comparison between the MC2010 and the calibrated constitutive laws of FRCS-25/1HE and FRCS-30/1HE.	123
Figure 6.14 Comparison of the experimental and calibrated simulation of HRCS ₁ -25/1HE, HRCS ₁ -30/1HE and HRCS ₂ -25/1HE.....	124
Figure 7.1 Methodology used to derive the correlation between tests.....	129
Figure 7.2 Gauss probabilistic law for Test A and B.....	131
Figure 7.3 Influence of the test on the number of uncomplying batches.	131
Figure 7.4 BCN in cylindrical and cubic specimens.....	134
Figure 7.5 Cracking mechanism and distribution of stresses.	135
Figure 7.6 Cubic specimens cut from the beams.	135
Figure 7.7 Residual strength in a) 3PBT and b) BCN.....	136
Figure 7.8 Influence of the rheology in the results of the a) 3PBT and the b) BCN.....	137
Figure 7.9 Orientation of fibres according to the content in a) cut and b) moulded specimens.	139

Figure 7.10 Residual strength with the BCN in cut and moulded specimens with a) SF and b) PF..... 139

Figure 7.11 Results of linear correlation analysis..... 141

Figure 7.12 Force measured in the 3PBT and estimated from the BCN with the correlation. 142

Figure 7.13 Real and predicted curves of 3PBT with confidence intervals..... 143

Figure 7.14 a) Three-point bending test and b) Barcelona test curve..... 145

LIST OF TABLES

Table 1.1 Specific objectives.....	5
Table 2.1 Methods to determine fibre orientation.....	12
Table 2.2 Methods to determine fibre orientation.....	13
Table 2.3 Stress-strain relation for DEWS and BCN.....	15
Table 2.4 Crack width equivalence between 3PBT and SRDP.	16
Table 2.5 Parameters k depending on the number of specimens tested (Cavalaro & Aguado 2015).....	17
Table 2.6 Studies on size effect of FRC under flexure.....	18
Table 2.7 Experimental and real case studies of FRC structural elements.....	23
Table 3.1 Concrete mixes.....	36
Table 3.2 Characteristics of the fibres.....	38
Table 3.3 Characteristic dimensions of the specimens for the three-point bending test.	39
Table 3.4 Results of compressive strength and modulus of elasticity.....	40
Table 3.5 Average flexural strengths of M90A, M190A, M90B and M190B.....	40
Table 3.6 Crack openings and strains according to FCO and ECO.....	44
Table 3.7 Constitutive laws according to FCO and ECO and experimental results.....	45
Table 4.1 Combinations of degrees of isotropy.....	61
Table 5.1 Concrete mix.....	81
Table 5.2 Characteristics of the fibres (provided by the manufacturer).....	82
Table 5.3 Summary of characterization tests.....	82
Table 5.4 Summary of the reinforcement of the slabs.....	83
Table 5.5 Results of air entrain, compressive strength and modulus of elasticity.....	89
Table 5.6 Results of compressive strength on cut specimens.....	90
Table 5.7 Three-point bending test results.....	91
Table 5.8 Barcelona test results.....	91
Table 5.9 Ductility ratios of MC2010.....	93
Table 5.10 Tensile strength of steel rebars.....	93
Table 5.11 Number of cracks and spacing.....	95
Table 5.12 Numerical results of the load-deflection curves.	98
Table 5.13 Parameters for the tensile constitutive model.....	100

Table 5.14 Isotropy and direction of preferential orientation.....	104
Table 6.1 Mechanical properties of concrete mixes.....	113
Table 6.2 Plain concrete σ -w calibration for AES.....	115
Table 6.3 FRC properties for fibre reinforced concrete slabs.....	117
Table 6.4 FRC properties for hybrid reinforced concrete slabs.....	118
Table 6.5 Plain concrete σ -w calibration for FEM.....	121
Table 6.6 FRC properties for FRCS-25/1HE and FRCS-30/1HE.....	122
Table 6.7 FRC properties for HRCS ₁ -25/1HE, HRCS ₁ -30/1HE and HRCS ₂ -25/1HE.....	124
Table 7.1 Mix proportioning of the dosages.....	132
Table 7.2 Mix proportioning of the dosages.....	133
Table 7.3 Main characteristics of the mixes.....	133
Table 7.4 Characteristics of the fibres (provided by the manufacturers).....	134
Table 7.5 Average values and CV of the fibre contribution for cut and moulded specimens.	138
Table 7.6 Constants and confidence interval of Eq. 7.1.....	142
Table 7.7 Bending test results of B1, B2 and B3.....	144
Table 7.8 Barcelona test result of B1, B2 and B3.....	144
Table 7.9 Calibrated parameters of correlation.....	145
Table 7.10 Experimental and correlated results.....	146

1 INTRODUCTION

1.1 PROLOGUE

Fibre reinforced concrete (FRC) is gaining ground in a wide range of structures in which traditional reinforcement has been commonly used. The use of fibres for structural applications can be beneficial in economic terms, manufacturing facilities, construction time and reinforcing effects. For this reason, and to encourage the use of FRC in structural applications, utmost importance should be given to providing enough tools to design safe and durable FRC structures.

Different types of fibres—steel, polymeric and natural—may be used as reinforcement for concrete. Among these, the most commonly used for structural purposes are steel fibres given their high strength, modulus of elasticity, ductility and good bond characteristics (Banthia et al. 2012). Even though FRC is used to a lesser extent than traditional reinforced concrete, its advantages enhancing the post-cracking strength, toughness and durability represent the main assets towards its increasing use. These advantages lie in the rheological and mechanical properties of FRC, which highly depend on the mix proportioning, type and content of fibres. This is demonstrated by different varieties of concrete such as self-compacting FRC (Grünewald 2004) or high-performance fibre reinforced concrete (Walraven 2013).

Besides these new developments in concrete technology, FRC has experienced an increasing use in recent years mainly due to the appearance of codes and guidelines providing tools for FRC design in a variety of applications. In this regard, specific design rules for FRC have been included in European codes (Blanco et al. 2013), along with reference recommendations and guidelines such as those of RILEM TC 162-TDF (Vandewalle et al. 2003) and the *fib* Model Code 2010 (MC2010) (fib 2010). The *fib* Model Code 2020 (MC2020), now in preparation, aims to go beyond the MC2010, integrating innovative

guidelines for the design of new and traditional reinforced concrete and FRC structures (Matthews et al. 2018).

Along with these design rules, the use of FRC has been also motivated by the high amount of research conducted in the last two decades. This is evidenced by the evolution of the number of scientific papers on the topic of FRC published since 1995. A quick search in Scopus for the words “*fibre reinforced concrete*” combined with “*orientation*” and “*design*” serves as an indicator of the growing interest in FRC exhibited in increasing trends as displayed in Figure 1.1. Following these trends in the years ahead, research on FRC is expected to keep growing.

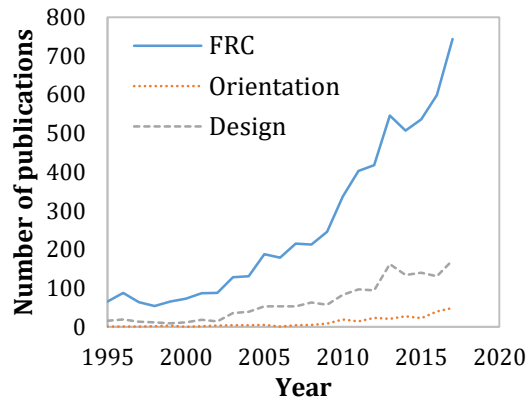


Figure 1.1 Number of publications on fibre reinforced concrete in Scopus.

Despite the remarkable advances in the field of FRC, research conducted on the orientation of fibres and FRC design represents a small fraction of the number of studies published. The close link between orientation and FRC tensile response is of paramount importance given that design relies primarily on performance-based approaches. In this sense, design of FRC is based on continuously developing constitutive models defined in codes and guidelines through bending tests. Some alternatives to these constitutive equations have been reported in literature (Blanco et al. 2014) using alternative tests that can also be used in quality control.

1.2 RESEARCH STRATEGY

The main topics that still raise some questions with respect to the performance of FRC have been identified and summarized in Figure 1.2. From a general perspective, this doctoral thesis primarily focuses on the highlighted topics, which can be combined to cover a comprehensive design approach from an optimization point of view. In this concern, it is important to analyse how the orientation of the fibres and the dimension of the structural elements affect design specifications. This leads to propose up to which extent the contribution of the fibres is able to replace traditional reinforcement to optimize the element response when in service. Additionally, the control of FRC to determine that it fulfils the specified requirements needs to be updated proposing the use of new methods.

The characterization of FRC can be addressed in two different lines: materials and design. The area of materials is oriented to the definition of the properties of FRC such as the residual strength, the pull-out behaviour and the orientation of the fibres. The area of design

focuses on determining and analysing new and current constitutive models, estimating the flexural strength of designed elements and the influence of the size of the element.

Characterization is followed by the analysis of real-scale elements. This involves the analysis of the real structure to verify the design requirements. Numerical modelling plays an important role since it is used to simulate the behaviour of the structural elements designed according to the constitutive models of the materials. In some cases, these constitutive models need to be analysed to determine their adequacy with regard to the designed elements (Blanco 2013). Quality control of the material is also relevant during the manufacture of the structure in order to verify that the material fulfils the requirements established at the design stage.

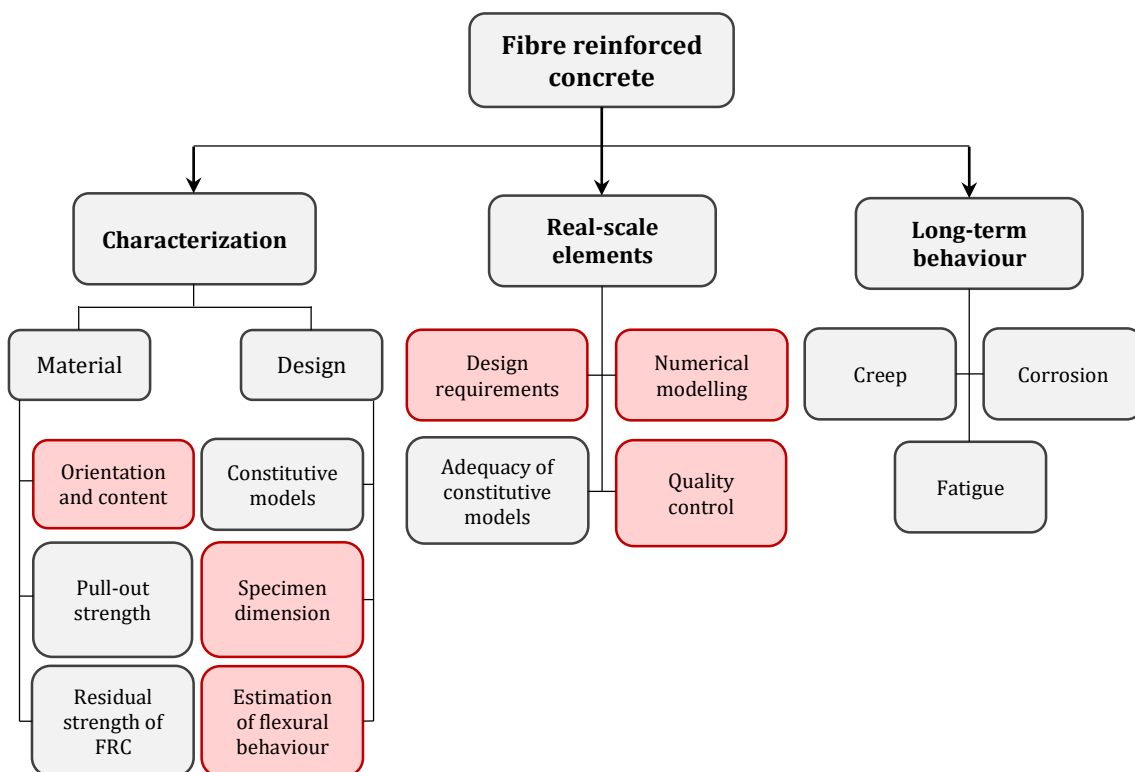


Figure 1.2 Topics defining the behaviour of FRC.

A complete design of the behaviour of FRC also needs to account for the long-term properties. These are probably the least studied characteristics of FRC given the long time required to obtain results. The post-cracking creep behaviour in FRC has been scarcely reported although, as a result of the RILEM Technical Committee 261-CCF, research on this topic is being encouraged. Similarly, there are no specific design methods to account for corrosion on steel fibre reinforced concrete (SFRC) or fatigue on concrete with steel or plastic fibres.

The influence of the specimen dimension on the behaviour of FRC is the first topic analysed in this doctoral thesis. Characterization tests are conducted in laboratories using specimens far smaller than structural elements. In this concern, several experimental programmes revealed how the size of the samples has important implications regarding the mechanical strength. Consequently, given that the results of characterization are used for the design of structural elements, the influence of the dimension of the element should be well defined in codes.

Additional research revealed that the size effect is mainly attributed to the orientation of the fibres in the cross-section. Indeed, as confirmed in a previous thesis of the group (Laranjeira 2010), the distribution and orientation of fibres at the cracked cross-section presents a specific profile subject to variations of fibre length and cross-sectional dimension. These findings reveal how the change of the element dimension has a direct influence on the orientation of the fibres at the cross-section and, hence, at the residual strength of FRC.

The distribution and orientation of the fibres should, therefore, be considered at the design stage to improve the efficiency of the structural element. An approach to account for the orientation has been already proposed in the MC2010 by means of a multiplying factor that depends on the favourable or unfavourable alignment of the fibres with the main stresses. However, no specific values are given, and these parameters need to be adjusted according to the criteria of the designer. In this regard, being able to estimate the residual strength according to the orientation of the fibres would be of great interest in terms of assessing the efficiency of the fibres contribution.

Replacing traditional reinforcement with fibres is still possible even if fibre orientation is not considered in the design, depending on the type and content of fibre added to the concrete mix. In this sense, it is of great interest to determine the flexural capacity of real-scale elements with different reinforcement combinations to determine the optimum contents of fibres to fulfil the ductility requirements specified in codes. However, results need always to be analysed from a critical point of view and determine whether the specifications defined in codes can be adapted to specific cases or need to be blindly followed.

This critical analysis also applies to the quality control procedure at the jobsite. Even though bending tests are among the most used methods to determine the post-cracking strength of FRC, alternative tests to determine the post-cracking properties of FRC have arisen. These tests are primarily aimed to simplify the testing procedure, increase repetitiveness and reduce both the variability of the results and the execution costs. Consequently, their use needs to be discussed given the advantages these alternatives present.

1.3 OBJECTIVES

Considering the motivations and the areas of interest presented in the research strategy, the main objectives to give response to questions still arising are defined as follows:

- Analyse the implications and advantages of using alternative tests to characterize the residual behaviour of FRC.
- Study the influence of the specimen dimension on the parameters defining the constitutive model for FRC.
- Analyse the main sources determining the orientation of the fibres and propose an approach to simulate the position and orientation of the fibres and their effect on the post-cracking behaviour of FRC.
- Determine the effect of the fibres when used as replacement of traditional reinforcement and verify up to what extent their effect contributes to achieving the design criteria specified in codes.

To fulfil these goals, the specific objectives in Table 1.1 were defined for each of the main topics addressed in this thesis.

Table 1.1 Specific objectives.

Topic	Specific objectives
Size effect	<ul style="list-style-type: none"> Analyse the post-cracking behaviour of specimens with different dimensions and identify the main sources of size effect on FRC. Propose an alternative approach to calculate the parameters that define the constitutive law in MC2010 according to the post-cracking strength of the specimens with different dimensions. Compare the analytical results of the proposed approach to the experimental bending tests results of the FRC specimens tested.
Orientation and distribution of fibres	<ul style="list-style-type: none"> Formulate an analytical model to simulate the distribution and orientation of the fibres based on the isotropy of the material. Estimate the flexural post-cracking performance of FRC based on the pull-out behaviour of the fibres. Analyse the influence of the type of concrete and fibre content on the proposed model.
Real-scale slabs	<ul style="list-style-type: none"> Conduct a critical analysis of the design criteria of structural elements in terms of ductility requirements. Analyse the flexural response of real-scale slabs with different combinations of traditional and fibre reinforcement. Compare the ductility of the slabs under flexural loading with the requirements of MC2010. Assess the orientation of the fibres within the slabs and their distribution on the cracked surface. Simulate the testing conditions of the slabs with numerical tools to predict their behaviour and determine optimum reinforcement combinations.
Quality control	<ul style="list-style-type: none"> Analyse the influence of the variability of different tests on the acceptance criteria based on established characteristic strengths. Compare the results of the mechanical characterization of FRC when tested by means of bending and Barcelona tests. Identify a correlation based on the parameters of the Barcelona test to calculate the residual strength of FRC when assessed through a bending test. Use the results of a real case to apply the correlation methodology and verify the acceptability of the results.

1.4 OUTLINE OF THE THESIS

The thesis has been divided into eight chapters dealing with different stages of design and characterization of FRC. The five central chapters of the thesis involving the analyses and the results have been divided into three parts. A schematic representation of the structure of the thesis is presented in Figure 1.3 to show the methodology followed.

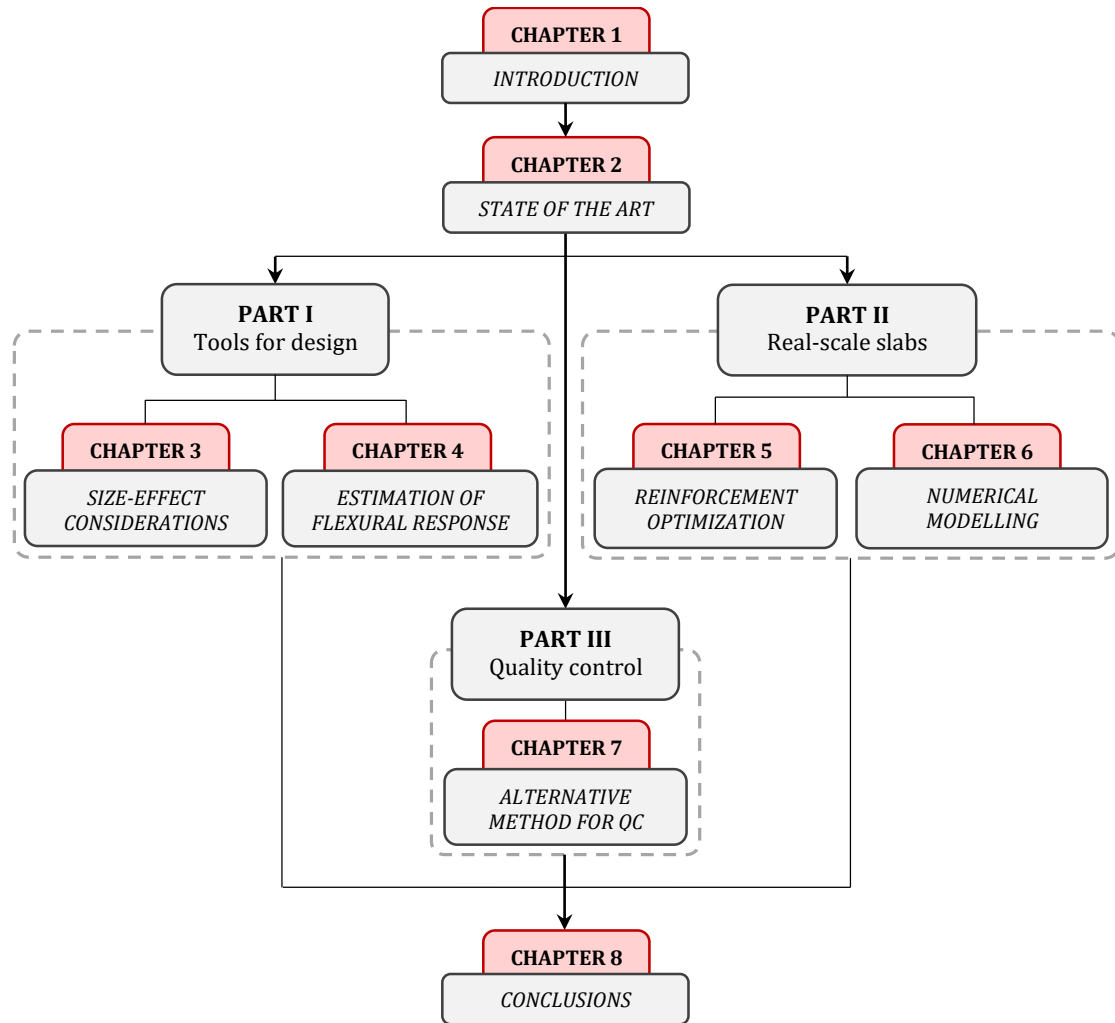


Figure 1.3 Outline of the thesis.

After the introductory chapter, a literature review is presented in Chapter 2, which is aimed at contextualizing the main topics of the thesis by reviewing the most relevant research conducted up to date. In this aspect, the chapter focuses on the areas of interest of the thesis, highlighting the recent advances in FRC that serve as a basis to identify the issues requiring special attention.

The main objective of PART I is providing additional tools towards a more efficient design of FRC by facing two subjects that need to be addressed to a larger extent in codes. An experimental campaign consisting of flexural tests on prismatic specimens of different dimensions was undertaken for this concern. The results of these tests were used in Chapter 3 to propose an approach aimed to calculate the parameters defining the constitutive law for FRC in MC2010 with non-standard sized specimens. The same experimental results were used to develop and validate a method in Chapter 4 intended to simulate the distribution and orientation of the fibres in an FRC element based on its isotropy.

PART II describes the analysis of real-scale elements, whose importance is reflected given the influence of the size effect reported in Chapter 3. The goal of Chapter 5 is to determine the behaviour of slabs with traditional reinforcement, fibre reinforcement and a combination of both. The analysis is oriented in terms of ductility and cracking performance. In Chapter 6, a numerical modelling of the same slabs is conducted with the aim of studying

the efficiency of the current approaches to predict the behaviour of large elements. With this analysis, the objective is to identify whether any parameters of the constitutive models require any adjustments to improve numerical simulations and predict more accurately the behaviour of FRC elements.

A description of the methodology to obtain a correlation between the Barcelona test and the bending test is shown in PART III. This is based on the possibility of using alternative tests to determine the properties of FRC as stated in the MC2010. The study is shown in Chapter 7 and lies in the optimization and simplification of quality control procedures, primarily intended for large construction works in which a thorough and extensive quality control needs to be conducted.

The thesis finishes with Chapter 8, in which the main conclusions of each of the topics addressed are presented. Additionally, future research lines are proposed to achieve a better understanding of FRC and improve the design procedures to encourage the use of this material in construction.

2 STATE OF THE ART

2.1 INTRODUCTION

Improving the design procedures of FRC is a key point to encourage the use of this material in the construction industry. Despite the extensive research conducted in this line, research community still faces many challenges in areas such as material characterization, constitutive laws, design optimization and quality control efficiency (Serna et al. 2009; di Prisco et al. 2013a). This chapter aims to present a review of these topics based on the published literature to identify the main gaps that need to be addressed. These topics have been usually studied separately, although, as in the chart shown in Figure 2.1, a connection between those can be identified under a general framework oriented towards the design of FRC.

Characterization tests represent the first step to determine the mechanical properties of FRC, strongly influenced by the type, content and orientation of fibres (Barros et al. 2005). Given the influence of the fibres on FRC mechanical strength, its characterization may include tools to assess and predict fibre distribution to analyse the extent of such influence. Fibre distribution is also affected by specimen's geometry and dimensions (Martinie & Roussel 2011; Zerbino et al. 2012), effect that needs to be taken into consideration in both characterization and design.

The mechanical characterization according to standardized tests provides the parameters for defining the constitutive models used for structural design. Even though constitutive laws for FRC of codes and guidelines are generally based on parameters obtained from bending tests, additional constitutive laws defined by alternative tests have recently aroused (di Prisco et al. 2013b; Blanco et al. 2014; Minelli & Plizzari 2015). These tests also represent an interesting solution in terms of quality control and assessment of mechanical properties given that can simplify testing procedures and mitigate disadvantages of bending

tests such as the scatter of results. The use of these alternative tests during quality control combined with the constitutive laws obtained through bending tests for design can lead to improved design procedures.

These design strategies are oriented to make the most of the material properties and optimize both the design and the response of the structure. In this line, the constitutive law for FRC of the MC2010 needs to be analysed to determine whether it is accurate enough for designing certain types of structures given the reported overestimations that constitutive laws may provide (Blanco et al. 2015a). This overestimation might be a consequence of the MC2010 ignoring the size effect and considering FRC as a homogeneous material without specific guidelines to consider the favourable or unfavourable reinforcing effect of the fibres.

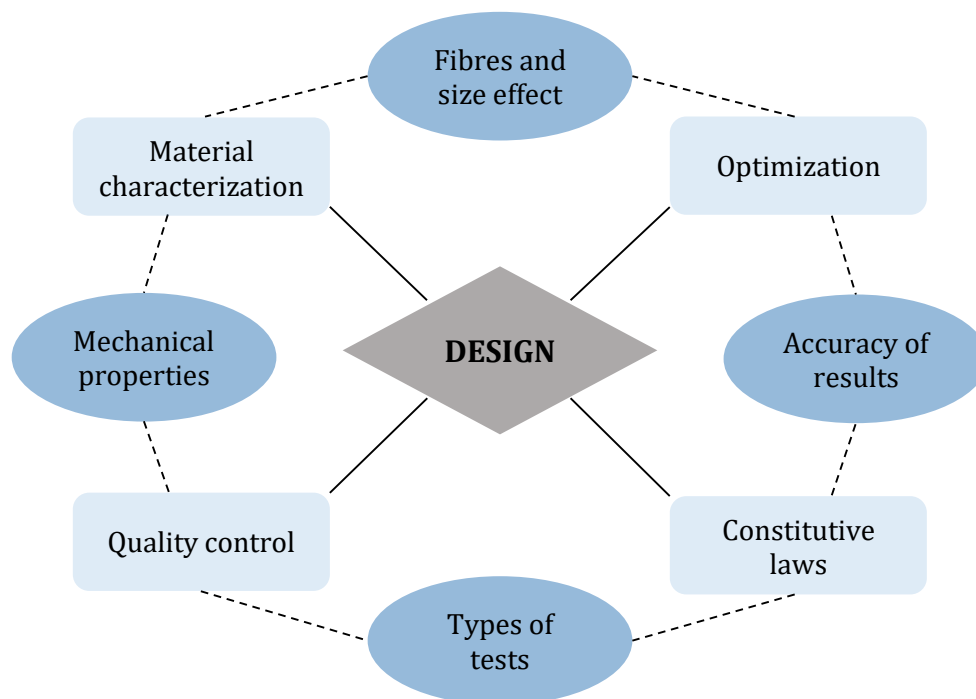


Figure 2.1 Main topics addressed for the design of FRC.

The first part of this chapter reviews several current tests to determine fibre orientation and content. Additionally, alternative methods to bending tests for the characterization of FRC are presented, focusing on those for which constitutive equations have been derived and the advantages these alternatives present concerning design and quality control. With regard to design, factors such as the influence of size effect, geometry, fibre orientation and partial safety factors are addressed given the relevance in terms of optimization. Several examples of FRC structural applications are presented along with design strategies described in previous works and experimental results.

2.2 CHARACTERIZATION OF FRC

2.2.1 Experimental determination of the fibre orientation

FRC performance strongly depends on the orientation of the fibres (Abrishambaf et al. 2017), with fibres aligned parallel to the stress flow enhancing the mechanical properties.

This issue is particularly relevant and highlights the importance of developing effective methods to assess fibre orientation in hardened concrete. Techniques such as those shown in Table 2.1 and Table 2.2 have been developed and used in different studies to determine the distribution or the orientation of fibres.

These techniques may be classified as destructive or non-destructive. Destructive tests present great limitations given that once conducted, specimens undergo irreparable damage and are no longer available for further analysis. To overcome this drawback, most of the research efforts focus on developing non-destructive tests so determining the orientation does not entail the loss of samples. The use of non-destructive tests has important implications regarding the application of these techniques on real structures, for these minimize both the impact and the damage on the structure.


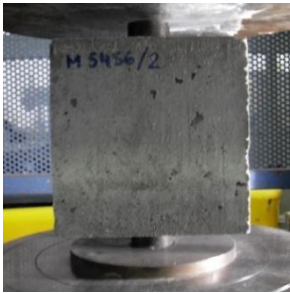
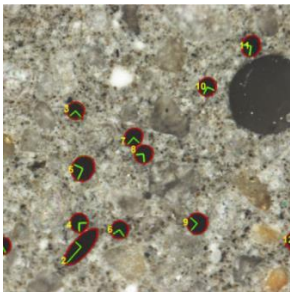
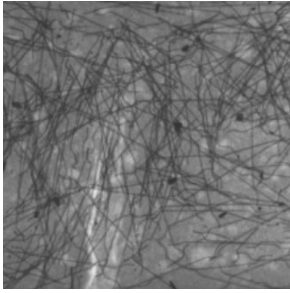
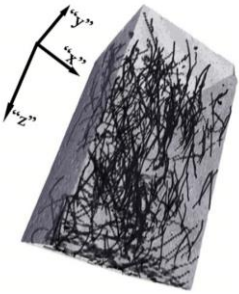
Halfway in between destructive and non-destructive tests, techniques such as image analysis, X-Ray or computed tomography may be categorized as quasi-destructive given that the specimens to conduct these tests require specific preparation. Image analysis is performed using high-resolution cameras, for which it is necessary to cut the specimens to make clearly visible the fibres intersecting internal surfaces. X-Ray analysis may require slicing the samples to obtain interpretable images. Computed tomography (CT) scanners may present some restrictions regarding the dimensions of the samples, which may need to be cut according to the admissible size of the CT equipment.

2.2.2 Alternative tests to determine the mechanical properties of FRC

Uniaxial tensile tests directly provide the most relevant parameters of the tensile behaviour of FRC. The procedure described by RILEM recommendations (Barr et al. 2003b) suggests using a cylindrical specimen with a circumferential notch at the centre. These specimens need to be glued to the testing machine and three extensometers mounted across the notch to measure the crack opening displacement. However, given that no specific standards are given to conduct this test, a wide variety of test setups and specimen geometries including dogbone-shaped, cylindrical and prismatic notched and unnotched specimens (Wille et al. 2014a) have been proposed.

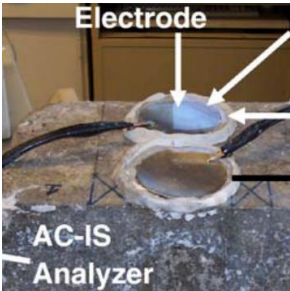

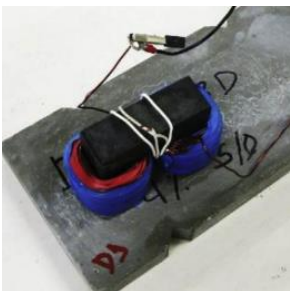
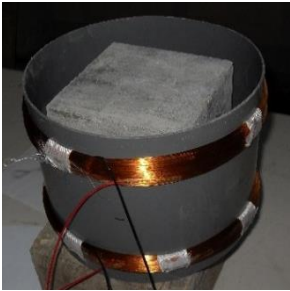

Bending tests are much simpler than uniaxial tensile tests (di Prisco et al. 2009), the former being, therefore, better candidates to characterize the behaviour of FRC. Indeed, the constitutive laws for FRC defined in most of the national and international codes and guidelines (Blanco et al. 2013) are based on the results of flexural tests according to three- and four-point bending configurations, whether notched or unnotched. However, the high scatter of the results in bending tests (Conforti et al. 2018) given the small fracture surface area still represents one of their major drawbacks. This has encouraged developing alternative methods (Figure 2.2) such as the Barcelona test (Molins et al. 2009), the Double-Edge Wedge Splitting test (di Prisco et al. 2013b), the Small Round Panel test (Minelli & Plizzari 2015) or the Montevideo test (Segura-Castillo et al. 2018b).

Table 2.1 Methods to determine fibre orientation.

	Technique	Description	Reference
Destructive (DT)	 <p>Manual counting</p>	<ul style="list-style-type: none"> • Specimens are crushed with a compression machine and a grinder to extract manually the fibres with a magnet. • Provides the content of fibres in either cast or cored specimens. 	<p>(Ferrara & Meda 2007) (Carmona et al. 2016)</p>
	 <p>Mechanical testing</p>	<ul style="list-style-type: none"> • Specimens are tested in different directions taking advantage of the relation between the post-cracking strength and fibre orientation. • Provides an estimation of the orientation of fibres in % according to the contribution in each direction. 	<p>(Pujadas et al. 2014b)</p>
Quasi-destructive (QDT)	 <p>Image analysis</p>	<ul style="list-style-type: none"> • Polished surfaces of concrete are photographed with a high-resolution camera. • Provides the inclination of the fibres by fitting ellipses to the fibres crossing the surface and calculating the length of the ellipses major and minor axes. 	<p>(Kang & Kim 2011) (Abrishambaf et al. 2013) (Nunes et al. 2017)* (Meng & Khayat 2017) (Zhang et al. 2018)</p>
	 <p>X-Ray</p>	<ul style="list-style-type: none"> • X-Rays penetrate inside the concrete and detect the fibres given the density difference between steel and concrete. • Provides images of the real internal distribution and the orientation of fibres in the specimen. 	<p>(Robins et al. 2003)* (Lataste et al. 2009) (Lim et al. 2018)</p>
	 <p>Computed tomography</p>	<ul style="list-style-type: none"> • Full samples are X-Rayed with a computed tomography scanner in slices of a specified width. • Provides a high-resolution image of the scanned slices that put together create a 3D representation of the sample. 	<p>(Pujadas et al. 2014a) (Švec et al. 2014) (Ponikiewski et al. 2015) (Zhou & Uchida 2017a) (Balázs et al. 2017)*</p>

*Pictures have been taken from the indicated references.

Table 2.2 Methods to determine fibre orientation.

Technique	Description	Reference	
 <p>AC-IS Analyzer AC-Impedance Spectroscopy</p>	<ul style="list-style-type: none"> Measures the conductivity between stainless steel circular electrodes submerged in a NaCl solution placed on the specimen surface. Provides the conductivity profile of the material to assess the fibre orientation inside the concrete. 	<p>(Woo et al. 2005) (Ozyurt et al. 2006)* (Ferrara et al. 2008)</p>	
 <p>Electrical resistivity</p>	<ul style="list-style-type: none"> Measures the electrical resistivity produced by the passage of the current from one electrode to another. Several electrodes provide the electrical resistivity in different directions to assess the fibres preferential orientation. 	<p>(Lataste et al. 2008) (Barnett et al. 2010)*</p>	
<p>Non-destructive (NDT)</p>	 <p>Magnetic</p>	<ul style="list-style-type: none"> An electric current generates a magnetic field whose permeability depends on the orientation of the fibres. Can be used to determine the orientation and the content of fibres in specimens and existing structures. 	<p>(Ferrara et al. 2012) (Nunes et al. 2016) (Nunes et al. 2017)*</p>
 <p>Inductive</p>	<ul style="list-style-type: none"> Cylindrical coil generating a magnetic field interacting with the steel fibres inside the concrete. Provides the orientation number of the fibres in each direction as well as the content of fibres inside the material. 	<p>(Torrents et al. 2012) (Cavalaro et al. 2015) (Cavalaro et al. 2016)</p>	
 <p>Translucent fluid</p>	<ul style="list-style-type: none"> Fibres are incorporated into a translucent fluid simulating concrete. Provides visual information of how fibres are oriented when pouring the material. 	<p>(Boulekbache et al. 2010)* (Zhou & Uchida 2017a)</p>	

*Pictures have been taken from the indicated references.



Figure 2.2 a) Barcelona test, b) DEWS (Nunes et al. 2017), c) SRDP (Conforti et al. 2018) and d) Montevideo test (Segura-Castillo et al. 2018b).

The Barcelona test (BCN) is an indirect test based on a double punch test configuration. It was originally developed to control the total circumferential opening displacement (TCOD) through a circumferential extensometer, although it was subsequently simplified by defining a correlation between the TCOD and the vertical displacement (Pujadas et al. 2013) to use the latter as the control variable. The test can be straightforwardly carried out in a regular compressive testing equipment, which makes it suitable for any laboratory. Additionally, the specimen is lighter than bending test beams given its shape and size (cylinders of $\phi 150 \times 150 \text{ mm}$) and has the added value of being applicable to cores extracted from existing structures.

The Double-Edge Wedge Splitting test (DEWS) is also an indirect tensile test conducted by applying a compressive load that induces a pure Mode I tensile fracture. The test is executed on thin square specimens with triangular grooves at 45° inclination, where steel rolls are placed and compressed. Notches are cut at the tip of the grooves and the crack opening is measured using three LVDTs placed at both sides of the specimen. DEWS specimens can be also obtained by coring existing structures and effectively characterize any desired orientation given that the fracture plane is prearranged according to the notches (di Prisco et al. 2013b).

The Small Round Determinate Panel test (SRDP) was proposed as a simplification of the Round Determinate Panel (RDP) given that the big dimensions and weight of the panels of the RDP test ($\approx 91 \text{ kg}$) hinder handling and placing of the samples. The SRDP specimens present a diameter of $\phi = 600 \text{ mm}$ and a depth of 60 mm , thus reducing the weight of the panel to 40 kg . An experimental programme conducted using SRDP specimens revealed that the smaller dimension of the round panel did not affect the scatter when compared to the dimension of the standard RDP. Indeed, recent investigations conducted by the same authors (Conforti et al. 2018) revealed that the scatter of SRDP may present slightly lower values than the scatter of RDP and certainly lower than four-point bending tests.

The Montevideo test (MVD) is conducted on cubic 150 mm specimens with a notch of 25 mm depth and 5 mm wide at one of the faces. A 28° inclination wedge is introduced into the notch by compression, thus producing crack initiation at the tip of the notch which leads to two separate rigid bodies connected by the fibres. The crack pattern is similar to that exhibited by three-point notched bending tests and the crack mouth opening can be measured using a displacement transducer.

Table 2.3 Stress-strain relation for DEWS and BCN.

Test	$\sigma - \epsilon$ diagram	Constitutive parameters
Double-edge wedge splitting test (DEWS)		<p>Softening</p> $\epsilon_{s,0.5} = \frac{0.5}{h_{el}}$ $\epsilon_{s,2.5} = \frac{2.5}{h_{el}}$
		<p>Hardening</p> $\epsilon_{peak} = \frac{COD_{peak}}{L_{COD}}$ $\epsilon_{h,0.5} = \epsilon_{peak} + \frac{0.5}{h_{el}}$ $\epsilon_{h,2.5} = \epsilon_{peak} + \frac{2.5}{h_{el}}$
Barcelona test (BCN)		$\sigma_1 = wF_{Pmax}$ $\epsilon_1 = \frac{\sigma_1}{E_{cm}}$ $\sigma_2 = wF_{0.02mm}$ $\epsilon_2 = \epsilon_1 + 0.1$ $\sigma_3 = wF_{0.75mm}$ $\epsilon_3 = 4.0$ $\sigma_4 = wF_{4mm}$ $\epsilon_4 = 20.0$

2.2.3 Constitutive FRC models based on alternative characterization tests

Besides the advantages in terms of characterization of the residual strength alternative tests may provide, it is important to account with an analytical formulation to estimate the tensile constitutive curves. The stress-strain ($\sigma - \epsilon$) relationship according to the DEWS was derived considering both the possible softening or hardening behaviour of the material (di Prisco et al. 2013b). For the BCN, a multilinear constitutive model describing the kinematic and mechanic fracture mechanism with predefined strain values was proposed (Blanco et al. 2014). However, the unpredictable number of fracture planes created while conducting

the BCN and the uncertainty regarding the characteristic length to determine the strain out of the crack opening (w) still raise some concerns. A summary of the $\sigma - \varepsilon$ diagrams based both on the DEWS and the BCN are shown in Table 2.3.

The Round Determinate Panel (RDP) test presents a predictable three crack pattern with a fracture surface about five times greater than four-point bending tests. Based on the results obtained by the SRDP and its reduced variability, further research was conducted with the aim of determining the parameters of the constitutive law for FRC of the MC2010 using the residual strength yielded by the SRDP (Minelli & Plizzari 2015). The method is performed through an analytical correlation of the post-cracking strength of the SRDP with the three-point bending test (3PBT) based on the crack openings. The residual strength of the 3PBT and the SRPD are calculated as shown in Eqs. 2.1 and 2.2, respectively. The equivalent crack widths between both tests are shown in Table 2.4, along with a typical load-crack width curve to identify the force associated with each crack width.

$$f_{R,j} = \frac{3F_j l}{2bh_{sp}^2} \quad (2.1)$$

$$f_{R,j} = \frac{0.00186F_j D}{t^2} \quad (2.2)$$

Table 2.4 Crack width equivalence between 3PBT and SRDP.

Crack width	3PBT	SRDP	Load - Crack width curve
w_1	0.50	0.40	
w_2	1.50	1.15	
w_3	2.50	1.90	
w_4	3.50	2.65	

2.2.4 Implications on design and quality control

A comparison of the scatter in different tests (Conforti et al. 2018) is shown in Figure 2.3. Beam tests conducted according to the specifications of the European (EN 14651), American (ASTM 1609) and Japanese (JCI-SF4) standards exhibit a greater variability than panel tests performed under an RDP and SRDP configuration. Among the reported tests, the largest scatter corresponds to the 3PBT under EN 14651 specifications whereas SRDP presented the lowest variability.

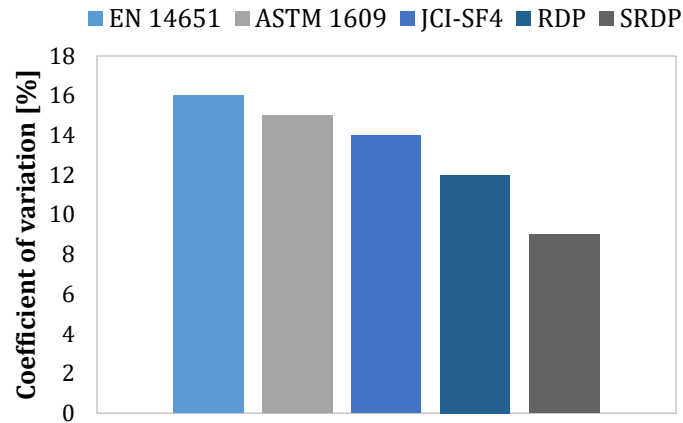


Figure 2.3 Variability of residual FRC strength according to five different tests (Conforti et al. 2018).

The importance of alternative tests with a lower variability lies in the fact that large scatter represents an important drawback when verifying the material acceptability. The characteristic strength (f_k) established within the design process and used as reference in quality control is defined as the minimum strength achieved by at least 95% of the strength determinations of all the volume of concrete under control. In FRC, f_{Rk} is the residual characteristic strength corresponding to the 5% fractile. This value is calculated as shown in Eq. 2.3, where \bar{f}_R is the average residual strength, σ is the standard deviation of the population and $Z = 1.64$ for the confidence interval of 95% probability assuming a normal distribution. Notice how the standard deviation and, by extension, the scatter of the results remarkably reduces f_{Rk} with respect to \bar{f}_R when tests with a high associated coefficient of variation are conducted.

$$f_{R,k} = \bar{f}_R - Z \cdot \sigma \quad (2.3)$$

Increasing the number of repetitions of a test is an effective strategy to reduce the scatter of the results. In statistical terms, the number of specimens tested has a direct influence on the reliability of the characteristic strength. According to the RILEM recommendations (RILEM TC 162-TDF 2003) and the specifications of Eurocode 1, this should be taken into account using the values of k shown in Table 2.5, which state for the number of specimens tested. Notice how $k = 1.00$ for a high number of specimens, which entails a closer similarity to a normal statistical distribution.

Table 2.5 Parameters k depending on the number of specimens tested (Cavalaro & Aguado 2015).

Number of specimens	3	4	5	6	8	10	20	30	∞
$k \cdot Z$	3.37	2.63	2.33	2.18	2.00	1.92	1.76	1.73	1.64
Z	1.64								
k	2.05	1.60	1.42	1.33	1.22	1.17	1.07	1.05	1.00

Reducing the dimensions of the specimens compensates for the additional concrete consumption resulting from increasing the number of standard specimens tested. However, previous studies have reported the higher variability of the results when reducing the size of concrete samples (Cavalaro & Aguado 2015) thus entailing a greater number of specimens to improve the reliability of the results. In response to that, alternative tests such

as those presented in Section 2.2.2 arise as a possible solution in terms of characterization and quality control.

2.3 CHALLENGES OF STRUCTURAL DESIGN WITH FRC

2.3.1 Influence of size and geometry effects

Tests for the characterization of the compressive strength and the modulus of elasticity are usually conducted on standard cylindrical specimens of $\phi 150 \times 300$ mm (CEN 2009; CEN 2014), even though compression may also be assessed by means of cubic samples. In this regard, the geometry should be taken into account given that cubic specimens commonly exhibit a higher compressive strength than cylindrical samples (Yi et al. 2006; Thienel 2018). Alternatively, compressive strength may be determined in cylindrical specimens of smaller dimensions ($\phi 100 \times 200$ mm), although results may also present higher values than in tests conducted on standard samples (Yazıcı & İnan Sezer 2007).

In spite of the relevance of compression strength in concrete, the main interest of FRC lies in the residual strength. With the aim of simplifying the current bending tests, research has been conducted to analyse the effect of reducing the dimensions of the prismatic beams used for bending tests. According to the results reported by previous authors (Giaccio et al. 2008), the three-point bending test conducted on standard specimens ($150 \times 150 \times 600$ mm) can be significantly simplified when using smaller specimens as long as both geometrical and test setup proportions remain equivalent.

Table 2.6 Studies on size effect of FRC under flexure.

Test setup	Concrete properties	Fibres	Dimensions of specimens	Reference
3PBT	$f_c = 150$ MPa $f_t = 9$ MPa $E_c = 45$ GPa	SF 2% Smooth 13/0.2	30x150x500 mm	(Mahmud et al. 2013)
			60x150x500 mm	
			90x150x500 mm	
			120x150x500 mm	
			150x150x500 mm	
4PBT	$f_c = 190$ MPa	SF 0.5-1.0%	50x50x150 mm	(Nguyen et al. 2013)
		Twisted 30/0.3	100x100x300 mm	
		Smooth 13/0.2	150x150x450 mm	
4PBT	$f_{ca} = 31$ MPa $f_{cb} = 48$ MPa $E_{ca} = 22$ GPa $E_{cb} = 29$ GPa	SF 0.75% Hooked 30/0.5	50x50x250 mm	(D.-Y. Yoo et al. 2016a)
			100x100x400 mm	
			150x150x550 mm	
4PBT	$f_c = 215$ MPa $E_c = 46$ GPa	SF 2%	50x50x250 mm	(D.-Y. Yoo et al. 2016b)
		Smooth 13/0.2	100x100x400 mm	
		Smooth 30/0.3	150x150x550 mm	
		Twisted 13/0.2		

Analyses regarding the size effect generally include the combination of experimental tests and numerical analyses. To experimentally determine the extent of the influence of the size effect, it is necessary to use of at least three dimensions of specimens to determine the constant parameters defining the size effect law (Bažant 2002). In this regard, the use of numerical modelling arises as an alternative to increasing the number of elements analysed,

especially those of greater dimensions that are usually more expensive to test. Accordingly, several authors have combined both approaches to study the size effect. A summary of several investigations conducted to determine the size effect of specimens under three- or four-point bending configurations (3PBT and 4PBT, respectively) is shown in Table 2.6.

Based on the results of different investigations, using smaller specimens to determine the flexural response of FRC has several implications regarding size effect that may present some inconsistencies. While some studies (Mahmud et al. 2013) conclude that the size effect on the flexural strength is almost negligible, other researchers (Spasojevic et al. 2008; Awinda et al. 2016) state that the size effect cannot be disregarded. This quandary was addressed in additional investigations (D.-Y. Yoo et al. 2016b) by analysing the residual strength of different sized concrete specimens with and without fibres and confirmed that increasing the size of the specimen leads to strength reduction (D.-Y. Yoo et al. 2016a). Therefore, the results of these investigations generally conclude that smaller elements indeed present higher residual strengths.

Despite the evidence of the presence of size effect on concrete, most of the design codes and standards currently into effect still assume that the behaviour of concrete follows the classical theories of elasticity and plasticity (Hoover & Bažant 2014). In this regard, it is broadly accepted that the strength of the structure is independent of the structure size, considering the absence of the size effect. In the case of FRC, the fact of being a relatively new material introduced for design purposes has also led to generally assume the case of no size effect.

Among the existing codes and guidelines with specific FRC constitutive laws, only the German code (DVB) and the RILEM recommendations (RILEM TC 162-TDF 2003) have been reported to account for the size effect (Blanco et al. 2013). In both design specifications, the approach to take into consideration the size effect consists in introducing a parameter to reduce the strength as the size of the specimen increases (Figure 2.4). However, the lack of consensus about how to calculate this parameter results in different correction factors to consider the size effect on FRC.

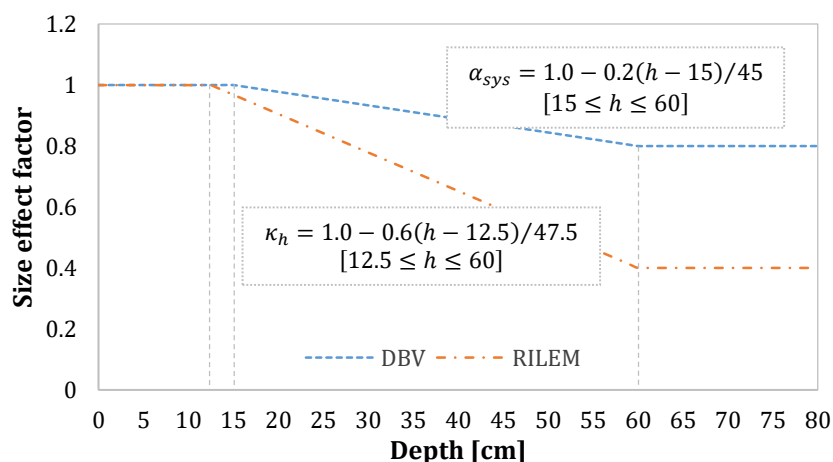


Figure 2.4 Comparison of the size effect factor in the German code DBV and RILEM (Pujadas 2013).

Constitutive models for the design of FRC real-scale elements are usually based on the results of prismatic shaped beams (150x150x600 mm) tested under a flexural configuration, assuming, therefore, an equivalent behaviour between both elements. It has

been reported (Blanco et al. 2015a) that the direct application of constitutive models on real-scale elements may lead to an unsafe design given the influence of the fibre orientation and geometry differences. These results are in accordance with previous studies (di Prisco et al. 2004) stating that size effect in FRC can be also attributed to the variations of the fibre distribution and orientation depending on the size of the element.

A numerical analysis conducted on FRC slabs of different geometries (Pujadas et al. 2014c) revealed that using the constitutive models of RILEM and EHE to perform the FEM analysis leads to a severe overestimation of the results when compared to the experimental curves. This effect is mainly attributed to the use of beams to characterize the residual strength parameters of FRC, which evidently present a different cracking behaviour than slabs and are not representative of certain real structures.

To overcome this drawback, a subsequent research was conducted (Pujadas et al. 2014d) with the aim of proposing geometry factors to adjust the constitutive equations according to the influence of the geometry. As reported in a previous study (Blanco et al. 2013), the main parameters addressed to adjust the constitutive equation were those defining the residual strength branch. In this regard, the geometric coefficients were found to present a close relation with respect to the length and the width of the slabs.

Unlike the RILEM constitutive law, the MC2010 constitutive model for FRC assumes an equivalent residual strength between the standard beam and the structural element. In this line, it needs to be analysed whether the overestimation reported by the RILEM and the EHE constitutive models also takes place and up to which extent when the MC2010 constitutive law is used.

2.3.2 Influence of fibre orientation

Given the complexity of the phenomena associated with assessing fibre orientation, extensive research has been conducted to identify the main factors influencing the distribution and orientation of the fibres. It is broadly accepted that the mixing procedure, the casting method, the formwork geometry and the dynamic effects are among the most important factors (Laranjeira et al. 2012; Švec et al. 2014). More specifically, both the flow direction and the wall-effect have been reported as the predominant aspects influencing the orientation of the fibres (Stroeven & Hu 2006; Martinie & Roussel 2011; Kang & Kim 2012). Under these effects, fibres tend to orientate towards a preferential direction which, in case of being perpendicular to the crack surface, may enhance the performance of FRC.

A relevant study on the distribution and orientation of the fibres at the cross-section is the round-robin test conducted by the RILEM TC 162-TDF (Barr et al. 2003a). This study described a methodology to count the fibres at the cross-section by dividing the cracked surface into nine equal areas in addition to the notch. A more detailed and thorough distribution of fibres at the cross-section was described by Dupont et al. (Dupont & Vandewalle 2005) taking into account both the length of the fibres and the boundary conditions of the specimen and defining three orientation regions on the cross-section. This model was later improved by Laranjeira et al. (Laranjeira et al. 2012), who developed a framework to determine the average orientation number in these three regions by accounting for the flowability of concrete, casting method and the geometry of the formwork.

Based on these studies, the fibre distribution, as well as the number and orientation of fibres, have been analysed at the fracture plane (Alberti et al. 2016b; Alberti et al. 2016c) as shown in Figure 2.5. Additional results concluded that synthetic fibres present slight differences regarding the prediction of orientation number when compared to the models based on steel fibres (Alberti et al. 2017).

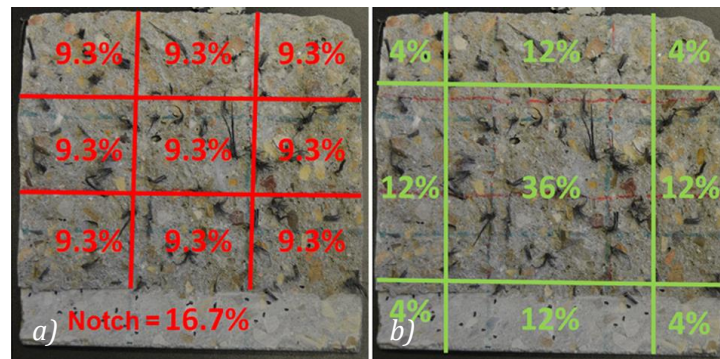


Figure 2.5 Distribution of fibres at the cross section (Alberti et al. 2016c) according to a) RILEM TC 162-TDF (Barr et al. 2003a) and b) Dupont (Dupont & Vandewalle 2005).

Many investigations address the influence of concrete flow on the orientation of the fibres and on the mechanical performance of FRC (Zerbino et al. 2012). Results reported in different experimental programmes (Abrishambaf et al. 2013; Pujadas et al. 2014a) confirm that a radial flow of concrete (such as in slabs or panels cast from the centre) makes fibres orientate perpendicular to the concrete flow direction, whereas a longitudinal flow (such as in beams) makes fibres orientate parallel to the flow direction. A recent investigation (Mínguez et al. 2018) analysed the characteristics of an SFRC wall cast from a vertical direction. A series of cores were analysed through the CT method revealing a preferential alignment towards the longitudinal direction of the wall (Figure 2.6) with fibres presenting a homogeneous distribution along the entire height.

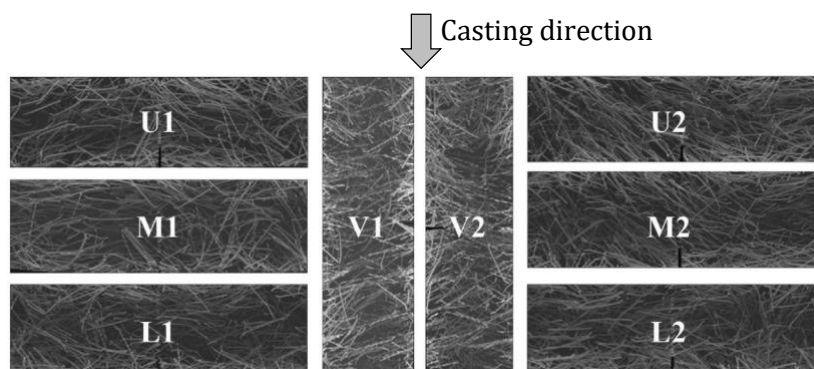


Figure 2.6 Fibre distribution in a vertical wall.

Additional results (Alberti et al. 2016a) provide the orientation number of the fibres along the length of several beams subjected to a longitudinal flow. The results show that the pouring position of concrete tends to accumulate a higher number of fibres than in the rest of the specimen. According to this, the casting of specimens should be conducted from the edges of the mould. In this regard, when bending tests were conducted, the cracked area would not present the greatest content of fibres, thus being more representative of a real structural element.

Despite the factors influencing the orientation of the fibres, constitutive models for FRC usually ignore the effect of fibre orientation on mechanical performance. One exception is found in the MC2010, which allows using an orientation factor parameter (K) to account for the favourable or unfavourable effect of the fibres on design although no specific values for it are suggested. The results presented by Blanco et al. (Blanco et al. 2015b) go a step further than only analysing the fibre orientation or the mechanical performance. The study provides a range of the multiplying factor K based on the predicted fibre distribution. This factor is used to increase or reduce the parameters defining the constitutive law according to the effect of the fibres to provide more accurate results when designing the FRC elements.

2.3.3 Partial safety factors

The recommended values of the partial safety factors for cracked FRC in tension provided by the MC2010 are the same as in plain concrete. Partial safety factors are of critical importance in design to ensure a safety margin accounting for the likelihood of an unfavourable deviation of the load or material strength with respect to the representative value. However, in the case of FRC, the uncertainty associated with the fibre distribution and the number of effective fibres resisting at the cracked section tends to decrease the characteristic residual strength with respect to the mean values due to the higher variability.

The analysis of full-scale elements results particularly interesting to obtain more realistic results of the structural behaviour given that the variability of the results tends to decrease when compared to the scatter of standard specimens (di Prisco et al. 2009). In this line, a study dealing with the calibration of FRC partial safety factors (de la Fuente et al. 2018) analysed the results of several case studies conducted on full-scale elements. The results revealed that considering a partial safety factor in FRC $\gamma_c = 1.50$ leads to meet the reliability requirements for SLS but not for ULS. Assuming such a partial safety factor may lead to a lower reliability index resulting in unsafe situations given the higher variability of FRC in terms of residual strength. According to the results of this study, a larger scatter requires a greater partial safety factor γ_c to compensate for the inherent variability of FRC to reach a reliability level equivalent to traditional reinforced concrete structures.

2.4 APPLICATION OF FRC IN STRUCTURES

The effect of fibres has been experimentally studied in concrete pipes, suspended flat-slabs, precast segments and walls, among other structural elements. In this line, previous authors highlight the relevance of FRC on precast segments for tunnel linings (de la Fuente et al. 2012b; de la Fuente et al. 2014) given the importance of crack propagation control (Plizzari & Tiberti 2007), these turning out to be among the most relevant type of elements in which fibres are being currently used. Several examples of different structural elements using fibres as the only reinforcement or combined with conventional rebars are shown in Table 2.7, whether experimental or real cases.

Table 2.7 Experimental and real case studies of FRC structural elements.

	Structure	Dimensions	Reinforcement	Reference
Experimental	Pipes	$D_i = 1.0\text{ m}$ $t = 0.09\text{ m}$ $l = 1.5\text{ m}$	SFRC HE 60/0.75 $C_f = 20/25/30\text{ kg/m}^3$	(de la Fuente et al. 2012a)
	Suspended slabs	$3 \times 1.5 \times 0.2\text{ m}$ $3 \times 2 \times 0.2\text{ m}$ $3 \times 3 \times 0.2\text{ m}$	SFRC HE 50/0.62 $C_f = 40\text{ kg/m}^3$	(Blanco 2013)
	Precast segments	$D_i = 10.9\text{ m}$ $t = 0.35\text{ m}$	RC + SFRC HE 50/1.00 $C_f = 30/60\text{ kg/m}^3$	(Liao et al. 2015)
	Wall	$1 \times 0.4 \times 0.1\text{ m}$	SFRC HE 45/1.2 $C_f = 140\text{ kg/m}^3$	(Mínguez et al. 2018)
Real application	Copenhagen district heating tunnel, Denmark	$D_i = 4.2\text{ m}$ $t = 0.3\text{ m}$	SFRC HE 47/0.75 $C_f = 35\text{ kg/m}^3$	(Kasper et al. 2008)
	Brennero Base Tunnel, Austria-Italy	$D_i = 5.6\text{ m}$ $t = 0.2\text{ m}$	RC, SFRC HE 30/0.35 $C_f = 40\text{ kg/m}^3$	(Caratelli et al. 2011)
	Line 9 Subway Barcelona, Spain	$D_i = 10.9\text{ m}$ $t = 0.35\text{ m}$	RC + SFRC HE 60/0.75 $C_f = 60\text{ kg/m}^3$	(de la Fuente et al. 2012b)
	Tunnel in Monte Lirio, Panama	$D_i = 3.2\text{ m}$ $t = 0.25\text{ m}$	SFRC HE 30/0.35-0.6-0.75 $C_f = 40\text{ kg/m}^3$	(Caratelli et al. 2012)
	Line 7 Subway Shenyang, China	$D_i = 5.4\text{ m}$ $t = 0.3\text{ m}$	RC + SFRC HE 60/0.75 $C_f = 25 - 30\text{ kg/m}^3$	(Meng et al. 2016)
	Rail tunnel Barcelona airport, Spain	$D_i = 9.6\text{ m}$ $t = 0.32\text{ m}$	RC + SFRC HE 50/1.0 $C_f = 45\text{ kg/m}^3$	(de la Fuente et al. 2017)

*Internal diameter (D_i); thickness (t); length (l); reinforced concrete (RC); steel fibre reinforced concrete (SFRC); hooked-end fibre of 50 mm length and 1.0 mm diameter (HE 50/1.0); content of fibres (C_f).

2.4.1 Design strategies

The combination of fibres with rebar reinforcement is particularly interesting to resist both diffused and localized tensile stresses (di Prisco et al. 2013a; Tiberti et al. 2014). In this situation, the contribution of fibres needs to be taken into consideration to optimize the reinforcement given that structural fibres can partially or totally replace conventional rebars. However, the lack of systematic methods to design fibre reinforced elements highlights the relevance of such methods to consolidate the use of this material.

Accordingly, a design strategy (Figure 2.7) mainly addressed for tunnel segments was described in a previous study (de la Fuente et al. 2014) to assess the optimum content of fibres to achieve the mechanical performance required in design specifications. The approach is based on the guidelines of the MC2010, which stipulates several ductility requirements including that the ultimate moment resisted by the structure (M_u) must be

equal or higher than the design cracking moment ($M_{cr,d}$) when the design moment $M_d \leq M_{cr,d}$. In case that $M_d \geq M_{cr,d}$, then $M_u = M_d$.

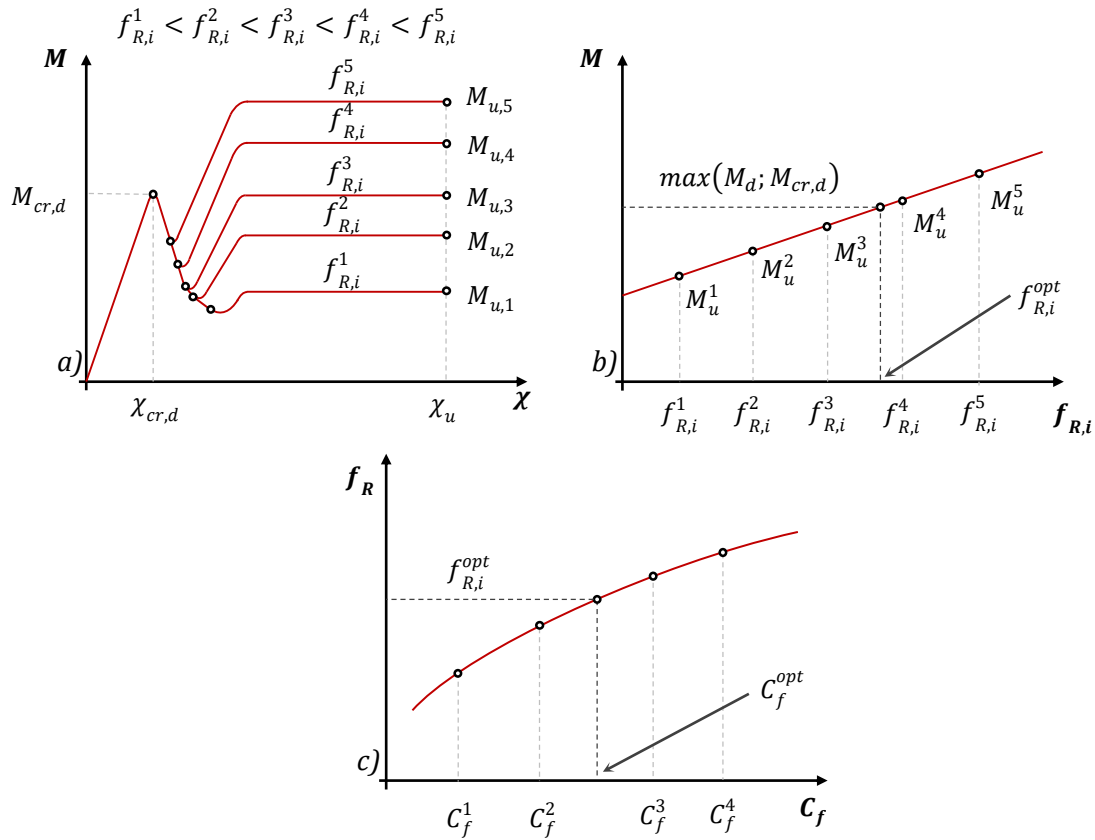


Figure 2.7 Approach to determine the optimum content of fibres on structural elements.

The approach is based on a sectional analysis to determine the moment-curvature diagrams ($M - \chi$) to identify the minimum residual strength leading to an ultimate moment verifying the ductility specifications (Figure 2.7a). The minimum residual strength to achieve the required ultimate moment is obtained through interpolation (Figure 2.7b). The content of fibres necessary to reach this residual strength corresponds to the optimum content of fibre reinforcement that needs to be blended into the concrete mix.

Based on the Model for the Analysis of Pipes (MAP) (de la Fuente et al. 2011), a similar procedure to determine the minimum content of fibres of steel fibre reinforced concrete pipes (SFRCP) can be followed. According to the crushing test, which involves an unloading-reloading process, three performance cases depending on the type and content of fibres were identified according to three stages describing the failing behaviour (Figure 2.8).

The first stage corresponds to the linear elastic behaviour, which finishes when the first crack appears (F_{cr}). During the second stage, the gradual activation of the fibres bridging the crack defines a drop of the load (snap-through) followed by a recovery finishing at load $F_{s,cr}$, when secondary cracks appear. The third stage takes place from $F_{s,cr}$ and begins with an additional snap-through that leads to a softening or hardening post-failure regime that depends on the content of fibres. A correlation between the critical loads defining the behaviour of SFRCP and the content of fibres provides the minimum content of fibres to meet loading requirements.

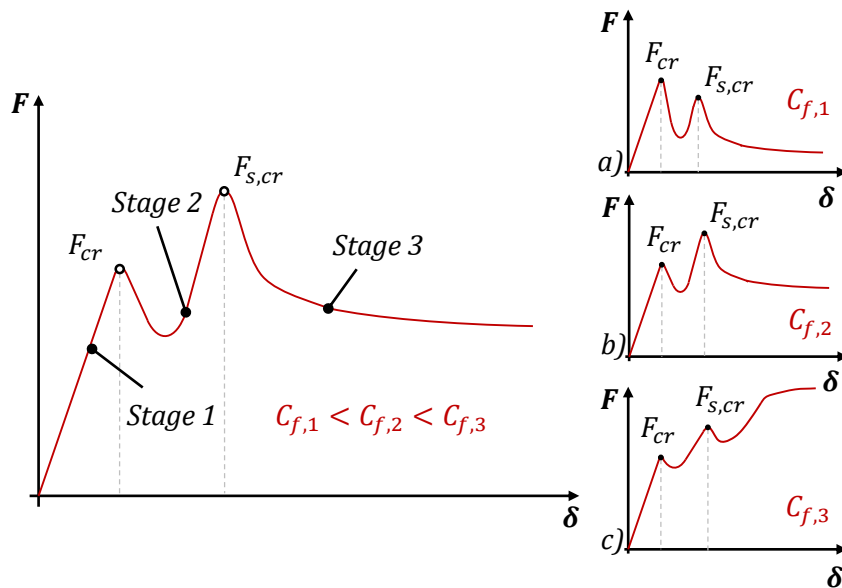


Figure 2.8 Typical $F - \delta$ curves for SFRC with different contents of fibres.

2.4.2 Crack formation and control

The addition of fibres as reinforcing material improves the transference of tensile stresses between cracks, which combined with traditional rebar reinforcement results in a reduced crack spacing and crack width (Tiberti et al. 2017). Cracks commonly follow a specific pattern depending on the position and loading procedure, whose analysis provides valuable information to determine the main orientation of the fibres, identify the weakest sections of the element and when the crack width is measured, adopt the necessary measures to improve durability.

In the case of SFRC, four main cracks describe the cracking pattern of a pipe subjected to the crushing test. According to the results reported in the study of SFRC (de la Fuente et al. 2012a), during the loading process cracks firstly appear at the top (1) and the bottom (2) of the pipe and subsequently at the laterals (3 and 3*). The crushing test configuration and the resulting crack patterns are shown in Figure 2.9.

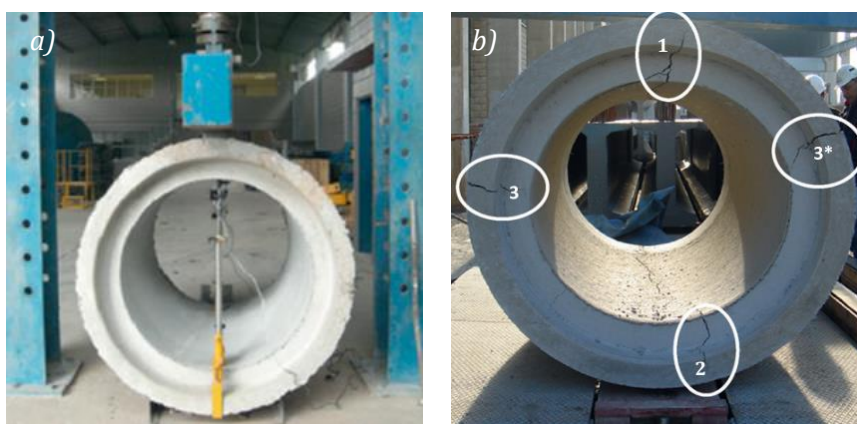


Figure 2.9 a) Crushing test and b) crack pattern in SFRC.

The crack formation of a slab subjected to central loading follows a radial crack pattern that extends from the loading point to the edges of the slab. An experimental study conducted

on a suspended slab (Blanco et al. 2015b) revealed that the opening of the main cracks was several times bigger than the secondary cracks. Main cracks produce a variation of the slab stiffness while secondary cracks are the result of the internal redistribution of stresses. An overview of the test setup and the resulting crack pattern can be observed in Figure 2.10.

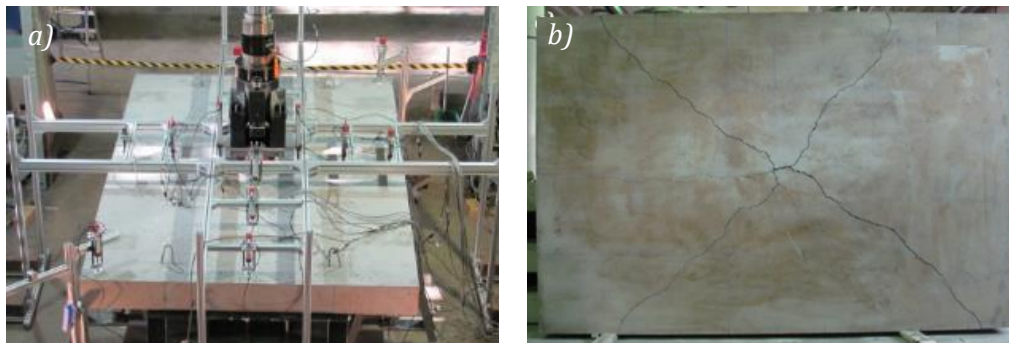


Figure 2.10 a) Central loading configuration and b) crack pattern of the slab.

Regarding the real application cases, the crack formation at the segments for the Brennero Base Tunnel (BBT) was analysed under a transversal loading placed at the centre of the element. The test configuration and the resulting crack patterns of the BBT segments are shown in Figure 2.11.

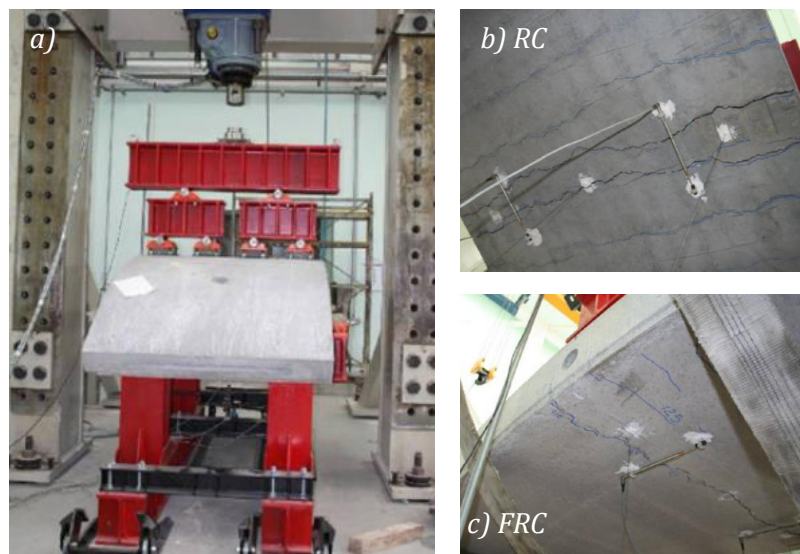


Figure 2.11 Test setup and crack patterns of BBT segments (Caratelli et al. 2011).

The crack formation at the segment intrados exhibited a different pattern according to the reinforcement. RC presents a main crack and several parallel secondary cracks propagating crosswise the segment at an average distance between them equivalent to the reinforcement spacing. Conversely, FRC only presents one main crack with several small and discontinuous cracks. Even though the FRC segment failed under a displacement and average crack opening much lower than RC elements, the results of the tests revealed an enhanced performance of FRC with respect to RC in terms of crack opening for the same load levels.

2.5 CONCLUDING REMARKS

The literature review has evidenced some of the main issues regarding the characterization and design of FRC. The most relevant conclusions that can be drawn from this analysis are presented as follows:

- Non-destructive tests arise as the best option for the characterization of fibre orientation given the possibility of combining them with mechanical tests to obtain a full characterization of the material.
- Characterization of FRC can be conducted according to alternative tests that present a lower scatter as well as a simpler test configuration and procedure with respect to 3PBT. Additionally, constitutive laws based on these alternative tests can be derived for FRC design.
- Reducing the scatter becomes significantly relevant in terms of design and quality control to obtain characteristic values of strength closer to the mean values. This can be achieved by using alternative tests with a lower associated variability and by increasing the number of repetitions.
- The change of the cross-sectional dimension unavoidably entails a change of the fibre orientation. Size and geometry effects in FRC are primarily attributed to the variation of the fibre distribution and orientation at the cracked section, especially as a result of the wall-effect and casting procedure.
- Segments for tunnel linings are among the most relevant structural applications of FRC. However, systematic methods for FRC design still need to be improved to increase FRC presence and competitiveness in construction.

3 SIZE EFFECT ON PRISMATIC BEAMS TO OBTAIN FRC DESIGN PARAMETERS

3.1 INTRODUCTION

The greater strength of high-performance fibre reinforced concrete (HPFRC) has become an asset for the construction and design of new structures, thus allowing the reduction of the dimensions of the cross-section and, consequently, the self-weight. Although dimensions are reduced in practice, this same principle is not applied in the characterization of the material given that standardized tests are used for any type of concrete. Smaller specimens could, therefore, simplify the tests and procedures in addition to being more representative of slender elements, which may be among the typical structures designed with HPFRC. However, the use of smaller specimens might induce a size effect that should be analysed and addressed from a design standpoint to identify the influence on the parameters used for design purposes (Giaccio et al. 2008).

The constitutive model for FRC of the *fib* Model Code 2010 (MC2010) is determined according to the results of three-point bending tests conducted on standard prismatic specimens. Even though this constitutive model aims to reliably approximate the behaviour of FRC for design purposes, the design rules are most of all based on the experience with steel fibre reinforced concrete (SFRC). Unlike the AFGC recommendations (AFGC 2013), the MC2010 does not include specific guidelines for HPFRC or UHPFRC and states that for these type of concretes additional rules may apply.

The French guidelines propose different dimensions of prismatic specimens be tested under a bending configuration depending on the length of the fibres. Conversely, the MC2010 only specifies one test dimension to determine the properties of FRC. However, none of them presents specific considerations regarding the mechanical size effect on these elements. In

this concern, it becomes necessary to analyse not only the cracking mechanism of the specimens used to determine the constitutive model but also the influence of the dimensions in case non-standard specimens are used.

The size effect has been an issue extensively studied and reported in the literature, with different theoretical approaches arising to explain this effect. Previous research regarding the size effect in HPFRC have been recently undertaken (Mahmud et al. 2013; Karihaloo et al. 2013; Awinda et al. 2016) through different approaches, albeit a better understanding of the influence of size effect is lacking.

3.1.1 Objectives

The MC2010 specifies clearly how to determine the constitutive law for FRC from testing standard specimens. However, the absence of a correction factor if specimens of other dimensions are used to determine the constitutive model arises as an issue that may affect the results. In light of this uncertainty and with the aim of shedding some light on this matter, several objectives have been defined in this chapter:

- Identify which parameters of the constitutive law are liable to be dependent on the size of the element.
- Assess how the cracking mechanism of the specimen affects the above-identified parameters and outline the approaches that can be applied to different sized specimens to determine the parameters of the constitutive model.
- Describe an alternative method to calculate the parameters of the constitutive laws for FRC of the MC2010 according to the approaches suggested and compute the resulting post-cracking strength analytical curves compliant with a procedure based on an inverse analysis.
- Compare the analytical curves with the experimental results to detect the main differences and establish which strategy to calculate the parameters of the constitutive law leads to a better fit of the results.

3.1.2 Outline of the chapter

In Section 3.2, the constitutive law for FRC according to the MC2010 is defined and two approaches to determine the parameters are described. The constitutive law is used to conduct a sectional back-analysis, whose procedure is detailed in the same section. The experimental programme is described in Section 3.3 showing both the mixes and the specimens cast and focusing on the dimensions of the samples to conduct flexural tests.

The results of the experimental programme are analysed in Section 3.4, displaying both the characterization of the material and the results of the inverse analysis. The differences between two approaches to determine the residual strength of the material are shown and compared to the experimental results of four fibre reinforced concrete mixes. Additionally, the influence of these approaches on the stress distribution and the neutral axis position (depth of the crack) at the cross-section is described.

3.2 ANALYTICAL ASSESSMENT OF THE POST-CRACKING STRENGTH

A procedure based on an inverse analysis is here presented to analytically compute the flexural results of FRC and obtain the load-deflection or load-crack opening curves. Among the current variety of constitutive models for FRC, the one described in the MC2010 has been selected. The main reason to choose this constitutive model lies essentially on the important repercussion and dissemination of the MC2010 recommendations in both research and construction industry.

3.2.1 Constitutive law for FRC

Reliable constitutive models are of great importance to reproduce accurately the behaviour of FRC. Different constitutive models in varying degrees of complexity and accuracy may be found in the literature and in national or international codes for FRC (Blanco et al. 2013) and even for ultra-high performance fibre reinforced concrete (AFGC 2013). However, the main particularity of the stress-strain tensile law of the MC2010 with respect to other codes is that it is able to distinguish among three cases of softening and hardening behaviour (Figure 3.1). These cases depend on the stress level achieved by the stresses at Service Limit State (SLS).

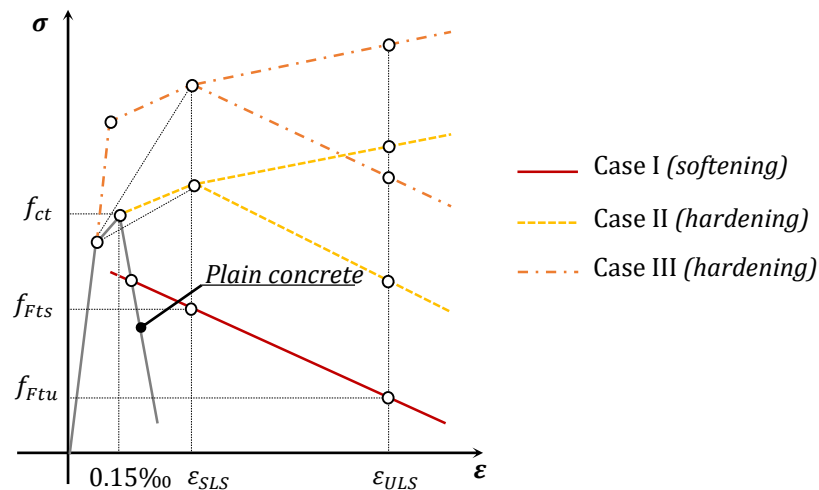


Figure 3.1 Constitutive law for FRC in tension.

Case I represents a material with a softening behaviour at SLS. The uncracked region up to the peak strength f_{ct} , as well as the stage describing the immediate post-peak stress drop, are defined in the same way as the tensile behaviour of plain concrete. Subsequently, the residual strength branch is defined by a linear post-cracking softening behaviour. Case II and III describe the performance of a material with hardening at SLS. Case II is again defined up to the peak strength f_{ct} as in plain concrete, but the stress at the first branch of the cracked region increases until f_{Fts} is achieved. In Case III, the elastic branch achieves a stress $0.9f_{Fts}$ and develops a second branch up to f_{Fts} . In all cases (I, II and III), the residual strengths f_{Fts} and f_{Ftu} are associated with the strains ϵ_{SLS} and ϵ_{ULS} , respectively, describing a linear post-cracking behaviour that can be hardening or softening.

The branches describing the strain-softening or strain-hardening post-cracking performance are defined by the stress and the strain at both Service and Ultimate Limit

State. The stress parameters are calculated through the results of the three-point bending test conducted according to the standard EN 14651:2007 (CEN 2007). The strain values may be obtained as the ratio between the crack opening and the characteristic length (Eq. 3.1). At ULS, the strain (ε_{ULS}) is limited to a value of 10‰ in hardening and 20‰ in softening.

$$\varepsilon = w/l_{cs} \quad (3.1)$$

The characteristic length (l_{cs}) is an indicator of the crack spacing used in calculations whose value is influenced by several factors such as the type or content of fibres, the matrix strength or the load level, among others (de Montaignac et al. 2012). Studies in the literature reveal that there is not a clear consensus to specify l_{cs} and researchers use different criteria to determine its value (Pujadas 2013). However, the MC2010 assumes l_{cs} to be equal to the depth of the element, which is used and validated by several authors (di Prisco et al. 2013a; di Carlo et al. 2016).

3.2.2 Approach to calculate the constitutive law for FRC

The parameters of the constitutive model of the MC2010 are based on the results of 150x150x600 mm beams tested under a three-point bending configuration according to the standard EN 14651. This test provides three strength values (f_{LOP}, f_{R1}, f_{R3}) which are used to calculate the parameters of the constitutive law f_{ct} , f_{Fts} and f_{Ftu} for FRC. These parameters are associated with specific crack mouth opening displacements (CMODs) of a standardized beam. However, the MC2010 lacks specific indications to calculate these parameters in case smaller non-standard specimens are used to simplify FRC characterization. The main issue lies in which CMOD should be considered when using smaller specimens to determine f_{Fts} and f_{Ftu} . In this regard, two approaches arise as possible options to calculate these parameters.

To describe the two approaches, the simplified failure mechanism of a beam under a three-point bending test setup considering the mid-upper point as a hinge bonding the two halves of the specimen is shown in Figure 3.2. The first approach, here referred to as Full Crack Opening (FCO), is represented in Figure 3.2a and assumes the use of same values of crack openings regardless of the size of the specimen. The philosophy of the second approach shown in Figure 3.2b, named Equivalent Crack Opening (ECO), assumes that smaller beams may require the use of equivalent crack openings and stresses in lieu of the standardized values.

In the FCO approach, smaller samples require a higher rotation (θ_2) than larger samples (θ_1) to achieve the same crack opening. In such case, considering that l_{cs} takes the value of the depth of the beam, the strain of a smaller specimen is higher than the strain of a larger sample. Conversely, the ECO approach assumes a constant rotation (θ) for any specimen size, thus achieving a lower CMOD and deflection in smaller samples. This approach leads to CMODs proportional to the depth of the specimen with identical associated strains for the different sized beams when considering again l_{cs} the depth of the beam. Consequently, the residual strengths f_{R1} and f_{R3} of the three-point bending tests in specimens with non-standard dimensions would be those associated to the equivalent crack openings.

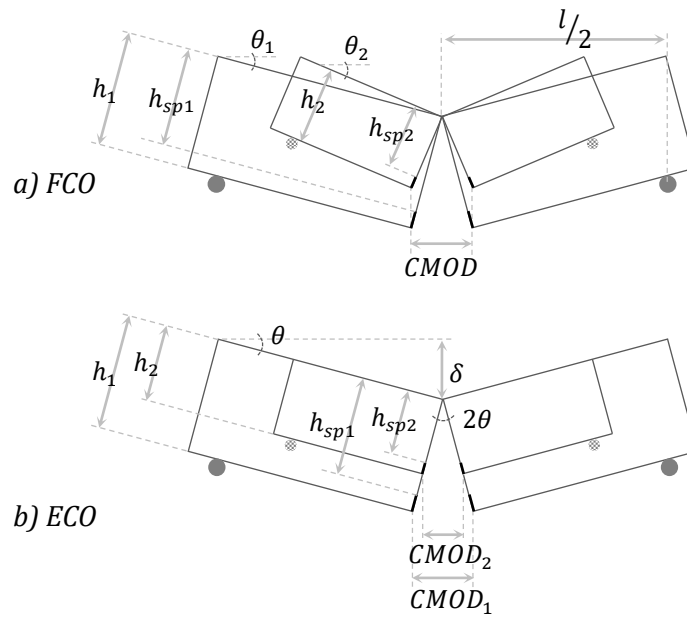


Figure 3.2 Failure mechanisms of the three-point bending test: a) FCO and b) ECO

The equivalent CMOD of a specimen of any size may be obtained through a relation between the specimen depths (Giaccio et al. 2008). According to the notation of Figure 3.2, the relations for rotation (θ), CMOD and deflection (δ) are expressed in Eq. 3.2 and 3.3.

$$\theta = \frac{CMOD}{2h_{sp}} = \frac{2\delta}{l} \quad (3.2)$$

$$2\theta = \frac{CMOD_1}{h_1} = \frac{CMOD_2}{h_2}; \quad CMOD_2 = \frac{h_2}{h_1} CMOD_1 \quad (3.3)$$

The strain at a certain crack opening is calculated by means of Eq. 3.1. Given that the crack opening remains constant with the FCO, ε_{SLS} and ε_{ULS} decrease while the specimen dimension increases. Conversely, the ECO results in identical ε_{SLS} and ε_{ULS} regardless of the specimen dimension due to the use of proportional crack widths and h_{sp} . The value of the CMOD calculated using the ECO approach results in smaller CMODs when reducing the specimen dimension, even though these are proportional crack openings. These variations of strain in the FCO and crack opening in ECO are shown in Figure 3.3.

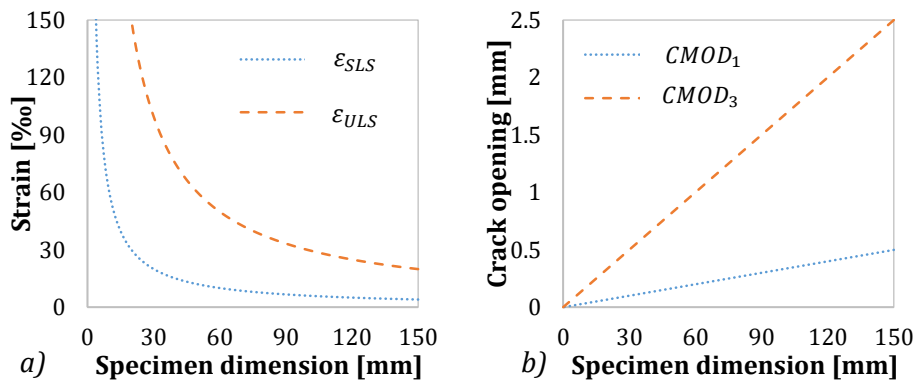


Figure 3.3 Strain according to a) FCO and b) ECO.

3.2.3 Analytical procedure

A back-calculation based on an analysis of evolutionary sections (AES) (de la Fuente et al. 2012a; de la Fuente et al. 2012c) with a multi-layer approach was used to determine analytically the flexural behaviour of FRC. This results in a very useful method especially in cases where a single dominant crack appears. Due to its simplicity and effectiveness, similar methods have been also used by several researchers (Liao et al. 2016; Mobasher et al. 2014; Mobasher et al. 2015; Yoo & Yoon 2015; López et al. 2015; López et al. 2016). In order to conduct the AES, several assumptions were adopted:

- (i) Sections remain plane after loading or imposed strains (hypothesis of Navier-Bernoulli).
- (ii) Strain compatibility: perfect bond between concrete and fibres is assumed.
- (iii) Shear stress strains are negligible and not considered (hypothesis of Euler-Bernoulli).
- (iv) The internal forces are applied on the symmetrical axis of the section.

Initially, the material properties in compression and tension are defined through the constitutive law of the MC2010 described in Section 3.2.1. To perform this analysis, the cross-section is discretized along its height into layers and it is assumed that tensile stresses are located at the bottom whereas compression stresses are placed at the top part of the section. The bottom layer of the section is taken as reference for the analysis, where a tensile strain ε_{bot} is assumed for the initial stage. Subsequently, a compressive strain at the top (ε_{top}) is assumed so the curvature χ and the strain at any layer may be calculated through Eq. 3.4 according to the combination of Navier-Bernoulli hypothesis with the strain compatibility assumption. A schematic representation of the discretization and the linear strain distribution is represented in Figure 3.4.

$$\chi = \frac{\varepsilon_{top} - \varepsilon_{bot}}{h} = \frac{\varepsilon_{top} - \varepsilon(z)}{z} \quad (3.4)$$

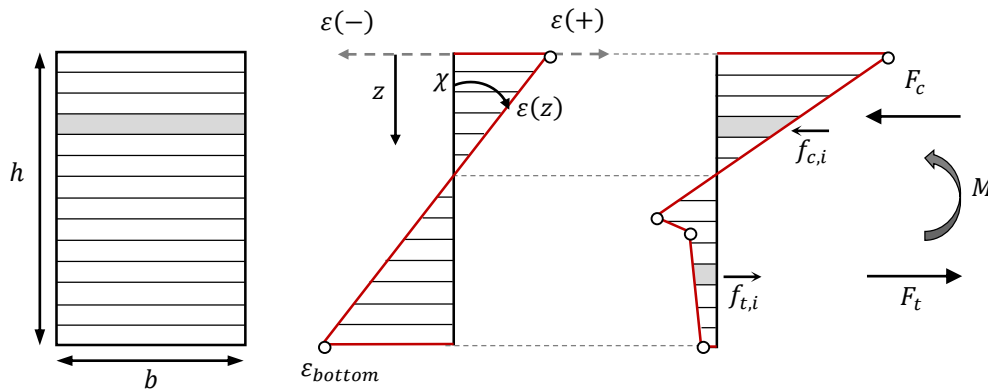


Figure 3.4 Schematic discretization of the cross-section and the linear distribution of strains and distribution of stresses.

The equilibrium condition between the internal and the external forces is satisfied by imposing Eqs. 3.5 and 3.6. For this, the predefined constitutive stress-strain law is used to calculate the stresses out of each strain from the linear distribution. The forces at each layer

are calculated through the stresses and assumed to be applied at the mid-thickness of its corresponding layer.

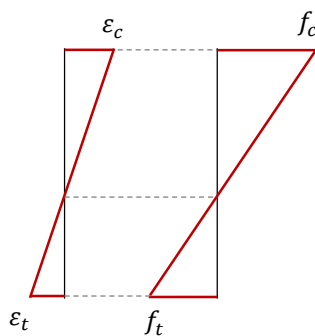
$$N = \int_{A_c} f_{c,i} dA_{c,i} + \int_{A_c} f_{t,i} dA_{c,i} \tag{3.5}$$

$$M = \int_{A_c} z f_{c,i} dA_{c,i} + \int_{A_c} z f_{t,i} dA_{c,i} \tag{3.6}$$

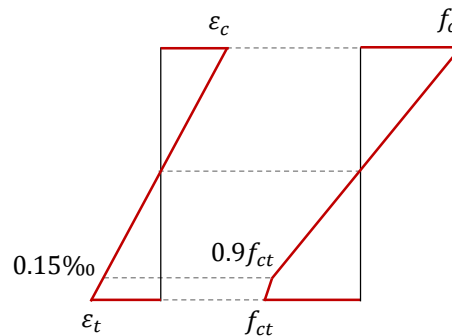
In the event that the equilibrium condition is not verified, a new ε_{top} is assumed and iterated until the equilibrium is satisfied. At this stage, the internal flexural moment at the section may be calculated. Additionally, the crack opening can be obtained through the strain at the bottom layer and the characteristic length ($w = \varepsilon \cdot l_{cs}$).

Each time the iterative process to determine ε_{top} is completed, ε_{bot} is progressively increased until the iterated result of ε_{top} achieves the ultimate compressive strain ε_{cu} . While increasing the value ε_{bot} , so does the crack width at the section. In this regard, the mechanism and the process of crack formation of FRC undergoes several steps (Figure 3.5) according to the constitutive law of MC2010.

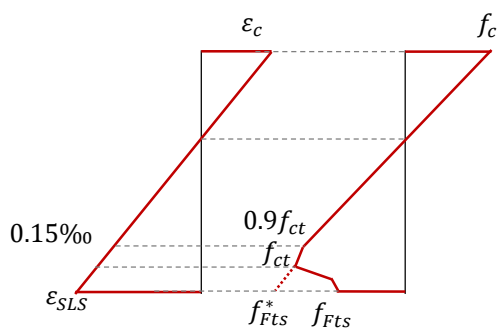
Step 1. Uncracked state. Linear elastic



Step 2. Linear elastic: microcracks in matrix



Step 3. Cracked state. Fibres bridging SLS



Step 4. Cracked state. Fibres bridging ULS

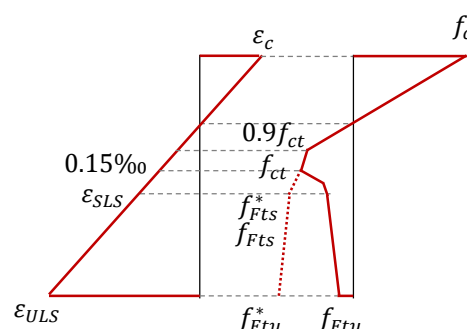


Figure 3.5 Fundamental steps undertaken by a cracked section of FRC.

Step 1 represents the linear-elastic behaviour of the material, where the tensile stresses f_t remains below the tensile strength (f_{ct}). Step 2 describes the region between $0.9f_{ct}$ and f_{ct} . At this stage, several microcracks may appear at the concrete matrix, which is evidenced by the change of the slope until reaching f_{ct} . Step 3 defines the beginning of the cracked state

and corresponds to the crack propagation branch with hardening or softening behaviour where fibres begin their bridging action up to the SLS strain. Step 4 shows the linear post-cracking behaviour up to the ULS stress and strain.

Notice how the depth of the neutral axis decreases for higher strains at the bottom surface. When the strain of the concrete at the top layer of the section achieves the ultimate strain ($\varepsilon_c = \varepsilon_{cu}$), the area under compression collapses by crushing. At this stage, the iterative process stops and the load-crack opening curve for all the iterated results are determined.

The analytical procedure for the AES is computed in several steps as shown in the flowchart of Figure 3.6. This method begins assuming an initial strain at the bottom fibre and calculates the strains at the cross-section by an iterative process checking whether the equilibrium conditions are satisfied. When a result is achieved, the strain at the bottom is increased and the iterative process starts over.

3.3 EXPERIMENTAL PROGRAMME

In order to analyse the influence of the size effect on the behaviour of fibre reinforced concrete, an experimental programme specifically designed for this aim was conducted. Concrete specimens of several dimensions reinforced with steel microfibers were manufactured and tested under a three-point bending configuration. The results of these tests are used to calibrate the parameters of the constitutive law of the MC2010 for the AES.

3.3.1 Materials and concrete mixes

The composition of the high-performance concrete mixes used in the experimental programme is detailed in Table 3.1. One plain concrete mix (M0) and four high-performance fibre reinforced concrete mixes with contents of 90 and 190 kg/m^3 were prepared. As in other studies (Wille et al. 2014a), the content of fibres was increased by replacing an equivalent volume of silica sand in order to keep constant the content of cement.

To achieve enhanced strength performances, nanosilica was introduced in all mixes as a highly reactive pozzolanic material in a content of 5% over the cement weight (o.c.w.). According to the results of previous research (Ghafari et al. 2014), powders with high specific surface increase the water demand to maintain workability, which has a direct influence on the content of water and superplasticizer. Notice how mixes M0, M90A and M190A have less water than mixes M90B and M190B, this compensated with a greater content of superplasticizer.

Table 3.1 Concrete mixes.

Materials	M0	M90A	M190A	M90B	M190B
CEM I 52.5R	800	800	800	800	800
Silica sand 3 – 4 mm	1161	1131	1098	1129	1098
Filler (CaCO ₃)	200	200	200	200	200
Water	129	129	129	185	185
Nanosilica (o.c.w.)	5%	5%	5%	5%	5%
Superplasticizer (o.c.w.)	4%	4%	4%	2%	2%
Steel fibres	0	90	190	90	190

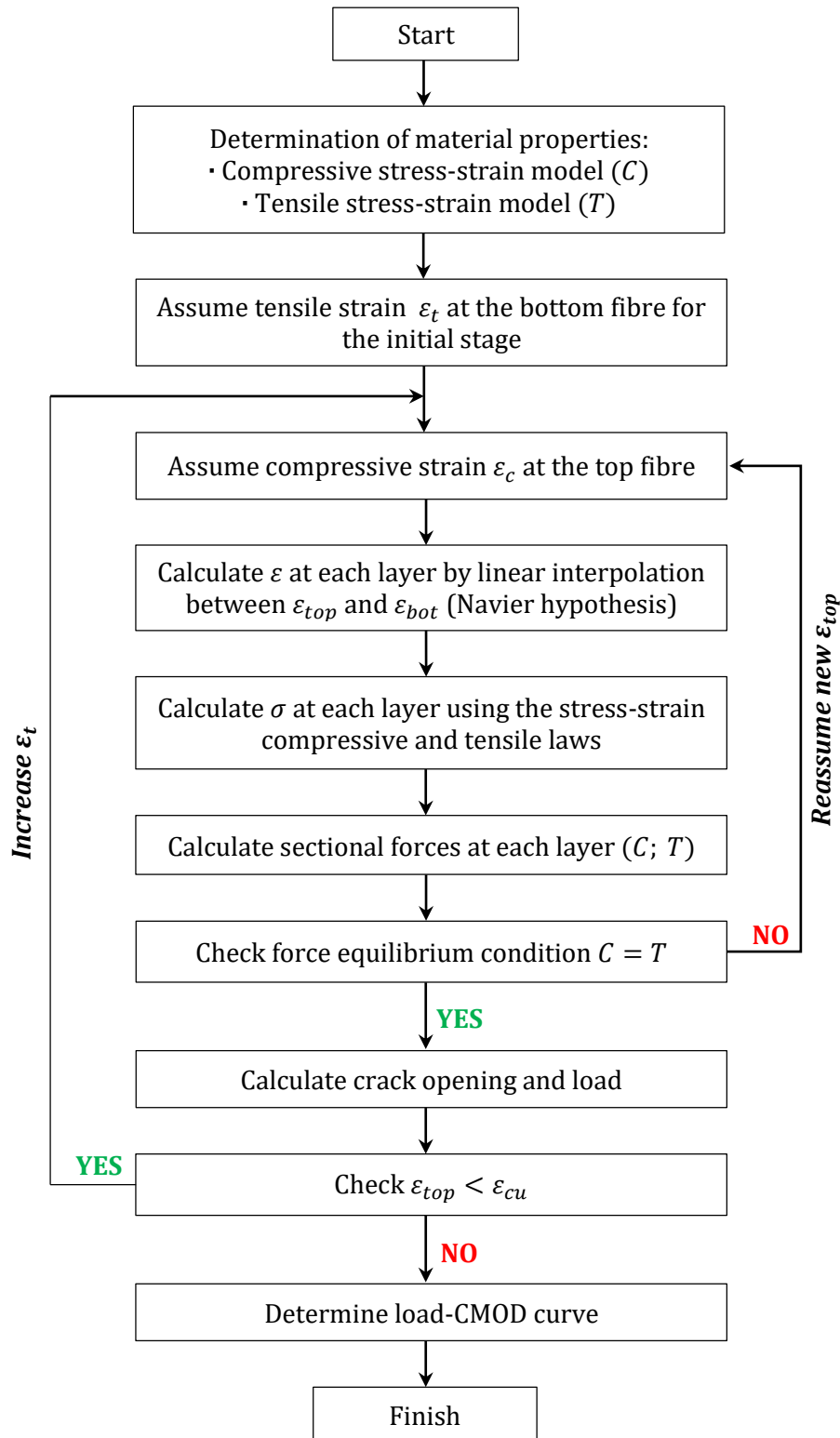



Figure 3.6 Flow chart of the analytical model.

Given that the main scope of this research is analysing the size effect of FRC, different dimensions of specimens need to be studied. In this regard, the production of small specimens limits the dimensions of the fibres, thus leading to the use of microfibers. As a result, the number of fibres per volume unit increases, which leads to a higher number of effective fibres as well as several advantages such as scatter reduction (Vandewalle 2006)

or improved shrinkage cracking control (Park et al. 2014). The properties of the microfibers used in this experimental programme are presented in Table 3.2.

Table 3.2 Characteristics of the fibres.

Property	Characteristic	Visual aspect
Fibre shape	Straight	
Length [mm]	13	
Diameter [mm]	0.20	
Tensile strength [MPa]	2750	
Elastic modulus [GPa]	200	

3.3.2 Concrete production and specimens

The concrete was produced in an industrial plant using a vertical axis mixer with an automatized system to weight and introduce the dried materials with the specified amount of water. The nanosilica, the superplasticizer and the fibres were introduced to the mix manually through an opening on the mixer. After mixing, the concrete mix was directly poured from the skip to the moulds. To prevent the loss of superficial water and a consequent early shrinkage, a curing layer was sprayed over the free surface of the specimens. Figure 3.7 shows a set of pictures illustrating several of the steps followed during production.

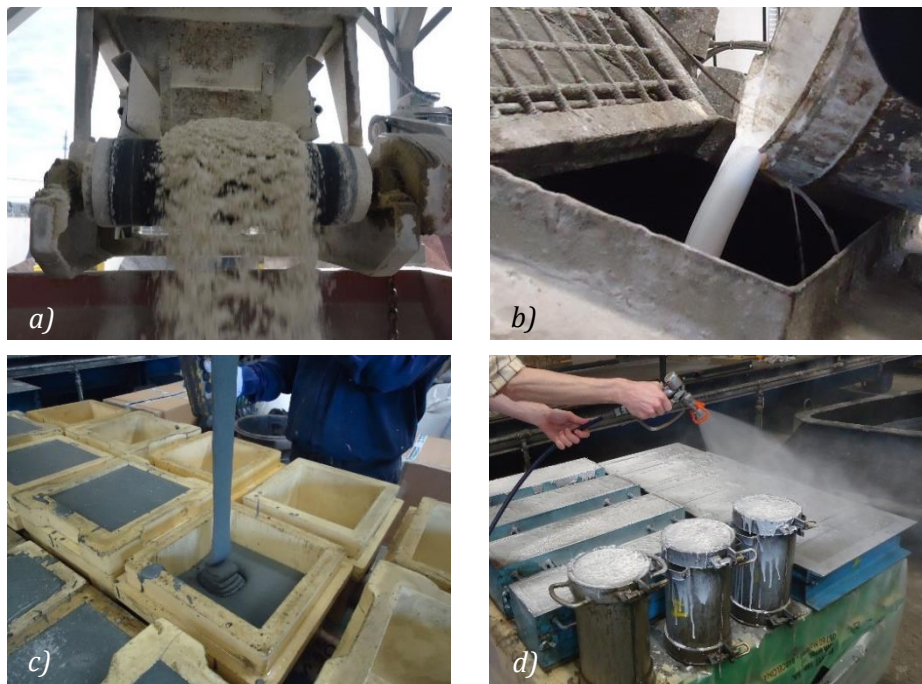


Figure 3.7 a) Conveyor belt for sand, b) nanosilica, c) pouring of concrete, d) spraying of curing layer.

For each concrete mix, 3 cubic specimens of 150x150 mm and 3 cylindrical $\phi 150 \times 300$ mm samples per mix were produced. Moreover, 3 prismatic samples with dimensions of 150x150x600 mm, 6 samples of 100x100x400 mm and 9 samples of 40x40x160 mm were cast (Figure 3.8), thus resulting in a total amount of 108 prismatic beams of three different

dimensions. The cubic specimens were used to perform the compressive test according with EN 12390-3 (CEN 2009), the cylindrical samples to assess the modulus of elasticity following the indications of EN 12390-13 (CEN 2014) and the prismatic specimens to determine the flexural and residual strength through the three-point bending test with EN 14651 (CEN 2007).

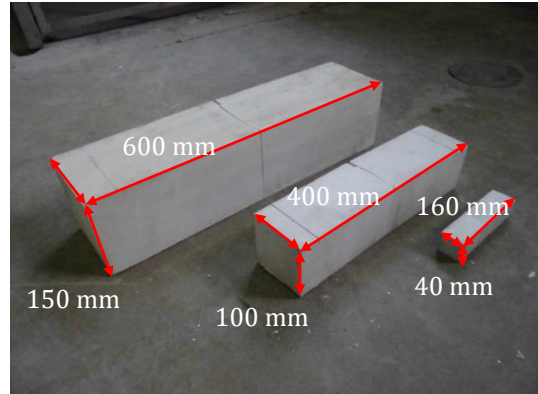


Figure 3.8 Prismatic specimens for three-point bending test.

The dimensions of the specimens for the three-point bending test as indicated in EN 14651 are prisms of 150x150x600 mm. To conduct the tests with smaller specimens 100x100x400 and 40x40x160 mm, the notch depth and the span length had to be adjusted according to the more reduced dimensions of these samples. For this, the depth-span and depth-notch ratios of the 150x150x600 mm beams were kept constant in order to maintain the proportions between the dimensions of the beams. Table 3.3 shows the effective depth (h_{sp}) and the span of the three different prisms sizes.

Table 3.3 Characteristic dimensions of the specimens for the three-point bending test.

Specimen dimension [mm]	Effective depth h_{sp} [mm]	Span [mm]
150x150x600	125.0	500
100x100x400	83.3	333
40x40x160	33.3	133

3.4 ANALYSIS OF RESULTS

The results in this section are presented in two fundamental cornerstones. First, the results of the experimental programme are addressed showing both the differences between mixes and the strength variations due to the dimensions of the specimens. Secondly, the analytical results of the AES performed with the constitutive law for FRC of the MC2010 are presented. In this part, the constitutive model is calculated with parameters obtained from the beams of different dimensions and the resulting load-CMOD curves compared with the experimental ones.

3.4.1 Compressive strength and modulus of elasticity

The average results of the compressive strength and the modulus of elasticity are detailed in Table 3.4. It shows the results of the tests conducted on three different sized cubic specimens for compressive strength and the modulus of elasticity performed on standard cylindrical samples.

Table 3.4 Results of compressive strength and modulus of elasticity.

Mix	Compressive strength [MPa]						Modulus of elasticity [MPa]	
	150x150		100x100		40x40		φ150x300	
	Average	CV	Average	CV	Average	CV	Average	CV
M0	111.2	1.8%	96.9	2.0%	97.4	7.2%	36429	0.5%
M90A	115.9	0.7%	109.5	2.9%	126.8	8.4%	36337	0.5%
M190A	117.2	0.5%	115.0	3.4%	133.6	6.4%	37674	0.5%
M90B	108.8	2.4%	102.1	1.6%	122.8	7.9%	32807	0.3%
M190B	100.3	6.8%	103.3	1.9%	124.9	6.4%	34095	9.3%

A comparison between FRC mixes with different water-cement ratios (w/c) reveals an expected reduction of the compressive strength for higher w/c ratios. This effect may also be appreciated in the modulus of elasticity, with lower values for higher w/c ratios. The higher content of water in the mix with greater w/c ratios is the main responsible of inducing a higher porosity in the concrete matrix and, therefore, reducing both the compressive strength and the modulus of elasticity.

In line with the results reported in other studies (Sorelli et al. 2005; Soutsos et al. 2012), the addition of fibres slightly increased the compressive strength with the exception of mixes M90B and M190B, which presented a reduction of the compressive strength from 108.8 to 100.3 MPa. This generalized increase of strength may be attributed to a certain confinement effect of the microfibers, inhibiting and delaying microcracking propagation produced by compression stresses when above $0.4f_{cm}$.

3.4.2 Flexural strength

The average flexural strengths of the three-point bending tests conducted on specimens 150x150x600 mm are shown in Table 3.5. The values show the strengths at the limit of proportionality (f_{LOP}) and at CMODs of 0.5, 1.5, 2.5 and 3.5 mm (f_{R1} , f_{R2} , f_{R3} and f_{R4}). These results were calculated as described in the standard EN 14651 (CEN 2007).

Table 3.5 Average flexural strengths of M90A, M190A, M90B and M190B.

Flexural strength	M90A		M190A		M90B		M190B	
	Average [MPa]	CV [%]	Average [MPa]	CV [%]	Average [MPa]	CV [%]	Average [MPa]	CV [%]
f_{LOP}	8.02	6.5	9.54	6.8	7.86	2.3	8.16	-
f_{R1}	14.58	5.8	17.83	7.6	12.06	6.9	16.35	-
f_{R2}	14.63	4.0	16.96	2.7	11.99	4.0	15.75	-
f_{R3}	13.03	3.8	14.73	4.6	10.36	3.9	13.00	-
f_{R4}	11.18	3.7	11.99	4.3	8.69	3.6	10.37	-

Increasing the content of fibres from 90 to 190 kg/m^3 enhanced f_{LOP} especially from mix M90A to M190A, with M190A presenting a f_{LOP} approximately 15% higher than M90A. Similar results have been reported in studies using steel microfibers (Pająk & Ponikiewski 2013), although in the results here presented this effect might have been accentuated by a possible manufacturing flaw. Notice that a comparison of f_{LOP} of mixes M90A, M90B and M190B presents a variation of only 1.9%, which is in line with the results reported in other

studies (Yoo et al. 2017a) given that f_{LOP} is mainly influenced by the properties of the matrix and the w/c ratio (Buratti et al. 2011; Alberti et al. 2016b). Conversely, the post-cracking results exhibited expected trends according to the content of fibres and the w/c ratios. In both groups of mixes (A and B), the increasing amount of fibres entailed a greater residual strength while the reduction of the w/c ratio resulted in lower bending stresses.

Notice also that the scatter is considerably low in comparison with the results of other studies (Lameiras et al. 2015; Alberti et al. 2016b). This is mainly attributed to the higher fibre density in the cracked surface (Sorelli et al. 2005) due to the use of microfibers. In this regard, an increased amount of fibres bridging the crack provides a higher homogeneity to flexural stresses.

To compare the average flexural strength between the different sized beams, the results need to be expressed in terms of an equivalent parameter to the different beams dimensions. The rotation (θ) in Figure 3.2b turns out to be the only parameter that remains constant and results in equivalent and comparable strengths for the different specimen sizes. Hence, instead of using the common curves load-CMOD, the flexural strengths of the four mixes of FRC are represented in Figure 3.9 with strength-rotation curves. The idea of using the rotation as an alternative parameter to CMOD in different sized specimens for comparison purposes has been also supported by other authors (Giaccio et al. 2008). In this regard, all mixes exhibit a rotation-hardening behaviour and a clear influence of the specimen size on the residual strength.

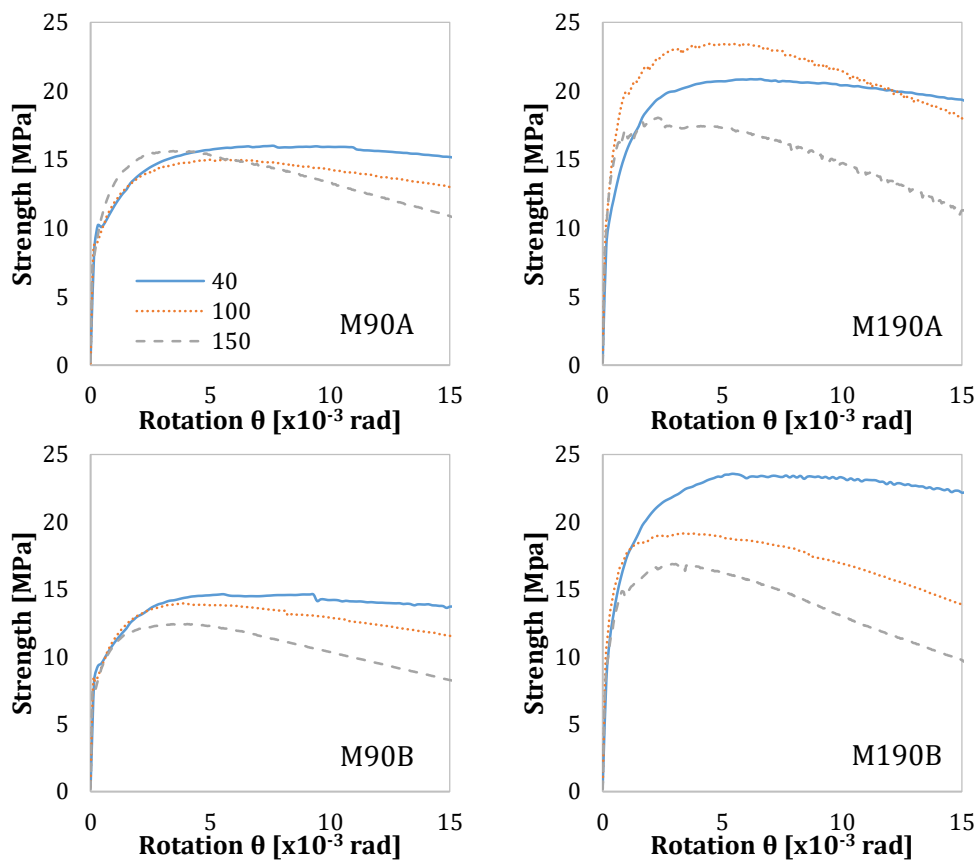


Figure 3.9 Average flexural stress in terms of strength-rotation.

In line with the results reported in previous studies (Nguyen et al. 2013; D.-Y. Yoo et al. 2016a; D.-Y. Yoo et al. 2016b), the strength in mixes M90B and M190B decreased as the specimen size increased. Two fundamental theories provide an explanation to this effect. First, and according to the deterministic size effect law of Bažant, this occurs because larger specimens release a higher energy into the crack front than smaller specimens. Second, the Weibull's statistical approach states that larger specimens present a larger possibility of presenting different flaws and, hence, exhibit a lower strength.

However, such a clear trend between the strength and the size of the specimen could not be identified in mixes M90A and M190A. In M90A, similar results were obtained for the three sizes of specimens up to a rotation of 0.006 rad . From this point onwards, the residual strength shows a behaviour inversely proportional to the dimension of the element as in the case of mixes M90B and M190B. The flexural results exhibited in M190A present the lowest residual strength for specimens of 150 mm depth, whereas the highest are obtained for the specimens of 100 mm . The smallest specimen (40 mm) displayed a greater performance when compared to the specimen of 150 mm , but lower in comparison to the 100 mm sample up to a rotation of 0.012 .

The observations in M190A differ with the findings of previous studies (Nguyen et al. 2013; D.-Y. Yoo et al. 2016a; D.-Y. Yoo et al. 2016b) with similar contents and types of fibres. Nonetheless, M190A was produced with a considerably low w/c ratio and a high content of fibres (0.16 and 190 kg/m^3 , respectively) in comparison to the aforementioned studies. The combination of these two variables results in a lower flowability of concrete (Wu et al. 2016a), which directly affects the orientation of the fibres in the element and the flexural strength (Zhou & Uchida 2017a).

Moreover, it is worth mentioning that each mix involved the production of approximately 320 specimens, many of them for additional studies not related to the research described herein. The long time required for casting such a large number of specimens could have initiated the setting of concrete even before of having finished the casting of the specimens. This may have had a negative impact on the hardened behaviour of the samples.

The average f_{LOP} and the average maximum strength of the four HPFRC mixes are shown in Figure 3.10 represented according to the specimen size. The general trend indicates a reduction of both strengths while increasing the dimension of the specimen.

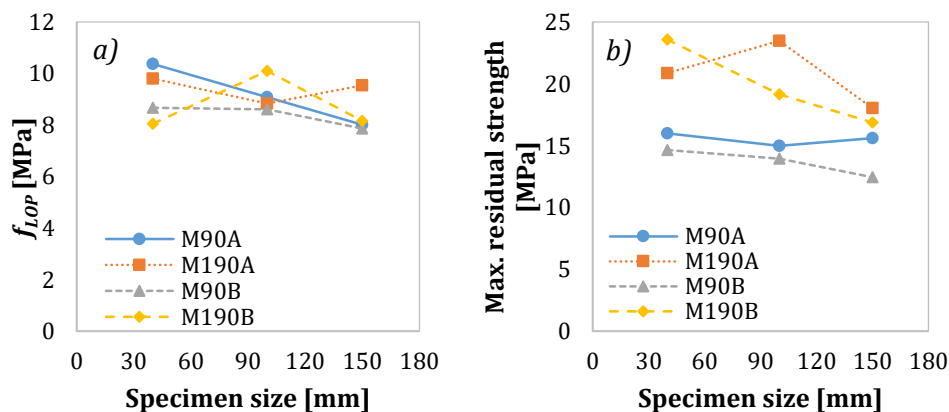


Figure 3.10 Size effect on a) f_{LOP} and b) maximum strength.

As previously seen in Table 3.5 and also reflected in Figure 3.10a, the addition of different contents of fibres did not have a significant effect on the results of f_{LOP} given that this parameter is mainly dependent on the matrix properties. This observation becomes more evident when analysing the f_{LOP} results of the smallest specimens. Mixes M90A and M190A presented higher values of f_{LOP} than mixes M90B and M190B, a behaviour that is the direct consequence of the difference in the w/c ratio. Moreover, the lower strength of mixes with 190 kg/m^3 with regard to their counterpart with 90 kg/m^3 confirms that increasing the content of fibres does not entail a greater cracking strength. Indeed, the lower results of mixes M190A and M190B with regard to M90A and M190B, respectively, may be a consequence of a higher induced porosity in the matrix as a result of the higher content of fibres (Yu et al. 2014; Söylev & Özturan 2014).

The results in Figure 3.10b clearly show how increasing the content of fibres enhances the maximum residual strength. This effect is a direct consequence of increasing the number of fibres in the cracked section (Zerbino et al. 2012; Zhou & Uchida 2017a). The results also indicate the influence of the w/c ratio on the residual strength due to an improved bond strength at the fibre-matrix interface for lower w/c ratios (Lawler et al. 2005).

Considering the relations between parameters shown in Eq. 3.1, the rotation at the maximum residual strength was assessed for the four mixes and three sizes of specimens. Figure 3.11 displays the rotation and the CMOD at the maximum flexural residual strength vs. specimen size relation. These results present a generalized trend showing a decrease of the rotation while increasing the dimension of the specimen, whereas crack opening increases with the specimen size.

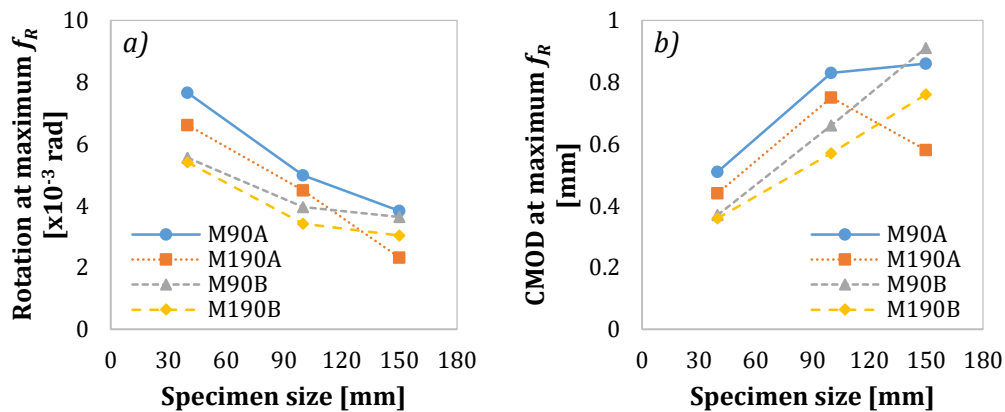


Figure 3.11 Size effect on a) rotation capacity and b) CMOD at maximum residual strength.

As the size of the specimen decreases, so does the rotation at the maximum residual strength. This decreasing trend with larger specimen dimensions is mainly attributed to the mutual dependency between the rotation and the maximum residual strength. Notice that the apparition of cracks activates the pull-out mechanism of the fibres. Furthermore, as described in Figure 3.11b, the crack opening in large specimens increases with the specimen dimension, thus leading to wider cracks than in small samples. Therefore, the necessary external load to produce the pull-out of the fibres should be higher in smaller than in larger specimens.

3.4.3 Constitutive models

To perform the AES, the constitutive model for FRC was calculated for each mix and specimen dimension according to the two approaches described in Section 3.2.2. For this, both strains ε_{SLS} and ε_{ULS} are calculated following the relation between crack opening and strain of the MC2010 as indicated in Eq. 3.1. In this regard, the characteristic length l_{cs} of each specimen corresponds to the effective depth h_{sp} of Table 3.3. Depending on the approach (FCO or ECO), the CMODs at SLS and ULS take different values for each specimen dimension resulting in the strains shown in Table 3.6.

Table 3.6 Crack openings and strains according to FCO and ECO.

Specimen dimension	Full crack opening FCO				Equivalent crack opening ECO			
	$CMOD_1$ [mm]	$CMOD_3$ [mm]	ε_{SLS} (‰)	ε_{ULS} (‰)	$CMOD_1$ [mm]	$CMOD_3$ [mm]	ε_{SLS} (‰)	ε_{ULS} (‰)
40 mm	0.50	2.50	15.00	75.00	0.13	0.67	4.00	20.00
100 mm	0.50	2.50	6.00	30.00	0.33	1.67	4.00	20.00
150 mm	0.50	2.50	4.00	20.00	0.50	2.50	4.00	20.00

Both f_{Fts} and f_{Ftu} of the constitutive law are calculated for each geometry according to the crack opening of the experimental characterization results $CMOD_1$ and $CMOD_3$, respectively. Given that the crack openings considered in both approaches are different, the strengths from the experimental results and, therefore, the strengths of the constitutive model will also result in different values. The constitutive laws for FRC are shown in Table 3.7 according to the two approaches considered, presenting clear differences between the two approaches. The experimental results in terms of strength-rotation are also shown for comparison purposes.

The main difference between both approaches lies in the strains at SLS and ULS. As previously stated, the FCO entails greater strains in smaller specimens due to the proportionally higher crack opening. This is clearly evidenced in the shape of the constitutive model calculated through the FCO, presenting lower strains for larger specimens at both SLS and ULS. This contrasts with the results of the constitutive model determined with the ECO. In this case, the crack openings for each specimen dimension are proportional to the specimen size and the strains remain constant regardless of the dimension of the element.

In general terms, all the constitutive model curves follow similar trends with smaller specimens showing the greatest strengths. A comparison of the experimental strength-rotation results with the constitutive laws reveals the similarities between the curves, thus suggesting which approach would be more appropriate to determine the constitutive law. In this regard, the resemblance of the experimental strength-rotation to the constitutive model is closer with the ECO than with the FCO. This is mainly caused by the two defining parameters: the strains and the stresses of the constitutive model. Additionally, the assumptions of the ECO entail that the rotation θ and the strain ε are directly proportional.

Table 3.7 Constitutive laws according to FCO and ECO and experimental results.

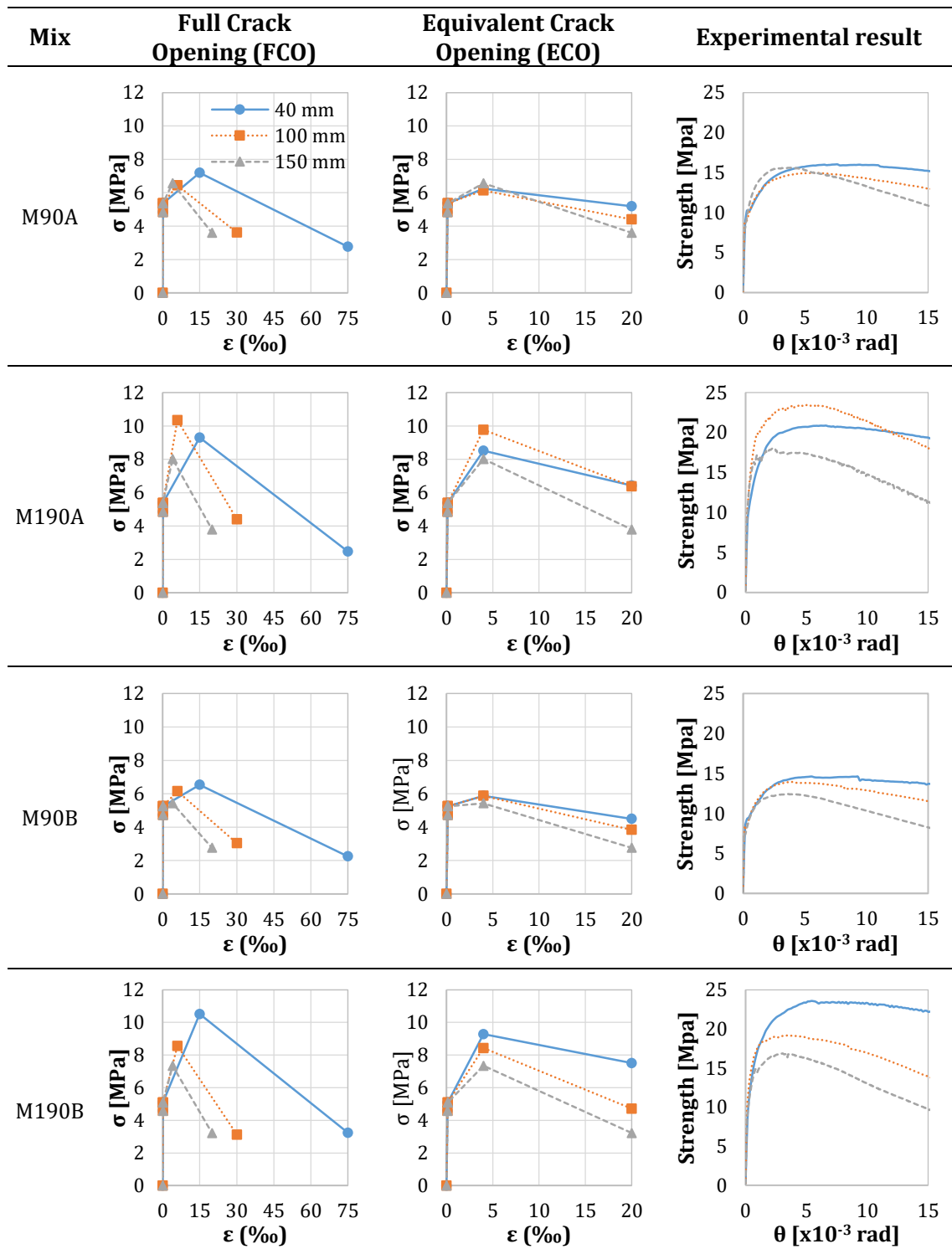


Figure 3.12 presents the constitutive model strength parameters f_{Fts} and f_{Ftu} for the three specimen sizes of the 4 mixes calculated according to both approaches FCO and ECO. The results reveal how the influence of the fibre content is more evident in the results of f_{Fts} than in f_{Ftu} , which suggests that the reinforcing effect of fibres takes place mainly at reduced strains and crack openings. The effect of the fibres is even stronger in smaller specimens. According to the FCO approach in specimens of 40 mm, M190A and M190B present f_{Fts} values around 30% and 60% higher than M90A and M90B, respectively. These

results contrast with the counterpart in specimens of 150 mm, whose f_{Fts} variation for FCO changes from 30% to 22% and from 60% to 36%.

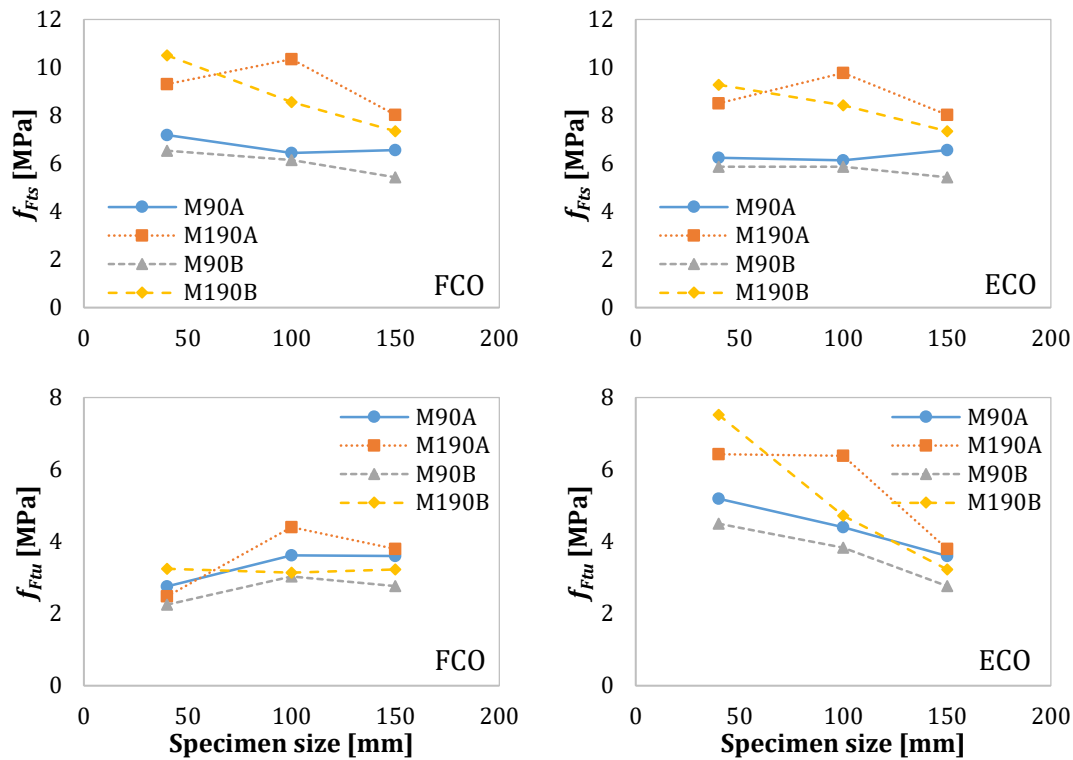


Figure 3.12 Size effect on f_{Fts} and f_{Ftu} according to FCO and ECO approaches.

A comparison between both approaches reveals a strong similarity between FCO and ECO in terms of f_{Fts} , although there are relevant differences between approaches in f_{Ftu} . In the case of FCO, f_{Ftu} presents a slightly increasing trend while the dimensions of the samples increase. Conversely, f_{Ftu} exhibits a clear decreasing trend when calculated according to the ECO approach. In this regard, f_{Ftu} presents considerably lower values for FCO than ECO in specimens of 40 mm.

3.4.4 Sectional analysis

The parameters of the constitutive law present different values depending on the approach and have a direct influence on the results of the sectional analysis. The results of the inverse analyses are presented in Figure 3.13. These results show the experimental curves of the four mixes compared to the analytical curves of the AES using the constitutive models calculated through the FCO and the ECO approaches shown in Table 3.7. The results are shown in terms of Strength-Rotation up to $\theta = 0.02 \text{ rad}$, which corresponds to a strain at the notch $\varepsilon = 40\%$. Notice that in specimens of 150 mm only one analytical curve is presented given that for this dimension the parameters of both approaches coincide.

A comparison between the analytical curves obtained using the FCO and the ECO approach reveals that when calculating the constitutive law using the latter, the analytical strength-rotation curves present a more accurate fitting with regard to the experimental results. These differences lay both in the strains and the strengths associated with each approach. Nonetheless, the analytical curves present a generalized trend to overestimate the experimental results.

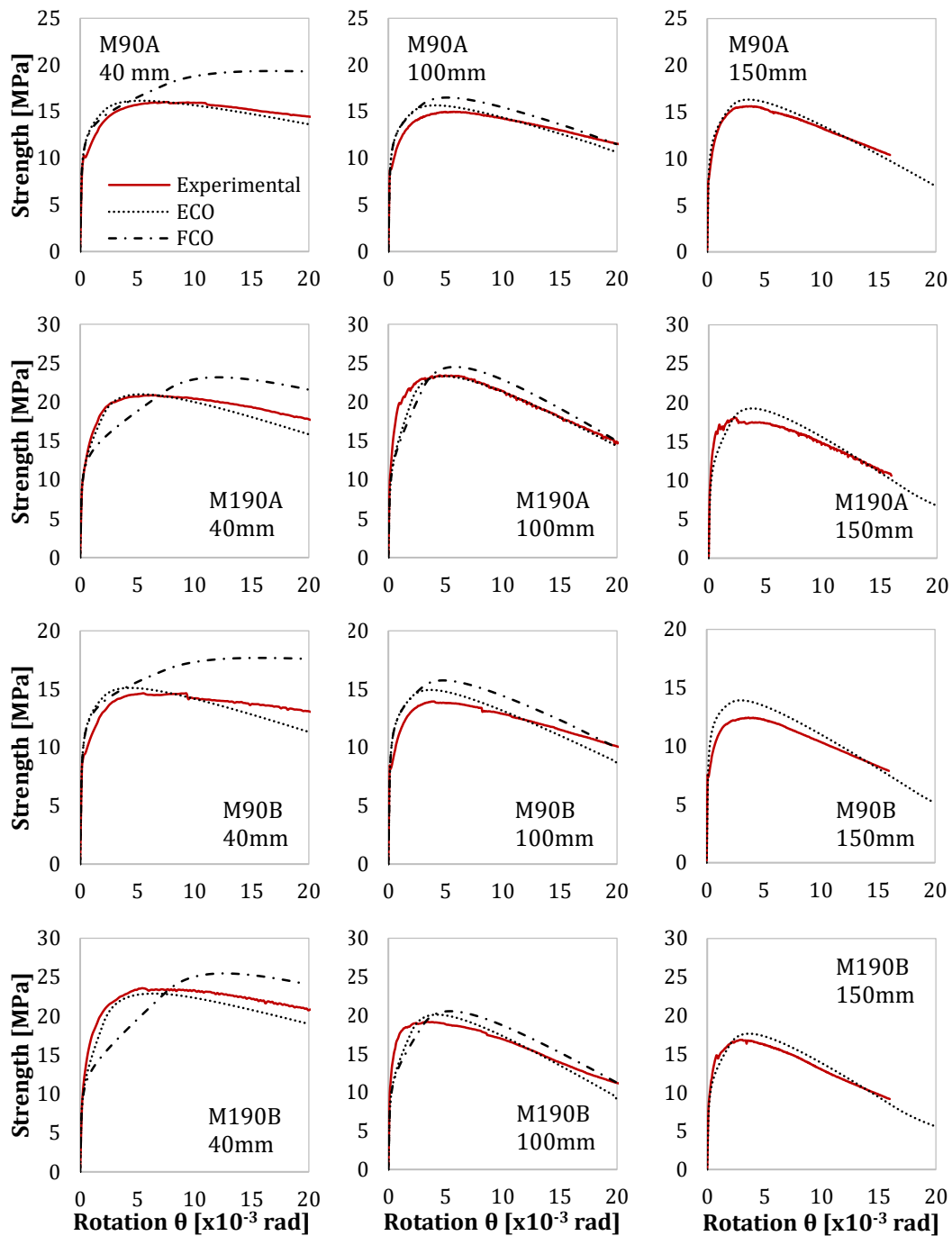


Figure 3.13 Comparison between experimental and MC2010 results.

Up to the cracking point, there are no significant differences between approaches and the experimental results. This is attributed to the fact that up to this point, both approaches are defined according to the tensile strength branch of plain concrete as described in the MC2010, with both approaches sharing the same parameters. From this point onwards, and at the cracked stage, the differences on the constitutive law arise entailing the variations between the experimental and the analytical results.

The differences between the experimental and the analytical results are stronger when using the FCO approach, smaller specimens or higher contents of fibres. For specimens of 40 mm and mix M90A, FCO and ECO presented a strength compared to the experimental results 2.8% and 5.2% higher at $\theta = 3.5 \cdot 10^{-3} \text{ rad}$, respectively. Only with the FCO

approach, this value increased from 2.8% to 33% at $\theta = 20 \cdot 10^{-3} \text{ rad}$, whereas the difference in ECO at this rotation remained 5.6% below the experimental value. Similar trends and results are obtained with mix M90B.

Regarding mixes with 190 kg/m^3 , differences between FCO and experimental results at small rotations increase in comparison with mixes blended with 90 kg/m^3 . At $\theta = 3.5 \cdot 10^{-3} \text{ rad}$, M190A calculated through FCO is 15% lower than the experimental result, whereas the difference at the same rotation between ECO and the experimental values is only 1.5%. At $\theta = 20 \cdot 10^{-3} \text{ rad}$, the differences with respect to the experimental results were 21% (FCO) and 11% (ECO). As in the case of mixes with 90 kg/m^3 , mix M190B presented analogous results to M190A.

In specimens of 100 mm , the differences between analytical and experimental results shrank. Almost identical results were exhibited through the FCO and the ECO up to a rotation of approximately $\theta = 2.5 \cdot 10^{-3} \text{ rad}$ in M90A, with FCO and ECO overestimating the experimental results at this rotation 8.7% and 8.5%, respectively. Regardless of the similarities between approaches, for greater rotations, the FCO provides higher results than both the ECO and the experimental curve. In mixes M190A and M190B, both FCO and ECO present again similar results although underestimate the experimental value up to a rotation that corresponds approximately to the maximum flexural strength. After this, the ECO presents more accurate results than the FCO, which again slightly overestimates the results of the descending branch of the curve.

The analytical curve in specimens 150 mm represents both FCO and ECO approaches. It shows a reasonable fitting, albeit it generally overestimates the results if compared to the experimental values. The most accurate fitting occurs for M90A, while the highest overestimation takes place in M90B.

3.4.5 Neutral axis and stress distribution

The neutral axis defines the boundary of the concrete section under compression and tensile stresses. The results of the AES provide the strains at the bottom and at the top layer of the section, which can be used to determine the neutral axis depth assuming the hypothesis of Navier-Bernoulli. The stress distribution and the relative position of the neutral axis to the specimen depth (x_n/h) at the cross-section of mixes M90A, M190A, M90B and M190B obtained through the AES are shown in Figure 3.14 for the three dimensions of beams analysed. The results show the stress distributions for a CMOD of 0.5 mm and a rotation of $5 \cdot 10^{-3} \text{ rad}$.

The results reveal the influence of the control parameter (CMOD or rotation) on the relative depth of the neutral axis depth x_n/h based on the strains and stresses patterns that satisfy the sectional equilibrium. If the crack opening is set to a certain CMOD regardless of the dimension of the specimen, the neutral axis leads to a lower x_n/h while the size of the element decreases. As previously stated, a given CMOD is comparatively higher in smaller specimens, thus entailing a greater ε_{bot} given the relation between the crack opening and the effective depth of the specimen ($\varepsilon = w/l_{cs}$). Consequently, if ε_{bot} is higher in smaller specimens, the position of the neutral axis shifts upwards the cross-section with regard to larger samples. Conversely, a constant rotation θ entails an identical ε_{bot} regardless of the dimension of the element given that the strain is determined as a function of the rotation

($\varepsilon = \theta/2$). This leads to the same relative position of the neutral axis x_n/h when using elements with different effective depths.

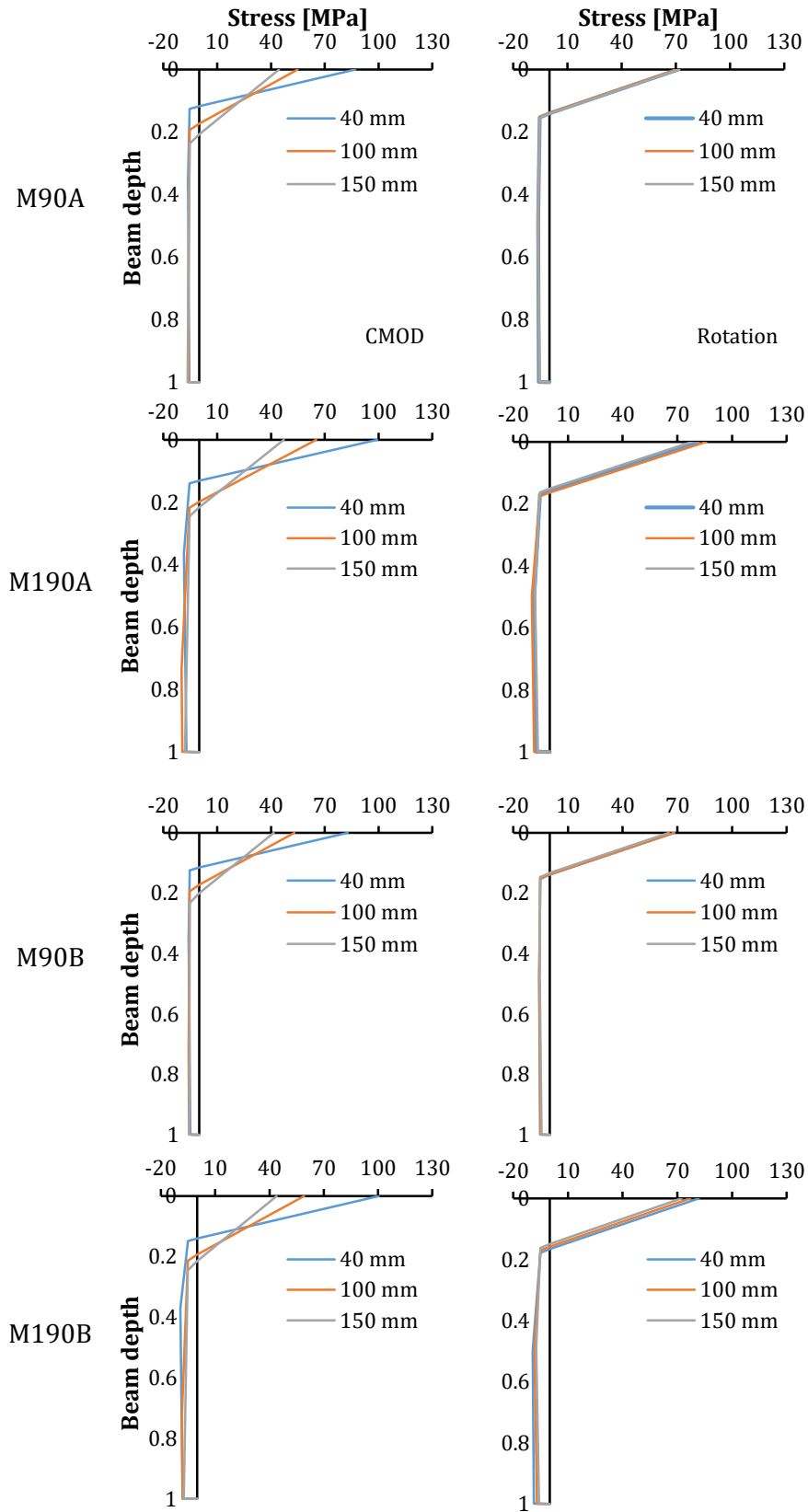


Figure 3.14 Stress distribution at the cross-section and relative neutral axis depth.

The position of the neutral axis x_n/h can be extended to other values of CMOD and rotation, leading to curves showing the position of x_n/h at different flexural stages. These results are exhibited in Figure 3.15 for mix M90A, presenting the evolution of x_n/h through increasingly crack openings (FCO) and rotations (ECO). These results show a generalization of the relative neutral axis depth depending on the control parameter and the size of the element. These results have not been differentiated on the content of fibres given that no significant differences were appreciated in the depth of the neutral axis in Figure 3.14.

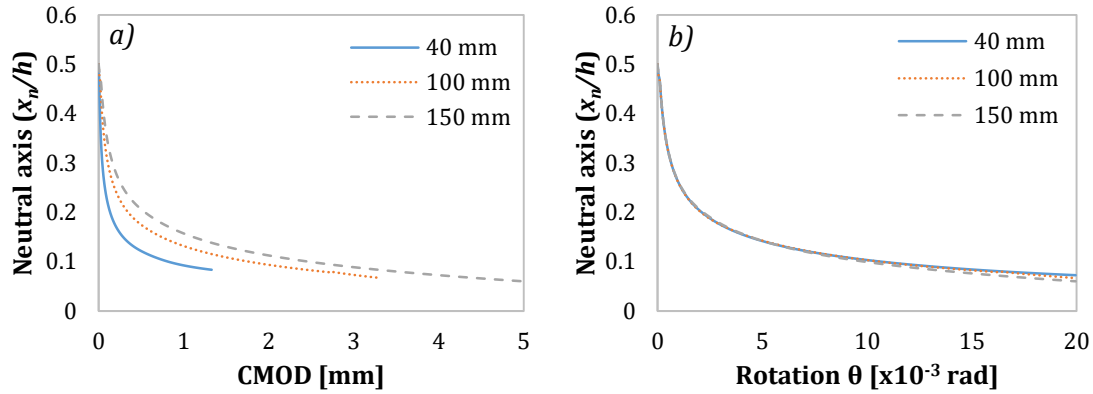


Figure 3.15 Neutral axis depth according to a) CMOD and b) rotation.

Notice that three curves—one for each specimen dimension—are obtained for both types of control: CMOD and rotation. Doubtlessly, the dependence on the size of the element is greater for FCO given that the strain for a given CMOD is higher in smaller specimens, shifting the neutral axis upwards the section. The slight variation of x_n/h vs. rotation with the specimen size basically lies in the different shape of the constitutive law. In this case, a given rotation entails the same strain, but the stress at the constitutive law associated with that strain may be different depending on the size of the specimen. This is in line with the sectional analyses shown in Figure 3.14, which shows three different positions of x_n/h for a given CMOD and a single x_n/h for a fixed rotation.

The sectional stress distribution obtained through the AES for a certain rotation at the mid-span cross-section of 150 mm beams of the four mixes is shown in Figure 3.16. These results correspond to a CMOD of 0.5 mm and a rotation $\theta = 0.002$ to compare the influence of the fibre content on the stress distribution and the neutral axis.

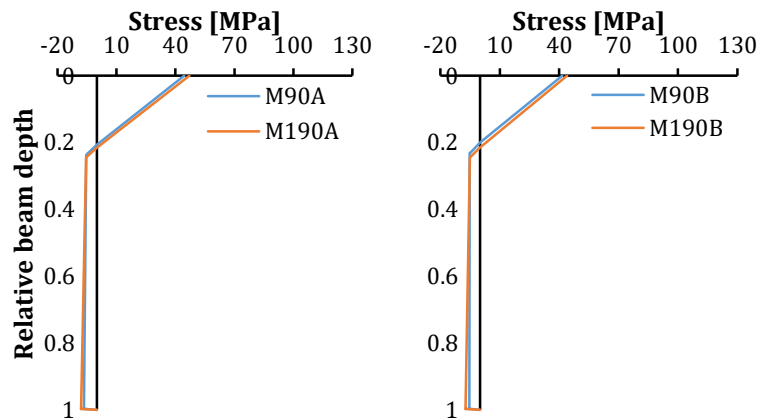


Figure 3.16 Neutral axis depth according to the content of fibres.

Notice that for this specific case of study, insignificant differences may be observed in x_n/h when comparing the results according to the content of fibres. This is in line with the results of previous studies (Yoo et al. 2015), which show that the position of the neutral axis is barely influenced by the content of fibres when the volume of fibres in the concrete mix exceeds a volume of 1.0%. However, these results may not be applicable to other cases given that the position of the neutral axis does not only depend on the type and content of fibres, but also on the compressive strength and the resulting equilibrium of forces at the sectional analysis.

According to this experience, a content of fibre reinforcement below 1.0% would lead to decreasing x_n/h . A comparison of the content of fibres throughout further rotations is shown in Figure 3.17, showing the scarce differences in x_n/h attributed to the content of fibres.

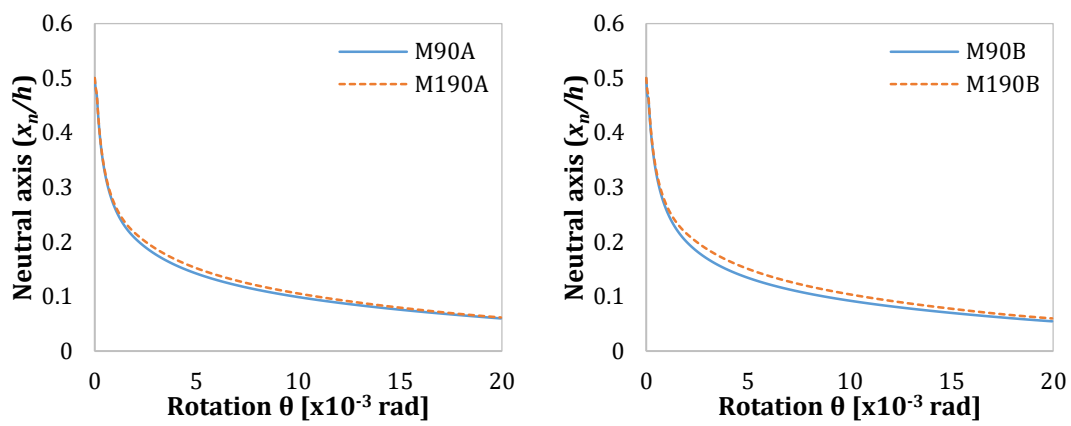


Figure 3.17 Extended neutral axis depth-rotation according to the content of fibres.

3.5 CONCLUDING REMARKS

This chapter works from the premise that the MC2010 only specifies the procedure to calculate the parameters of the constitutive law for FRC using standard specimens. Accordingly, in case of using non-standard specimens, this procedure should be adapted to the characteristics of the alternative non-standard prismatic dimensions. Based on the results of an experimental programme involving flexural tests on HPFRC beams of different dimensions, two approaches to determine the constitutive law for FRC have been analysed using sectional inverse analysis. The conclusions drawn from this study state as follows:

- The FCO assumes the same CMODs to calculate f_{R1} and f_{R3} regardless of the dimension of the specimen, which results in crack openings comparatively higher in smaller specimens. The rotation considered in the ECO provides different values of CMOD that are proportional to the specimen depth, leading to comparable values of f_{R1} and f_{R3} with regard to a crack opening proportional to the size of the element.
- After failure under compression in FRC, fibres still provide a remaining strength. In this regard, it is suggested that the constitutive law for concrete under compression should be extended to strains beyond 3.5‰. This is not explicitly stated in the MC2010, although has aroused as a necessity when conducting the AES to reach the equilibrium between compressive and tensile stresses in the sectional analyses.

- There is a generalized trend to reach higher strengths while the size of the element decreases. This effect mainly depends on the depth of the beams, which corresponds to the characteristic length l_{cs} .
- The defining parameters of the constitutive model for FRC are based on the post-cracking results of standardized beams of $150 \times 150 \times 600 \text{ mm}$. However, the strain at the cracked section of a beam for a specific crack opening is proportionally higher in smaller specimens. The results indicate that using the rotation as a reference parameter (ECO) in lieu of the CMOD (FCO) leads to constitutive tensile laws with a higher resemblance to the experimental results regardless of the size of the specimen.

As has been also described, the content of fibres has a clear effect on the residual strength, mainly due to the number of fibres crossing the cracked section. In addition to this, the pull-out behaviour, as well as the position and orientation of the fibre within the cracked section, play a determining role on the post-cracking behaviour of FRC.

4 ISOTROPY-BASED ESTIMATION OF THE POST-CRACKING STRENGTH IN FRC

4.1 INTRODUCTION

The study of Chapter 3 proposed an alternative approach to determine the parameters defining the constitutive law of FRC. The standard procedure to determine these parameters is usually taking as reference the crack opening of prismatic beams under a three-point bending configuration. In this regard, the analysis of the size effect revealed that using an equivalent crack opening depending on the dimension of the specimen would be a more suitable solution to obtain the constitutive law parameters. In practice, this consists in considering the rotation of the element instead of the crack opening so strains remain constant regardless of the specimen dimension.

Even though the specimen size has proved to be an important factor in the post-cracking performance of FRC, the overall behaviour of FRC is determined by the fibres. Plenty of research has focused on the influence of the type or geometry of the fibres (Lawler et al. 2005; Kim et al. 2008; Wu et al. 2016a), however, it is the distribution and orientation of the fibres that remain unresolved yet. According to previous research (Abrishambaf et al. 2017; Zhou & Uchida 2017a; Zhou & Uchida 2017b), fibre orientation is particularly relevant given their ability to substantially modify the behaviour at the post-cracking stage.

It is therefore important to account with numerical tools that take these factors into consideration to simulate the behaviour of the material under a three-point configuration aimed for pre-design purposes. Hence, the present chapter describes an analytical method to distribute the fibres within the cross-section of an element following a predefined orientation. Each fibre is assumed to contribute independently to the overall flexural strength according to its specific pull-out properties. Assembling the contribution of all the

fibres provides a representative curve of the post-cracking strength of the analysed element. Given the major challenge in simulating these phenomena, the results of the model may be used as a predictive tool to evaluate the material behaviour.

4.1.1 Objectives

The general objective stated in this chapter is developing a model to assess the behaviour of FRC under flexural stresses. Based on the properties of the concrete matrix and the fibres and the importance of the interaction between these two elements, the model estimates the flexural behaviour of specimens subjected to a three-point bending configuration. The interaction between the matrix and the fibres is mainly regarded in terms of fibre orientation and concrete-fibre bond. For this, the analytical model consists of three parts arising as a solution with the specific objectives defined as follows:

- Determine the distribution and orientation of the fibres at the cross-section according to a specific isotropy based on the orientation number of the fibres in the three-dimensional directions.
- Assess the number of effective fibres crossing the cracked section and the profile distribution depending on the dimensions of the cross-section and the isotropy of the material.
- Analyse the influence of the orientation and the embedded length on the pull-out performance of the effective fibres crossing the cracked section based on the pull-out law defining the behaviour of each fibre.
- Determine the flexural behaviour of a FRC beam under a three-point bending test based on the combined response of all the fibres contributing to the residual strength. Analyse whether the results of the model reflect the particularities of the concrete or fibre type properties.

4.1.2 Outline of the chapter

The description of the analytical model is presented in Section 4.2 and divided into several steps. First, the basic concept of the model is shown while detailing its key points. The dimensions and the position of the section object of study are defined while describing the procedure to distribute the fibres according to a specified isotropy. Additionally, the assumptions made for the analysis of the model are presented defining the different degrees of isotropy and the input parameters.

The results of the model are presented in subsequent sections according to the different parts of the model. The distribution and orientation of the fibres in the cross-section according to different degrees of isotropy are shown in Section 4.3. The pull-out response of the fibres depending on the orientation and the embedded length is described in Section 4.4. The post-cracking strength is shown in Section 4.5 regarding the content of fibres, the geometry of the element and the influence of the isotropy of the material.

4.2 ISOTROPY-BASED DISTRIBUTION OF FIBRES

4.2.1 General description of the model

The model simulates the behaviour of FRC under flexural stresses taking into account only the fibres that contribute to resisting the load to which the element is subjected. This becomes a major asset given the reduction of the number of calculations that need to be conducted. The model is the combination of the three analytical models represented in Figure 4.1. Model I describes the theoretical sectional framework to predict the behaviour of an element under flexural load using Models II and III. These two models aim to determine the position and orientation of the fibres within the critical section and the response of the fibres when pulled out of the concrete matrix. With this, it is possible to determine the number of fibres crossing the cracked section and relate them to the flexural response of the beam.

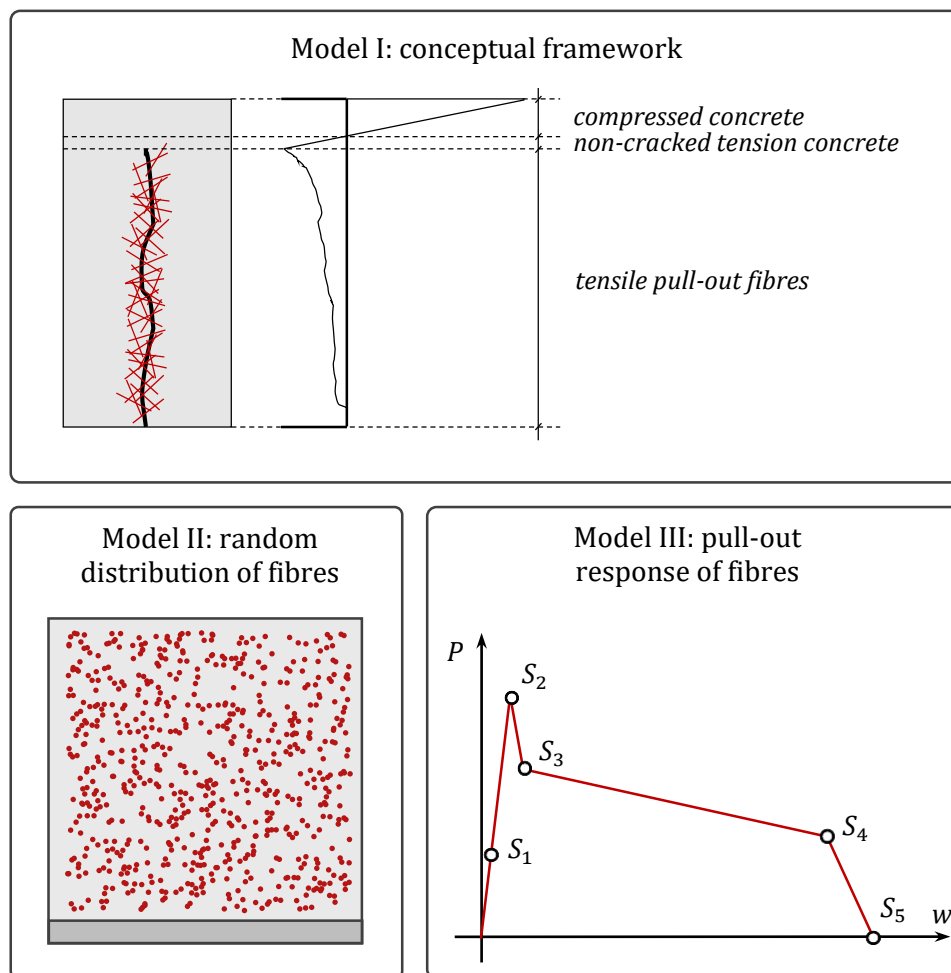


Figure 4.1 Models for the estimation of FRC flexural behaviour.

Model I is based on the procedure for fibre reinforced concrete described by Robins et al. (Robins et al. 2001) and subsequently used in additional research by the same authors (Prudencio et al. 2007; Jones et al. 2008). This model is built on the idea that the behaviour of a cracked section of FRC is dominated by the pull-out strength of each fibre bridging the crack. As a result, the contribution of concrete on the tensile stress is negligible in the post-cracked regime, with fibres as the only elements providing the residual strength to FRC.

To determine the pull-out response of the fibres, several factors such as the position, the embedded length or the orientation angle of the fibre with respect to the crack surface need to be assessed. These parameters are defined using Model II according to a probabilistic procedure (Cavalaro & Aguado 2015) that randomly calculates these three variables for all the fibres in the critical section where the crack appears. The pull-out mechanisms of fibres in concrete have been addressed by different authors (Robins et al. 2002; Abdallah et al. 2017b) leading to several available models to predict the pull-out behaviour of fibres (Laranjeira et al. 2010a; Laranjeira et al. 2010b; Zhan & Meschke 2014). Any of these models can be implemented in Model III to assess the pull-out constitutive law of the fibres.

To determine the tensile block produced by the pull-out of the fibres on the sectional diagram for a given crack opening, each fibre needs to be addressed individually. The model is analysed in terms of crack opening at the front tip (w_1), although each fibre has a specific crack opening (w_2) that depends on its position with regard to the depth of the specimen (Figure 4.2). The crack opening associated to each fibre is used to determine the pull-out load obtained with Model III.

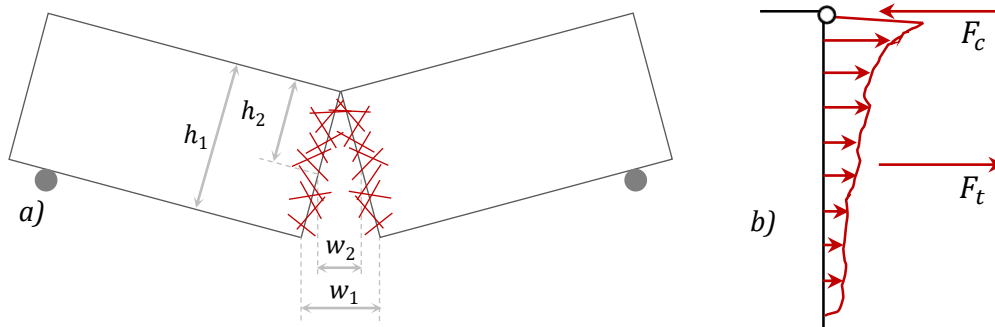


Figure 4.2 a) Failure mechanism and b) sectional forces.

At the post-cracking stage, fibres are the only elements contributing to resist the flexural stresses the beam undergoes. The failure mechanism of a beam under flexure is therefore represented considering the upper point as the hinge bonding the two halves of the element when the crack appears. This assumption is an approximation of the real failure mechanism and simplifies the assessment of the internal forces equilibrium for a certain crack opening. As shown in Figure 4.2b, this simplification leads to disregard the depth of the compressed block considering that the sectional compression forces act on the hinge. This leads to determine the flexural moment equilibrium taking into account only the pull-out forces of the fibres under tensile stresses. This assumption is valid and frequently considered for strain-softening FRC sections (without steel bars).

4.2.2 Critical section

The dimensions of the critical section are mainly defined by the fibres bridging the crack, which are the only ones that contribute to the residual strength of FRC. This critical section is shown in Figure 4.3 and corresponds to the volume enclosed between planes AA' with dimensions $l_f \times b \times h$. The dimension of the specimen defines the size of the cross-sectional area ($b \times h$), while fibres oriented perpendicularly to the main crack define the width of the critical section (l_f).

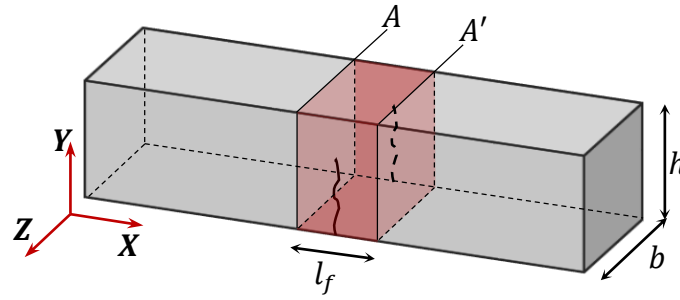


Figure 4.3 Position and dimension of the critical section.

The distance between planes AA' corresponds to the length of a fibre l_f with the crack located in the middle of the distance between AA'. This entails that the distance from the crack to either plane A or A' corresponds to half of the length of the fibre $l_f/2$. Therefore, the width of section AA' coincides with the maximum possible embedded length ($l_{e,max}$) of the fibres. This length is achieved by those fibres verifying two conditions: (i) the central point of the fibre is located at the crack surface and (ii) is oriented perpendicular to the crack (parallel to X-axis). Fibres satisfying conditions (i) and (ii) reach the maximum embedded length $l_{e,max} = l_f/2$.

The average number of fibres in the critical section (N_f) is given by Eq. 4.1 and depends on the volume of the critical section (V_c) as well as on the content (C_f), volume (V_f) and density (ρ_f) of the fibres. The orientation of the fibres within the critical section defines whether they cross the crack surface or not. This orientation depends on the degree of isotropy of the material and, therefore, the theoretical number of fibres crossing the cracked surface (N_{cs}) can be estimated according to the orientation factor of the fibres (Krenchel 1975) as shown in Eq. 4.2. The orientation factor (η) is representative of the anisotropic structure of the material given that it is directly related to the fibre alignment and preferential orientation.

$$N_f = C_f \frac{V_c}{\rho_f \cdot V_f} \quad (4.1)$$

$$N_{cs} = \eta N_f \quad (4.2)$$

The orientation factor takes values from $\eta = 0$ when no fibres cross the section to $\eta = 1$ when all fibres are perpendicular to the cross-section. Extensive research has been conducted on the orientation factor addressed to determine its value according to the anisotropy of the material (Nunes et al. 2017; Alberti et al. 2017; Segura-Castillo et al. 2018a). Stereological principles assuming an isotropic distribution of the fibres (Bastien-Masse et al. 2016) can be used to extend measurements conducted on 2D cross-sections to 3D. In this regard, an isotropic orientation of the fibres in a three-dimensional case leads to $\eta = 0.5$, as long as fibres are far enough from the boundaries of the formwork and are not subjected to the wall-effect (Martinie & Roussel 2011).

4.2.3 Position and orientation of the fibres

The distribution of the fibres in the model is defined according to probabilistic laws that govern both the position and the orientation. Based on previous research (Abrishambaf et

al. 2013; Nguyen et al. 2014; Carmona et al. 2016), the distribution of the fibres within the cross-section is generally uniform although the position and the orientation follow a probability density function that fits a normal distribution. Even though in the case of accentuated preferential distributions a Gumbel probabilistic law could be more suitable for extreme values (Laranjeira et al. 2011), the Gaussian law has been taken as the fundamental hypothesis mainly due to the linear relation between the orientation number and the number of fibres crossing the cracked section (Krenchel 1975).

Fibres are known to present a preferential alignment under the influence of several factors such as the flow direction, geometry of the formwork or vibration, among others (Laranjeira et al. 2012). The anisotropic nature of FRC leads to a different mechanical behaviour when tested in different directions (Abrishambaf et al. 2013; Pujadas et al. 2014b), revealing the maximum efficiency when stresses are perpendicular to the main direction of the fibres. These aspects make the orientation of the fibres a key parameter on the performance of FRC that should be considered. The fibre distribution is, therefore, generated in the model based on the orientation defined in the three main directions.

The fibre content is a known parameter when manufacturing FRC and the number of fibres in a specific volume of concrete may be inferred through Eq. 4.1. The procedure to distribute these fibres within the concrete matrix consists of three steps schematically represented in Figure 4.4. First, the coordinates of the middle point of each fibre (P_X, P_Y, P_Z) are determined. After this, the orientation of the fibres is given by the unitary vector of the direction of the fibre $\vec{D} = (D_X, D_Y, D_Z)$, thus being possible to determine the position of the edges of the fibre according to its length. The final step consists in verifying whether the edges of the fibre are inside the boundaries of the specimen. In case that any of the edges is outside the specimen, the model includes an iterative process that recalculates a new direction until both edges of the fibre remain inside the specimen.

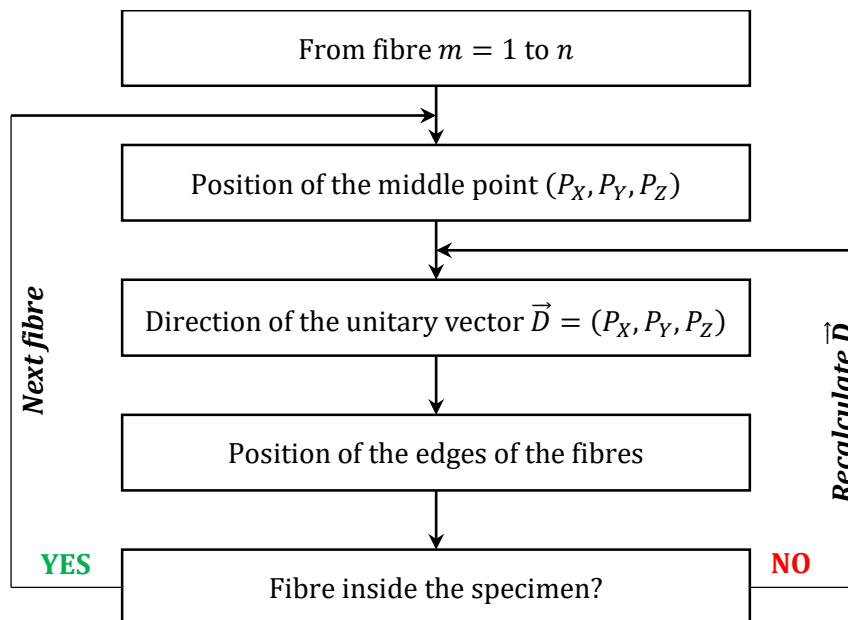


Figure 4.4 Procedure for distributing the fibres in the concrete matrix.

Each component of the coordinates of the position (P_X, P_Y, P_Z) and the unitary vector of the direction $\vec{D} = (D_X, D_Y, D_Z)$ are calculated according to an independent probabilistic law

associated with each of the components in axes X, Y and Z. This probabilistic law would present the shape of a uniform distribution when fibres present the same probability to be in any position. In case the fibres present a tendency to be in a certain position (not uniformly distributed), the probabilistic law would present a standard distribution. The typical shape of a standard distribution is presented in Figure 4.5, for which the probability density function and the cumulative normal distribution is shown.

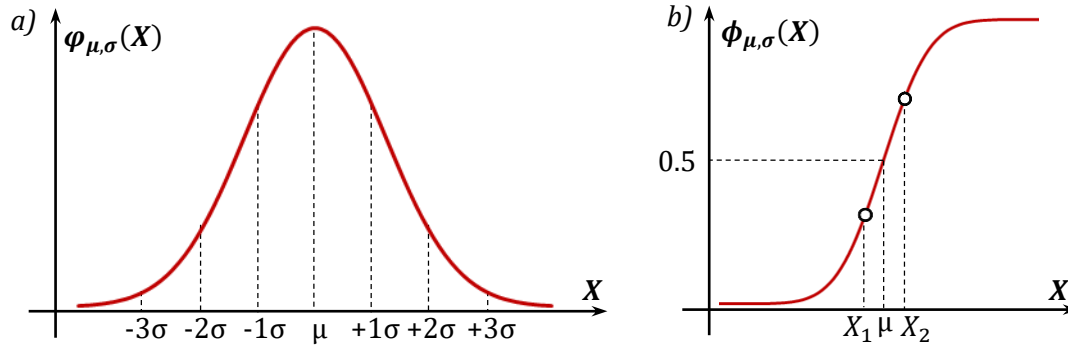


Figure 4.5 a) Probability density function and b) cumulative normal distribution.

In this model, a uniform distribution of the fibres is assumed, which can be represented as a particular case of a standard distribution. For this, the standard deviation (σ) and the mean value (μ) that define the standard distribution need to present a relation $\sigma \gg \mu$. This leads to a flatter shape of the probability density function that entails a cumulative probability $\phi_{\mu,\sigma}(X) \approx 0.5$ for values $X \approx \mu$. Therefore, a random value $X \in [X_1, X_2]$ with $X_1 < \mu < X_2$ can be assessed with a probability $\phi_{\mu,\sigma}(X) \approx \phi_{\mu,\sigma}(X_1) \approx \phi_{\mu,\sigma}(X_2) \approx 0.5$.

Considering the above, the three coordinates of the position of the central point of a fibre (P_X, P_Y, P_Z) can be randomly evaluated assuming a uniform distribution along any of the axes X, Y or Z. The procedure to determine the position in a general axis i (P_i) between a maximum and a minimum position $P_{i,max}$ and $P_{i,min}$ is described in the following steps:

1. Determine the mean value μ and define a standard deviation $\sigma \gg \mu$ so the probabilistic law follows a uniform distribution.
2. Assess the maximum and the minimum position of the central point of the fibre so that $P_{i,min} < \mu < P_{i,max}$ and $P_{i,min} \approx \mu \approx P_{i,max}$ given that $\sigma \gg \mu$.
3. Calculate the difference between the cumulative normal distributions of the maximum and the minimum position of the fibre $\Delta(\phi_{\mu,\sigma}(P_{i,max}), \phi_{\mu,\sigma}(P_{i,min}))$.
4. Generate a random number $k \in [0, 1]$ and obtain the cumulative normal distribution of a random position $\phi_{\mu,\sigma}(P_i) = \phi_{\mu,\sigma}(P_{i,min}) + k \cdot \Delta(\phi_{\mu,\sigma}(P_{i,max}), \phi_{\mu,\sigma}(P_{i,min}))$.
5. Interpolate $\phi_{\mu,\sigma}(P_i)$ to obtain $P_i = \frac{\phi_{\mu,\sigma}(P_i) - \phi_{\mu,\sigma}(P_{i,min})}{\phi_{\mu,\sigma}(P_{i,max}) - \phi_{\mu,\sigma}(P_{i,min})} \cdot (P_{i,max} - P_{i,min}) + P_{i,min}$.

A similar procedure is used to determine the three components of the directional vector $\vec{D}_t = (D_{tx}, D_{ty}, D_{tz})$ with the interpolation described in Step 5 adapted as shown in Eq. 4.3. These three components of \vec{D}_t are subsequently normalized as shown in Eq. 4.4 to assess the unitary vector of the direction of the fibres $\vec{D} = (D_X, D_Y, D_Z)$.

$$D_{ti} = \frac{\phi_{\mu,\sigma}(D_{ti}) - \phi_{\mu,\sigma}(D_{ti,min})}{\phi_{\mu,\sigma}(D_{ti,max}) - \phi_{\mu,\sigma}(D_{ti,min})} \cdot (D_{ti,max} - D_{ti,min}) + D_{ti,min} \quad (4.3)$$

$$D_i = \frac{D_{ti}}{\sqrt{D_{tx}^2 + D_{ty}^2 + D_{tz}^2}} \quad (4.4)$$

The maximum and the minimum value of the components of the unitary vector are influenced by the degree of isotropy of concrete and the preferential orientation of the fibres. The MC2010 specifies that, in general, an isotropic orientation of the fibres can be assumed. However, as long as the fibres are aligned towards a preferential orientation, the material cannot be considered isotropic (di Prisco et al. 2013). As a result, the MC2010 includes an orientation factor (K) to account for the effect of fibre orientation. Nevertheless, this factor is vaguely defined given that does not indicate specific values and only establishes $K < 1.0$ or $K > 1.0$ for favourable or unfavourable effects, respectively.

The degree of isotropy of FRC is defined in the model according to the maximum and the minimum values of the components of the directional vector (D_{tx}, D_{ty}, D_{tz}) . In case of a perfect isotropic FRC these components reach values $D_{ti,max} = 1.0$ and $D_{ti,min} = -1.0$, whereas a preferential alignment of the fibres entails a certain degree of anisotropy leading $D_{ti,max}$ and $D_{ti,min}$ to present absolute values below 1 and reach 0 when perfect anisotropy (Cavalaro et al. 2015; Cavalaro et al. 2016). This issue needs to be regarded due to the influence of induced effects such as the type of concrete, the casting and flow direction, vibration or the formwork geometry on the alignment of the fibres (Laranjeira et al. 2012).

After determining the position and the direction of the fibres, the coordinates of both edges of the fibres are calculated to check whether they remain inside the sample. If any edge of the fibre is beyond the boundaries of the specimen, the unitary vector is recalculated and the edges checked again. When verified that the fibre is inside the specimen, the next fibre of the model is calculated following the same procedure from the position to the verification of the edges. This iterative process reduces the possible number of orientations that the fibres may assume when they are close to the boundaries of the specimen given the influence of the wall-effect.

4.2.4 Assumptions for the analysis of the model

The anisotropy of the material is taken into account by assigning different values to the directional vectors $\vec{D}_t = (D_{tx}, D_{ty}, D_{tz})$ that define the main orientation of the fibres. In the model, the direction vector components can be either positive or negative, however, they are presented in absolute values for the sake of brevity. In the absence of any factor leading to a preferential orientation of the fibres, concrete presents a full isotropic distribution of the fibres with a directional vector $(D_{tx}, D_{ty}, D_{tz}) = (1.0, 1.0, 1.0)$. Hence, a preferential orientation of the fibres as in self-compacting concrete (SCC) would lead to a degree of isotropy such as $(D_{tx}, D_{ty}, D_{tz}) = (1.0, 0.5, 1.0)$ according to results of previous research (Laranjeira et al. 2012; Cavalaro & Aguado 2015).

Given that the isotropy degree of the material is defined according to the components of the directional vector, several degrees of isotropy may be analysed. Therefore, two degrees of

isotropy have been considered in the study in addition to those mentioned above. The first one states for an intermediate anisotropy $(D_{tx}, D_{ty}, D_{tz}) = (1.0, 0.8, 1.0)$ between full isotropic distribution and SCC. The second describes a case of concrete with a certain anisotropy on the Z-axis with a directional vector $(D_{tx}, D_{ty}, D_{tz}) = (1.0, 0.5, 0.8)$. A summary of the four combinations of isotropy degrees is shown in Table 4.1.

Table 4.1 Combinations of degrees of isotropy.

Degrees of isotropy	D_{tx}	D_{ty}	D_{tz}	Notation
Isotropic concrete	1.0	1.0	1.0	ID1
Quasi-isotropic concrete	1.0	0.8	1.0	ID2
Self-compacting concrete	1.0	0.5	1.0	ID3
Anisotropic concrete	1.0	0.5	0.8	ID4

The model is analysed according to the results of the concretes used in Chapter 3, which were manufactured using steel straight short fibres. Accordingly, the pull-out model proposed by Laranjeira (Laranjeira et al. 2010a) for straight fibres has been used in Model III to reproduce the pull-out behaviour. This model has been chosen given the simplicity of its implementation and the good agreement with the experimental results the author used to validate the model.

The input parameters for the pull-out model are based on those adopted in previous studies (Laranjeira et al. 2010a; Cavalaro & Aguado 2015). A friction coefficient $\mu = 0.6$ between the steel fibre and the concrete is assumed, while the ultimate tangential debonding stress was estimated at 51% of the tensile strength of concrete. The tensile strength of concrete was calculated according to the specifications of MC2010.

4.3 STAGE I: ANALYSIS OF THE CROSS-SECTION

4.3.1 Number of fibres, distribution and orientation

The model is based on a uniform distribution of the fibres in the cross-section assuming that fibres are homogeneously dispersed in the concrete structure. Consequently, it becomes particularly relevant to control both the concrete composition as well as the fibre type and content so that this hypothesis can be realistic. Any failure in the concrete proportioning or mixing procedure may entail an improper dispersion of fibres or even the formation of fibre clusters (Boulekbache et al. 2010) such as shown in Figure 4.6.

The orientation number in a certain direction i (η_i) is the projected length of the fibre along direction i divided by the length of the fibre. The orientation factor takes $\eta_i = 1$ when the fibre is completely aligned with the i axis and $\eta_i = 0$ in case the fibre is perpendicular to the specific axis. In the model described, η_i is calculated as the average of the directional component i of the unitary vector \vec{D} of the fibres analysed.

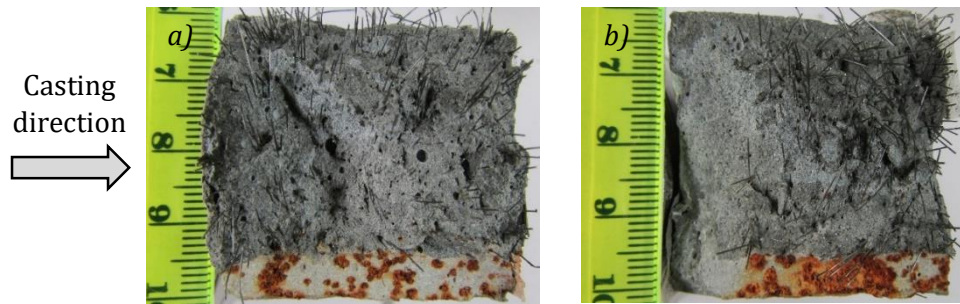


Figure 4.6 a) Efficient dispersion of fibres and b) cluster of fibres in the cracked section.

The relation between the average η_i and the four degrees of isotropy (ID) presented in Table 4.1 is shown in Figure 4.7. These results show how the anisotropy of the material has a direct influence on the preferential orientation of the fibres. A clear interdependence of the orientation number in each direction in any given degree of isotropy can be appreciated.

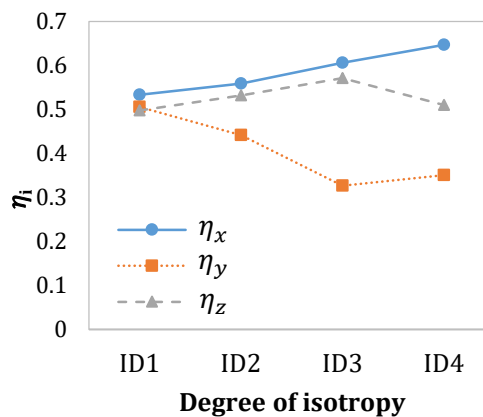


Figure 4.7 Orientation numbers according to the degree of isotropy.

An isotropic material ($ID1$) yields almost identical results of the orientation number in the three directions ($\eta_i \approx 0.5$). This fits the results reported by previous researchers (Dupont & Vandewalle 2005; Martinie & Roussel 2011; Bastien-Masse et al. 2016; Nunes et al. 2017) when determining the orientation number of the fibres according to stereological principles in an isotropic distribution. The slight differences in the orientation number in the three directions can be attributed to the orientation constraints introduced in the model near the boundaries of the formwork. Given that the orientation towards Y- and Z-axis is partially restricted due to the closeness to the walls of the formwork, the orientation number η_x unavoidably increases with respect to η_y and η_z .

The reduction of the degree of isotropy in Y-axis in $ID2$ and $ID3$ leads to a preferential orientation of the fibres along X- and Z-axis. This is reflected in an increasing value of the orientation numbers η_x and η_z at the expense of reducing η_y . As with the orientation numbers yielded by $ID1$, η_z presents values slightly below η_x due to the orientation restriction when near the boundaries. The orientation numbers yielded by $ID3$ may lead to consider a concrete under such a degree of isotropy as self-compacting concrete (Laranjeira et al. 2012).

Estimations of the orientation number in the three axes pointed out in certain studies (Blanco et al. 2015b) coincide with those obtained with $ID4$. A comparison between $ID4$ and $ID2$ or $ID3$ reveals that reducing η_z leads to a higher η_y , thus entailing also a greater

value of η_x . The orientation numbers obtained according to *ID4* can, therefore, be considered representative of specific real cases of beams and even slabs.

The number of fibres at the cracked section obtained from the model and a comparison of this result with Krenchel's theoretical approach is shown in Figure 4.8. The number of fibres was calculated according to the geometry of the fibres of Chapter 3 and three cross-sectional dimensions (150x150, 100x100 and 40x40 mm) with the four degrees of isotropy defined in Section 4.2. The number of fibres crossing the cracked section N_{cs} is shown in relative terms to the volume of the critical section of each cross-sectional size and the orientation number η_x is calculated as the average of the orientation number of all the fibres in the critical section.

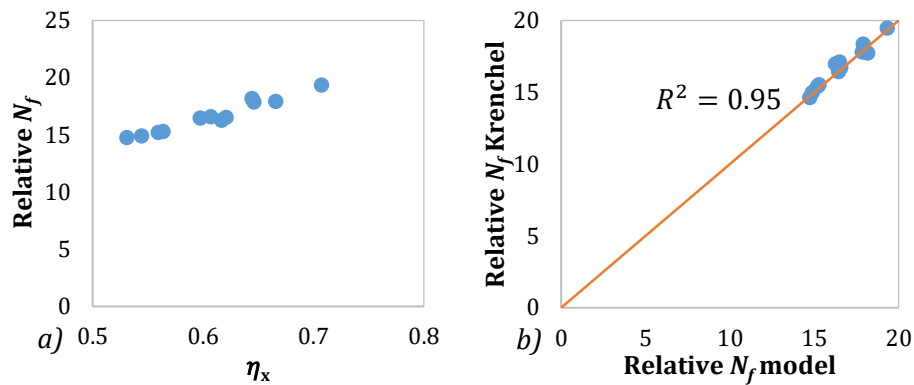


Figure 4.8 a) N_{cs} of the model according to η_x and b) comparison of N_{cs} of the model and Krenchel.

Figure 4.8a reveals that an increasing orientation number of the fibres leads to a higher number of fibres crossing the cracked section. A higher orientation number in a certain direction entails a preferential orientation of the fibres along the specified axis. Accordingly, an increasing η_x leads to a greater number of fibres preferentially oriented parallel to the X-axis and perpendicular to the crack surface simultaneously. In Figure 4.8b, a comparison between the number of the fibres crossing the crack according to the model and the theoretical number of fibres across the crack surface based on Krenchel's approach shows a goodness of fit of $R^2 = 0.95$.

The number of fibres oriented in a certain direction can be assessed with the values of η_x , η_y and η_z of each fibre provided by the model. This is particularly interesting to analyse the orientation distribution within the cross-section. Figure 4.9 shows the relative number of fibres in the critical section presenting an orientation number η_x . Four distributions represent the four degrees of isotropy previously defined.

The results in Figure 4.9 reflect that increasing the anisotropy of the material induces a higher number of fibres to present a preferential orientation towards a certain direction. Notice how for *ID1* and *ID2* the orientation number of the maximum number of fibres is $\eta_x \approx 0.7$, followed by a drop of the number of fibres with higher η_x . Conversely, isotropies *ID3* and *ID4* keep on increasing the number of fibres together with the orientation number. Hence, the number of fibres and their respective orientation number have a direct influence on the average orientation number in each direction as shown in Figure 4.1.

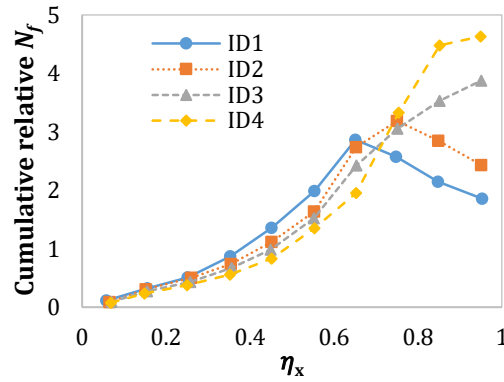


Figure 4.9 Cumulative relative N_f according to orientation number η_x .

The position of each fibre in the critical section is determined according to the procedure described in Section 4.2.3. Since the orientation number η_x is known, the position of each fibre crossing the cracked surface can be drawn as shown in Figure 4.10. The schematic representation of the cracked surface shows the cross-section profile of fibres with the isotropy degrees $ID1, ID2, ID3$ and $ID4$ highlighting the fibres with an orientation number $0.9 \leq \eta_x \leq 1.0$. Notice that all the fibres crossing the cracked section are not represented to avoid saturation of data.

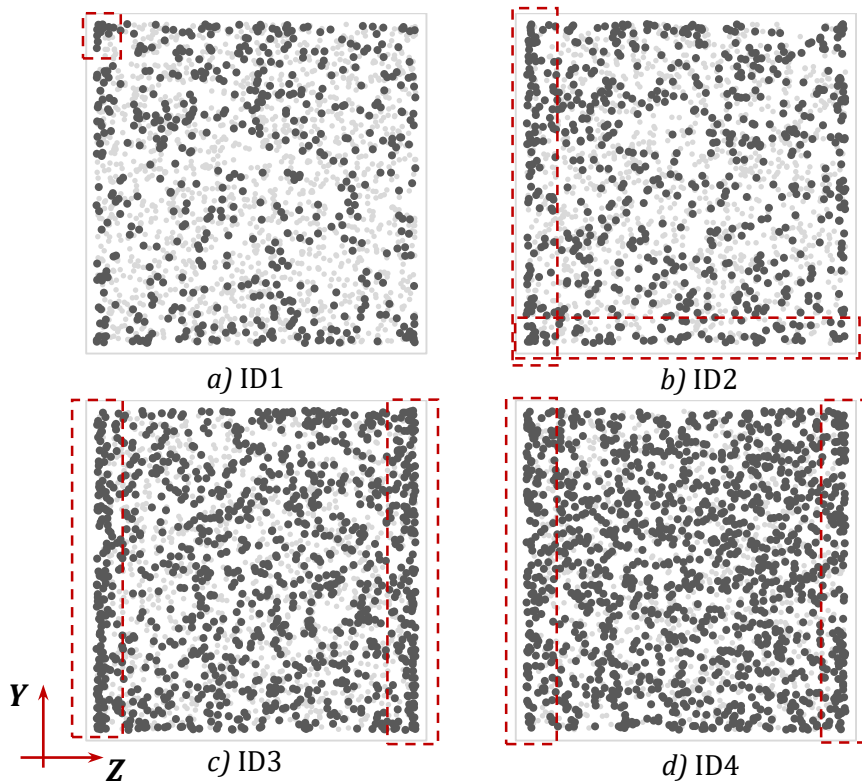


Figure 4.10 Orientation profile of the fibres with a) ID1, b) ID2, c) ID3 and d) ID4.

The profile distribution of the fibres in Figure 4.10 shows a clear increase of the density of fibres with an orientation number $0.9 \leq \eta_x \leq 1.0$ with the anisotropy of the material. The degrees of isotropy introduced in the model reflect the effect of the concrete flow, the vibration or the wall-effect. Even though these three effects jointly contribute to a preferential orientation of the fibres along the X-axis, the wall-effect is clearly visible on the cross-section profile.

The highlighted areas near the walls of the formwork and at the corners of the cross-sections tend to accumulate more fibres with higher orientation number. A comparison of the profiles yielded by $ID1$, $ID2$ and $ID3$ shows a clear accumulation of fibres with greater η_x when the anisotropy of the material increases. Even though this effect also takes place for $ID4$, the growing density of fibres at the cracked surface due to the higher anisotropy outshines the accumulation of fibres at the boundaries and corners.

Counting the fibres was firstly conducted by diving the cross-section into equal areas (Barr et al. 2003a). However, and according to the analyses conducted by other authors (Dupont & Vandewalle 2005; Laranjeira et al. 2012), the cross-section can be more conveniently divided into three different regions as shown in Figure 4.11. The boundaries of these regions are defined by the specimen dimension and the fibre length l_f . The area of these regions mainly depends on the number of formwork walls they are in contact with.

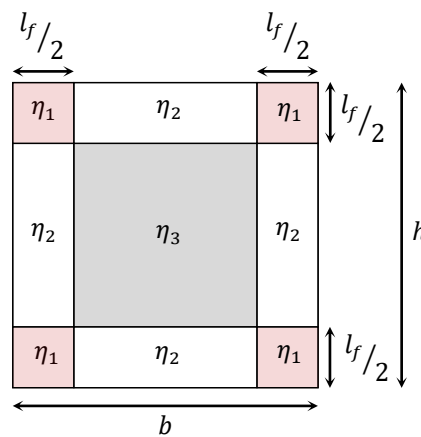


Figure 4.11 Theoretical distribution of the orientation number of the fibres in the cross-section.

While zone 1 lies on each corner of the cross-section and is defined only by the length of the fibres, zones 2 and 3 also depend on the dimension of the cross-section. Hence, the size of the cross-section does not have any influence on the area comprising zone 1, although it does on the areas of zones 2 and 3. Given that the area of zone 1 is invariable with the cross-section dimension, a reduction of h or b leads to a higher relative area of zone 1 with regard to the whole cross-section while decreasing the contribution of zones 2 and 3.

Due to the wall-effect, the areas in contact with the boundaries of the formwork tend to display a higher orientation number than the bulk. According to this, the more walls in contact with a zone, the higher its orientation number ($\eta_1 > \eta_2 > \eta_3$). Such a distribution of the orientation number has been experimentally confirmed and reported by authors analysing the orientation number of fibres within a cracked section (Alberti et al. 2016b; Alberti et al. 2016c).

According to these considerations, the average orientation number of the cross-section consequently depends on its dimension. Reducing the cross-sectional dimension results in a greater influence of zone 1, which given its higher η_x , prompts an increasing η_x of the whole cross-section while reducing both η_y and η_z . The variation of the orientation numbers η_x , η_y and η_z with the size of the specimen is shown in Figure 4.12.

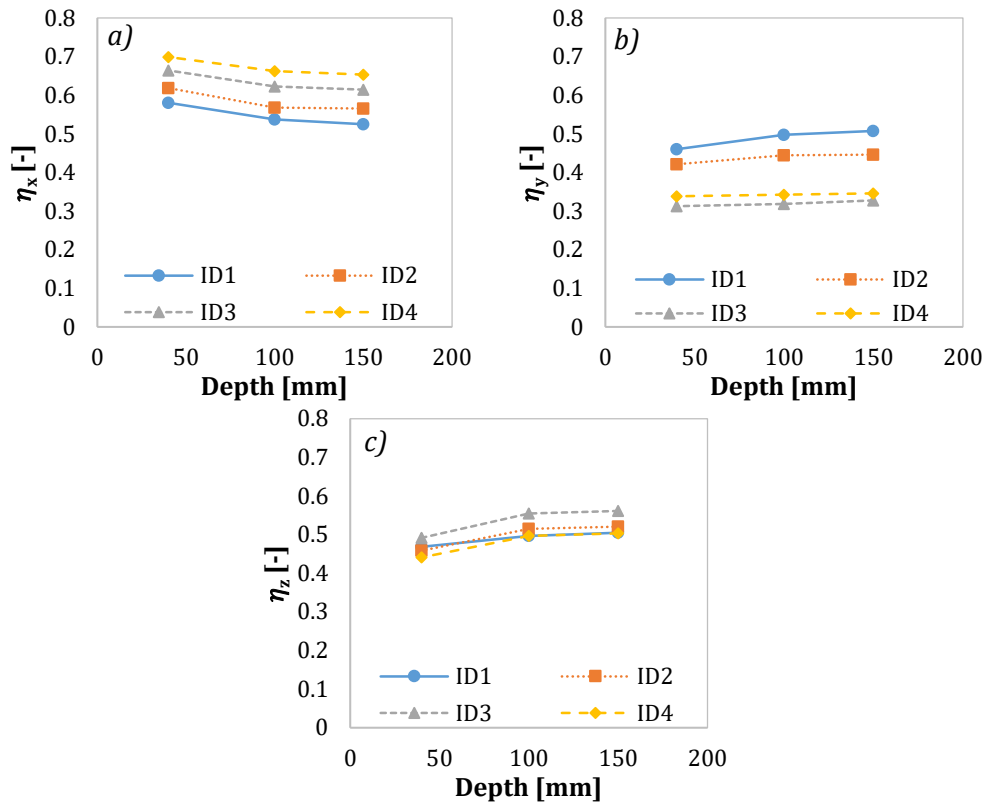


Figure 4.12 Orientation numbers η_x , η_y and η_z vs. specimen dimension.

The results present variable trends depending on the direction of the orientation number analysed. As expected, η_x decreases for higher dimensions of the cross-section. The reduction of η_x when increasing the size of the specimen leads to higher values of both η_y and η_z . This effect is again explained by stereological principles, which declare that the orientation numbers in orthogonal directions are inversely related (Bastien-Masse et al. 2016; Nunes et al. 2017). The orientation numbers in these two directions present an increasing trend with the dimension of the samples. This trend is almost negligible for η_y , even though it is noticeable for η_z .

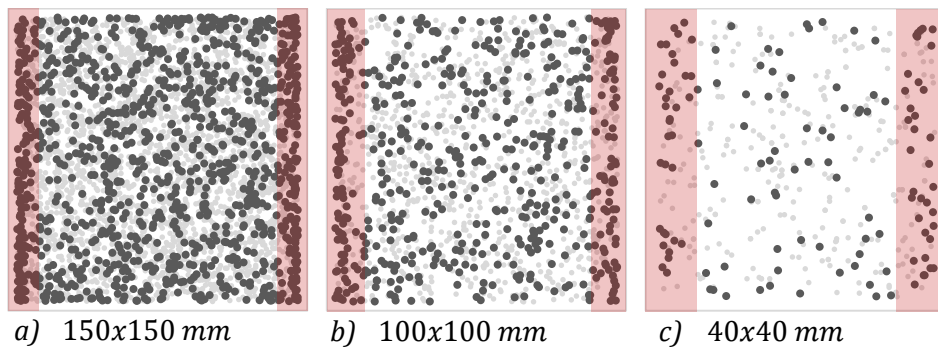


Figure 4.13 Distribution profile of fibres.

The fibre profiles of three cross-sections with different dimensions and a degree of isotropy $ID3$ are shown in Figure 4.13 to illustrate the distribution of the fibres with $\eta_x > 0.9$. For convenience, the three dimensions of the cross-section are shown with the same size. As a result, the density of fibres in the cross-section 150x150 mm seems much higher than in 100x100 and 40x40 mm cross-sections. In spite of this, the density of fibres with $\eta_x > 0.9$

is 5.03, 5.44 and 8.25 *fibres/cm²* in 150x150, 100x100 and 40x40 mm cross-sections, respectively.

Notice that the distribution of fibres with a degree of isotropy *ID3* obtained with the model does not fully fit the distribution profile of Figure 4.11. This is due to three factors governing the orientation profile of the fibres within the cross-section:

1. The degree of isotropy *ID3* restricts the orientation of the fibres on the vertical direction Y-axis.
2. The horizontal boundaries at the top and the bottom of the formwork limit the orientation of the fibres on the vertical direction. In this case, the top surface can be assumed to present the same boundary condition as the bottom or vertical walls (Dupont & Vandewalle 2005).
3. The left and right vertical boundaries of the formwork restrict the orientation of the fibres on the horizontal plane.

The combination of these three factors entails that while fibres can unrestrictedly orientate on the horizontal plane at the top and bottom boundaries, the vertical boundaries obstruct the free orientation on the horizontal plane. This leads to a higher amount of fibres with a greater orientation number when close to the vertical left and right formwork boundaries.

4.3.2 Variability of results

Given the probabilistic distribution introduced in the model, each repetition of the model results in different orientation numbers and, consequently, different number of fibres crossing the cracked section. An example of this is presented in Figure 4.14, showing the variability of the orientation number in the three directions under isotropies *ID1* and *ID4* according to the dimension of the specimen when the content of fibres is set to 90 *kg/m³*. These results were calculated out of 10 repetitions of the model.

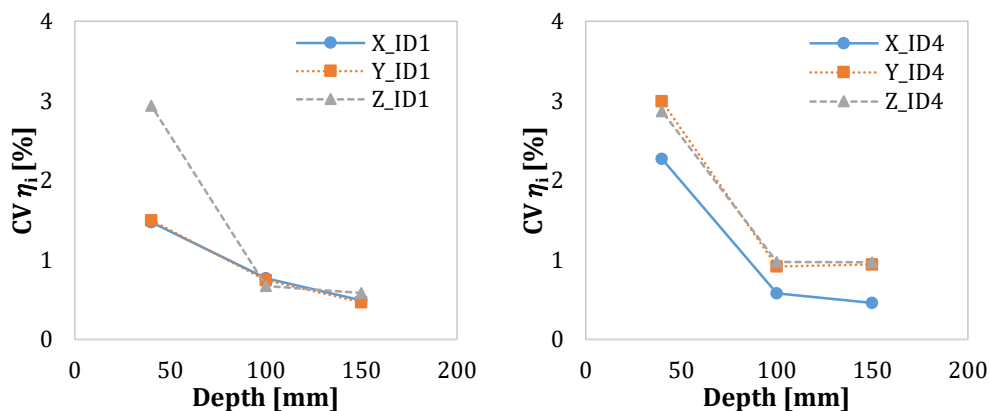


Figure 4.14 Variability of the orientation number.

The results indicate the inherent randomness of the model when calculating the position and the orientation of the fibres. This variation tends to decrease when the dimension of the specimen increases, an effect that is mainly attributed to the higher number of fibres in larger specimens. A similar trend is obtained with regard to the variation in the number of fibres according to the results of the model, as shown in Figure 4.15. These results present the CV of the number of fibres crossing the cracked section for the four mixes of Chapter 3 and the degrees of isotropy *ID1* and *ID4*.

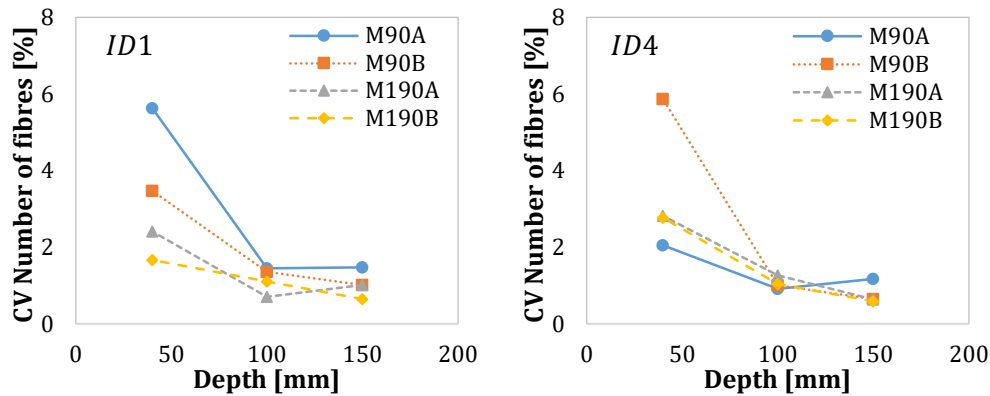


Figure 4.15 Variability of the number of fibres at the cracked section.

At this stage, the number of fibres at the cracked section only depends on the degree of isotropy of the model, such that there is no influence of the properties of concrete. However, the results reveal that even if the content of fibres is the same, the number of fibres at the cracked section varies between mixes. This indicates that the model is capable of taking into account the variability of FRC.

4.4 STAGE II: ANALYSIS OF THE PULL-OUT STRENGTH

The pull-out strength of the fibres is one of the factors defining the post-cracking behaviour of FRC. As described in Section 4.2, the pull-out contribution of each fibre in the cracked section is taken into account to subsequently determine the post-cracking strength of the material. Given that the pull-out strength is related to the fibre itself, both the degree of isotropy of the material and the element size turn out to be irrelevant to analyse the pull-out response of single fibres.

4.4.1 Inclination of the fibres

The angle between the fibre and the direction of the pull-out force has a strong influence on the shape of the pull-out diagram (Laranjeira et al. 2010a; Laranjeira et al. 2010b), whose distinctive points are shown in Figure 4.16a. The effect of five orientation angles with respect to the longitudinal direction X-axis on the load-crack width response of fibres is shown in Figure 4.16b. For comparison purposes, an embedded length $l_e = 4.0 \text{ mm}$ was considered for each fibre. Notice how the inclination angle of the fibre with regard to the load direction proves to be essential in the pull-out mechanism leading to four main differences among the curves.

The points depicted in the diagram of Figure 4.16a are represented in Figure 4.17 and correspond to different stages of the pull-out of the fibre:

- The first point states for the debonding initiation load of the fibre, which decreases when the inclination angle of the fibre increases.
- The second point, which represents the end of the full debonding of the fibre, occurs at higher crack widths with greater angles.
- The third point stands for the initiation of the fibre removal after full debonding.
- The fourth point is associated with the final pull-out force during the slippage of the fibre increases while increasing the angle.

- The fifth represents the end of the pull-out of the fibre, with the total crack width decreasing for a greater inclination angle of the fibre.

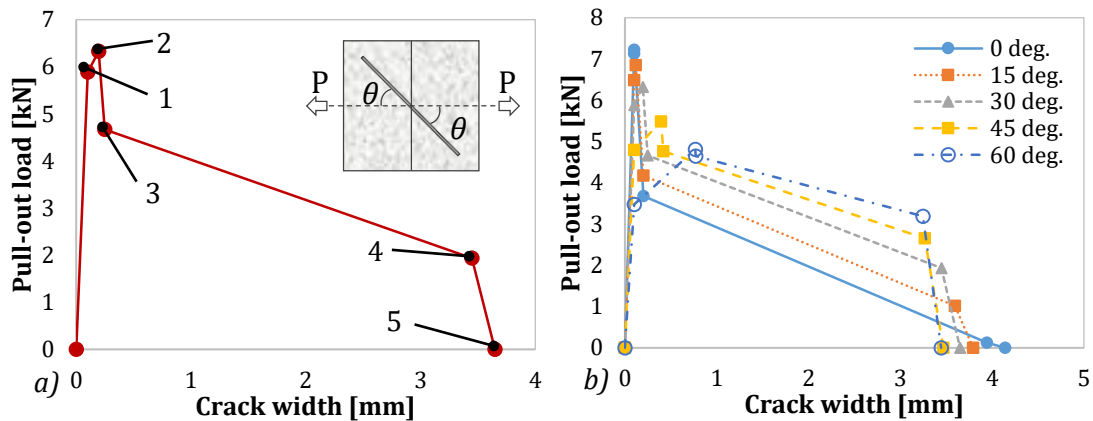


Figure 4.16 a) Points of the pull-out law and b) pull-out force for different inclination angles.

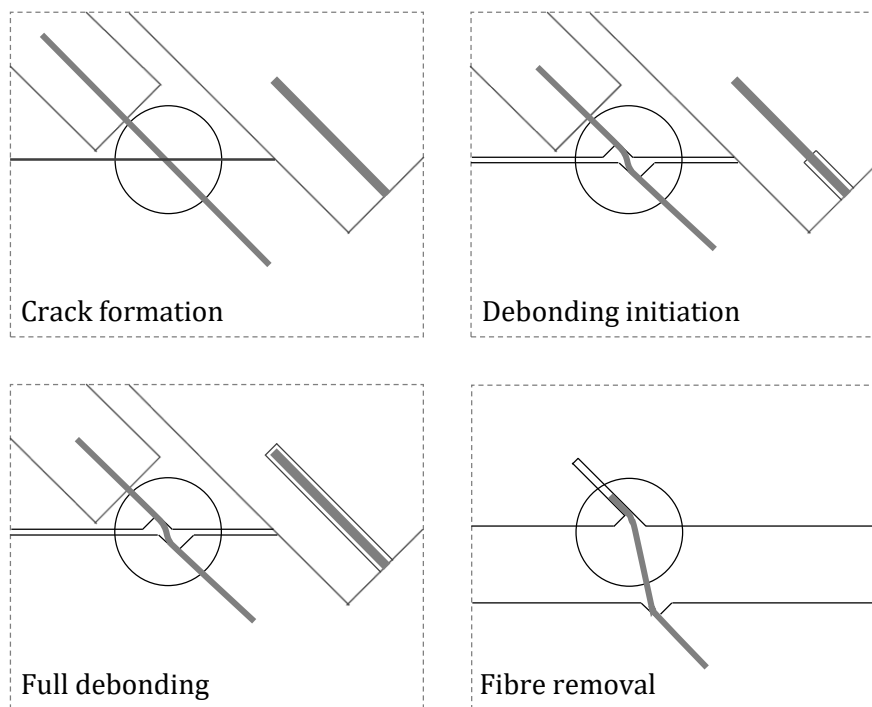


Figure 4.17 Stages of fibre pull-out (Laranjeira et al. 2010a).

The influence of the inclination angle on these critical points is shown in Figure 4.18. The first difference on the diagram occurs at small crack widths when debonding initiation takes place. The value of the pull-out load at this point is mainly governed by the elastic transmission of stresses and depends on the fibre orientation angle (Figure 4.18a). At this stage, fibres are still embedded in the concrete matrix, no slippage has already occurred and the crack opening is negligible (Lee et al. 2010; Zhan & Meschke 2014). Therefore, fibres cannot bend and the pull-out load is aligned with the direction of the fibre. As reported by other authors (Robins et al. 2002; Laranjeira et al. 2010a), the pull-out load at debonding initiation decreases with increasing the orientation angle.

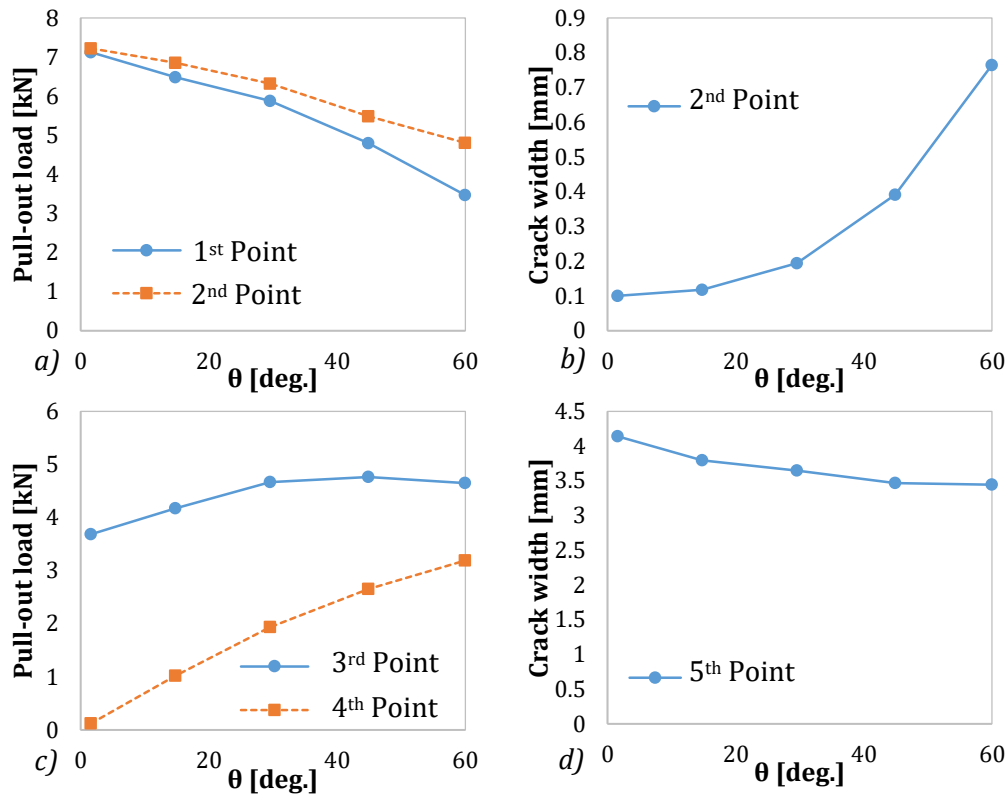


Figure 4.18 a) Debonding initiation, b) crack width at the end of debonding, c) final pull-out load and d) final crack width.

From this point onwards, the debonding starts along the length embedded in the matrix and the crack opening begins to increase. This stage ends at full debonding of the fibre, whose pull-out load presents a decreasing value with greater orientation (Figure 4.18a). During the debonding stage, the fibre bends along the direction of the external pull-out force, producing a stress concentration and spalling of the matrix when the fibre achieves a critical deviation angle. The spalled length of concrete matrix increases with the orientation angle (Cunha et al. 2010; Lee et al. 2010; Wille et al. 2014a) and so does the protruded length of the fibre previously embedded in the spalled portion of the concrete matrix. As a result of matrix spalling, the crack width dramatically increases (Zhan & Meschke 2014) due to the release of the protruded length. This produces an increasing crack width that varies with the orientation angle of the fibre as shown in Figure 4.18b. Both the crack opening due to debonding and matrix spalling are considered to happen at the same stage (Lee et al. 2010).

The diagram presents a sudden drop of the force due to the energy released after the full debonding, which softens for higher orientation angles. At this point, the stage during which the fibre is removed from the concrete matrix starts. The slippage is mainly dominated by the frictional bond between the matrix and the fibre. This stage shows a decreasing value of the pull-out load while the fibre is progressively being removed from the matrix and the crack opening increases.

Notice that fibres with a higher orientation angle generally require a greater pull-out load during this whole stage. The pull-out load both at the beginning and the end of the slipping stage—before total removal—is shown in Figure 4.18c. This effect for which the bridging force increases with the inclination of the fibres is known as the snubbing effect (Lee et al. 2010).

The last main difference on the behaviour of the pull-out diagrams of fibres with different inclinations is shown at the final crack width achieved. Figure 4.18d shows the crack width reduction with the increase of the orientation angle. This is a direct consequence of the reduction of the fibre embedded length due to the spalled matrix at the early stages of pull-out.

4.4.2 Embedded length

To determine the influence of the embedded length of the fibres on the pull-out behaviour, five different embedded lengths (2, 3, 4, 5 and 6 mm) were investigated. Given the paramount role of fibre orientation in the pull-out behaviour, two orientation angles (30 and 60 degrees) were considered in the analysis. The results are shown in Figure 4.19.

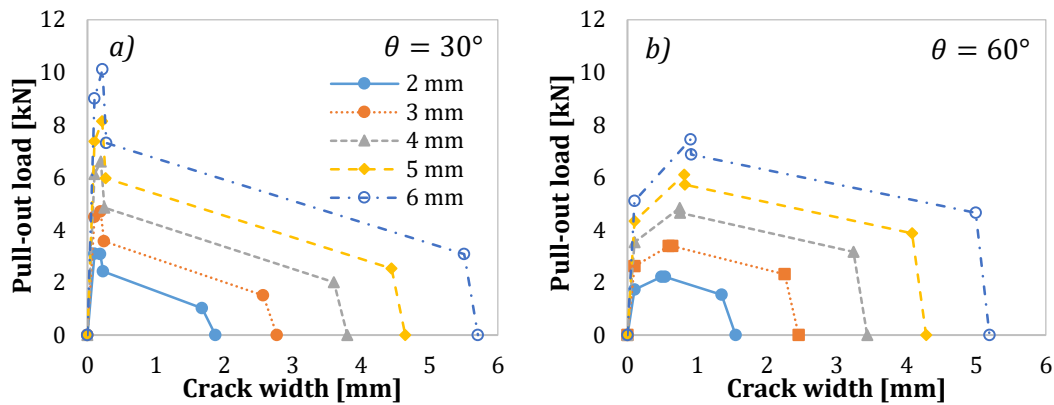


Figure 4.19 Influence of the embedded length for orientation angles a) $\theta = 30^\circ$ and b) $\theta = 60^\circ$.

In accordance with the results of previous studies (Cunha et al. 2010; Yoo et al. 2017a), increasing the embedded length enhanced the pull-out performance and revealed higher crack widths providing pull-out diagrams with a parallel shape with regard to the different embedded lengths. The points defining the pull-out diagram display a linear increase with the embedded length. This effect is shown in Figure 4.20 for the five embedded lengths defined and orientation angles of 15, 30, 45 and 60 degrees. The points described are those in which the fibre begins the debonding process and those before the full removal of the fibre from the matrix.

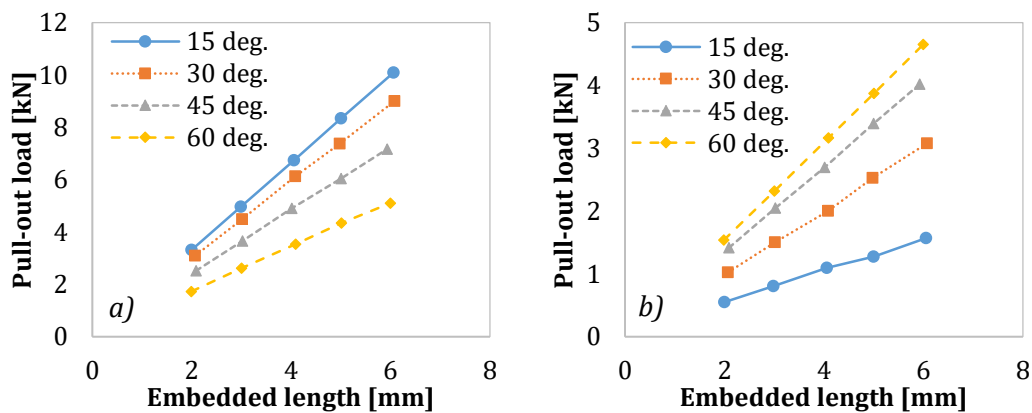


Figure 4.20 Influence of orientation angle and embedded length on the pull-out load at a) debonding initiation and b) fibre removal.

This effect responds to the higher bond strength in the fibre-matrix interface that the external load needs to reach for a longer embedded length. The increase of the pull-out load is attributed to the proportional dependence of the interface bond strength on the embedded length. This relation is independent on the inclination of the fibre, which is revealed in the results given that the pull-out increases regardless of the orientation angle of the fibre.

4.5 STAGE III: ANALYSIS OF THE POST-CRACKING STRENGTH

The model proposed is used to simulate the three-point bending test on notched beams, which present a weakened mid-span cross-section to impose the development of the crack at the centre of the beam. Introducing the notch in the model reduces the effective cross-sectional area contributing to the residual strength and directly affects to the number of fibres at the cracked section (the fibres virtually crossing the notch do not contribute to the residual strength of FRC).

As in previous stages, the input parameters of the model are selected according to the type of fibres and concrete class of the experimental programme reported in Chapter 3. A description of the influence of the different variables is presented showing how the model follows the trends described by the experimental results.

4.5.1 Influence of the content of fibres

A comparison of the full Residual strength (f_R) – *CMOD* curves obtained by the model for the mixes described in Chapter 3 (M90A, M190A, M90B and M190B) is shown in Figure 4.21. The results are presented for prismatic specimens of dimensions 150, 100 and 40 mm with a defined degree of isotropy *ID4*.

According to the experimental results shown in Chapter 3 and those reported in other studies (Yoo et al. 2017a), the results of the model reveal how increasing the fibre content leads to an enhanced post-cracking performance. In addition, the effect of the matrix strength due to the *w/c* ratio represents an additional factor influencing the residual strength of FRC (Abu-Lebdeh et al. 2011; Yoo et al. 2017b). In this case, both M90A and M190A with a *w/c* = 0.16 result in a stronger matrix leading to higher residual strengths than M90B and M190B (*w/c* = 0.23). The *w/c* ratio is not a defining parameter of the model, although its influence on the compressive, flexural and residual strength—inputs of the model—affect the matrix properties, the pull-out response of the fibres and, consequently, the residual strength curves.

4.5.2 Influence of the geometry

Figure 4.22 shows the results of the model when using the input data of mixes M90A, M190A, M90B and M190B for three specimen dimensions and a degree of isotropy *ID4*. The results show a clear influence of the element size on post-cracking strength, which decreases with the size of the element.

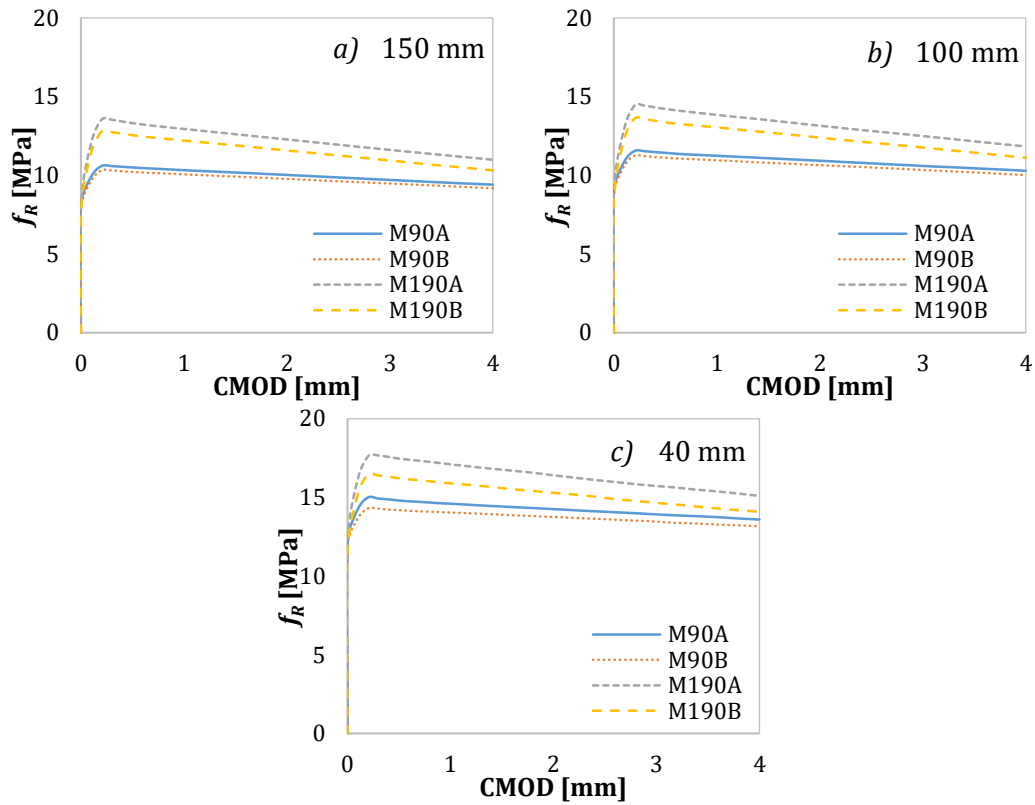


Figure 4.21 Residual strength-CMOD curves for specimens of a) 150, b) 100 and c) 40 mm.

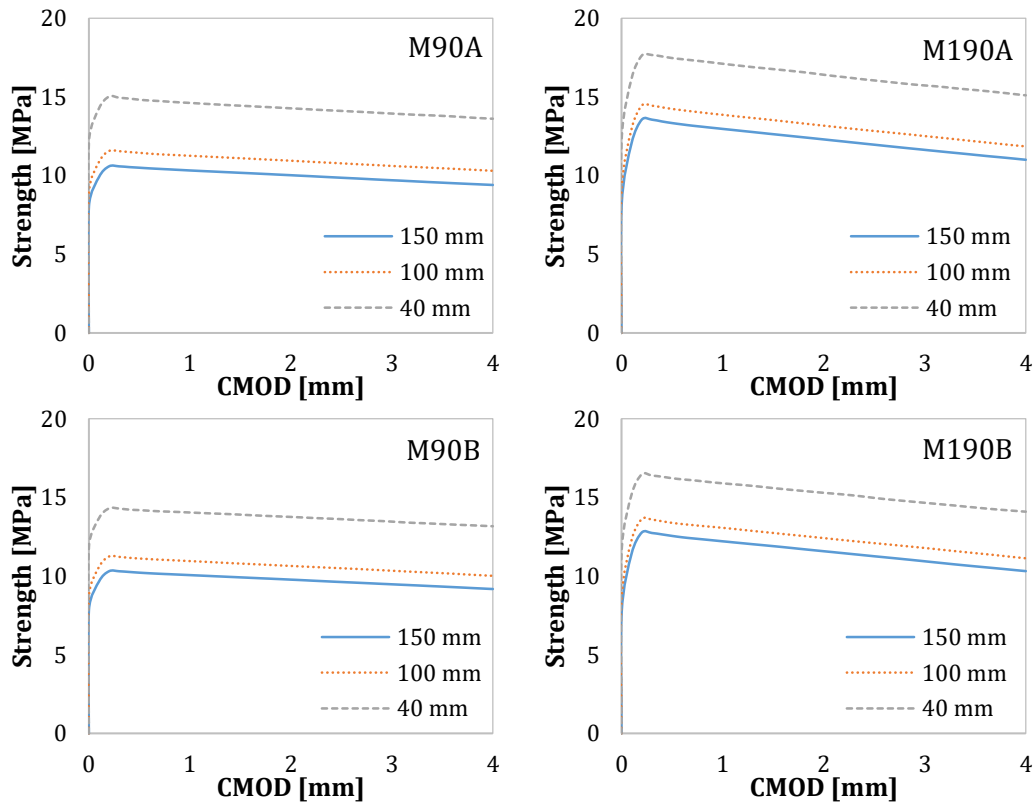


Figure 4.22 Comparison of the residual strength of three specimen dimensions.

The results of the model exhibit an evident size effect that recreates the variation of the strength with regard to the specimen dimension. The cross-section of a 100x100 mm beam is 56% smaller than that of a 150x150 mm beam. Such reduction entails an average increase of the strength of 8.2%. The reduction from 100x100 mm to 40x40 mm is 84% and represents an average increase of strength of 27%.

This may be attributed to the strong dependence of the flexural behaviour on the number of fibres with a higher orientation number in a perpendicular direction to the cracked surface when reducing the cross-section (Zerbino et al. 2012). Indeed, some studies attribute the increasing strength of FRC when reducing the specimen dimension to the wall-effect and the orientation of the fibres rather than to the size effect itself (di Prisco et al. 2004; Alberti et al. 2016c).

Given that the flexural residual strengths f_{R1} and f_{R3} are used by many codes and guidelines to estimate the constitutive equation of FRC, the evolution of these two parameters with the increasing dimensions of the elements is shown in Figure 4.23. The values presented correspond to the four mixes described under a degree of isotropy $ID4$. The results clearly represent the influence of the geometry of the elements as well as the effect of the content of fibre and the matrix strength.

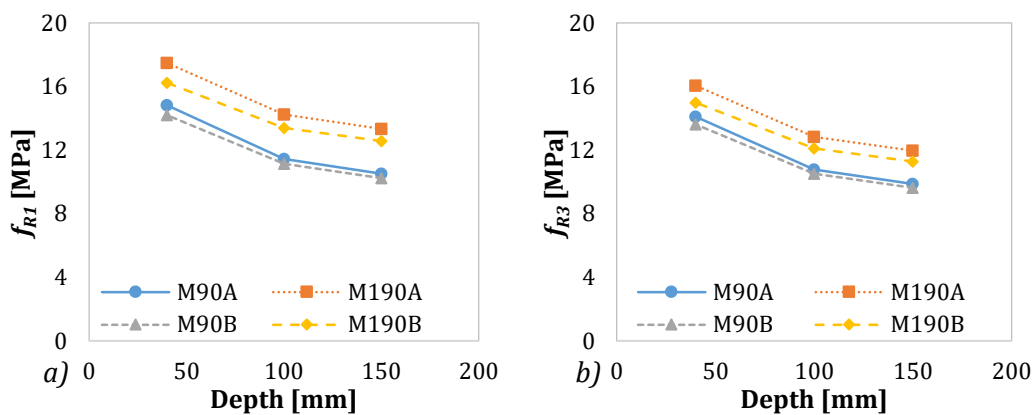


Figure 4.23 Residual strengths f_{R1} and f_{R3} according to the specimen dimension.

The average relative number of fibres at the cracked surface with regard to the area of the cross-section along with its variability is presented in Figure 4.24. These results are based on 10 repetitions of the model, which provides a different result each time the model conducts the analysis.

The number of fibres crossing the cracked section only depends on the degree of isotropy and the dimension of the cross-section defined in the model. As a result, an almost identical average number of fibres for a given specimen dimension is obtained for the same content of fibres as detailed in Figure 4.24. Consequently, and according to the results of both Figure 4.23 and Figure 4.24, the differences in the residual strength f_{R1} and f_{R3} calculated through the model between mixes with the same content of fibres are attributed to the input properties of concrete.

Notice that, even though being hardly noticeable, the relative number of fibres at the cracked section decreases as the specimen dimension increases. This is a direct consequence of the higher orientation number η_x in smaller specimens due to the higher contribution of zones 1 and 2 (see Figure 4.11). Accordingly, a higher number of fibres

aligned towards X-axis contributes and an additional factor to achieve higher residual strengths f_{R1} and f_{R3} in smaller specimens.

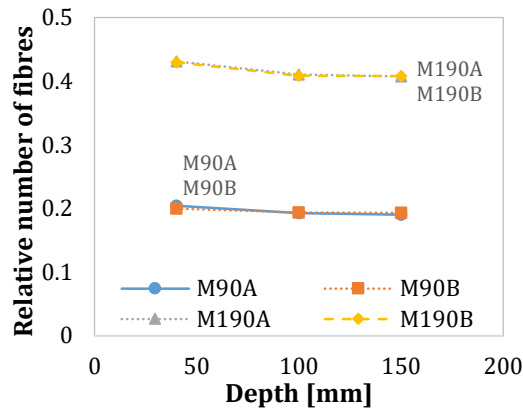


Figure 4.24 Relative number of fibres and variability at the cracked surface.

4.5.3 Influence of the degree of isotropy

Four degrees of isotropy for the material were defined to conduct the model and determine how different distributions of fibres on the cross-section affect the post-cracking strength. The results of Figure 4.25 show the influence of the degrees of isotropy that state for an isotropic ($ID1$) and an anisotropic concrete ($ID4$) on the residual strengths f_{R1} and f_{R3} . The results also depict the evolution of the residual strengths obtained for different specimen sizes with cross-sectional dimensions of 150×150 , 100×100 and 40×40 mm. The results are shown for straight fibres in a content of 90 kg/m^3 .

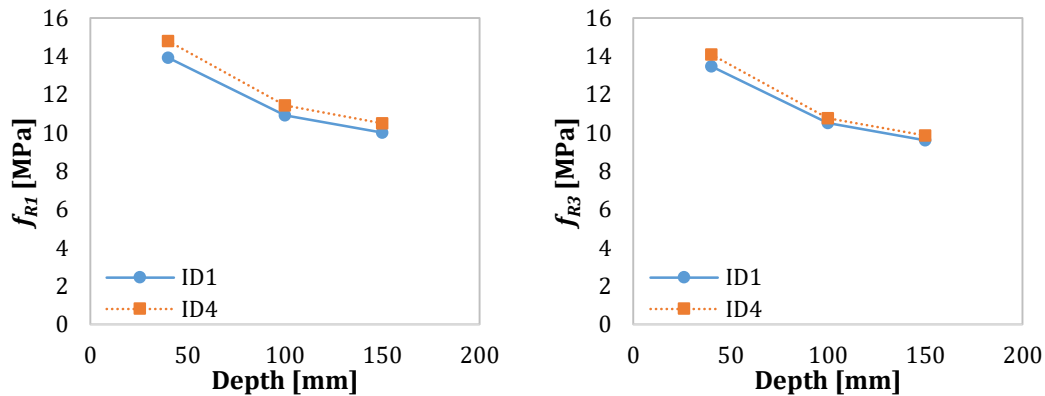


Figure 4.25 Influence of the degree of isotropy on a) f_{R1} and b) f_{R3} .

Even though $ID4$ entails a higher orientation number of the fibres in the direction perpendicular to the failure plane, Figure 4.25 reveals that the variation of the isotropy degree leads to almost negligible differences on the residual strength. In this line, even the scatter of the experimental results might be higher than the differences on the residual strength exhibited between the two analysed degrees of isotropy. This highlights that, in some cases, even though casting and vibration procedures may lead to different orientations, the impact of these two factors may be lower than expected.

4.6 CONCLUDING REMARKS

An analytical model based on the distribution and the pull-out of fibres to estimate the flexural performance of FRC has been proposed. Each time the model runs, the position and the orientation of the fibres within the critical section are slightly different given the probabilistic distribution used to calculate these parameters. According to this, each time the model runs, the results exhibit a slight variation that represents the inherent scatter of FRC. Pursuant to the results yielded by the model, several conclusions regarding the model may be drawn:

- The estimated number of fibres crossing the cracked section obtained through the model verifies Krenchel's approach involving the orientation number. These fibres present a distribution profile according to a cross-section division that accumulates the fibres with higher orientation along the walls of the formwork and particularly at the corners.
- The orientation number strongly depends on the dimension of the cross-section. This is a direct consequence of the distribution profile and leads to a preferential orientation towards a perpendicular direction to the cracked surface when decreasing the size of the element.
- Inclined fibres are more effective in terms of pull-out load during the removal stage given the increasing bridging capacity when fibres present higher angles with respect to the pull-out load direction. However, this also leads to a reduction of the final the crack width as a result of the higher protruded length released by the larger amount of spalled concrete matrix during pull-out.
- The results revealed that the model can recreate the influence of the size effect, the content of fibres and the degree of isotropy. This has a direct effect on the post-cracking estimation accordingly increasing or decreasing the residual strength.

This model is presented as a tool to estimate the contribution of fibres to the residual strength of FRC at the design stage, providing the possibility to use any type of fibre if implementing the pertinent pull-out law. Even though the model may present some limitations adjusting real flexural results, it reflects the influence of the size effect and the distribution and orientation of the fibres on the post-cracking strength. For this reason, it becomes particularly relevant to determine the real behaviour of full-scale elements when reinforced with fibres or even in the presence of different reinforcement combinations.

5 DUCTILITY ASSESSMENT AND CHARACTERIZATION OF REAL-SCALE ISOSTATIC STRUCTURES

5.1 INTRODUCTION

The first part of this thesis focused on the influence of the size effect in both the cracking and post-cracking strength of FRC specimens, showing a trend in which smaller elements generally lead to greater strengths. When designing laboratory tests, one of the main objectives should be designing a setup representative of a real structure to closely simulate the real behaviour of the element. However, concrete specimens used in laboratories have some limitations regarding the dimensions, mostly due to the loading capacity of the testing equipment. In this regard, small elements are easily manageable and suitable for design purposes given that the material properties may be assessed in a straightforward way. These limitations hinder the study of larger and more complex elements which, due to their own nature, need to be analysed on a larger scale.

Flexural tests are conducted on standardized beams to characterize the post-cracking behaviour of FRC. However, these type of tests aim to determine the response of FRC with fibres as the only reinforcement when, in practice, it is common to find structures with a combination of fibres and traditional reinforcement (Chiaia et al. 2009a; Caratelli et al. 2012; de la Fuente et al. 2012b). The interaction of the two types of reinforcement may lead to the partial or total replacement of the traditional reinforcement by fibres. In all cases, the proportion of fibres and rebars required to fulfil the design requirements must be assessed.

Among all the possible solutions, it is important to find the one that complies with the criteria and optimizes the manufacturing costs to become more competitive. In this regard,

among other advantages, the use of structural fibres as reinforcement enhances the toughness, improves the resistance to fire and reduces the effects of fatigue (Ferrara & Meda 2007). Segments for tunnel linings are an example of the successful replacement of traditional reinforcement by fibres with structural purposes (Caratelli et al. 2011; Caratelli et al. 2012; Liao et al. 2015; di Carlo et al. 2016; Liao et al. 2016).

5.1.1 Objectives

In this chapter, real-scale slabs with different combinations of reinforcement subjected to bending under an isostatic support setup are analysed based on the MC2010. The main objective of the chapter is verifying whether the minimum ductility requirements of the MC2010 are necessary or if, conversely, less restrictive requirements would ensure compliance with the specified design ductility. For this purpose, several specific objectives are defined:

- Determine the influence of fibre type and content on the behaviour of FRC.
- Analyse the structural response under flexural loading of slabs with different combinations of fibres and traditional reinforcement.
- Verify the ductility of the slabs according to the requirements of the MC2010.
- Assess the orientation and distribution of the fibres within the slabs and identify an orientation pattern.

5.1.2 Outline of the chapter

Section 5.2 describes the ductility requirements of the MC2010 to design FRC elements. Subsequently, the experimental programme conducted to determine the behaviour of the slabs is presented in Section 5.3. First, the materials and the mix considered in the experimental programme are detailed. Additionally, the geometry and the reinforcement combinations of the real-scale slabs is shown, along with the equipment and setup to perform the tests.

The results of the experimental programme are presented in Section 5.4. The materials properties are shown and analysed regarding the type and contents of fibres used. The behaviour of the slabs is addressed by comparing the influence that the different reinforcements have on the structural behaviour. The ductility of the elements according to the moment-curvature response is determined. Also, the orientation of the fibres is presented, as well as the preferential direction within the element. Finally, the main conclusions of the analysis are gathered in Section 5.5.

5.2 DESIGN STRATEGY OF FRC ELEMENTS

According to design specifications, structural elements need to present a certain degree of ductility in failure regime. This ductility is provided by a minimum amount of reinforcement that guarantees that the ultimate failure moment M_u of the structure is greater than the cracking moment M_{cr} . This reinforcement has traditionally consisted of steel rebars, which presents undeniable efficiency given that it is thoroughly calculated and strategically placed to resist the external forces where the loads produce the most unfavourable effects. However, the developments in materials technology and advanced research have proved

that fibres may also be used to replace partially or totally rebar reinforcement and provide the required ductility to a structure (Caratelli et al. 2011; Caratelli et al. 2012; Liao et al. 2015; di Carlo et al. 2016).

According to the MC2010, it is possible to replace the traditional reinforcement by fibres as long as FRC verifies several ductility requirements to avoid brittle failure. These requirements refer both to the ductility of the material and to the ductile behaviour of the structure. The MC2010 expresses these requirements in terms of relations between the defining parameters of the material and the response of the structure.

Regarding the properties of the material, two conditions need to be verified to guarantee ductility in case of failure: $f_{R1k}/f_{LOP} > 0.4$ and $f_{R3k}/f_{R1k} > 0.5$. These relations are defined to ensure that the material presents a minimum residual strength even at large crack widths. In this regard, the residual strengths f_{R1k} and f_{R3k} depend on the amount of fibres and directly influence the post-cracking response of FRC. Consequently, the content of fibres plays an essential role in the contribution of fibres to the ductility of the element and in the replacement degree of traditional reinforcement by fibres. It must be noticed that the different sources of scatter are intrinsically taken into account by considering characteristic values of f_R .

In relation to the structural design, the MC2010 imposes three criteria that must be fulfilled to avoid brittle failure when using fibres as reinforcement in a structure. These conditions, based on the loads and the displacements displayed by the structure under a loading situation, need to satisfy:

- The ultimate post-cracking load (P_u) should always be higher than both the load at cracking initiation (P_{cr}) or the maximum service load (P_{SLS}).
- The ultimate displacement (δ_u) must be 20 times larger than the displacement at maximum service load (δ_{SLS}) calculated through the assumption of uncracked concrete and initial elastic Young's modulus.
- The displacement at the maximum load (δ_{peak}) must be at least 5 times greater than δ_{SLS} .

The parameters of the three conditions above mentioned are presented in the MC2010 in a load-displacement ($P - \delta$) curve, although may also be expressed in terms of moment-curvature ($M - \chi$) as in Figure 5.1 (Chiaia et al. 2009a; Chiaia et al. 2009b; de la Fuente et al. 2012b; Liao et al. 2015; Liao et al. 2016) when dealing with the design of statically determinate structures. The relations between the ultimate and the cracking bending moments (M_u and M_{cr}) display three possible ductility scenarios depending on the ductility degree achieved by the structure.

The first condition $M_u \geq M_{cr}$ ensures a remaining strength capacity to avoid the brittle failure in case of reaching the cracking bending moment. This criterion establishes the minimum content of reinforcement to guarantee a ductile behaviour. If $M_{cr} \geq M_d$, the minimum reinforcement needs to verify that $M_u = M_{cr}$. In case that $M_d > M_{cr}$, the reinforcement of the structure ought to be calculated with the condition $M_u = M_d$. When the structure works as a statically redundant element, the minimum deformability established in the two displacement requirements needs to be guaranteed to activate the bending moment redistribution capacity. However, when working under an isostatic

configuration, only the condition $M_u \geq M_{cr}$ is necessary to guarantee the ductile behaviour as the absence of redistribution would not require any minimum deformability.

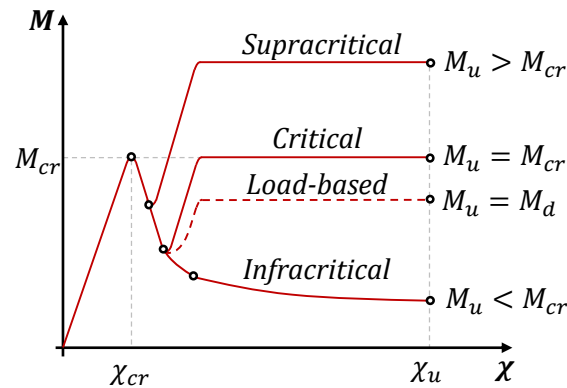


Figure 5.1 $M - \chi$ diagram for sectional behaviour.

There are structural elements subjected to low bending moments ($M_d < M_{cr}$) which would only need the minimum reinforcement to avoid a brittle failure in case of cracking. A typical structural element responding to this situation would be a segment for a tunnel lining, which behaves as an isostatic slab under transient situations such as demoulding, stocking, transport or manipulation (Figure 5.2). These transitory situations usually lead to higher bending moments in comparison to those that occur in operational stages (provided seismic loads are not expected), since this type of elements work predominantly under a hyperstatic compressed state during the service life. Consequently, the transient stages present more restrictive conditions and the reinforcement must be calculated for these situations.



Figure 5.2 Transient stages of the segments.

During transient stages, basically subjected to the self-weight or, at most, the weight of additional elements when stacking, segments are designed not to crack. These loads produce low bending moments that are not high enough to achieve M_{cr} (de la Fuente et al. 2012b). It is at this situation that the total replacement of the rebar reinforcement by fibres becomes a technical and economically suitable solution. If cracking occurs due to any

circumstances not related to loading, M_{cr} would not be achieved and failure could only happen if the loads subsequently applied were high enough to reach M_u .

Taking this into account, the alternative design strategy here described proposes that the MC2010 ductility conditions should be reconsidered and open the possibility of analysing each individual case to reach an optimal solution. This strategy is based on a load-based design of the minimum reinforcement considering $M_u = M_d$ even in the case that $M_d < M_{cr}$. In this regard, should cracks appear during transitory stages, the structure would still present a remaining ductility able to resist the loads applied in addition to the safety margin provided by the safety factors. This would reduce the reinforcement with respect to a design based on $M_u \geq M_{cr}$, thus optimizing and reducing the content of fibres to a minimum necessary.

5.3 EXPERIMENTAL PROGRAMME

The experimental programme consisted of two stages: (1) material and (2) mechanical characterization of real-scale slabs. The first one aimed to determine the properties of the materials used to produce the slabs. For this part, several tests were conducted to determine the influence of different types and contents of fibres on the behaviour of concrete and to analyse the performance of the steel rebars used in the slabs. The second stage involved the characterization of real-scale slabs without reinforcement (plain concrete, PC); reinforced with steel corrugated bars (RC); reinforced with steel fibres (SFRC) and with a combination of both reinforcement types (hybrid reinforced concrete, HRC).

5.3.1 Materials and concrete mix

The concrete mixes designed in this study were developed to be used in segments for tunnel linings. In this sense, the concrete proportioning was designed to meet the specific requirements of this type of element. Several batches with the same concrete proportioning (Table 5.1) were produced in this experimental programme. The difference between the batches lies in the content and type of steel fibres used in each of them.

Table 5.1 Concrete mix.

Material	Content [kg/m ³]
Cement II B-M 42.5R	400
Microsilica	16
Water	143
Natural sand 0/8	387
Sand 0/8	461
Coarse aggregate 8/16	352
Coarse aggregate 16/22	652
Superplasticizer	1.5% o.c.w.
Air Entraining Agent	0.03 – 0.10% o.c.w.
Polypropylene fibre - $\phi 0.18 \text{ mm} / L = 6 \text{ mm}$	1.5

The high content of cement simulates the necessity of the segments of achieving high strengths at early ages for demoulding and stacking purposes. For this reason, also microsilica was used in the proportioning, since silica-based reactives increase the strength

of concrete at early ages (Nili & Ehsani 2015; Wu et al. 2016b). The use of hooked-end steel fibres reduces the workability of concrete (Wu et al. 2016a), which was improved using superplasticizer in a content of 1.5% over the cement weight (o.c.w.). An air entraining agent was included in contents from 0.03 to 0.10 % o.c.w. In fresh state, the air ball-bearing effect improves the workability (Kim et al. 2012), while in hardened state the air entrain agent improves the durability against frost and salt scaling (Wong et al. 2011). Short polypropylene fibres were also included in the mix in a content of 1.5 kg/m^3 to reduce the likelihood of spalling in the segments in the event of fire (Pichler et al. 2006; Maluk et al. 2017; Yermak et al. 2017).

The ductility of concrete was provided by different types of steel fibres in different contents. The fibres used had simple hooked-end (1HE) and double hooked-end (2HE) anchorages, which would result in different pull-out responses and residual strengths (Abdallah et al. 2016b). The geometrical and mechanical properties of the steel fibres are shown in Table 5.2.

Table 5.2 Characteristics of the fibres (provided by the manufacturer).

Characteristic	Simple hooked-end (1HE)	Double hooked-end (2HE)
Length [mm]	35	35
Diameter [mm]	0.55	0.55
Aspect ratio [-]	64	64
Tensile strength [MPa]	1325	1850
Mod. of elasticity [GPa]	200	200

5.3.2 Stage I. Characterization of the material

The material characterization consisted of five concrete mixes based on the mix presented in Table 5.1. One plain concrete (PC) mix without fibres was produced as reference for comparison purposes. Two mixes with fibres 1HE in contents of 25 and 30 kg/m^3 (FRC-25/1HE and FRC-30/1HE) and two additional dosages with 2HE fibres in contents of 20 and 25 kg/m^3 (FRC-20/2HE and FRC-25/2HE) were also produced. The tensile properties of the steel rebars subsequently used in the slabs were also analysed. A summary of the tests conducted with the dimensions of the specimens is shown in Table 5.3. All the tests performed to characterize the material were standardized tests and were conducted according to the specifications.

Table 5.3 Summary of characterization tests.

Test	Type of specimen [mm]	Standard
Air entrain	-	EN 12350-7
Compression	$\phi 150 \times 300$ 150x150x150	EN 12390-3
Modulus of elasticity	$\phi 150 \times 300$	EN 12390-13
Three-point bending test	150x150x600	EN 14651
Barcelona test	150x150x150	UNE 83515
Steel tensile test	$\phi 8 - \phi 10 - \phi 12 - \phi 16$	EN 10080

5.3.3 Stage II. Characterization of real-scale slabs

For this part of the experimental programme, four-point flexural tests were conducted on the slabs. Once tested, cores were drilled and cut to obtain $\phi 150 \times 150 \text{ mm}$ specimens to analyse additional properties of the concrete once cast in real elements. In this regard, the inductive test was performed on the drilled specimens to characterize the fibre distribution and orientation within the slabs.

Properties and production of the slabs

To simulate the mechanical behaviour of a segment during transitory situations in which bending moments are likely to occur (demoulding, stacking, transport and manipulation), fourteen slabs with a length of 3.0 m, a width of 1.0 m and a height of 0.4 m were cast. All the slabs were produced with the same concrete mix shown in Table 5.1. The reinforcement of these slabs consisted of 12 different combinations of rebars and steel fibres (except in the case of one slab, which did not include any type of reinforcement). A summary of these combinations is gathered in Table 5.4.

Table 5.4 Summary of the reinforcement of the slabs.

Slab	Rebar reinforcement	Fibre reinforcement
PCS	NO	NO
RCS ₁	R ₁	NO
RCS ₂	R ₂	NO
FRCS-20/2HE	NO	20 kg/m ³ 2HE
FRCS-25/1HE	NO	25 kg/m ³ 1HE
FRCS-30/1HE	NO	30 kg/m ³ 1HE
HRCS ₁ -25/1HE (a,b)	R ₁	25 kg/m ³ 1HE
HRCS ₁ -30/1HE (a,b)	R ₁	30 kg/m ³ 1HE
HRCS ₂ -25/1HE	R ₂	25 kg/m ³ 1HE
HRCS ₁ -20/2HE	R ₁	20 kg/m ³ 2HE
HRCS ₁ -25/2HE	R ₁	25 kg/m ³ 2HE
HRCS ₂ -20/2HE	R ₂	20 kg/m ³ 2HE

The proposal for the combination R₁ consisted of 5 ϕ 8 + 2 ϕ 10 + 2 ϕ 8 at the upper face and 8 ϕ 8 + 2 ϕ 8 at the bottom face. The combination R₂ consisted of 3 ϕ 8 + 2 ϕ 10 + 2 ϕ 8 at the upper face and 6 ϕ 8 + 2 ϕ 8 at the bottom face. A layout of the qualitative reinforcement configuration is shown in Figure 5.3.

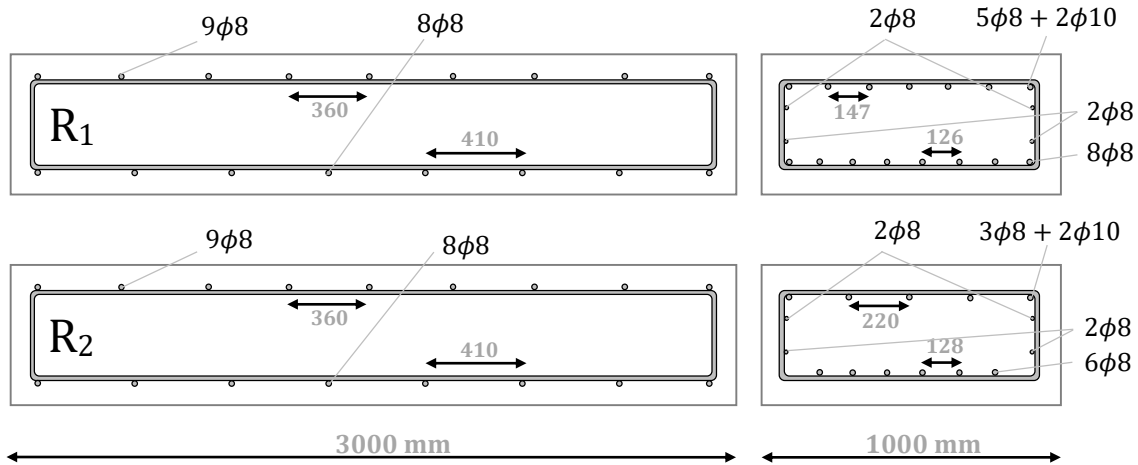


Figure 5.3 Geometry of the slabs and reinforcement configuration.

For the casting of the concrete, formworks with the specific size of the slabs were constructed. The rebars were placed into the formworks following the indications of the reinforcement design for each slab. Additionally, several moulds were also prepared for the casting of the specimens to characterize the concrete. The concrete was poured inside the formworks and finally vibrated as depicted in Figure 5.4.

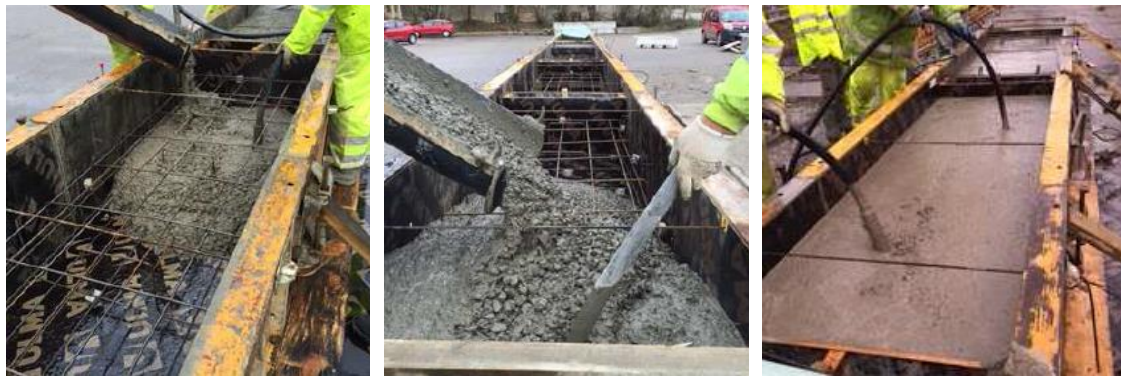


Figure 5.4 Pouring and vibration of the slabs.

Test setup

The tests were performed using a load frame with a capacity of 1000 kN with a total jack displacement of 500 mm. The piston connected to the load frame applied the load through a stiffened steel beam made of two UPN 280, which transmitted the load to two HEB 140 placed crosswise along all the width of the slab (Figure 5.5). Under the HEB 140 beam and over the slab, a neoprene sheet of 10 mm thickness and 100 mm width was placed to ensure full contact on the surface of the slab. As depicted in Figure 5.5, the supports at the edges of the slabs consisted of two neoprene sheets of 20 mm thickness and 200 mm width.



Figure 5.5 a) General configuration of the test and b) neoprene support.

The tests were designed considering an isostatic configuration similar to a four-point test with a span of 2.7 m and a distance between lines of 0.9 m. A scheme of the configuration is depicted in Figure 5.6.

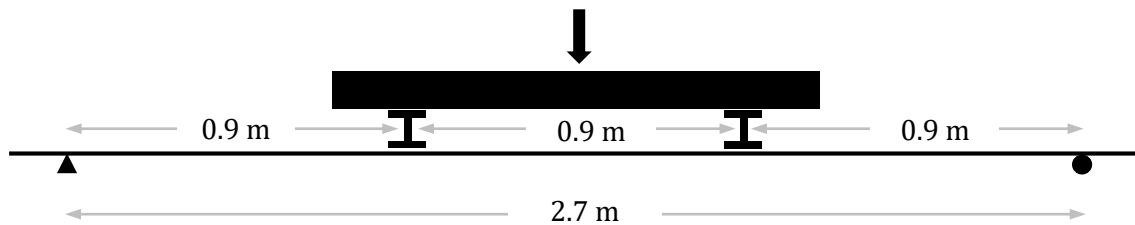


Figure 5.6 Isostatic setup of the test and dimensions.

The test was performed with displacement control, thus allowing to record the plastic phenomena and the ductile structural responses. The loading process was divided into two stages with different loading rates to increase the precision of the data collection during the test. In the first stage, the displacement rate was set to 0.4 mm/min and lasted until the element cracked. Subsequently, the rate increased to 1.0 mm/min during the post-cracking stage.

In addition to the vertical displacement of the piston and the load, other parameters were recorded. The deflection at the mid-span was registered using a laser placed over the surface of the slab at both sides of the element and at 50 mm from the lateral edge. The crack opening was also measured at both sides of the slab through two displacement transducers placed encompassing the total distance between the two HEB beams. Additionally, one LVDT with gauge capacity of ± 5 mm measured the vertical displacement of each support. These LVDTs were located at the centre of the longitudinal edges on direct contact with the slabs. Figure 5.7 shows further details of the measuring instrumentation.

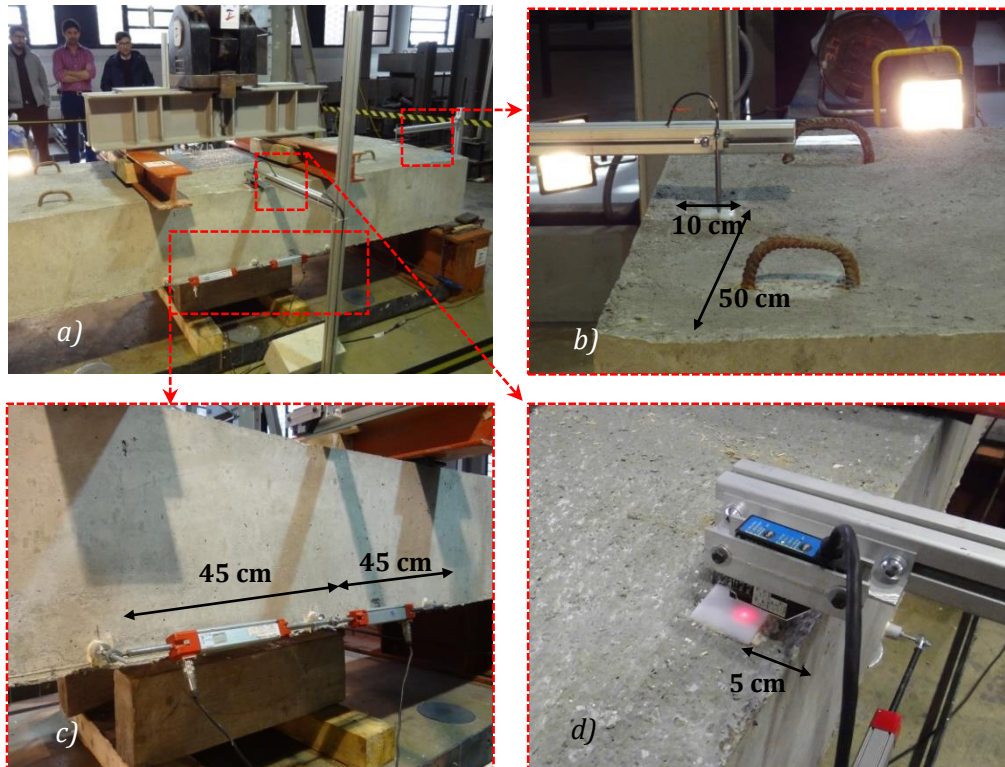


Figure 5.7 a) General configuration of the instrumentation, b) LVDT transducer, c) displacement transducers and d) laser.

Drilling of cores from the slabs

After the tests, cylindrical cores were drilled from the three slabs reinforced only with fibres. The slabs with traditional reinforcement were not considered suitable for the study since the rebars could interfere with the orientation of the fibres. The main objective was to determine the orientation of the fibres in the slab and their distribution along their depth.

Cores were drilled from one half of the slab, assuming the distribution is centrally symmetrical. Due to the importance of the location of the cores in the slab, their position and orientation with respect to the slab were strictly determined. The external part of the hooks placed in each slab was removed to simplify the task of drilling. To extract the cores, a drill bit of 150 mm of internal diameter and length of 500 mm was used. Figure 5.8 shows the preparation of the slabs and the drilling.



Figure 5.8 a) Position of the cores, b) removal of hooks and c) drilling of cores.

A sketch with the exact position of the thirty-two cores extracted from the 3 slabs was drawn after drilling. Figure 5.9 shows a map of the three slabs, the location of the cores and

sensor element of the system, as shown in Figure 5.10. A small electrical current goes through the coil and produces a magnetic field around the device, interacting with the steel fibres inside the concrete.



Figure 5.10 Analyser and cylindrical sensor.

Five measurements in different positions were taken in each of the cylindrical specimens prepared from the cores. By spinning the specimen around these directions, it is possible to obtain the orientation of the fibres inside the material. The arrows in Figure 5.11 show the directions and the angles in which the inductance was measured. The inductance measured in the different directions of the cores allows determining the orientation number and the contribution of the fibres in any in-plane of the specimen (Cavalaro et al. 2016). Hence, it is possible to obtain a full orientation profile of the fibres within the sample. This is a valuable tool to characterize the orientation of the fibres within the horizontal plane and the influence of concrete flow.

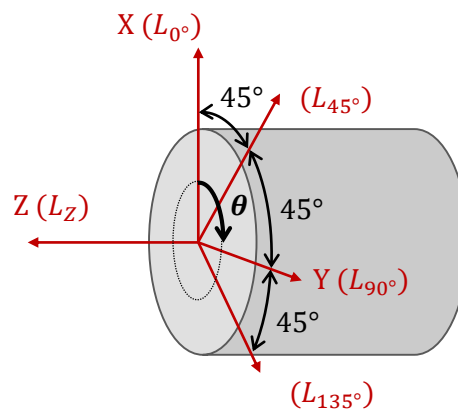


Figure 5.11 Measurement directions of inductance.

5.4 RESULTS OF STAGE I: MATERIALS

5.4.1 Air entrain, compressive strength and modulus of elasticity

The specimens were cured in a steam bath for a period of 6 hours after casting to reproduce the curing conditions of the segments. Steam-curing conditions accelerate the production of CSH gel, thus producing higher compressive strengths at early ages (Gonzalez-Corominas et al. 2016) and able to achieve more than 95% of the compressive strength at 28 days (Ramezani pour et al. 2013; Ramezani pour et al. 2014). The results of the air entrain,

compressive strength and elasticity modulus are shown in Table 5.5. The air entrain was measured after mixing each batch of concrete. For each mixture, three cylindrical specimens were produced to determine the average compressive strength at a minimum age of 28 days. The average modulus of elasticity was determined using fourteen specimens tested after the compressive strength and at the same age.

Table 5.5 Results of air entrain, compressive strength and modulus of elasticity.

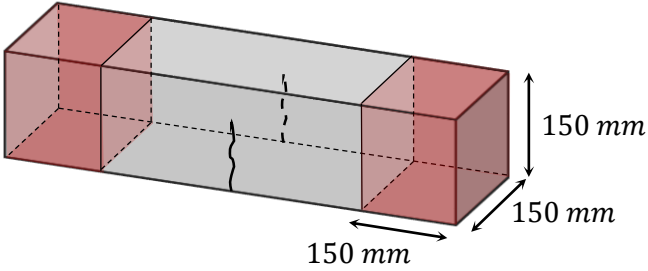
Mix	Entrained air [%]	Average f_{cm} [MPa]	CV [%]	Average E_{cm} [MPa]	CV [%]
PC	1.5	65.8	3.9%	37442	3.6%
FRC-25/1HE	2.5	64.2	4.3%	35510	1.4%
FRC-30/1HE	2.8	67.9	2.3%	39760	1.2%
FRC-20/2HE	6.6	38.7	5.2%	28627	5.7%
FRC-25/2HE	4.6	48.1	0.4%	33359	2.8%

In line with the results obtained in other studies (Yu et al. 2014; Söylev & Özturan 2014), the use of fibres clearly increases the air content in FRC. Among the mixes produced, the maximum value of air entrain reaches 6.6% in FRC-20/2HE, exceeding the tolerated 6% value for precast elements established by the Spanish Code (EHE 2008). Noticeable differences were also observed between the mixes produced with fibres 1HE, these presenting air contents considerably lower than in dosages with fibres 2HE. This effect may be attributed to the longer geometry of the fibres in comparison to the aggregates. This difference produces an interaction between fibres and aggregates resulting in a lower packing density of concrete that leads to a higher air content.

The lowest results of compressive strength are obtained in mixes FRC-20/2HE and FRC-25/2HE, which also present the highest air entrain contents. It has been extensively documented (Neville 1996; Mehta & Monteiro 2006) how the porosity is especially influential on the compressive strength and, hence, how increasing the air entrain in the mix reduces the compressive strength (Kim et al. 2012). A clear example of this effect may be identified in FRC-20/2HE, which presents the highest air entrain content thus triggering the lowest compressive strength among the analysed mixes. This effect may be attributed to the use of fibres 2HE, which increased the content of entrained air and produced the drop of compressive strength. This analysis shows that the type of fibre indirectly influenced the compressive strength of concrete.

Given the unusual low compressive strength of some mixes, especially in FRC-20/2HE, the compressive test was repeated in cubic specimens. These cubes were obtained by cutting the beams used in the flexural test after testing them under the three-point bending test. The cylindrical specimens and the beams were cast with the same batches, so the properties of the concrete were the same in both types of specimen. Table 5.6 shows the results and a sketch detailing the location of the cubes in the beam. No results are shown for PC since this mix did not have fibres and no beams were produced to be tested under the flexural test.

Table 5.6 Results of compressive strength on cut specimens.

Mix	f_{cm} [MPa]	Section tested
PC	-	
FRC-25/1HE	81.5	
FRC-30/1HE	96.8	
FRC-20/2HE	60.6	
FRC-25/2HE	73.6	

The results reveal that the compressive strength should be above 60 MPa. Hence, the reduced compressive strength of the results in Table 5.6 may be attributed to a wrong compaction or vibration of the specimens during casting. In any case, even with cubic specimens, the compressive strengths of FRC-20/2HE and FRC-25/2HE are lower when compared to the rest of the mixes. This confirms the previous hypothesis regarding the influence of the type of fibre on the compressive strength due to the higher induced porosity.

As reported in previous research, there is a close relation between the compressive strength and the modulus of elasticity (Yoo et al. 2014) with no significant variations in the magnitude attributed to the use of fibres (Akçay & Tasdemir 2012). The general trend observed indicates that a higher amount of porosity entails lower values of the modulus of elasticity. As in the compressive strength, the main differences in the modulus of elasticity may be the result of additional porosity introduced by the fibres during mixing.

5.4.2 Post-cracking strength

The influence of the content and the geometry of fibres on the post-cracking behaviour of FRC has been extensively reported (Naaman 2003; Barros et al. 2005; Soutsos et al. 2012; Wu et al. 2016a). However, only a few investigations analyse the influence of fibres with multiple hooks (Abdallah et al. 2016b; Venkateshwaran et al. 2018; Abdallah & Fan 2017). In line with these studies, the results here presented confirm that increasing the content of fibres leads to greater residual strengths. The type of fibre also affects the post-cracking performance, with 2HE fibres exhibiting higher strengths than 1HE fibres.

The flexural results of the four FRC mixes obtained through a three-point bending test (3PBT) are presented in Table 5.7. Three specimens were tested for mixes FRC-25/1HE, FRC-30/1HE and FRC-20/2HE, whereas only one beam was tested for FRC-25/2HE. The results show the average flexural strength and the coefficient of variation for the limit of proportionality (f_{LOP}) and for the residual strengths at crack openings of 0.5, 1.5, 2.5 and 3.5 mm (f_{R1} , f_{R2} , f_{R3} and f_{R4} , respectively).

Table 5.7 Three-point bending test results.

Concrete mix		f_{LOP}	f_{R1}	f_{R2}	f_{R3}	f_{R4}
FRC-25/1HE	Average [MPa]	5.48	3.33	1.84	0.91	0.65
	CV [%]	4.5	20.5	27.0	23.1	24.5
FRC-30/1HE	Average [MPa]	6.03	3.87	2.14	1.39	1.02
	CV [%]	16.2	33.8	30.7	21.0	14.7
FRC-20/2HE	Average [MPa]	4.94	3.22	2.65	2.41	2.09
	CV [%]	9.7	18.5	17.2	16.8	17.9
FRC-25/2HE	Average [MPa]	6.48	6.24	5.64	4.76	3.64
	CV [%]	-	-	-	-	-

In addition to the three-point bending test, the Barcelona test was also performed to analyse the behaviour of the fibres in the post-cracking stage. The Barcelona test is an alternative method to analyse and control the tensile properties of FRC (Molins et al. 2009). In this experimental programme, three cubic specimens (Pujadas et al. 2013) were produced and tested for each of the four FRC mixes. The results in Table 5.8 show the average peak and residual strengths at vertical displacements of 0.5, 1.5, 2.5 and 3.5 mm.

Table 5.8 Barcelona test results.

Concrete mix		$f_{R,peak}$	$f_{R,0.5}$	$f_{R,1.5}$	$f_{R,2.5}$	$f_{R,3.5}$
FRC-25/1HE	Average [MPa]	4.88	1.32	0.71	0.49	0.37
	CV [%]	2.0	18.3	14.0	24.5	31.0
FRC-30/1HE	Average [MPa]	5.30	2.10	0.71	0.41	0.29
	CV [%]	6.5	13.3	27.1	17.6	12.9
FRC-20/2HE	Average [MPa]	3.70	2.07	1.27	0.92	0.72
	CV [%]	3.0	8.0	9.9	10.9	12.1
FRC-25/2HE	Average [MPa]	4.33	2.85	1.92	1.44	1.19
	CV [%]	5.1	12.6	27.2	25.8	26.1

According to the contents of steel fibres established in the four dosages and the numerical model described in Chapter 4, the number of fibres in the cracked section of the beams used for the bending test have been estimated. The relation between the number of fibres and the residual strengths are displayed in Figure 5.12. The post-peak strengths obtained with the Barcelona test are also shown in Figure 5.12 according to the fibre content. The post-peak strengths have been identified for fibres 1HE or 2HE to show the effect of the anchorage geometry.

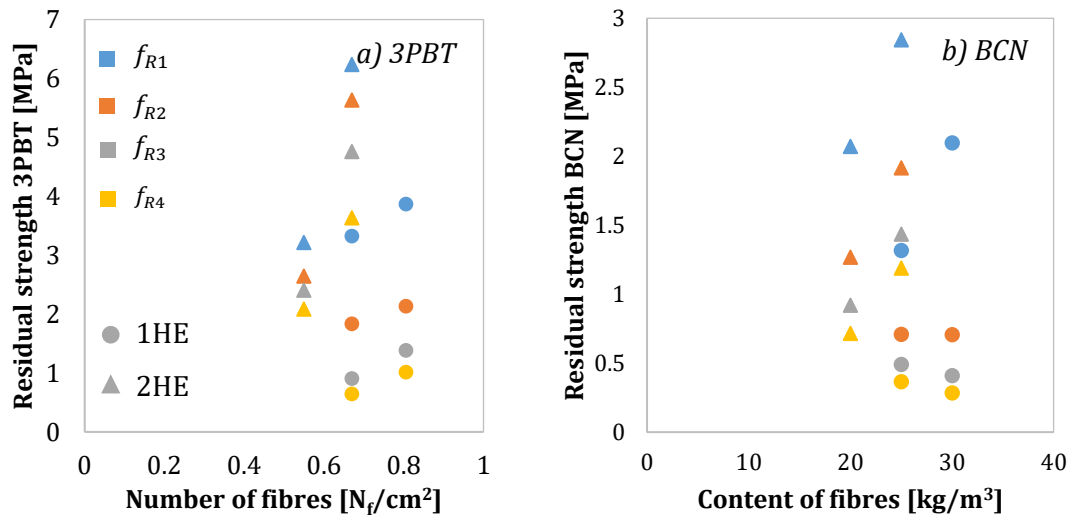


Figure 5.12 a) Flexural residual strength and b) Barcelona test results.

The results confirm how greater contents of fibres enhance the residual strength. This effect is the result of an increased bridging capacity at the cracking surface due to the higher number of fibres at this section, which is in line with the results obtained by other authors (Abrishambaf et al. 2012; Lameiras et al. 2015; Alberti et al. 2016c). The results also exhibit a decreasing residual strength for wider crack openings and displacements, i.e. the contents of fibres were too low to produce a hardening behaviour.

A comparison between the behaviour of fibres revealed that fibres 2HE performed significantly better than fibres 1HE. According to the results of the bending test, FRC-20/2HE presents a residual strength f_{R1} almost identical to its counterpart in FRC-25/1HE even with a lower content of fibres. Noticeable is also the difference between f_{R1} of FRC-25/1HE and f_{R4} of FRC-25/2HE, being the former slightly lower than the latter with the same fibre content. The values of the residual strengths between the Barcelona test and the three-point bending test present noteworthy magnitude differences due to the nature of the cracking mechanism which take place in each test. Nevertheless, and in general terms, the results follow very similar trends regardless of the test.

The greater tensile strength of fibres 2HE with respect to 1HE (1850 N/mm^2 and 1325 N/mm^2 , respectively) may also have influenced on the better performance of the mixes reinforced with fibres 2HE. Despite of this, the performance differences are mainly attributed to the improved geometry of fibres 2HE anchorages (Abdallah et al. 2016a). This effect has played a fundamental role on the load bearing capacity of FRC enhancing the bond mechanism between the fibre and the matrix (Holschemacher et al. 2010; Shah & Ribakov 2011).

5.4.3 Ductility requirements of FRC

As described in Section 5.2, the MC2010 specifies two ductility requirements ($f_{R1k}/f_{Lk} > 0.4$ and $f_{R3k}/f_{R1k} > 0.5$) that FRC needs to verify to be used as replacement of traditional concrete. These conditions aim to ensure enough ductility of the material that depends on the residual strength. These ratios have been calculated for the characteristic results of three-point bending test and are shown in Table 5.9. Given that only one beam was tested for FRC-25/2HE, the standard variation of f_{LOP} , f_{R1} and f_{R3} to determine the

characteristic value was assumed to be the average of the standard variation of f_{LOP} , f_{R1} and f_{R3} of the other three mixes.

Table 5.9 Ductility ratios of MC2010.

Concrete mix	f_{R1k}/f_{Lk}	f_{R3k}/f_{R1k}
FRC-25/1HE	0.44	0.26
FRC-30/1HE	0.39	0.53
FRC-20/2HE	0.54	0.78
FRC-25/2HE	0.87	0.88

The results show that only FRC-30/1HE does not verify the first condition ($f_{R1k}/f_{Lk} > 0.4$) and that FRC-25/1HE is the only one not fulfilling the second ($f_{R3k}/f_{R1k} > 0.5$). According to the MC2010, neither FRC-25/1HE nor FRC-30/1HE achieve enough ductility to be used in the substitution of traditional reinforcement. A possible solution lies in increasing the content of fibres 1HE, which would entail higher residual strengths f_{R1k} and f_{R3k} thus leading to greater ratios f_{R1k}/f_{Lk} and f_{R3k}/f_{R1k} .





The enhanced residual strengths of mixes FRC-20/2HE and FRC-25/2HE provided higher ductility ratios than the minimum required. It is also noteworthy how the greater amount of fibres in FRC-25/2HE than in FRC-20/2HE produced a considerably higher ratio f_{R1k}/f_{Lk} . This difference in the content of fibres had no effect on fulfilling this ductility requirement and, therefore, FRC-20/2HE already met both ductility conditions even with a lower fibre content.

5.4.4 Tensile strength of steel rebars

Rebars from two different manufacturers (SR1 and SR2) were tested to assess the tensile properties. Three diameters were tested for SR1 whereas four diameters were tested for SR2. The results of the tensile strength are shown in Table 5.10 for both types of steel and the different diameters.

The results present similar tensile strengths regardless of the type of steel; while SR1 shows an average tensile strength of 652.8 MPa, rebars SR2 achieve 658.7 MPa. As a result of the high homogeneity of steel, the scatter of the results reaches a maximum of 3.2%. Given the negligible difference on the tensile strength and for economic matters, the rebars selected for the manufacture of the slabs were SR1.

Table 5.10 Tensile strength of steel rebars.

Diameter [mm]	Tensile strength [MPa]		
	SR1	SR2	
$\phi 16$	-	648.1	$\phi 16mm$ 
$\phi 12$	633.2	655.7	$\phi 12mm$ 
$\phi 10$	675.0	650.0	$\phi 10mm$ 
$\phi 8$	650.2	680.8	$\phi 8mm$ 

5.5 RESULTS OF STAGE II: REAL-SCALE SLABS

5.5.1 Crack patterns

The crack pattern of each slab was thoroughly sketched at the end of each test. The cracks formed at each side are represented in Figure 5.13 taking the bottom surface as the symmetry axis. The main cracks are highlighted in red thicker lines while secondary cracks are shown in grey. As may be seen, the number of cracks is closely related to the type and the quantity of the reinforcement.

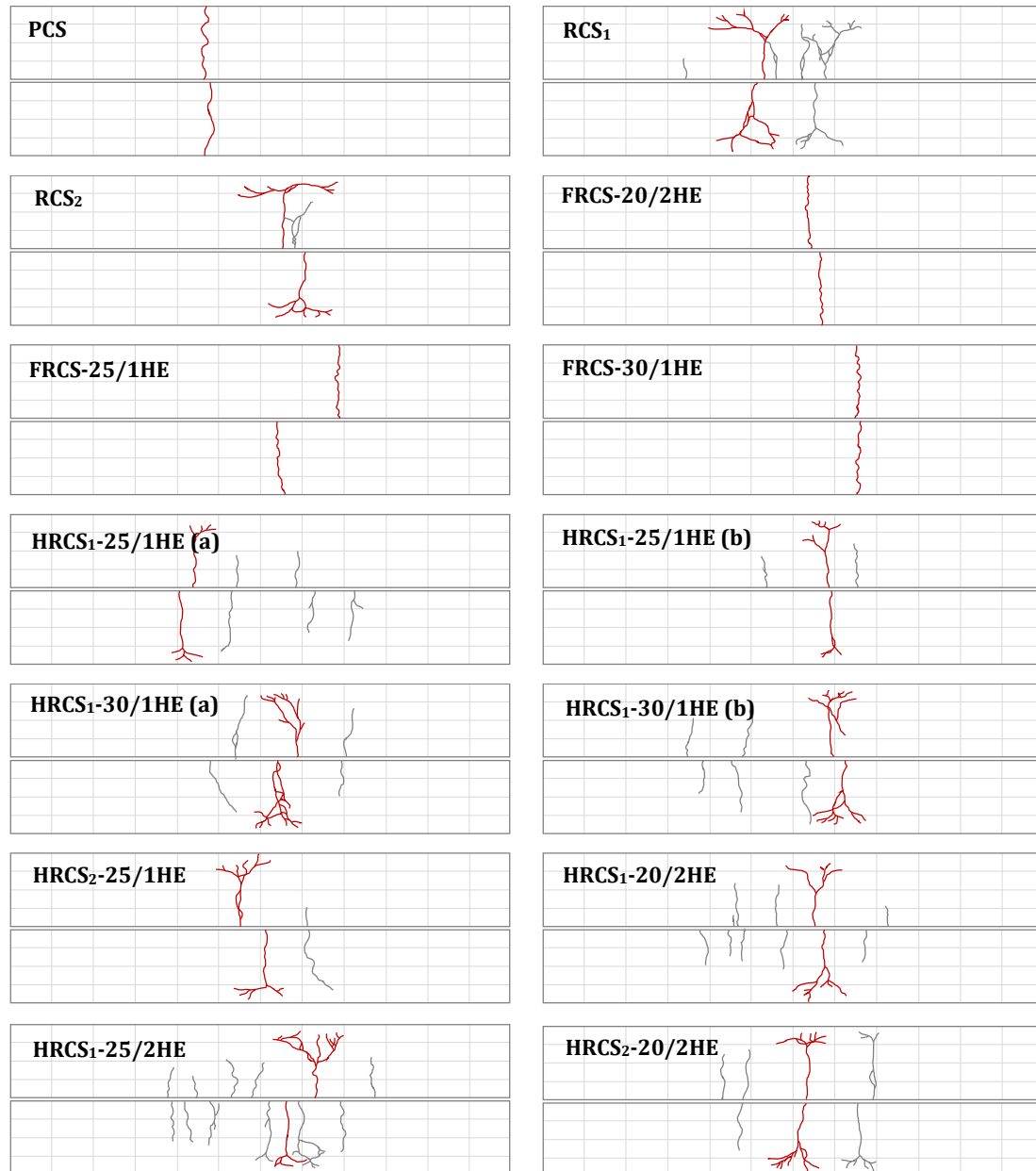


Figure 5.13 Crack patterns in slabs under flexural test.

The four slabs without rebar reinforcement (PCS, FRCS-20/2HE, FRCS-25/1HE and FRCS-30/1HE) were the only elements that presented crack localization. The rest of the slabs, either with the R₁ or R₂ reinforcement combination, presented two cracks in at least one of the faces. In line with previous studies (Pujadas et al. 2012), ramifications appeared

especially at the main cracks. These ramifications branch off at the half top of the slab and tend to follow the direction of the longitudinal compressed reinforcement.

Two regions were defined for determining both the average number of cracks (n) and the average spacing ($s_{r,m}$). The first region encompasses the whole length of the slab, while the second region is limited to the central 90 cm to consider only the flexural-caused cracks and avoid shear contribution. The number and spacing of the cracks of each slab is shown in Table 5.11.

Slabs with traditional reinforcement R_1 generally presented a greater number of cracks than those reinforced with the combination R_2 . As previously reported in other studies (Bernardi et al. 2016), the addition of fibres leads to a higher number of cracks. This effect is directly attributed to the higher residual strength provided by the fibres and the reduction of the bond transfer length (Bischoff 2003).

These results also highlight the important role of the geometry of the fibres on the cracking behaviour. Notice that the use of 2HE fibres clearly increases the number of cracks and reduces the spacing between them. The double hook of the fibres 2HE enhances the anchorage effect and provides a higher residual strength than 1HE fibres (Abdallah et al. 2016b; Abdallah & Fan 2017). This increased amount of cracks contributes to an improvement of crack control since both their width and the spacing between them decrease (Vasanelli et al. 2014; Tiberti et al. 2015).

Consequently, the variability in the number of fibres and the spacing of the analysed slabs is mainly caused by the type of fibre rather than the content. Nevertheless, a greater amount of fibres also increases the number of cracks (Blanco 2013; Pujadas 2013), producing an internal redistribution of stresses that leads to the ramification observed. This has very beneficial durability consequences, since a higher number of cracks also reduces the crack width thus hindering the ingress of external agents.

Table 5.11 Number of cracks and spacing.

SLAB	Total length		Centre - 90 cm	
	n [-]	$s_{r,m}$ [cm]	n [-]	$s_{r,m}$ [cm]
PCS	1	-	1	-
RCS ₁	3.5	28.0	3	23.7
RCS ₂	1.5	7.6	1.5	7.6
FRCS-20/2HE	1	-	1	-
FRCS-25/1HE	1	-	1	-
FRCS-30/1HE	1	-	1	-
HRCS ₁ -25/1HE (a)	3.5	33.2	3	36.4
HRCS ₁ -25/1HE (b)	2	27.7	2	27.7
HRCS ₁ -30/1HE (a)	3	36.6	2.5	38.8
HRCS ₁ -30/1HE (b)	3.5	36.7	2.5	44.9
HRCS ₂ -25/1HE	2	32.6	2	32.6
HRCS ₁ -20/2HE	5	25.1	4	21.6
HRCS ₁ -25/2HE	6.5	21.2	5	21.8
HRCS ₂ -20/2HE	3.5	32.4	3.5	32.4

5.5.2 Crack width

The displacement transducers measured the longitudinal increment produced by the cracks within the 90 cm of each side of the slabs. This distance was divided by the number of cracks that appeared in these 90 cm to obtain an average crack width. Figure 5.14 represents the load-crack width relation for crack widths up to 0.5 and 5 mm. These results mainly show the influence of the type and content of fibres and the influence of the traditional reinforcement configuration.

Given the crack localization of RCS₁ and RCS₂, only one crack works to dissipate the stresses provoked by the load thus producing a single crack with a large width. Unlike these two slabs, the greater number of cracks of the hybrid reinforced elements present a smaller average crack width due to the higher number of cracks. In these cases, failure is produced for narrower average crack widths. Nevertheless, it should be noticed that in all slabs appeared one main crack whose total width exceeded the width of the rest secondary cracks. At a certain width of the primary crack, the load dropped due to the failure of the rebar.

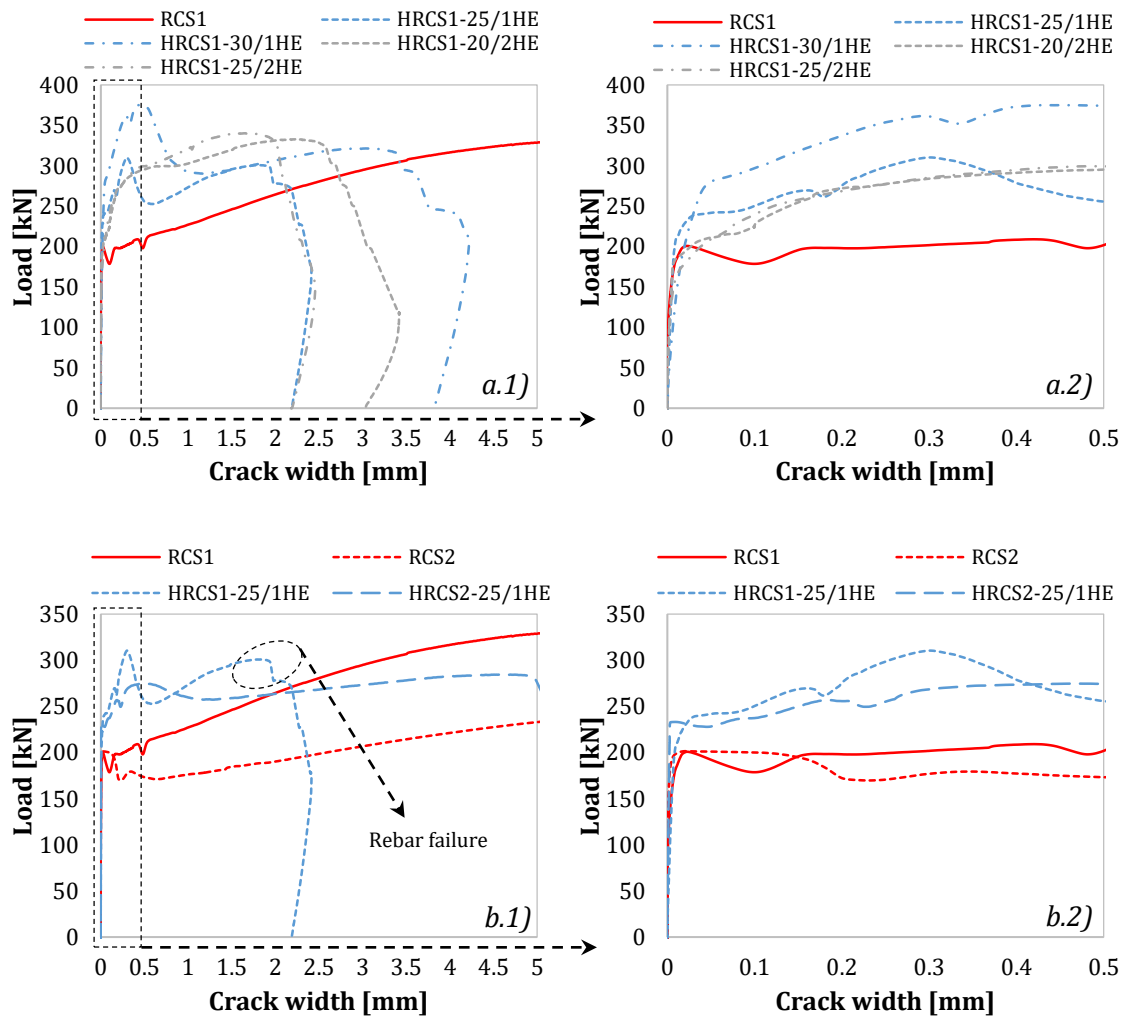


Figure 5.14 Curves load-crack width for a) HRCS₁-25/1HE, HRCS₁-30/1HE, HRCS₁-20/2HE, HRCS₁-25/2HE and b) HRCS₁-25/1HE, HRCS₂-25/1HE.

In Figure 5.14 a.1) and a.2), the influence of the type and content of fibres on the load-crack width relation may be assessed. After the cracking load, the use of fibres 1HE and 2HE increased the load capacity of the slabs. Fibres 1HE present a peak load at average crack widths around 0.5 mm , with a subsequent load drop. This behaviour is mainly attributed to the debonding of the hooks, producing an energy release that transfers the main load bearing capacity to the rebars. Notice that after this load drop, the slope of the curve is parallel to the slope exhibited by RCS_1 .

Conversely, fibres 2HE revealed a response lacking the peak load exhibited by fibres 1HE. Using a reinforcement with fibres 2HE produced a gradual increase of the load after cracking. However, there is a change of the slope in the curves at crack widths of 0.5 mm ($HRCS_1-25/2HE$) and 1 mm ($HRCS_1-20/2HE$). This new slope is, as in fibres 1HE after the load drop, parallel to RCS_1 and indicates the contribution of the rebar reinforcement to the load resistance.

In terms of small crack widths (up to 0.5 mm), the addition of fibres enhanced the behaviour of the elements with respect to those reinforced with only traditional rebars (RCS_1). Increasing the content of fibres 1HE from 25 to 30 kg/m^3 entailed an improved response of the slab. However, there is no difference on the load bearing capacity when increasing the content of fibres 2HE.

The results shown in Figure 5.14 b.1) and b.2) confirm the expected results for which RCS_1 presents a higher load resistance than RCS_2 . The generally higher number of cracks in elements reinforced with R_1 reinforcement configuration was evidenced in the discussion of the crack patterns. This higher number of cracks directly influences the average crack width, thus resulting in narrower crack widths at failure as in the case of $HRCS_1-25/1HE$. At small crack widths, a comparison between the reinforcement configuration did not reveal significant differences, neither with nor without fibres.

5.5.3 Midspan deflection

The influence of the reinforcement in terms of load-midspan deflection is presented in Figure 5.15. The results of the 12 slabs are shown and gathered according to the reinforcement type. Slabs with no reinforcement, fibre reinforcement only and hybrid reinforced slabs with different types of fibres are presented in four different figures. A summary of the numerical results for each slab is included in Table 5.12. These results show the age at which the slabs were tested, the cracking load (P_{cr}) and the maximum load discarding the initial peak load (P_{max}). The midspan deflections associated to these two load parameters are also shown.

The cracking load (P_{cr}) varies from 164 kN ($FRCS-20/2HE$) to a maximum value of 297 kN ($FRCS-30/1HE$), achieving the average of P_{cr} (P_{crm}) a value of 220 kN and $CV = 16.4\%$. This scatter is mainly related to the variation of the flexural tensile strength of the concrete ($f_{ct,fl}$), due to the intrinsic variability of this parameter (Parmentier et al. 2008). Moreover, it should be highlighted that the slabs were tested at different ages, this leading to different degrees of cement hydration.

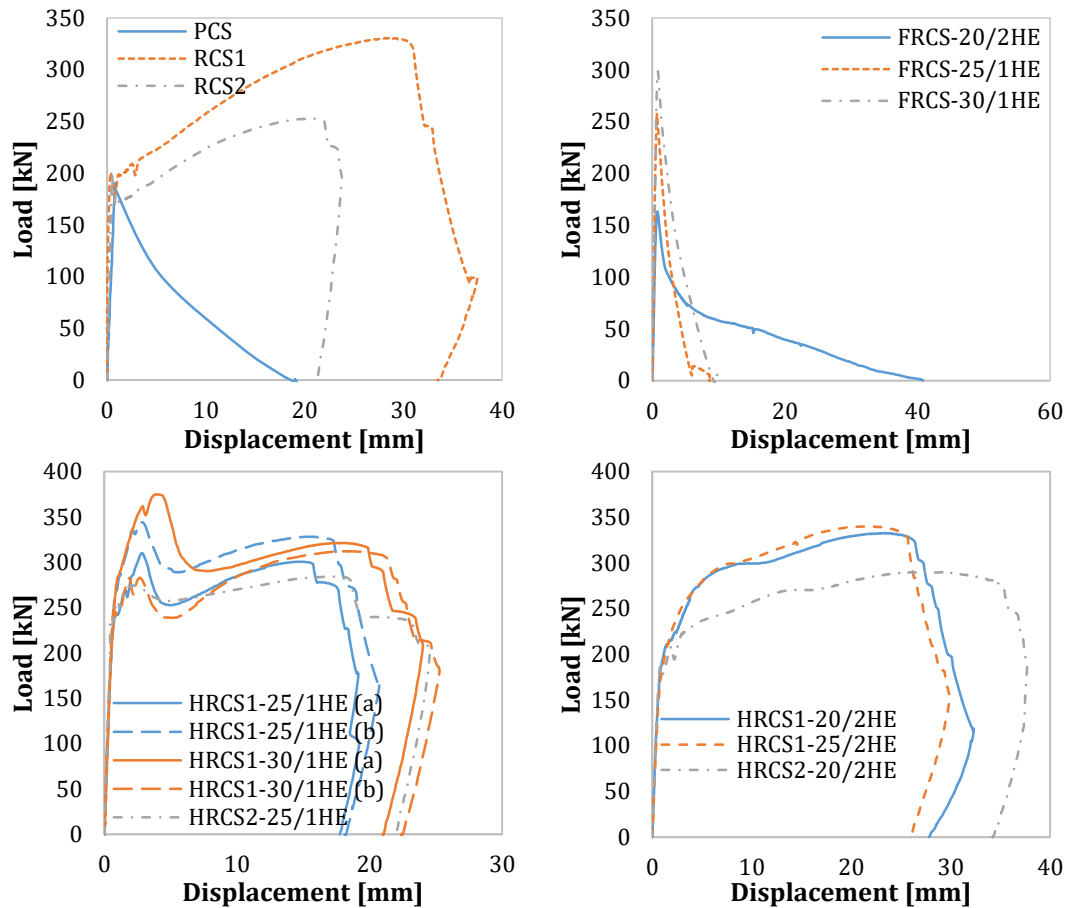


Figure 5.15 Curves load-displacement for a) PCS and RCS, b) FRC, c) HRCS with fibres 1HE and d) HRCS with fibres 2HE.

Table 5.12 Numerical results of the load-deflection curves.

SLAB	Age (days)	P_{cr} [kN]	P_{max} [kN]	δ_{cr} [mm]	δ_{max} [mm]
PCS	34	190	-	0.80	-
RCS ₁	34	201	330	0.33	29.33
RCS ₂	18	200	252	0.51	21.07
FRCS-25/1HE	34	256	-	0.76	-
FRCS-30/1HE	47	297	-	0.89	-
FRCS-20/2HE	35	164	-	0.71	-
HRCS ₁ -25/1HE (a)	34	232	301	0.61	14.88
HRCS ₁ -25/1HE (b)	34	249	328	0.72	16.37
HRCS ₁ -30/1HE (a)	34	237	322	0.66	18.73
HRCS ₁ -30/1HE (b)	35	246	312	0.68	18.56
HRCS ₂ -25/1HE	19	228	284	0.42	17.49
HRCS ₁ -20/2HE	34	204	333	1,15	24.93
HRCS ₁ -25/2HE	35	180	340	0.88	22.49
HRCS ₂ -20/2HE	47	184	290	0.76	28.71

The traditional reinforcement in RCS₁ and RCS₂ did not increase significantly the cracking strength with respect to plain concrete, although clearly improved the ductility of the slabs.

After cracking, the rebars carry the tensile stresses increasing the strength and the deformations, which for R_2 are lower than for R_1 due to difference in the reinforcement amount. The load bearing capacity of RCS_1 and RCS_2 was controlled by the deformability of the rebars, which failed sequentially once the maximum load P_{max} was reached. This kind of failure was expected considering the high compressive concrete strength, the dimensions of the cross section and the relative low amount of reinforcement.

The plain concrete slab (PCS) and the slabs reinforced only with steel fibres (FRCS-20/2HE, FRCS-25/1HE and FRCS-30/1HE) exhibited a brittle behaviour after cracking. However, the midspan deflection of FRCS-20/2HE was approximately four times higher than for FRCS-25/1HE and FRCS-30/1HE even when the content of fibres 2HE in FRCS-20/2HE was lower than the content of fibres 1HE in FRCS-25/1HE and FRCS-30/1HE. In this regard, the behaviour of FRCS-20/2HE may be attributed to the mechanical performance of both the material and the anchorage of the 2HE fibres. The slab FRCS-30/1HE was also expected to perform with a higher degree of ductility with respect to FRCS-25/1HE. Nevertheless, the unexpected high value of P_{cr} (297 kN) may have led to a sudden release of energy unable to be resisted by the relative low amount of fibres.

Hybrid reinforced slabs with 2HE fibres also exhibited a greater deflection. The vertical displacement reached by HRCS₁-20/2HE, HRCS₁-25/2HE and HRCS₂-20/2HE was in all cases higher than in slabs HRCS₁-25/1HE, HRCS₁-30/1HE and HRCS₂-25/1HE regardless of the content of 1HE or 2HE fibres. This effect is a direct consequence of the greater strength and enhanced bond-slip performance of the double hooks, which provide a higher deformability of the elements before failure.

Regarding the maximum load bearing capacity, an increment of 20% of C_f from HRCS₁-25/1HE to HRCS₁-30/1HE did not lead to a clear increase of P_{max} (315 kN and 317 kN in average, respectively). Even the slab RCS_1 (R_1) presented a higher P_{max} than HRCS₁-25/1HE and HRCS₁-30/1HE. This might be attributed to the scatter related with both the fibre amount and orientation of the fibres. Additionally, rebars bear the great part of the tensile stresses in failure regime while fibres bridge the cracks and activate secondary cracking.

Similarly, for the slabs with R_1 configuration and 2HE fibres, the slabs HRCS₁-20/2HE and HRCS₁-25/2HE did not perform significantly better in terms of maximum load ($P_{max} = 333$ kN and $P_{max} = 340$ kN for the slabs HRCS₁-20/2HE and HRCS₁-25/2HE, respectively) with respect to the slab RCS_1 ($P_{max} = 330$ kN). Nevertheless, these slabs presented a crack pattern consisting of, at least, four cracks at each lateral face of the slabs. Therefore, tension-stiffening occurs due to the addition of fibres that would help to reduce the crack width. Also, hybrid reinforced concrete slabs with R_2 rebar configuration (HRCS₂-25/1HE and HRCS₂-20/2HE) reached P_{max} higher than the $P_{max} = 252$ kN observed for the reference slab RCS_2 with the reinforcement R_2 . This might be attributed to the low reinforcement amount ($A_s = 402$ mm²) placed into these slabs and the synergistic contribution of the fibres even in failure regime.

5.5.4 Ductility assessment according to MC2010

The tensile behaviour of the slabs was analytically computed according to the constitutive laws of the MC2010 for FRC. Both the constitutive model diagram and the defining equations of the tensile behaviour are shown in Figure 5.16 along with the numerical

parameters gathered in Table 5.13 used for the different concretes produced. The tensile strength law was used in combination with the tensile stresses provided by the reinforcing rebars in hybrid reinforced slabs. In those elements in which only fibres were used, the tensile contribution of the fibres was only used.

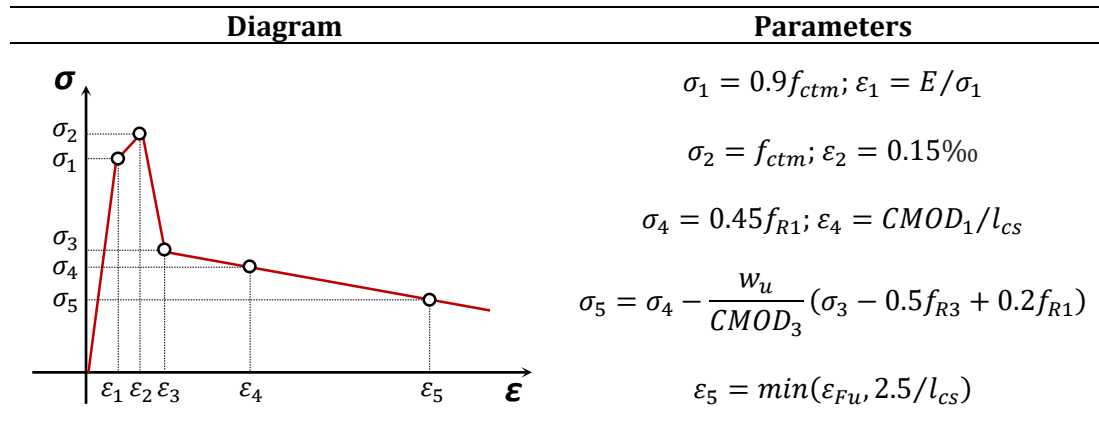


Figure 5.16 Constitutive model for FRC.

Table 5.13 Parameters for the tensile constitutive model.

	f_{cm}	f_{ctm}	Stress [MPa]					Strain [‰]				
			σ_1	σ_2	σ_3	σ_4	σ_5	ϵ_1	ϵ_2	ϵ_3	ϵ_4	ϵ_5
PCS	65.8	4.29	-	-	-	-	-	-	-	-	-	-
FRC25/1HE	81.5	4.69	4.22	4.69	1.90	1.50	0.00	0.12	0.15	0.28	4.00	18.03
FRC30/1HE	96.8	5.02	4.52	5.02	2.17	1.74	0.00	0.11	0.15	0.27	4.00	19.31
FRC20/2HE	60.6	4.14	3.73	4.14	1.66	1.45	0.56	0.13	0.15	0.29	4.00	20.00
FRC25/2HE	73.6	4.50	4.05	4.50	3.20	2.81	1.13	0.12	0.15	0.21	4.00	20.00

The $M - \chi$ diagrams shown in Figure 5.17 exhibit the sectional behaviour of the slabs computed through the method of the Analysis of Evolutionary Sections (AES) described in Chapter 3. The response of the elements undertakes three stages that may be represented in terms of $M - \chi$: a linear-elastic stage, the snap-through and the ductile behaviour.

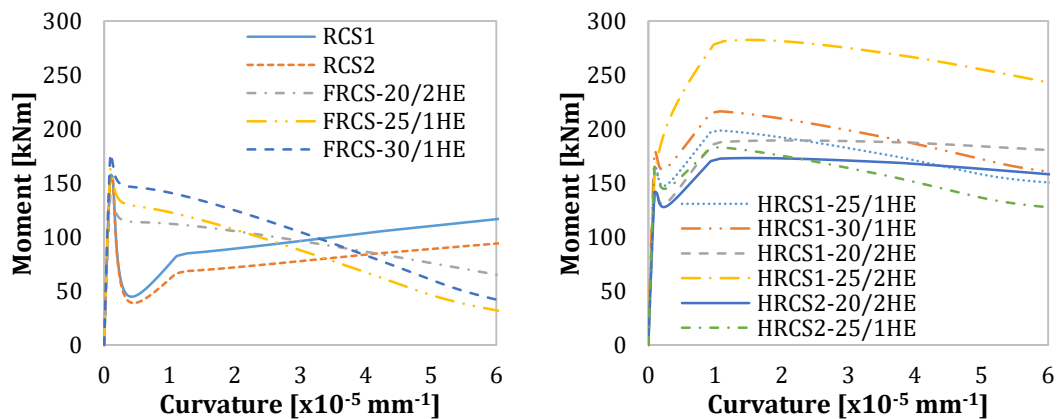


Figure 5.17 $M - \chi$ diagrams of the slabs.

The $M - \chi$ diagrams are shown according to the mechanical response, namely infracritical, critical or supracritical. According to the analytical results, all the elements reinforced only with traditional reinforcement or only fibres presented an infracritical behaviour.

Conversely, the hybrid reinforced elements exhibited a critical or supracritical response regardless of the type or content of fibre. However, despite the ductile behaviour, the elastic branches of the $M - \chi$ diagrams show in all cases similar slopes due to akin modulus of elasticity and stiffness. At the end of the linear-elastic stages, the cracking moments of the section (M_{cr}) are achieved with results that directly depend on the tensile behaviour of concrete, whose value may be calculated as function of the compressive strength according to the specifications of the MC2010. The different M_{cr} obtained in the slabs are, hence, a direct consequence of the variability of the compressive response, as shown by the characterization results of the material and mainly attributed to the addition of fibres, which do not contribute mechanically in this stage though.

Slabs RCS₁ and RCS₂ exhibited a sharp drop of the curve after M_{cr} . Such a decrease in the $M - \chi$ diagram after M_{cr} (snap-through) indicates a low tensile reinforcement that may not remain on the safe side and potentially produce a fragile response of the structure. As expected, the higher reinforcement ratio of RCS₁ exhibited an improved behaviour when compared to RCS₂. Nevertheless, the fibres presented an enhanced performance when compared to the traditional reinforcement at small curvatures. In this case, increasing the content of fibres entailed a better response of the structure after M_{cr} , regardless of whether the fibre was 1HE or 2HE.

To achieve the minimum ductility required by the MC2010 according to relation between the design and the critical moment, the reinforcement ratio was increased by combining the traditional reinforcement with fibres to reach a critical or supracritical behaviour. Five hybrid reinforced slabs presented a critical and one a supracritical behaviour. The supracritical behaviour was achieved by fibres 2HE in a content of 25 kg/m^3 combined with the rebar reinforcement R₁. The improved behaviour of this type and content of fibre was already evidenced in the results of the post-cracking strength, showing the highest residual strength of the four FRC analysed.

Among the hybrid reinforced slabs with a critical behaviour, HRCS₂-20/2HE showed the lowest strength and HRCS₁-30/1HE the maximum. A comparison between the slabs with the same rebar reinforcement and type of fibre shows that the higher content of fibres improves the behaviour of the elements in all cases. Furthermore, the type of fibres affects the slope of the curve when cracks stabilize after the snap-through: in fibres 1HE the bending moment decreases with the curvature faster than it does with fibres 2HE. As described in the material post-cracking results, the anchorage of fibres 2HE provides an improved pull-out strength that results in an enhanced bond-slip behaviour to resist the flexural loads.

5.5.5 Orientation of the fibres

Using the inductive test on cylindrical specimens it is possible to obtain a whole profile of the orientation number of the fibres (Figure 5.18a). Given the amount of data (notice that 64 cores were evaluated), it became necessary to present the results in a simplified and straightforward way. Figure 5.18b shows a system of polar coordinates that represents the orientation numbers of each specimen at each direction of the circumferential plane. The graphical representation of the results draws an ellipse whose major and minor axes correspond to the maximum and the minimum orientation number, respectively.

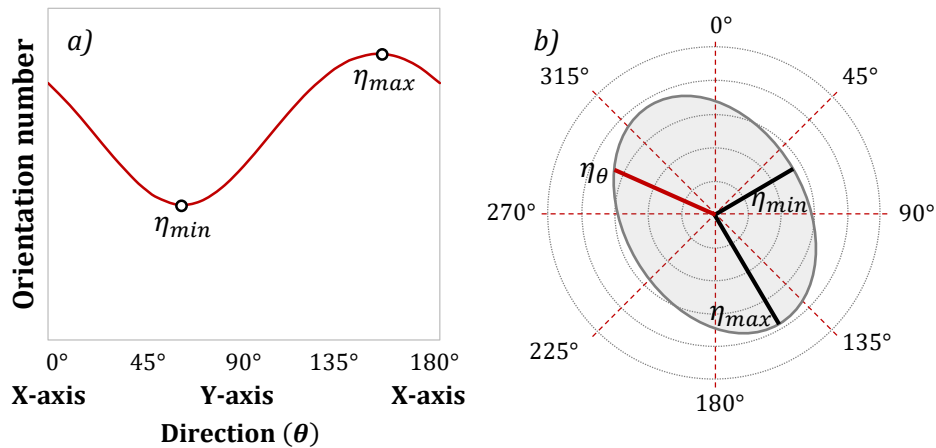


Figure 5.18 a) Orientation number (η) profile in different directions and b) representation of η in polar coordinates.

The position of the two cylindrical specimens of $\phi 150 \times 150 \text{ mm}$ obtained out of each core are represented in the bottom and the middle layer of the analysed slabs FRCS-20/2HE, FRCS-25/1HE and FRCS-30/1HE, as shown in Figure 5.19. An ellipse that represents qualitatively the full profile of the orientation number of each specimen was drawn in the position of each sample according to the results of the inductive test. The dashed line crossing each ellipse corresponds to the direction of preferential orientation or maximum η . Additionally, a picture of one of the specimens of each layer is shown with the ellipse of the orientation number superposed on it. The cracks in the pictures of the specimen correspond to the crack formation after being tested under the Barcelona test.

A colour scale is included to identify and compare the isotropy level of the orientation of the fibres of each specimen. The level of isotropy of the orientation number (Ω) may be calculated through the dimensions of the ellipses. The ratio $\Omega = \eta_{min}/\eta_{max}$ between the two axes provides a value from 0 to 1, being 1 the value for a perfect isotropy ($\eta_{min} = \eta_{max}$) and a value tending to 0 an anisotropic orientation ($\eta_{min} \ll \eta_{max}$). This result shows at which extent the fibres are oriented in a certain preferential direction.

Although no clear trend is detected regarding the isotropy of the distribution, the results suggest that the closer the specimen to the edge of the slab, the greater the anisotropy. This result is in accordance with numerous studies (Švec et al. 2014; Martinie & Roussel 2011; Boulekbache et al. 2010), where the wall-effect is extensively described and considered the responsible of the alignment of the fibres in a parallel direction to the wall when close to the formwork. The average isotropy of each layer and the angle with respect to the X-axis of the preferential orientation are included in Table 5.14 together with their respective coefficient of variation (CV).

For slabs FRCS-25/1HE and FRCS-30/1HE, the bottom layer presents a higher average isotropy than the top layer, whereas for slab FRCS-20/2HE the average isotropy is the same in the two layers. Regarding the CV, the results indicate that its value is higher for the top layers, thus resulting in the presence of regions with a high anisotropy and others with high isotropy. Such outcome matches the results of Žirgulis et al. (Žirgulis et al. 2016), which showed how the fibre orientation is more isotropic at the bottom and more anisotropic at the top due to a greater influence of the concrete flow in the latter.

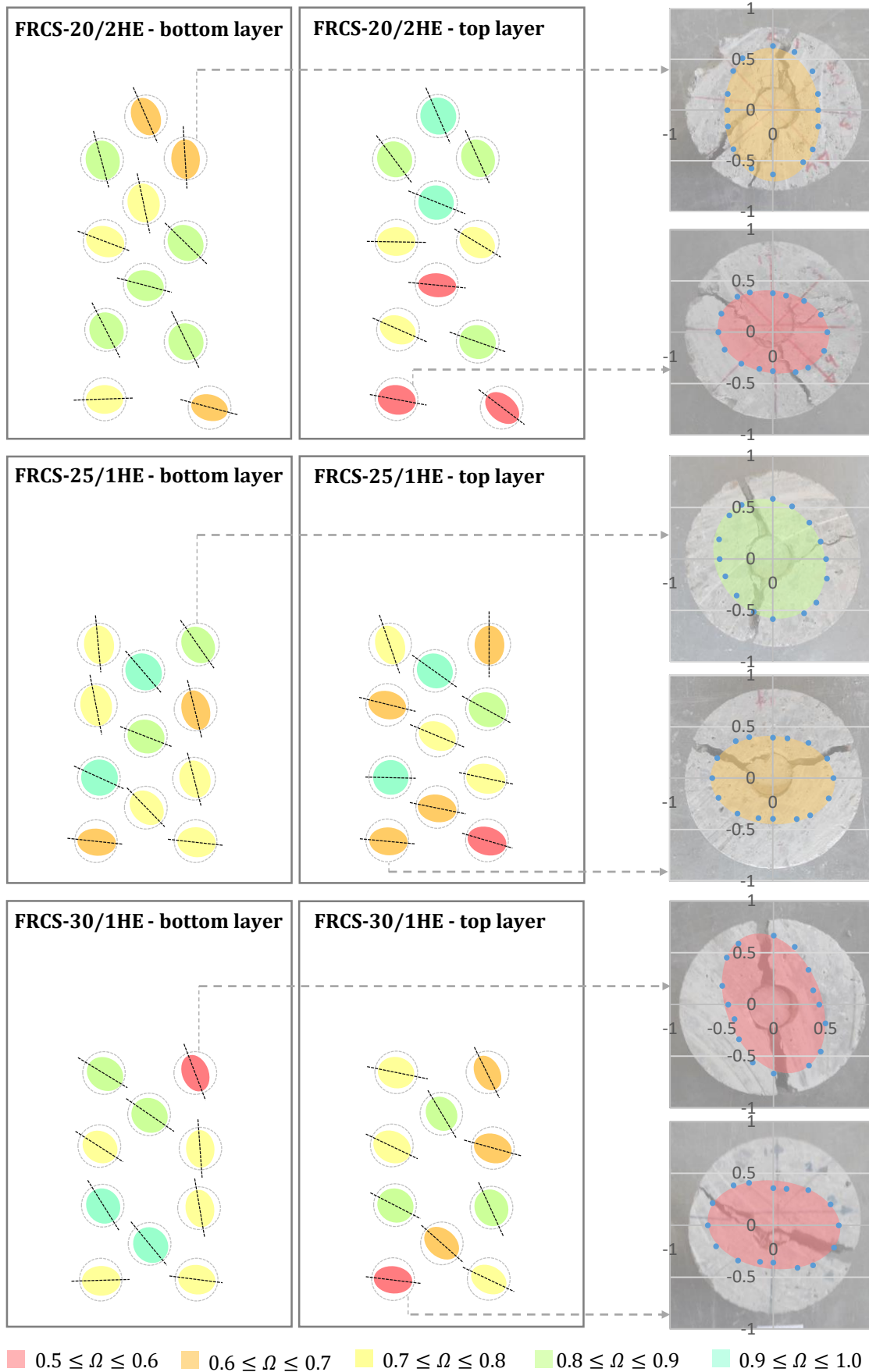


Figure 5.19 Isotropy, η , preferential orientation and main crack direction of the cores in FRCS slabs.

Table 5.14 Isotropy and direction of preferential orientation.

Parameter	FRCS-20/2HE		FRCS-25/1HE		FRCS-30/1HE	
	Bottom	Top	Bottom	Top	Bottom	Top
\bar{n}	0.78	0.78	0.80	0.73	0.78	0.75
CV	10.7%	17.0%	12.1%	17.7%	14.7%	14.8%
$\bar{\theta}$	115.5°	141.8°	122.3°	140.0°	118.5°	132.5°
CV	18.7%	23.3%	24.1%	19.4%	15.7%	22.4%

The influence of the concrete flow on the orientation of the fibres has been described in previous studies (Abrishambaf et al. 2013; Pujadas et al. 2014a; Barnett et al. 2010) and is closely related to the wall-effect. When concrete flows unrestrictedly, fibres tend to orientate perpendicularly to the flow of concrete. If nearby the walls of the formwork, the induced speed gradient makes fibres align parallel to the direction of the flow. The results show that the direction of the preferential orientation of the fibres ranges between 115° and 140°, with CVs between 15 and 24%. These results suggest that the concrete was poured from the top-right corner of the sketches presented in Figure 5.19. Considering that each sketch represents one half of the slab, this would mean that the concrete was poured from the centre of the slab and from one of its lateral edges.

The Barcelona test allows indirectly determining the approximate preferential orientation of the fibres (Pujadas et al. 2014b). The cracks should appear in the direction corresponding to the preferential orientation of the fibres. This means that the direction of minimum orientation is perpendicular to the crack since the energy required to propagate the crack would be smaller when the amount and orientation of fibres bridging the crack are lower.

The pictures of the tested cores shown in Figure 5.19 have the aim of highlighting how the direction of maximum orientation number matches the direction of the main crack. Each picture represents one core of each layer with the ellipses of the orientation number superposed. The images reveal how the major axis of each ellipse, which is the direction of maximum orientation, corresponds approximately to the main crack of the core. The differences in the direction of the major axis and the crack are caused due to the variability and heterogeneity of the material.

5.5.6 Distribution of the fibres within the cross-section

After testing the slabs, a grid was drawn in each cross-section of the three slabs FRCS-20/2HE, FRCS-25/1HE and FRCS-30/1HE and the number of fibres was counted. Figure 5.20 shows the dimensions of the grid generated, which presents 40 elements of 10x10 cm.

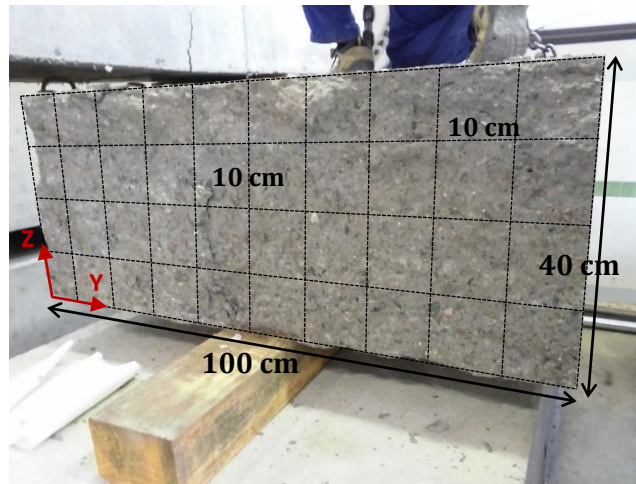


Figure 5.20 Dimensions of the grid generated in the cross-section.

The number of fibres in each square of the grid is shown in Figure 5.21 for each cross-section of the slabs FRCS-20/2HE, FRCS-25/1HE and FRCS-30/1HE. The profile of the distribution is represented through a colour scale, where red indicates a low density of fibres and green a high one.

FRCS-20/2HE

21	31	18	23	13	25	18	25	25	24
16	18	23	28	25	20	17	30	26	23
29	25	24	28	20	17	21	16	24	29
25	36	30	18	40	19	14	13	16	33
TOTAL									926

FRCS-25/1HE

26	20	26	22	33	42	19	26	21	28
20	21	14	31	21	19	20	27	25	35
17	29	25	22	24	21	27	21	32	30
52	34	19	29	29	25	23	27	20	33
TOTAL									1035

FRCS-30/1HE

43	26	26	32	22	27	25	35	23	17
30	42	34	32	40	29	32	24	20	26
24	29	15	25	32	27	14	28	21	40
31	32	33	30	20	53	36	35	28	34
TOTAL									1172

Figure 5.21 Grid and number of fibres in the cracked cross-section of the slabs FRCS-20/2HE, FRCS-25/1HE and FRCS-30/1HE.

The counting showed that the number of fibres in the cross-section of each slab increases as the content of reinforcing fibres rises. Although a greater amount of fibres bridging the cracked section should improve the post-cracking strength as shown in the characterization of the material, some additional factors ought to be taken into account. In this case, the type of fibres played an important role on the residual strength. As described in the flexural tests

to characterize the material, fibres 2HE performed better than fibres 1HE even with lower content amounts. This is also depicted in the load-displacement curve of Figure 5.15, where the post-cracking strength of the slab FRCS-20/2HE exceeded the residual response of the slabs FRCS-25/1HE and FRCS-30/1HE.

Although the part of the grid with a higher density of fibres was found at the bottom of each section for the three slabs, the overall distribution of the fibres was generally homogeneous. In this regard, no clear trend showing a preferential distribution or agglomeration of fibres could be identified.

5.6 CONCLUDING REMARKS

This chapter presented the results of an experimental programme involving tests on real-scale concrete slabs with different combinations of fibres and traditional reinforcement. The ductility requirements according to the MC2010 were presented and discussed and it was determined whether the reinforcement configurations fulfilled these specifications. The fibre distribution and orientation were also assessed through tests performed on cores drilled from the slabs. The main conclusions derived from these results are presented subsequently:

- The use of fibres increased the air content in concrete, directly affecting the compressive strength of the material. Concretes reinforced with fibres 2HE presented lower compressive strengths than those reinforced with fibres 1HE given that the double hooks of fibres 2HE reduce the packing density of FRC producing a higher air content. These differences in the compressive strength affect M_{cr} , since this value is obtained through the sectional analysis based on the constitutive laws of the material.
- Increasing the content of fibres produced greater residual strengths in FRC. This effect was clearly enhanced when using fibres 2HE as a result of the improved anchorage provided by the double hooks. Given the greater strength of fibres 2HE at larger crack widths, the ductility of FRC improved when compared to using fibres 1HE.
- The use of fibres clearly increased the number of cracks, reducing the average width and the spacing between them. While the traditional reinforcement absorbed most of the tensile stresses, the fibres activated secondary cracks. The improved bridging capacity of fibres 2HE also prompted a higher number of cracks than elements reinforced with fibres 1HE.
- Slabs reinforced with only traditional reinforcement of fibres presented an infracritical ductility behaviour and did not meet the minimum ductility requirements of the MC2010. All hybrid reinforced slabs presented a critical behaviour regardless of the type of fibre or content in the mix. Only one slab presented a supracritical behaviour mainly attributed to the enhanced anchorage of fibres 2HE.
- Although there is not a clear trend on the isotropy of the orientation of the fibres, the results suggest that the orientation becomes more anisotropic when fibres are closer to the edge of the slab. The analysis of the fibre orientation revealed differences of the orientation profile within the depth of the slab and a preferential orientation of the fibres

closer to edges towards a direction parallel to the wall. This effect might be attributed to the influence of the flow of concrete as well as the wall-effect.

In general terms, the results show that different reinforcement combinations may be adopted as long as the ductility criteria are verified. However, in elements working in an isostatic configuration, this reinforcement ratio could be reduced given that under this situation M_d does not reach M_{cr} . In this regard, a design based on M_d in the $M - \chi$ diagram even if $M_d < M_{cr}$ would be enough to guarantee the ductile response of the element.

6 MODELLING THE FLEXURAL BEHAVIOUR OF REAL-SCALE ISOSTATIC SLABS

6.1 INTRODUCTION

The size effect and the influence of the orientation of the fibres on FRC performance have been evidenced in the first part of this thesis. To mitigate the size effect, RILEM recommendations define a factor κ_h that depends on the dimension of the element to adjust the residual strength of the constitutive law. Conversely, the MC2010 does not consider the influence of size effect and assumes an equivalent post-cracking flexural response of the FRC between standardized specimens and structural elements. As presented in Chapter 3, the MC2010 specifications to determine analytically the performance of small specimens exhibit a different behaviour if compared to the experimental results. Consequently, similar trends should be expected in case of using larger elements.

Accordingly, an analysis of the suitability of the constitutive model for FRC of the MC2010 to predict the behaviour of real-scale elements has been conducted using 2D and 3D analyses. The two-dimensional study has been performed through sectional analyses whereas the three-dimensional study has been carried out through Finite Element Methods (FEM). The results have been compared to the experimental results of Chapter 5 and the parameters of the constitutive law have been calibrated to make the analytical and the FEM results fit the experimental values.

The relevance of the study lies in the fact that the slabs are representative of real elements in terms of dimensions and reinforcement configuration. According to previous studies (Pujadas et al. 2014d; Blanco et al. 2015a), constitutive models significantly overestimate the behaviour of hyperstatic slabs. In this line, the slabs herein analysed were tested under

an isostatic configuration as used to test the specimens aimed to determine the properties of FRC.

6.1.1 Objectives

The main objective of this chapter is analysing the suitability of the constitutive law for FRC of the MC2010 based on standard $150 \times 150 \times 600$ mm specimens to simulate the behaviour of real-scale elements.

- Simulate the flexural response of the real-scale slabs through sectional analysis and FEM according to the MC2010 specifications.
- Compare the results of the simulations with the experimental results and calibrate the parameters that define the properties of the material to achieve closer results between the simulation and the experimental curves.
- Identify the parameters with major influence on the results of the simulation.
- Assess the differences between the results obtained between the sectional analysis and the FEM simulation.

6.1.2 Outline of the chapter

The modelling strategy for the bi-dimensional and the three-dimensional analyses is presented in Section 6.2. The procedure to account for the contribution of the traditional reinforcement in the AES model is described along with the constitutive models used to simulate the material properties. Subsequently, the FEM model used to simulate the flexural behaviour of the slabs is presented focusing on the model type and the boundary conditions.

In Section 6.3 and 6.4, the results of the simulations in 2D and 3D are shown and compared to the experimental load-displacement ($P - \delta$) curves of the slabs obtained in Chapter 5. The parameters defining the material behaviour in the simulation are subsequently calibrated to achieve simulated curves that provide a better fit of the experimental results. These calibrations are compared to the MC2010 parameters to determine how accurate are the results provided by the MC2010 constitutive model. Finally, in Section 6.5 the main conclusions of the study are highlighted.

6.2 MODELLING STRATEGY

Stress-strain ($\sigma - \varepsilon$) and stress-crack opening ($\sigma - w$) constitutive equations can both be used to model the behaviour of FRC. According to previous studies (Buratti et al. 2013), $\sigma - \varepsilon$ is more suitable for elements with a combination of FRC and standard reinforcement due to the distribution of cracking, while elements reinforced only with fibres usually exhibit a single crack and $\sigma - w$ relations may be more recommendable. The design guidelines of the MC2010 establish a $\sigma - w$ relation for the tensile behaviour of plain concrete to take into account the tension-stiffening effect and a $\sigma - \varepsilon$ model for FRC either combined or not with standard reinforcement. These relations are described and analysed to determine whether they can accurately simulate the behaviour of slabs with rebars, fibres and a combination of both reinforcements.

6.2.1 2D simulation: AES routine

The behaviour of the slabs was analytically modelled using the AES routine (de la Fuente et al. 2012c) described in Chapter 3. The rebar reinforcement of the slabs is considered by superposition of the steel rebars tensile stress simulated as concentrated-area elements and the tensile constitutive law of FRC. A schematic representation of the profile of a concrete section with rebars and fibres is shown in Figure 6.1.

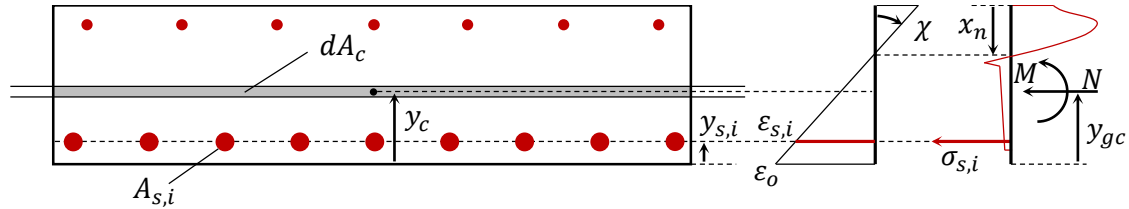


Figure 6.1 Distribution of strains and stresses of a concrete cross-section with fibres and steel rebars.

The tensile response of FRC is simulated according to the MC2010, simplifying the tensile elastic branch by removing the stress at $0.9f_{ctm}$ so $\sigma_1 = f_{ctm}$ and $\epsilon_1 = f_{ctm}/E$. The reinforcing steel is modelled using the idealized stress-strain relation of the MC2010. Figure 6.2 represents the constitutive curves of FRC and reinforcing steel in both tension and compression, defined according to the experimental results of Chapter 5.

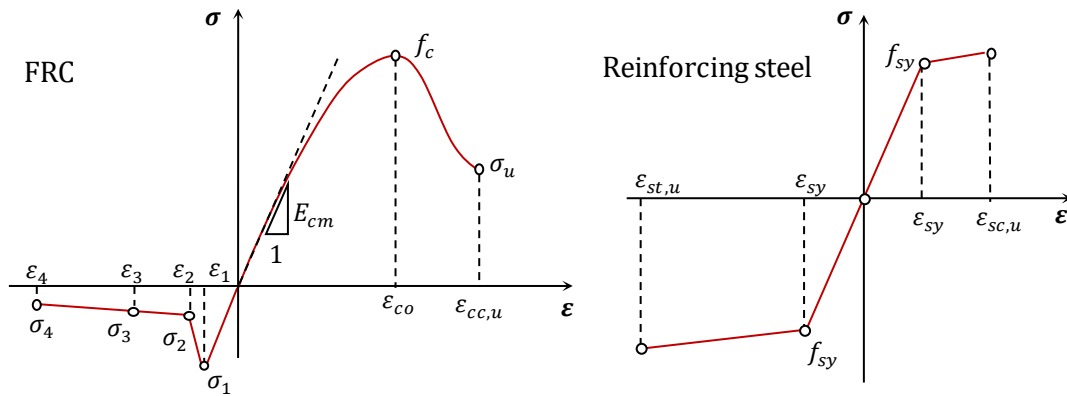


Figure 6.2 Constitutive models for FRC and steel rebars in MC2010.

6.2.2 3D simulation: Finite elements model (FEM)

The flexural response of the slabs under a four-point configuration was simulated through FEM using the ABAQUS package. In line with the analyses conducted in previous studies (Alfarah et al. 2017), plain concrete and FRC were meshed with three-dimensional solid continuum elements of eight nodes (C3D8R) whereas the bars for traditional reinforcement were modelled using truss binodal elements (T3D2). A mesh size of 25 mm was selected so the elements were bigger than the aggregate size and to avoid the hourglassing effect and the distortion of elements C3D8R with coarse mesh (Genikomsou & Polak 2015). The embedded element technique was used to define the interaction between rebars and concrete to achieve a perfect bond such that there is no slip between those.

Given the geometry of the slabs, a symmetrical model simulating half of the slab was assumed for the sake of computational optimization. The boundary conditions at the

element plane YZ of symmetry include displacement and rotation constraints $u_x = \theta_{xy} = \theta_{xz} = 0$. At the supports, either the vertical displacement in Y direction and the displacement in Z direction at the central section were restricted ($u_y = u_z = 0$). A schematic representation of the symmetric half of the beam with the boundary conditions and the two conventional reinforcement configurations is shown in Figure 6.3.

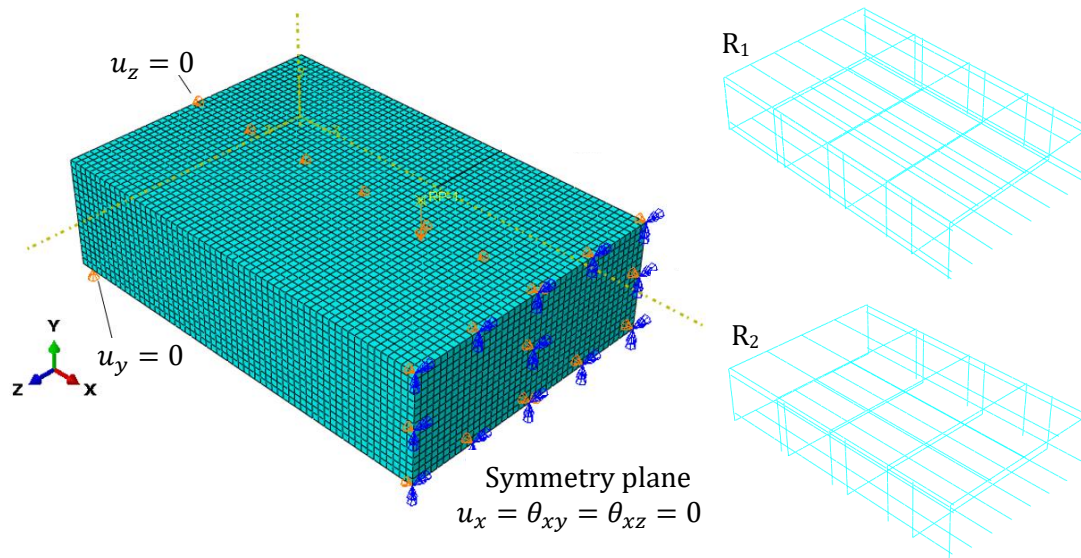


Figure 6.3 Boundary conditions and traditional reinforcement configuration.

Nonlinear simulation of the slabs was conducted using the concrete damage plasticity (CDP) model for RCS, FRCS and HRCS. Reinforced concrete behaviour is better described with models combining both damage and plasticity (Alfarah et al. 2017). Damage models are suitable to represent the complete inelastic behaviour of concrete, in compression or tension, accounting for damage development due to cracking (Avanaki et al. 2018) whereas plasticity models describe better the response of steel rebars. Based on previous experience (Mahmud et al. 2013), the default value of the five plasticity parameters required to define the CDP model was used given the negligible effect on the results. Loading rate effects were taken into consideration by including a dynamic solution for the analysis.

The tensile response of plain concrete in RCS was modelled using the $\sigma - w$ relation for tension-stiffening. FRC was modelled as a homogeneous material (fibres were considered to be uniformly distributed in the matrix) and the tensile properties of the steel rebars were obtained from direct tensile tests.

6.2.3 Parameters for the simulation of the slabs

The 2D and 3D simulations were conducted defining the input properties of the materials according to the experimental results of Chapter 5. The content and the type of fibres used in each slab establish the input value based on the results of the material characterization. As shown in Table 6.1, the same parameters were used in slabs with the same fibre reinforcement regardless of being FRCS or HRCS.

Table 6.1 Mechanical properties of concrete mixes.

Param. [MPa]	Slabs				
	RCS ₁ RCS ₂	FRCS-25/1HE HRCS ₁ -25/1HE HRCS ₂ -25/1HE	FRCS-30/1HE HRCS ₁ -30/1HE	FRCS-20/2HE HRCS ₁ -20/2HE HRCS ₂ -20/2HE	HRCS ₁ -25/2HE
E_{cm}	37442	35510	39760	28627	33359
f_{cm}	65.8	81.5	96.8	60.6	73.6
f_{R1}	-	3.33	3.87	3.22	6.24
f_{R3}	-	0.91	1.39	2.41	4.76

6.3 2D SIMULATION: PARAMETRIC STUDY OF THE CONSTITUTIVE MODEL

Inverse analyses are common procedures to determine the parameters of $\sigma - \varepsilon$ relations from experimental results (López et al. 2015; López et al. 2016). An inverse analysis using the AES on a 2D simplification of the slabs has been conducted to simulate the load-displacement curves with the aim obtaining the closest approximation to the experimental results of the slabs characterized in Chapter 5. The approach consists in computing the analytical load-displacement curve using the AES with the parameters of the MC2010 constitutive laws. Subsequently, these parameters were calibrated through an iterative process to recalculate the new load-displacement curves using AES.

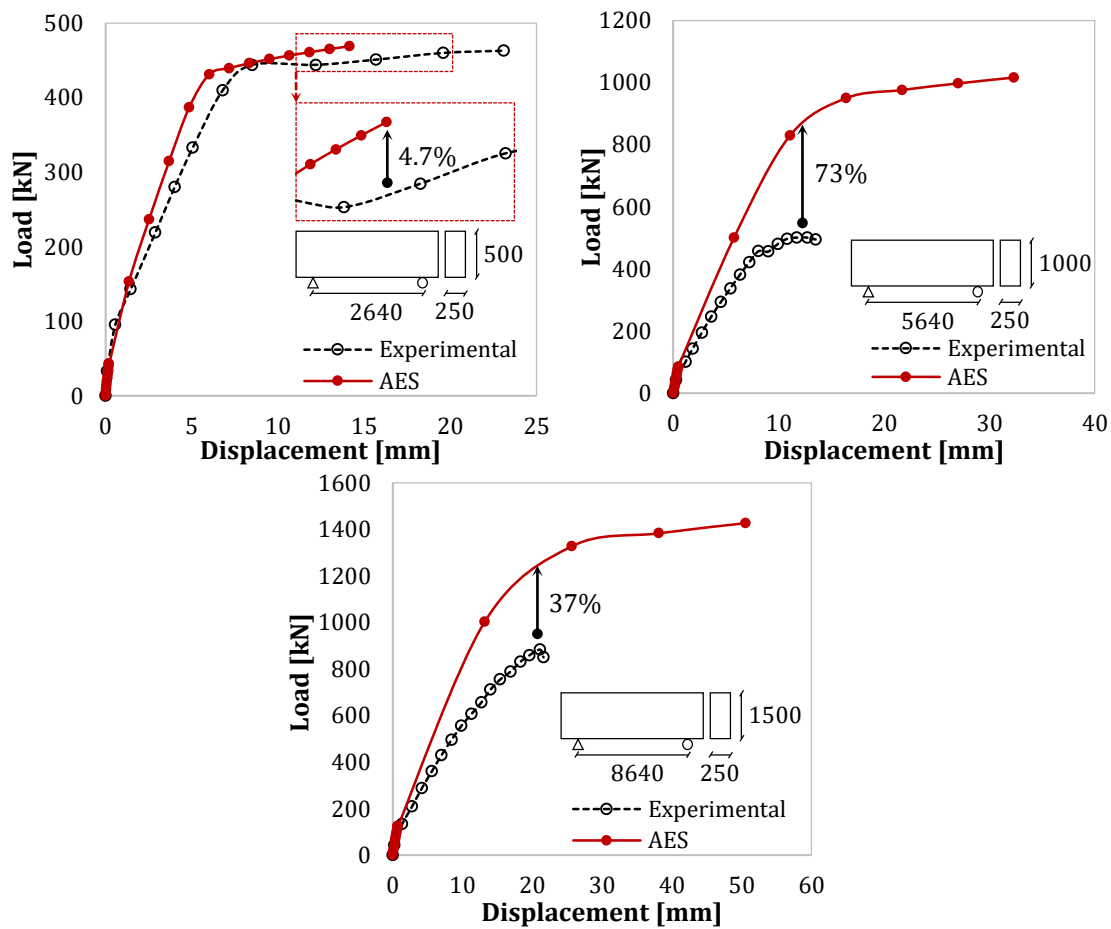


Figure 6.4 Comparison between AES and experimental results of HRCS (Minelli et al. 2014).

The AES model was validated with the experimental results of large beams reinforced with different combinations of fibres and rebars tested under a three-point bending configuration (Minelli et al. 2014). The curves shown in Figure 6.4 exhibit how the results of the AES overestimate the experimental values.

6.3.1 Reinforced concrete

The $\sigma - w$ relation of the tensile behaviour of plain concrete and the $\sigma - \varepsilon$ curve of steel rebars have been combined to simulate the response of RCS₁ and RCS₂. The load-displacement curves of the experimental results of RCS₁ and RCS₂ along with the estimations obtained from the MC2010 and the calibrated results are shown in Figure 6.5. Additionally, the results of the tests conducted on plain concrete slabs are also presented to show the contribution of the steel rebars.

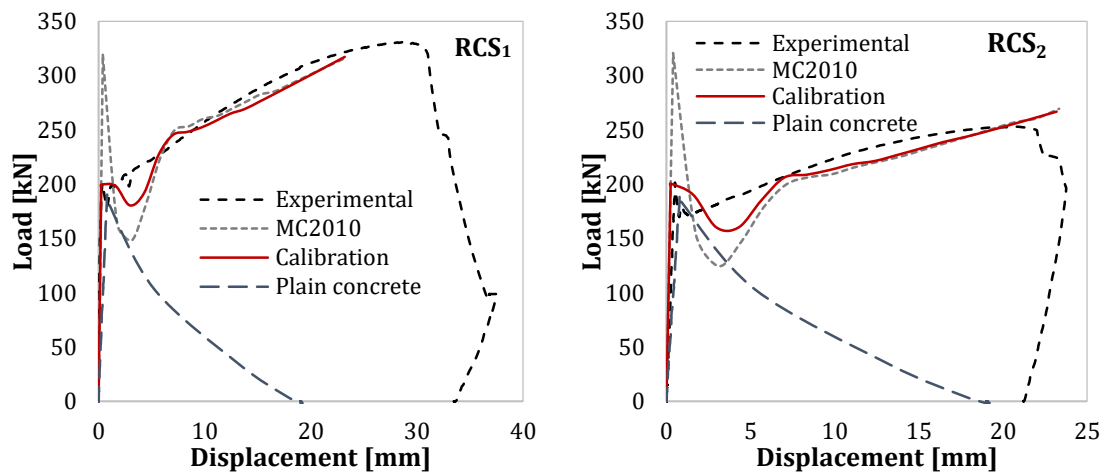


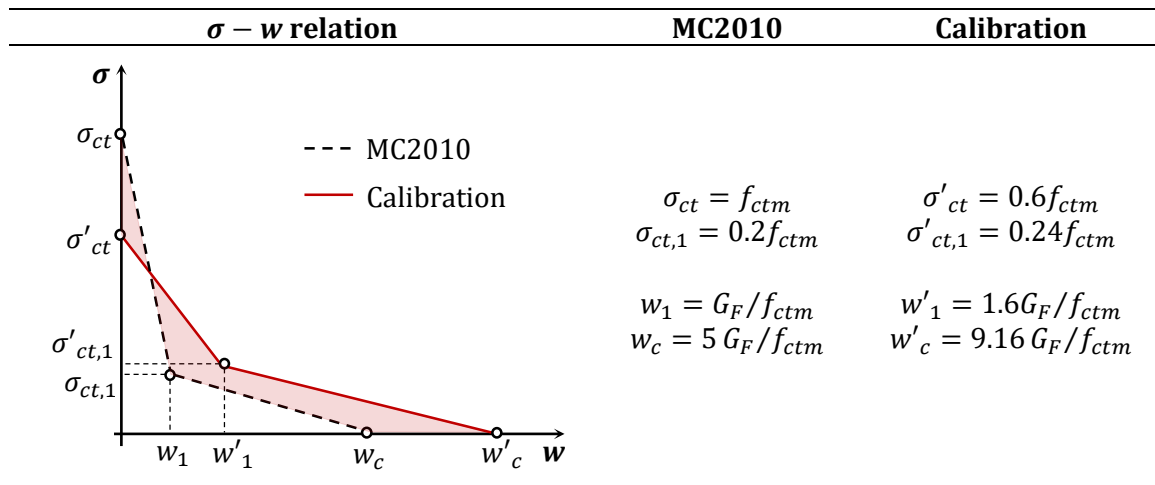
Figure 6.5 Experimental, MC2010, plain concrete and calibrated $P - \delta$ curves of RCS₁ and RCS₂.

The curves yielded by the model exhibit three stages: cracking, snap-through and reinforcement contribution. According to the specifications of the MC2010 and as reported by previous authors (Cunha et al. 2012; Abrishambaf et al. 2015), the resulting cracking load in both slabs is approximately 60% higher when compared to the experimental value. However, it should be taken into account that the value of f_{ctm} introduced in the model was estimated according to the equation of the MC2010 involving f_{cm} . In this regard, if tensile or flexural tests had been performed, either f_{ct} or $f_{ct,fl}$ could have been introduced in the model thus reducing the error at the cracking load. Likewise, there exist tensile stresses at the extreme layers due to the differential drying shrinkage (self-compensated stress state) that also reduce the effective f_{ct} , which were not considered in this analysis. The simulated snap-through exhibits a sharper load drop than the one obtained in the experimental test. This is subsequently followed by the load-bearing capacity activation of the steel rebars, whose simulated behaviour presents maximum differences with regard to the experimental curves of 4.4% and 5.5% in RCS₁ and RCS₂, respectively.

Given the overestimation of the cracking load and the sharp snap-through obtained in the simulation, a calibration of the parameters defining the bilinear stiffening response of the MC2010 has been conducted to fit the analytical curves to the experimental results. The parameters defining the $\sigma - w$ relation of plain concrete have been modified accordingly as

shown in Table 6.2 to reduce the cracking load and smoothen the snap-through. The highlighted area indicates the variation of the fracture energy (G_F).

Table 6.2 Plain concrete $\sigma - w$ calibration for AES.



The average tensile strength f_{ctm} out of which the cracking point is obtained has been reduced to 60% of its value. The stress at a crack opening w_1 has been increased from 20% to 24% of f_{ctm} . Finally, the final crack opening has also been modified from $w_c = 5 \cdot G_F/f_{ctm}$ to $w'_c = 9.16 \cdot G_F/f_{ctm}$. An identical calibration of the $\sigma - w$ relation has been used for RCS₁ and RCS₂ given that both slabs were manufactured with the same concrete.

6.3.2 Fibre reinforced concrete

Figure 6.6 shows the experimental load-displacement curves of the slabs FRCS-20/2HE, FRCS-25/1HE and FRCS-30/1HE compared to the results of the analytical simulation obtained using the MC2010 and the subsequent calibrated parameters. In the three cases, the results obtained using the parameters calculated as defined in the MC2010 exhibit significant overestimations of the load-bearing capacity of the slabs, thus leading to an unsafe prediction of the structural response.

According to the results of Figure 6.6, the slab reinforced with fibres 2HE exhibited a higher displacement when compared to slabs with fibres 1HE regardless of the reinforcing fibre content. Consequently, strains achieved higher values in FRCS-20/2HE than in FRCS-25/1HE and FRCS-30/1HE. This effect is illustrated in the MC2010 and the calibrated $\sigma - \varepsilon$ relations shown in Figure 6.7, with FRCS-20/2HE presenting the highest strains and FRCS-30/1HE exhibiting greater strengths than FRCS-25/1HE as a result of the content of fibres.

The parameters defining the constitutive model calculated according to the MC2010 and the calibrated results are shown in Table 6.3. In all cases, the calibrated tensile stresses have been reduced with respect to the parameters of the MC2010 to fit the experimental curve. Regarding the strains, both ε_1 and ε_3 were kept constant whereas ε_2 and ε_4 were modified.

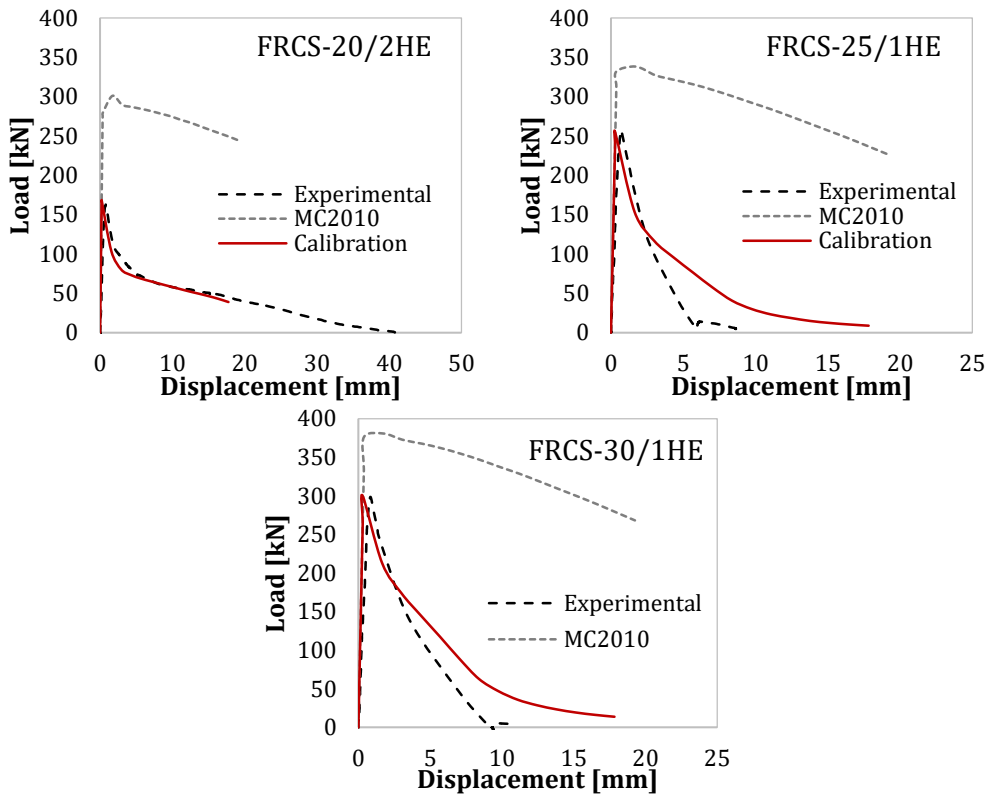


Figure 6.6 Experimental, MC2010 and calibrated $P - \delta$ curves of FRCS-20/2HE, FRCS-25/1HE and FRCS-30/1HE.

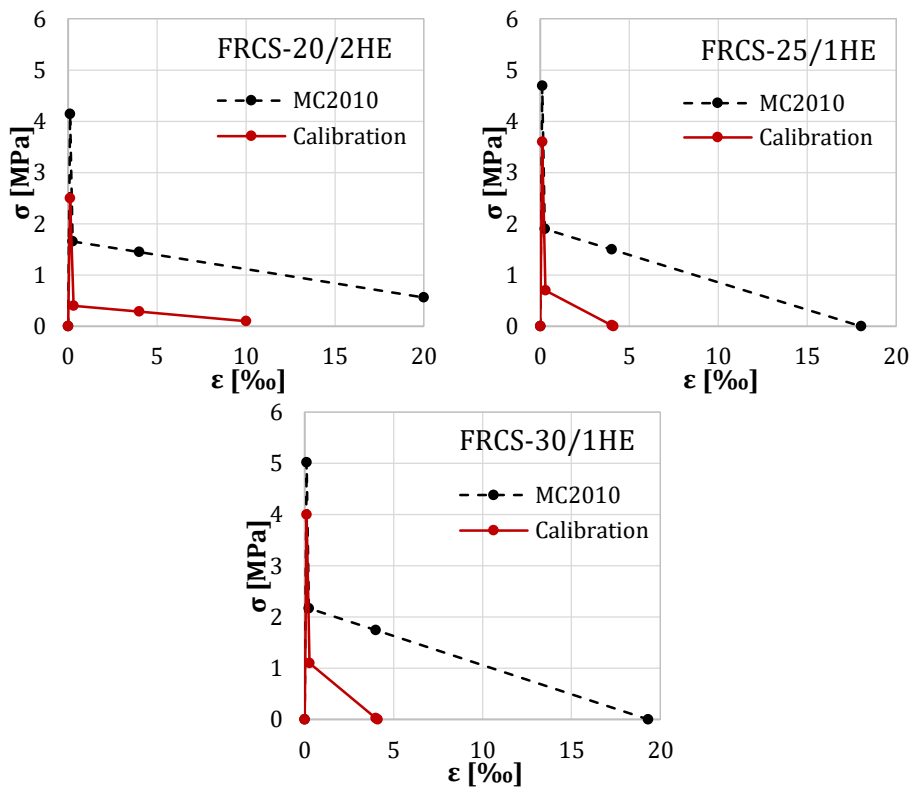


Figure 6.7 Comparison between the MC2010 and the calibrated constitutive laws of FRCS-20/2HE, FRCS-25/1HE and FRCS-30/1HE.

Table 6.3 FRC properties for fibre reinforced concrete slabs.

Parameters	Slab	σ_1	ϵ_1	σ_2	ϵ_2	σ_3	ϵ_3	σ_4	ϵ_4
MC2010	FRCS-20/2HE	4.14	0.11	1.66	0.26	1.45	4.00	0.56	20.00
	FRCS-25/1HE	4.69	0.11	1.90	0.25	1.50	4.00	0.00	18.03
	FRCS-30/1HE	5.02	0.11	2.17	0.24	1.74	4.00	0.00	19.31
Calibration	FRCS-20/2HE	2.50	0.11	0.40	0.31	0.29	4.00	0.10	10.00
	FRCS-25/1HE	3.60	0.11	0.70	0.28	0.02	4.00	0.00	4.10
	FRCS-30/1HE	4.00	0.11	1.10	0.27	0.03	4.00	0.00	4.10

A reduction of 40% in σ_1 was found to fit the experimental cracking load in FRCS-20/2HE, whereas only a reduction of 23% and 20% of σ_1 in FRCS-25/1HE and FRCS-30/1HE was necessary. As in the case of RCS, such reduction may be partially attributed to the use of an estimated f_{ctm} instead of the experimental f_{ct} . Notice there is a similar reduction in 1HE fibres regardless of the content, but much lower than the reduction in 2HE fibres. A similar effect occurs in σ_3 and σ_4 although at different percentages.

Strains ϵ_2 and ϵ_4 have been respectively increased and decreased given that they control the slope of different stages of the curves. In the three cases, ϵ_2 has been increased to avoid the sharp load drop produced after cracking. Conversely, ϵ_4 needs to be decreased given the flat shape of the MC2010 simulation at the end of the $P - \delta$ curve. Notice that the calibrated value of ϵ_4 in FRCS-25/1HE and FRCS-30/1HE is approximately 78% below the parameter obtained through the MC2010, whereas the reduction in FRCS-20/2HE is 50%.

In this regard, the results exhibit how fibres mainly contribute during Service Limit State (SLS) and lose effectiveness at Ultimate Limit State (ULS). This effect is evidenced according to the type of fibres, which achieve maximum strains of 4.10‰ and 10‰ in 1HE and 2HE, respectively. These results are in accordance with the total displacement exhibited in the $P - \delta$ experimental curves of the slabs, in which fibres 2HE presenting a higher strain also achieved a greater displacement than slabs reinforced with fibres 1HE.

The necessity of reducing σ and ϵ to fit the results of the slabs reveals the overestimation of the parameters of the MC2010, which are obtained according to tests conducted on standardized beams (150x150x600 mm). This means that the defining properties of the material exhibit higher strengths in smaller elements. These results are in line with those reported in Chapter 3, which stated that reducing the dimensions of specimens leads to higher strengths.

6.3.3 Hybrid reinforced concrete

The behaviour of HRC is simulated combining traditional reinforcement and fibres. For this, the constitutive models of both elements are superimposed to determine the simulated curve resulting of the contribution of rebars and fibres. The results of modelling the HRC slabs considering the MC2010 constitutive properties of FRC are presented in Figure 6.8, showing a generalized overestimation of the experimental curves.

The stress and strain parameters of the FRC used in the six combinations of HRCS are summarized in Table 6.4. As in FRCS, the parameters calculated according to the MC2010 specifications and the calibrated values are presented. Similarly, both ϵ_2 and ϵ_4 were modified while ϵ_1 and ϵ_3 remained constant.

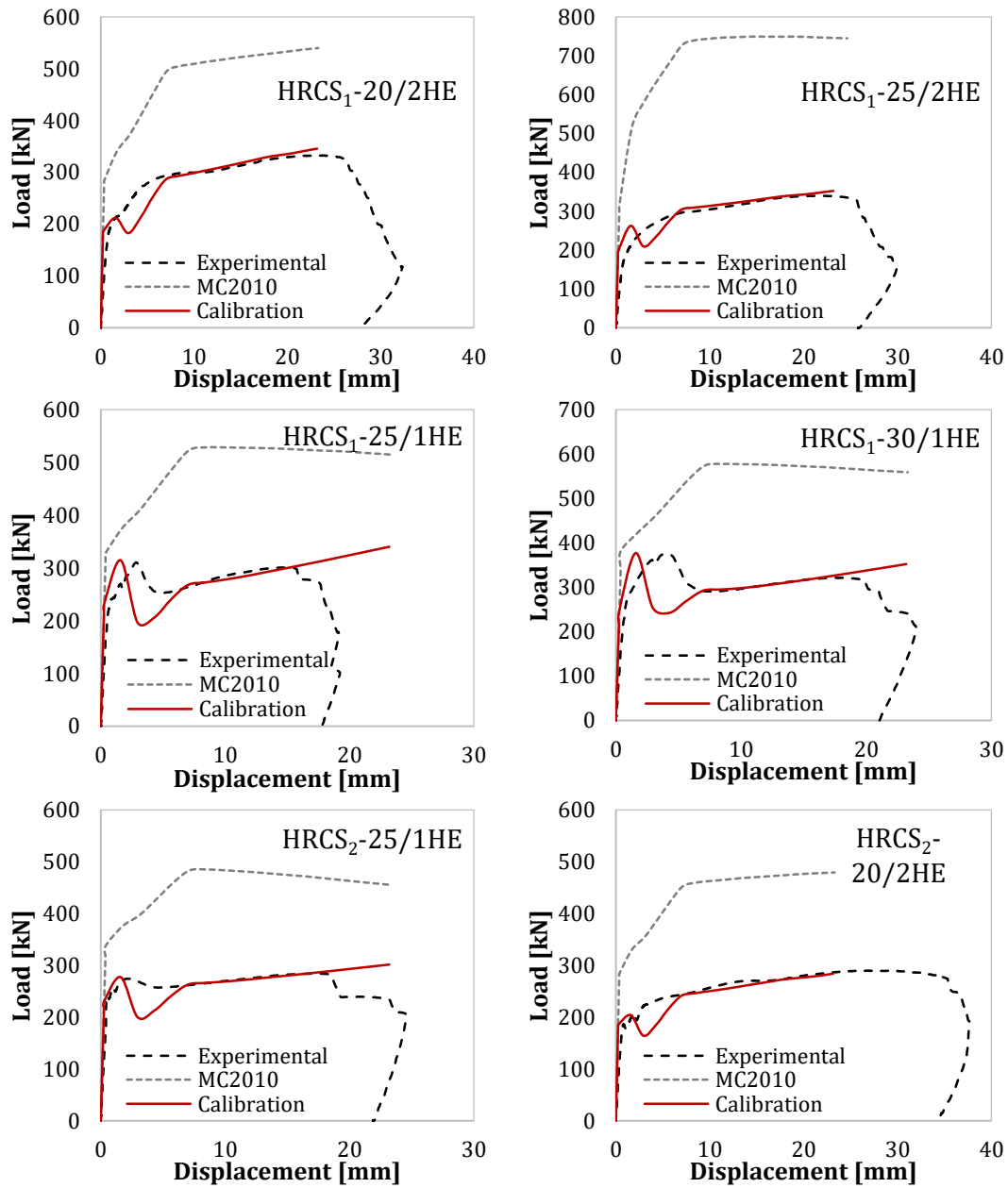


Figure 6.8 Experimental, MC2010 and calibrated $P - \delta$ curves of HRCS.

Table 6.4 FRC properties for hybrid reinforced concrete slabs.

Parameters	Slab	σ_1	ϵ_1	σ_2	ϵ_2	σ_3	ϵ_3	σ_4	ϵ_4
MC2010	HRCS ₁ -20/2HE	4.14	0.11	1.66	0.26	1.45	4.00	0.56	20.00
	HRCS ₁ -25/2HE	4.50	0.11	3.21	0.18	2.81	4.00	1.13	20.00
	HRCS ₁ -25/1HE	4.69	0.11	1.90	0.25	1.50	4.00	0.00	18.03
	HRCS ₁ -30/1HE	5.02	0.11	2.17	0.24	1.74	4.00	0.00	19.31
	HRCS ₂ -25/1HE	4.69	0.11	1.90	0.25	1.50	4.00	0.00	18.03
	HRCS ₂ -20/2HE	4.14	0.11	1.66	0.26	1.45	4.00	0.56	20.00
Calibration	HRCS ₁ -20/2HE	2.70	0.11	0.30	0.60	0.23	4.00	0.10	10.00
	HRCS ₁ -25/2HE	2.80	0.11	0.40	0.70	0.29	4.00	0.10	10.00
	HRCS ₁ -25/1HE	3.20	0.11	0.10	0.85	0.08	4.00	0.00	15.00
	HRCS ₁ -30/1HE	3.20	0.11	0.20	1.10	0.16	4.00	0.00	15.00
	HRCS ₂ -25/1HE	3.20	0.11	0.40	0.70	0.31	4.00	0.00	15.00
	HRCS ₂ -20/2HE	2.70	0.11	0.30	0.60	0.23	4.00	0.10	10.00

The calibrated σ_1 has been reduced in average 34.5%, whereas in the case of σ_3 and σ_4 reductions were between 80% and 95%. Regarding the strains, ε_2 increased in all cases and ε_4 was reduced 50% in fibres 2HE and around 20% in fibres 1HE. These results suggest that, unlike in FRCS, there is not a clear trend indicating up to which extent parameters should be calibrated depending on the type of fibre when these are combined with traditional reinforcement.

A comparison between HRCS and RCS reveals that fibres increased the load bearing capacity of the slabs at small displacements. This is in line with results reported in certain studies (Meda et al. 2012; Bernardi et al. 2016) stating that FRC improves the behaviour at Service Limit State (SLS) with respect to crack and displacement control. The tension-stiffening effect due to the activation of the fibres after concrete cracking contributes to increase the load carrying capacity of the slab at the initial stage.

According to the experimental curves of Figure 6.8, the enhanced performance in SLS was higher in slabs reinforced with fibres 1HE than in those with fibres 2HE. The strains achieved in the constitutive calibrated parameters also indicate there is a contribution of fibres in Ultimate Limit State (ULS). In this case, ε_4 reaches in fibres 1HE a value of 15‰ whereas in fibres 2HE this value decreases to 10‰.

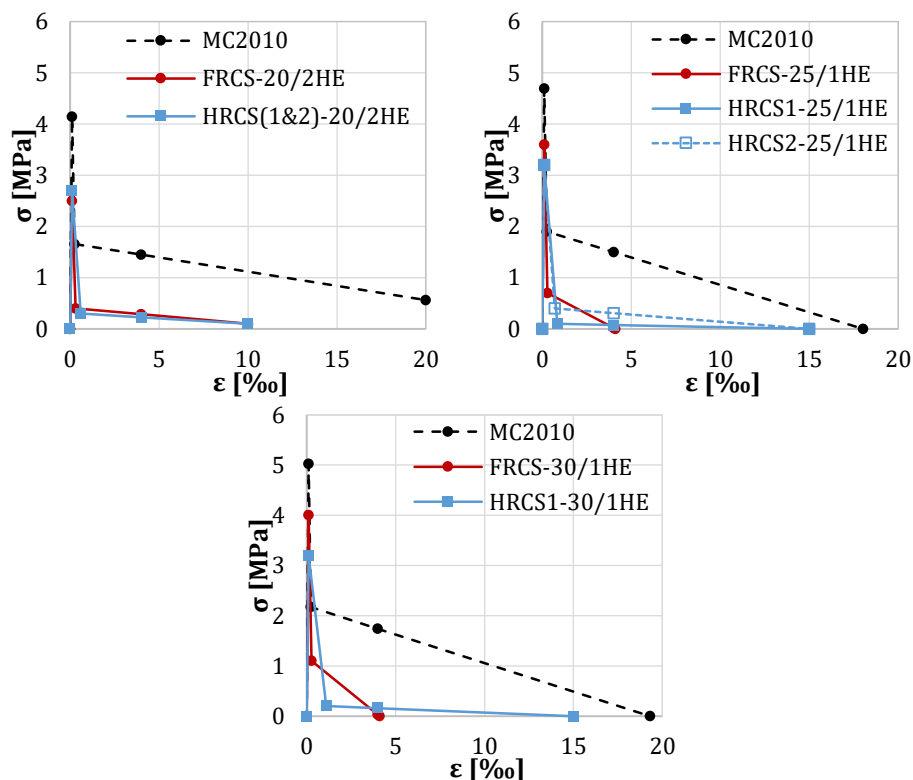


Figure 6.9 Comparison between the MC2010 and the calibrated constitutive laws of HRCS.

There is a noticeable difference between the calibrated parameters of HRCS and FRCS, especially when using fibres 1HE. Figure 6.9 shows a comparison between the parameters of the MC2010, the calibration of slabs reinforced with fibres and the parameters fitting the results of the hybrid slabs. Slab HRCS₁-25/2HE is missing given that this fibre reinforcement configuration was not tested in FRCS. The curve of HRCS(1&2)-20/2HE corresponds to slabs HRCS₁-20/2HE and HRCS₂-20/2HE given that both slabs presented the same calibration results.

A comparison of the results between HRCS and FRCS suggests a lower reinforcing contribution of the fibres when used in combination with rebar reinforcement. This effect is barely noticeable in HRCS₁-20/2HE or HRCS₂-20/2HE, thus revealing an equivalent contribution of fibres 2HE in the presence or not of traditional reinforcement. Conversely, the effect can be clearly appreciated when using fibres 1HE, which tend to present a smaller contribution in terms of strength although achieving greater strains when combined with traditional reinforcement.

6.4 3D SIMULATION: PARAMETRIC STUDY OF THE CONSTITUTIVE MODEL

A similar procedure to the 2D analysis has been conducted in the 3D model: the numerical parameters of the MC2010 have been used to obtain the load-displacement curve and have been subsequently calibrated to find the closest approximation to the experimental results. In the three-dimensional FEM analysis, the tensile behaviour of plain concrete and FRC can be defined in the CDP model by means of stress-strain, stress-crack width or fracture energy criteria. In this case, and to minimize convergence issues and mesh size dependency due to spurious strain-softening localization, the tensile response of the material was modelled according to the stress-crack width displacement ($\sigma - w$) (Abrishambaf et al. 2015; Genikomsou & Polak 2015).

In the case of the 3D analysis, only the slabs reinforced with fibres 1HE have been simulated. The main reason for this is that the current constitutive models were developed based on the use of this type of fibres. Additionally, the use of fibres 1HE is more extended than the use of fibres 2HE, although increasing research of the reinforcing properties of fibres 2HE is recently being conducted (Abdallah et al. 2016b; Venkateshwaran et al. 2018; Lim et al. 2018).

6.4.1 Reinforced concrete

A comparison between the load-displacement experimental curve and the calibrated FEM simulation of slabs RCS₁ and RCS₂ is shown in Figure 6.10. As in the results of the 2D analyses according to the AES, the three main stages identified as cracking, snap-through and reinforcement contribution can be appreciated in the simulated curves.

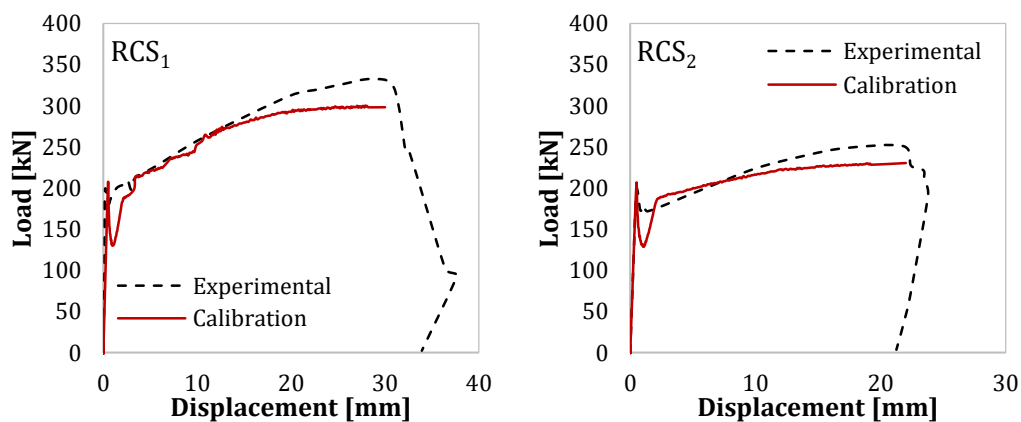
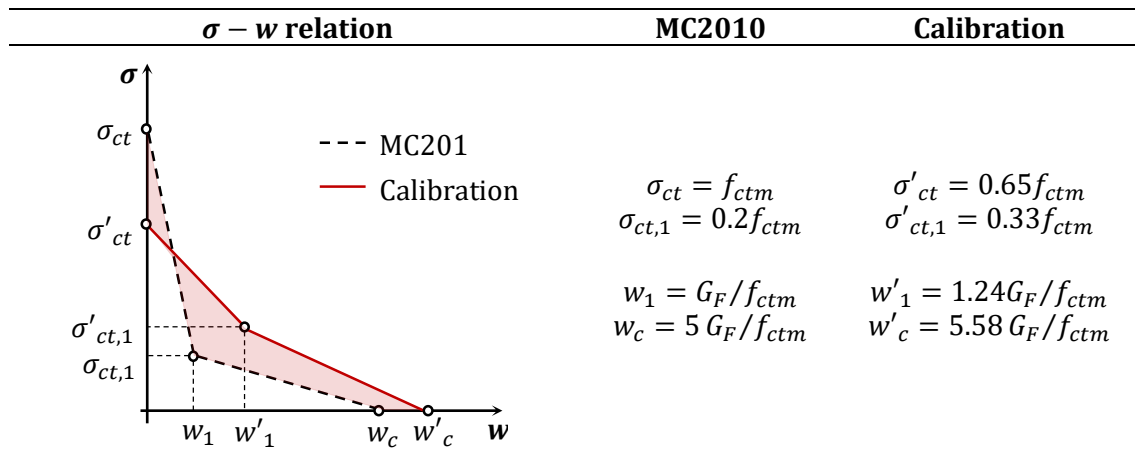


Figure 6.10 Experimental and calibrated $P - \delta$ curves of RCS₁ and RCS₂.

The calibrated curves exhibit an overestimation of the cracking load of 5% with respect to the experimental values in both slabs. As in the 2D case, the simulated snap-through is

sharper than the one in the real behaviour, leading the rebar activation of the load-carrying capacity to start at a displacement of approximately 2 mm. Regarding the maximum load, the simulation underestimates the experimental response in 8.3% and 9.7% for RCS₁ and RCS₂, respectively. These results are obtained by calibration of the tension-stiffening effect taken into account according to the stress-crack opening relation of plain concrete at the cracked section as shown in Table 6.5.

Table 6.5 Plain concrete $\sigma - w$ calibration for FEM.



The results show a similar trend between the calibration used in 2D and 3D, although presenting different results. In this case, the tensile strength σ'_{ct} was reduced to 65% of the theoretical value, which is only slightly higher than in the 2D case. However, the stress at crack opening w_1 increased from 20% to 33% of f_{ctm} , whereas the final crack opening increased from $w_c = 5 G_F/f_{ctm}$ to $w'_c = 5.58 G_F/f_{ctm}$. According to these results, the tension-stiffening curve requires a flatter shape than the one specified in the code to reduce the cracking strength and avoid an excessive load drop at the snap-through. As in the 2D case, the reduction of the tensile strength may be a consequence of estimating f_{ctm} out of the compressive strength. In case of having used f_{ct} from experimental tests, the simulation may have resulted in more accurate results.

The simulation provided coherent results with the bending moment diagram of a four-point loaded element. In Figure 6.11, the rebar reinforcement of half of both slabs is shown indicating that the highest stresses take place at the central part of the beam, defined by the area between loading points.

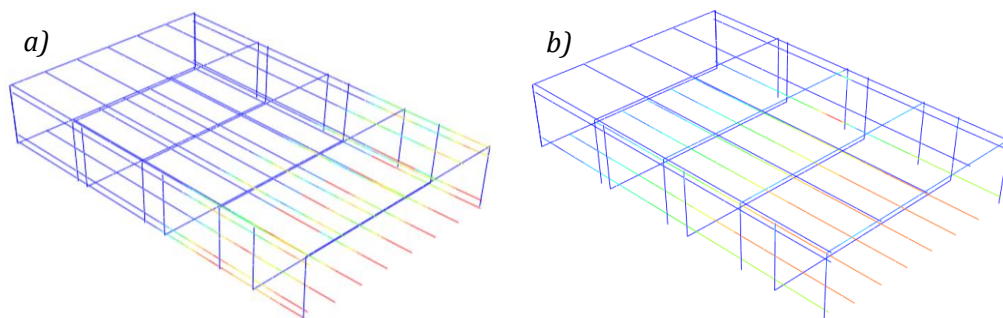


Figure 6.11 Steel rebars load-carrying capacity in a) RCS₁ and b) RCS₂.

6.4.2 Fibre reinforced concrete

The numerical simulation of fibre reinforced concrete slabs FRCS-25/1HE and FRCS-30/1HE compared to the experimental response is shown in Figure 6.12. In general, the simulation provides an accurate approximation of the performance of the slab.

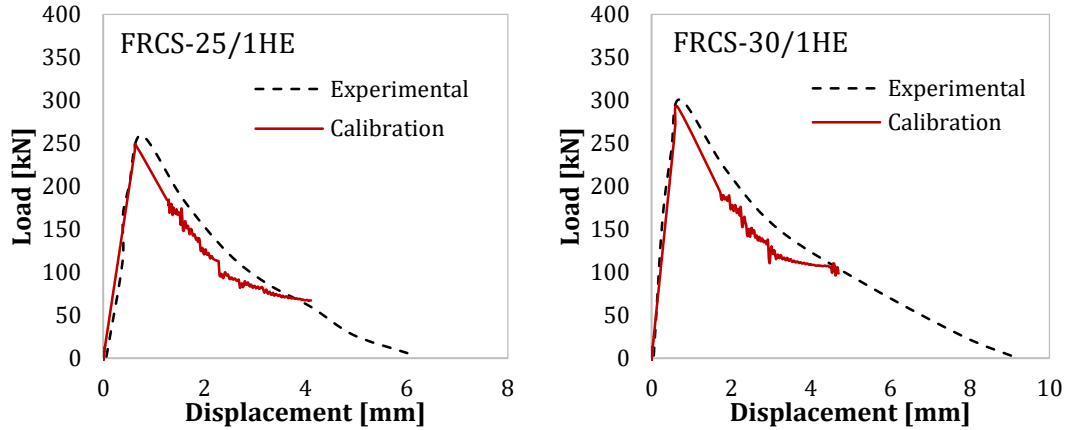


Figure 6.12 Comparison of the experimental and calibrated simulation of FRCS-25/1HE and FRCS-30/1HE.

The elastic branch provided by the simulation fits accurately the elastic stage of the experimental curves of both slabs. The cracking load of the simulated curves underestimate in 4.1% and 2.9% the experimental results obtained in FRCS-25/1HE and FRCS-30/1HE, respectively. After cracking, the results of the numerical model in both slabs exhibit lower load values for a given displacement when compared to the experimental curve. At a displacement of approximately 4 mm, the numerical curve begins to present a horizontal trend intersecting the experimental curve and starts to overestimate the flexural response of the slabs.

A comparison between the MC2010 and the calibrated $\sigma - \varepsilon$ constitutive law is shown in Figure 6.13. Unlike the results obtained in the 2D simulation, the differences in the $\sigma - \varepsilon$ relation between the MC2010 and the calibration of the FEM analysis were not as relevant. In this case, the load-displacement curves obtained according to the MC2010 and the simulation presented close results and only minor modifications on the MC2010 constitutive law were conducted to achieve a closer fit to the experimental result.

A summary of the parameters defining both the MC2010 and the calibrated $\sigma - \varepsilon$ constitutive law is presented in Table 6.6. To calibrate the parameters, a similar philosophy to the 2D analysis was followed: each value of σ was slightly modified whereas strains ε_1 and ε_3 were kept constant and ε_2 and ε_4 increased.

Table 6.6 FRC properties for FRCS-25/1HE and FRCS-30/1HE.

Parameters	Slab	σ_1	ε_1	σ_2	ε_2	σ_3	ε_3	σ_4	ε_4
MC2010	FRCS-25/1HE	4.69	0.11	1.90	0.25	1.50	4.00	0.00	18.03
	FRCS-30/1HE	5.02	0.11	2.17	0.24	1.74	4.00	0.00	19.31
Calibration	FRCS-25/1HE	4.40	0.11	1.74	0.39	1.48	4.00	0.34	20.00
	FRCS-30/1HE	4.80	0.11	1.97	0.38	1.68	4.00	0.38	20.00

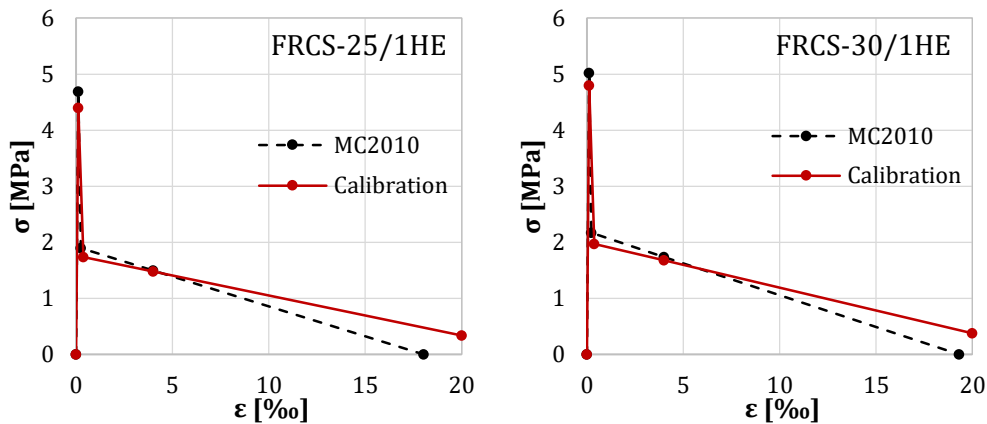


Figure 6.13 Comparison between the MC2010 and the calibrated constitutive laws of FRCS-25/1HE and FRCS-30/1HE.

The tensile stress σ_1 was reduced 6.2% and 4.4% in FRCS-25/1HE and FRCS-30/1HE with respect to the MC2010 specified value. For the rest of the tensile stresses, both slabs exhibited the same trend regarding the modification of the parameters: σ_2 and σ_3 of the original constitutive laws reduced their values to fit the experimental results whereas σ_4 increased to fit the last stretch of the curve. Strain ε_2 is required to increase 54.8% and 59.2% respectively for FRCS-25/1HE and FRCS-30/1HE in comparison to the value calculated according to the MC2010. Conversely, strain ε_4 underwent a more reduced increase if compared to ε_2 with a percentage increase of only 10.9% and 3.6% in FRCS-25/1HE and FRCS-30/1HE.

The results of the calibration suggest that the parameters of the constitutive law with major influence on the structural behaviour are those that define the immediate post-cracking response. However, the comparison of the MC2010 and the calibrated constitutive laws as shown in Figure 6.13 exhibits a great similarity between both curves. These results reveal that using the MC2010 constitutive law to predict the behaviour of the studied slabs according to the FEM simulation exhibit load-displacement curves close to those obtained experimentally. This contrasts with the results reported in previous studies (Blanco et al. 2015a), which revealed a significant overestimation of the results when simulating the response of hyperstatic slabs. Nevertheless, the slabs herein analysed and the bending tests used to obtain the constitutive models are based on an isostatic configuration. Accordingly, the absence of stress redistribution due to a hyperstatic configuration might be the reason for the similarity between the parameters of the MC2010 and the calibrated constitutive laws.

6.4.3 Hybrid reinforced concrete

A comparison between the load-displacement curves of the calibrated simulations and the experimental results for slabs HRCS₁-25/1HE, HRCS₁-30/1HE and HRCS₂-25/1HE are shown in Figure 6.14. In this case, the calibrated parameters of slabs FRCS-25/1HE and FRCS-30/1HE have been used in combination with the slabs RCS₁ and RCS₂.

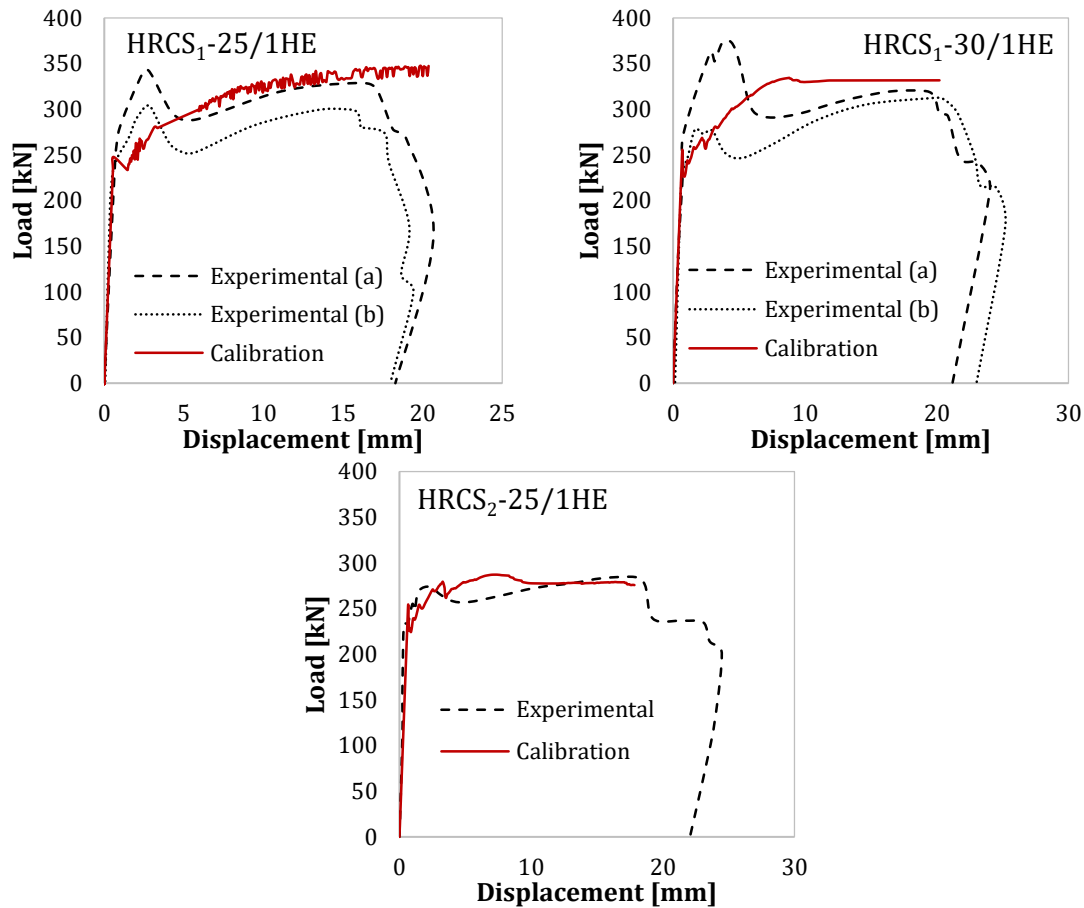


Figure 6.14 Comparison of the experimental and calibrated simulation of HRCS₁-25/1HE, HRCS₁-30/1HE and HRCS₂-25/1HE.

The calibrated curves present close results to the experimental values. The parameters defining the constitutive concrete behaviour of the three hybrid reinforced concrete slabs according to the MC2010 along with the calibrated values to simulate the response of the slabs are shown in Table 6.7. Notice that the calibrated parameters are those used to simulate slabs FRCS-25/1HE and FRCS-30/1HE, case in which provided a good fitting of the simulated curves if compared to the experimental results. In the chase of hybrid reinforced slabs, using the same parameters to define the FRC properties also provided a general good simulated performance of the real behaviour.

Table 6.7 FRC properties for HRCS₁-25/1HE, HRCS₁-30/1HE and HRCS₂-25/1HE.

Parameters	Slab	σ_1	ϵ_1	σ_2	ϵ_2	σ_3	ϵ_3	σ_4	ϵ_4
MC2010	HRCS ₁ -25/1HE	4.69	0.11	1.90	0.25	1.50	4.00	0.00	18.03
	HRCS ₁ -30/1HE	5.02	0.11	2.17	0.24	1.74	4.00	0.00	19.31
	HRCS ₂ -25/1HE	4.69	0.11	1.90	0.25	1.50	4.00	0.00	18.03
Calibration	HRCS ₁ -25/1HE	4.40	0.11	1.74	0.39	1.48	4.00	0.34	20.00
	HRCS ₁ -30/1HE	4.80	0.11	1.97	0.38	1.68	4.00	0.38	20.00
	HRCS ₂ -25/1HE	4.40	0.11	1.74	0.39	1.48	4.00	0.34	20.00

Two slabs were tested for HRCS₁-25/1HE and HRCS₁-30/1HE, revealing that the accuracy of the simulated curve also depends on the variability of the experimental response of the elements. Given the inherent scatter of FRC, both the MC2010 and the calibrated parameters

defined in Table 6.7 are subjected to the material performance variability. In this regard, it should be emphasized that the scatter of the parameters defining the material properties unavoidably influences the results and the accuracy of the simulations.

6.5 CONCLUDING REMARKS

This chapter revealed how the simulation of the flexural behaviour of real-scale elements according to the constitutive model of the MC2010 may exhibit significant differences with regard to the real flexural behaviour. Accordingly, the parameters defining the constitutive model of FRC were calibrated to obtain results that fit the experimental values. However, different results were obtained when the predicted results were calculated through bi-dimensional and three-dimensional simulations. In this line, the following conclusions can be drawn:

- Tension-stiffening effect plays an important role in the immediate post-cracking behaviour of plain concrete, leading to a snap-through sharper than the obtained experimentally. Consequently, a flatter shape of the stress-crack opening relation of the cracked section in plain concrete needs to be considered.
- In FRCS, fibres primarily contributed at SLS and lost effectiveness at ULS. According to the results of the calibration conducted in the AES, fibres 1HE presented a higher contribution to SLS than fibres 2HE, which contributed to a lesser extent in SLS but were able to resist strengths at higher strains.
- The results of HRCS suggest there is an overall reduction of the contribution of fibres when combined with traditional reinforcement. This might be attributed to rebars absorbing the greatest tensile stress, thus relegating the contribution of fibres. However, the higher strain achieved immediately after cracking accounting for the activation of the fibres lead to a higher load carrying capacity of the slab at the initial stage.
- The AES overestimation of the performance prediction of FRCS and HRCS with the MC2010 confirms a clear size effect. The fact of reducing the value of the constitutive law parameters to fit the real behaviour of the slabs indicates that the small samples used to determine f_{Fts} and f_{Ftu} exhibit a higher strength.
- Small modifications were required to calibrate the parameters defining the tensile strength of FRC in FRCS and HRCS to achieve a good approximation of the FEM simulation to the real behaviour of the slabs. In this case, the same parameters defining the tensile FRC strength were used in both FRCS and HRCS.

It is important that constitutive laws can reproduce the real performance of structures as accurately as possible to replace tests for simulations when possible. Tests conducted on such elements are expensive and require specific equipment that can only be found in specialized laboratories. In this line, and to encourage the use of fibres, it is important to account with enough tools that simplify the design of structures reinforced with fibres while providing structural safety.

7 CORRELATION BETWEEN THE BARCELONA TEST AND THE BENDING TEST TO OPTIMIZE QUALITY CONTROL

7.1 INTRODUCTION

The optimization of resources and materials has a great relevance at all stages of the design and construction of a structure. The first part of this thesis focused on the characterization of FRC specimens at a laboratory scale identifying the influence of the size effect on the post-cracking response. The behaviour of real-scale elements was subsequently addressed in the second part. In this regard, the ductility requirements as established by the MC2010 were verified and a FEM model was analysed to predict the behaviour of the slabs. The third part of this thesis consists of an approach to simplify the quality control of FRC and describe its advantages through a statistical point of view.

The quality control of fibre reinforced concrete (FRC) used in structural applications should include tests for the assessment of the post-cracking response of the material. The selection of suitable testing methods for this purpose becomes particularly relevant given the high intrinsic scatter associated with the post-cracking response (Cavalero & Aguado 2015). In this context, it is important to count with simple and fast methods that may provide enough repetitions for a reliable statistical analysis of the results that lead to representative average and characteristic values of the post-cracking strength of the material.

Throughout this thesis, several tests to assess the properties of FRC have been presented. The most extended method to determine the residual strength in FRC is the three-point bending test (3PBT) according to EN 14651:2007 (CEN 2007). It presents a coefficient of variation usually above 20% (Parmentier et al. 2008; Molins et al. 2009) and a complex

setup if compared to other tests, requiring special equipment and relatively big specimens. For these reasons, as suggested by the Belgian standard NBN B 15-238 (NBN 1992), the 3PBT is not considered suitable for the systematic quality control of FRC. Thereby, alternative tests were developed in an attempt to overcome the drawbacks previously mentioned (Löfgren et al. 2005; di Prisco et al. 2010; di Prisco et al. 2013b). In this context, and according to the Spanish Code (EHE 2008), the use of alternative tests to obtain the residual strength of FRC can be accepted if correlation factors are proven.

The use of correlations between concrete properties measured in different test methods is a common and widely accepted procedure, even when the cracking mechanisms involved in each of them are completely different. For example, equations relating the compressive strength and the tensile strength are present in the majority of structural concrete codes and guidelines. Moreover, several equations are available to transform the indirect tensile strength measured in the Brazilian test into the indirect flexural strength measured with bending tests (Perumal 2015). In the case of FRC, Minelli et al. (Minelli & Plizzari 2010) already proposed a correlation between the Round Panel Test and the UNI flexural test based on the energy released and the residual strength. Correlations between different typologies of tests also provide an opportunity for developing new simplified stress-crack width laws for FRC (Abrishambaf et al. 2015; Minelli & Plizzari 2015).

One alternative to characterize the tensile residual strength of FRC is the Barcelona test (BCN) proposed by Molins et al. (Molins et al. 2009) and included in the standard UNE 83515:2010 (AENOR 2010). Recently, it has been improved by Pujadas et al. (Pujadas et al. 2013; Pujadas et al. 2014b) and a constitutive equation based on the results of the test was proposed by Blanco et al. (Blanco et al. 2014). The BCN is simpler than the 3PBT in terms of execution since 75% lighter specimens are used and no closed-loop is required. It also presents smaller scatter (Pujadas et al. 2014b) with a coefficient of variation of the results below 13% (Molins et al. 2009).

Therefore, the main objective of this chapter is to propose a correlation between the results of the BCN and the bending test so the first may be used as a complementary method to characterize the properties of FRC. For this, an experimental programme involving 21 mixes of FRC with either steel or plastic fibres was performed. The influence of the type of fibres or the rheology were analysed and a reliability study by means of a statistical analysis was conducted. The correlation proposed represents a tool towards a simpler, faster and less expensive quality control of FRC based on the BCN. This approach is in line with the *fib* Model Code 2010 and may also serve as an example for future correlations with other tests applied to FRC.

7.1.1 Objectives

The general purpose of this chapter is to present a methodology to characterize FRC by means of alternative tests at the quality control stage. In order to fulfil this general objective, several steps responding to specific objectives have been conducted and are described subsequently:

- Highlight the importance of the efficiency in quality control and determine the influence of selecting the suitable test.

- Conduct an experimental programme in FRC testing the material by means of the three-point bending test and the Barcelona test.
- Identify the main properties governing the behaviour of FRC and their influence on the results of each type of test.
- Propose an equation to calculate the parameters of the three-point bending test using the results of the Barcelona test with properly defined safety margins.

7.1.2 Outline of the chapter

The correlation is addressed in three stages divided into different steps as presented in Figure 7.1. In the first stage, the results of the experimental programme performed are analysed and compared. In the second stage, linear regressions are performed considering different variables involved in the mechanical material response. This helps determining whether a universal correlation between both tests is possible or if different formulations are needed depending on the type of concrete, the type of fibre or the fibre content. Finally, the third stage presents a multi-variable parametric study conducted in order to obtain the final correlations.

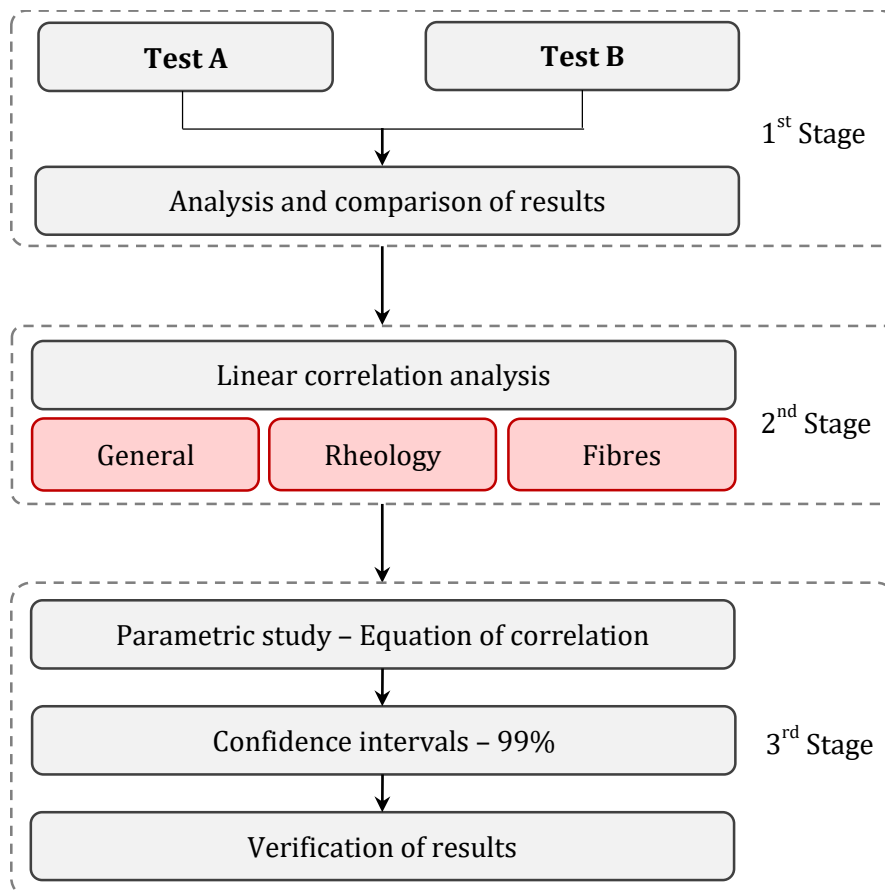


Figure 7.1 Methodology used to derive the correlation between tests.

The relevance of performing an appropriate and efficient quality control on the material is explained in Section 7.2. This issue is firstly addressed by comparing the influence of the inherent scatter of different tests on the acceptance criteria of the material. The effect of the testing method on the acceptability of concrete batches is described according to a brief example of a tunnel work.

Subsequently, the experimental programme conducted to determine the correlation between the 3PBT and the BCN is described in Section 7.3. An analysis of the results and the approach proposed to determine the correlation between these two tests is presented in Sections 7.4 and 7.5, respectively¹. An example of how to implement the correlation is shown in Section 7.6, using results of a real case in which the correlation was used.

7.2 EFFICIENCY OF QUALITY CONTROL

Enhancing the efficiency and the optimization in every stage of construction processes leads to cost reductions. For this reason, minimizing the use of resources maintaining the desired performance of the material becomes an appropriate strategy to cut costs. In concrete manufacturing, as in any other industrial process, it is of utmost importance to verify whether the material meets the minimum quality requirements and design project specifications. In this regard, selecting the most suitable tests to perform the quality control may also lead to optimization of the material mechanical requirements during execution (e.g., relaxation of the minimum strength requirement while keeping the same structural safety level).

In order to improve the efficiency during the process of quality control, the scatter of the results needs to be taken into account. The coefficient of variation (CV) highly depends on the type of test and greater values of CV increase the uncertainty of the results. For this reason, and also to improve the reliability of the results, it becomes necessary to use tests with the minimum associated scatter (test intrinsic variability).

To exemplify the importance of the CV in a massive FRC concrete production, two different types of tests for characterizing the post-cracking residual strength of the same batch of FRC are analysed: Test A with a CV of 20% and Test B with a CV of 10%. Assuming that the results of the tests follow a Gaussian law, it is possible to calculate the probabilistic distribution considering that the measured average strength in both tests $f_{Ri,m} = 3.0 \text{ MPa}$. Based on the average residual strength and the CV specified for each test, the standard deviations are 0.6 and 0.3 for Test A and Test B, respectively. Figure 7.2 displays the Gauss probabilistic distribution of the residual strength $f_{Ri,m}$ for both tests, with Test A presenting a flatter distribution than Test B as a result of the difference in the variability of the results.

Assume now that project specifications require a minimum residual strength $f_{Rk} = 2.4 \text{ MPa}$. According to the statistical distributions of the results, Test A and Test B present characteristic strengths $f_{Rk}^A = 2.0 \text{ MPa}$ and $f_{Rk}^B = 2.5 \text{ MPa}$, respectively. These results show that f_{Rk}^A does not reach the minimum residual strength specified, thus leading to disregard the batch of concrete manufactured. Conversely, given that f_{Rk}^B presents a residual strength above the minimum required, the batch would be accepted. Notice how the differences on the intrinsic variability of the test influence the acceptance of the batches.

¹ Part of this study was published in:

Galeote, E., Blanco, A., Cavalaro, S.H.P., de la Fuente, A. Correlation between the Barcelona test and the bending test in fibre reinforced concrete. *Construction and Building Materials*, 2017, vol. 152, p. 529-538.

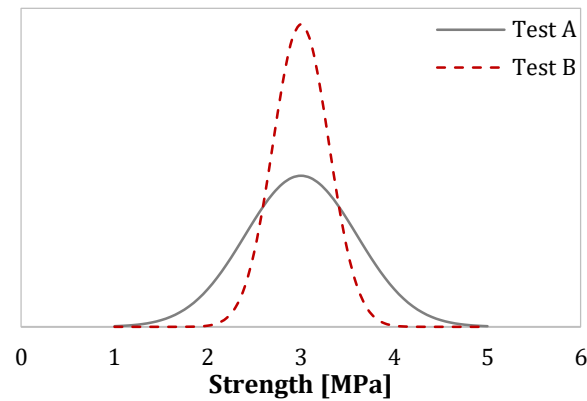


Figure 7.2 Gauss probabilistic law for Test A and B.

The acceptance proportion of batches is shown in Figure 7.3. Based on the specific case of minimum project requirements $f_{Rk} = 2.4 \text{ MPa}$, the number of rejected batches increases when conducting Test A (CV 20%). Consequently, the mere fact of changing the test methodology reduces the amount of batches rejected and, hence, the costs while meeting the acceptability criteria.

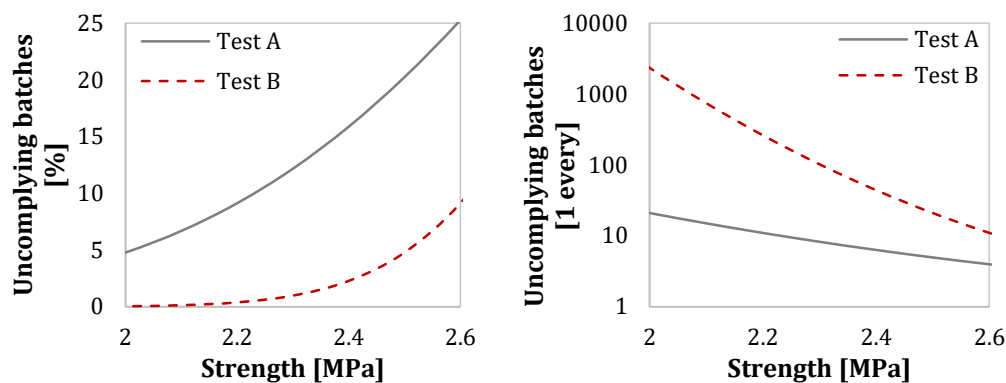


Figure 7.3 Influence of the test on the number of uncomplying batches.

The influence of the test variability on the acceptance criteria has a direct impact on the number of concrete batches rejected during production. This effect is especially noticeable in massive productions given that the increasing number of uncomplying batches entails high economic losses. Therefore, it is of utmost importance to determine the effect of the test methodology by quantifying the potential volume of material rejected as a result of the variability of the testing procedure.

As an example, and in line with the case suggested in Chapter 5, the production of segments for tunnel linings needs to be subjected to a quality control and fulfil the specified project requirements. A tunnel of 20 km with rings of an internal diameter of 5.2 m, thickness of 0.25 m and width of 1.40 m (de la Fuente et al. 2012b) represents a concrete production of 42000 m³ and 14285 rings. Assuming that the quality control of the concrete is conducted with one set of 3 specimens every 10 rings, each set represents a volume of concrete of 30 m³. According to the results of Figure 7.3, the probability of not achieving the minimum strength would entail rejecting 2300 rings (6800 m³) when conducting the tests by means of Test A. Conversely, Test B would require rejecting up to 340 rings (1000 m³), which represents only 15% of the volume of concrete rejected when performing control with Test A.

7.3 EXPERIMENTAL PROGRAMME

7.3.1 Materials and mixes

Mixes with conventional concrete (CC) and self-compacting concrete (SCC) were produced. The flowability of concrete may influence the residual strength of FRC since it affects the orientation of the fibres (Stähli et al. 2008; Boulekbache et al. 2010; Ferrara et al. 2011; Kang et al. 2011; Zerbino et al. 2012; Abrishambaf et al. 2013). In total, 21 concrete mixes were designed with water-to-cement ratios ranging from 0.19 to 0.56. Different types of cements were used, with total contents between 275 and 700 kg/m^3 . Hooked-end steel fibres (SF) were added in contents from 30 to 60 kg/m^3 , whereas the content of 3 types of plastic fibres (PF1, PF2 and PF3) varied from 3.5 to 25 kg/m^3 . The mix proportioning for the 21 dosages is shown in Table 7.1 and Table 7.2, where the contents of the different materials used are detailed.

Table 7.3 summarizes the mixes depending on the main variables of the study. The compressive strength in each mix is the average of 3 specimens of $\phi 150 \times 300$ mm tested under compression according to EN 12390-3 (CEN 2009). The nomenclature includes the type of fibre and the content used. Table 7.4 shows the main characteristics of each type of fibre.

Table 7.1 Mix proportioning of the dosages.

Material	D1	D2	D3	D4	D5	D6	D7	D8	D9	D10	D11
Filler		40	40	40	40	40					
Sand 0-4	1050	1050	1050	1050	1050	1050					
Sand 0-5							817	817	817	1200	1200
Aggreg. 4-10	470	470	470	470	470	470					
Aggreg. 5-15							404	404	404	500	500
Aggreg. 10-20	250	250	250	250	250	250					
Aggreg. 12-20							810	810	810	200	200
Water	155	153	160	153	157	160	156	156	156	165	165
CEM I 52.5 N/SR	390	360		360	360	360					
CEM I 42.5 N/SR			380								
CEM I 52.5 R CEM II/A-L 42.5 R							312	312	312	380	380
Steel fibres	50	50	50			50	30	45	60	30	45
Plastic fibres PF1				3.5	3.5						
Plastic fibres PF2											
Plastic fibres PF3											
Superplast. 1	1.23	1.19	1.00	1.49	1.20	1.49	0.70	0.80	0.80	1.40	1.20
Superplast. 2											
Superplast. 3											
Superplast. 4											
Accelerating agent				3.33		3.33	2.00	2.00	2.00	2.00	2.00

Table 7.2 Mix proportioning of the dosages.

Material	D12	D13	D14	D15	D16	D17	D18	D19	D20	D21
Filler										
Sand 0-4		1086	1086	1086	1155	1155	1155	1177	1161	1154
Sand 0-5	1200									
Aggregate 4-10					726	726	726	328	325	324
Aggregate 5-15	500									
Aggregate 10-20		804	804	804						
Aggregate 12-20	200									
Water	165	155	155	155	155	155	162	136	136	136
CEM I 52.5 N/SR										
CEM I 42.5 N/SR										
CEM I 52.5 R	380							700	700	700
CEM II/A-L 42.5 R		275	275	275	290	290	290			
Steel fibres	60									
Plastic fibres PF1		4	6	8						
Plastic fibres PF2					4	6	8			
Plastic fibres PF3								10	20	25
Superplast. 1	1.20									
Superplast. 2		0.87	0.87	0.87	1.07	1.17	1.17			
Superplast. 3		1.10	1.10	1.10	1.10	1.10	1.10	0.30	0.30	0.30
Superplast. 4								5.00	5.00	5.00
Accelerating agent	2.00									

Table 7.3 Main characteristics of the mixes.

Rheology	Strength classification	Compressive Strength [MPa]	Fibre		Nomenclature
			Type	Content [kg/m ³]	
Conventional concrete (CC)	>60 MPa	66.4	SF	30	CC_H60_SF_30
		65.1	SF	45	CC_H60_SF_45
		66.2	SF	60	CC_H60_SF_60
		85.0	PF3	25	CC_H60_PF3_25
	<60 MPa	47.7	PF1	4	CC_L60_PF1_4
		46.1	PF1	6	CC_L60_PF1_6
		48.1	PF1	8	CC_L60_PF1_8
		51.6	PF2	4	CC_L60_PF2_4
		52.9	PF2	6	CC_L60_PF2_6
		52.5	PF2	8	CC_L60_PF2_8
Self-compacting concrete (SCC)	>60 MPa	71.9	SF	30	SCC_H60_SF_30
		67.6	SF	45	SCC_H60_SF_45
		60.2	SF	50	SCC_H60_SF_50
		66.9	SF	60	SCC_H60_SF_60
		82.6	PF3	10	SCC_H60_PF3_10
		77.2	PF3	20	SCC_H60_PF3_20
	<60 MPa	50.1	SF	50	SCC_L60_SF_50A
		40.4	SF	50	SCC_L60_SF_50B
		34.4	SF	50	SCC_L60_SF_50C
		57.4	PF1	3.5	SCC_L60_PF1_3.5A
	52.4	PF1	3.5	SCC_L60_PF1_3.5B	

Table 7.4 Characteristics of the fibres (provided by the manufacturers).

Properties	SF	PF1	PF2	PF3
Material	Steel	Polypropylene	Polypropylene	Polyvinyl alcohol
Elastic Modulus [GPa]	500	4.0	4.8	8.5
Tensile strength [MPa]	1000	400	338	800
Length [mm]	50	48	40	12
Diameter [mm]	1.00	0.84	0.75	0.20
Aspect ratio [-]	50	57	53	60

7.3.2 Specimens and test procedure

As shown in Figure 7.4, the BCN consists of a double punch test on a cylindrical $\phi 150 \times 150$ mm or cubic 150×150 mm specimen. The test is performed by placing, concentrically above and below the specimen, cylindrical steel punches with a height of 25 mm and a diameter equal to $\frac{1}{4}$ of the smaller dimension of the cross-section of the specimen. The hydraulic press applies a load to the punches at a constant displacement rate of 0.5 ± 0.05 mm per minute. In the process, a conical triaxial state is formed from the centre to the edges of the specimen, leading to internal tensile stresses that increase with the load. Cracks appear (Figure 7.4) when the stresses reach the tensile strength of the concrete matrix. After that, the fibres bridge the crack, providing a residual strength. The results obtained may be represented through a load-total circumferential opening displacement (TCOD) curve or load-axial displacement relationship depending on the equipment used in the test, as depicted in Figure 7.4.

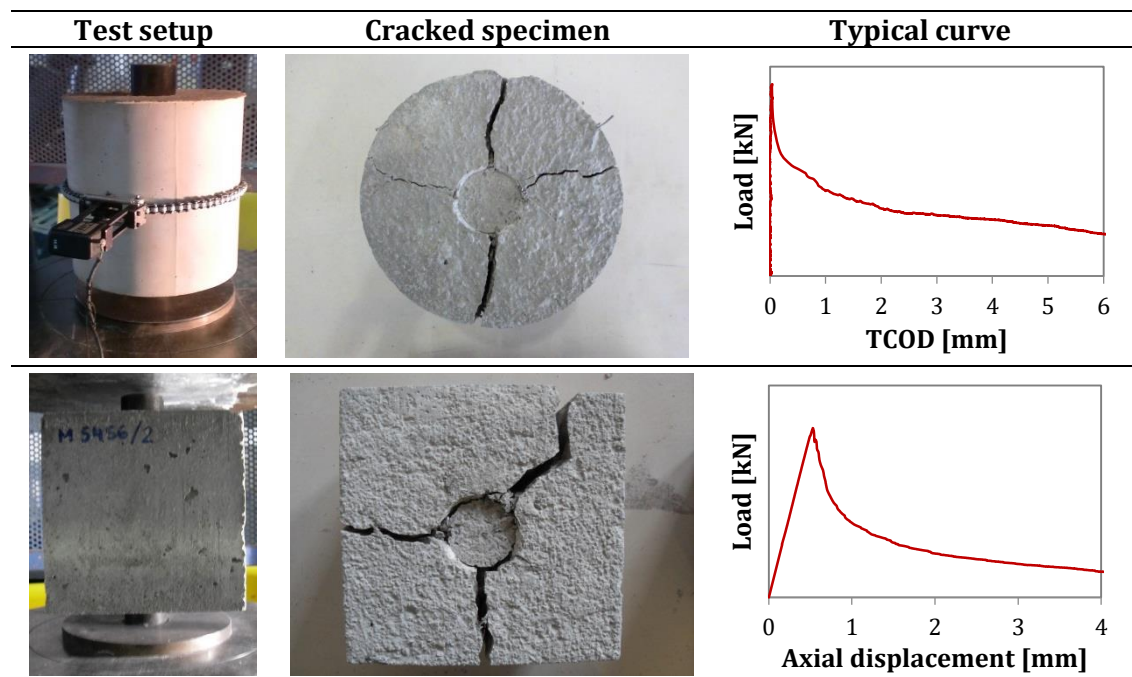


Figure 7.4 BCN in cylindrical and cubic specimens.

The main difficulties to obtain acceptable correlations lay on the differences in the crack mechanism observed in both tests and, especially, the high variability intrinsic to the FRC. The fracture mechanism of the 3PBT is purely dominated by Mode I, while in the BCN the propagation of the crack is a mixed response between Modes I and II. This is shown in Figure

7.5, which shows how the penetration of the two cones into the specimen (Mode II) produces the opening of several radial cracks where tensile stresses appear perpendicular to the fracture surface (Mode I).

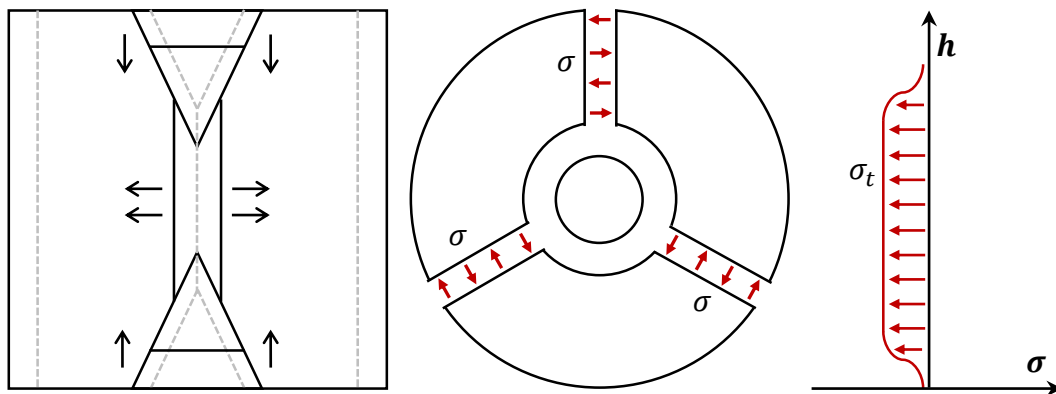


Figure 7.5 Cracking mechanism and distribution of stresses.

Even though the failure mechanisms between 3PBT and the BCN might be different, this should not pose a problem to obtain a correlation between both tests. In fact, several codes and studies from the literature propose correlations between the results of test methods with completely different cracking mechanisms (for example, between compressive and tensile strength or between tensile and flexural strength, among others).

For all mixes produced here, 2 shapes of moulded specimens were manufactured: 72 beams of $150 \times 150 \times 600 \text{ mm}$ for the 3PBT (according with the EN 14651:2007) and 72 cubes of 150 mm of side for the BCN. Once the 3PBT were concluded, each beam was cut in order to obtain $150 \times 150 \text{ mm}$ cubic specimens, resulting in 144 additional samples for the BCN test. As depicted in Figure 7.6, these cuts were performed disregarding the first 50 mm from the extremities of the beam and the central 200 mm , to avoid either the influence of the wall-effect and the crack produced during the 3PBT, respectively.

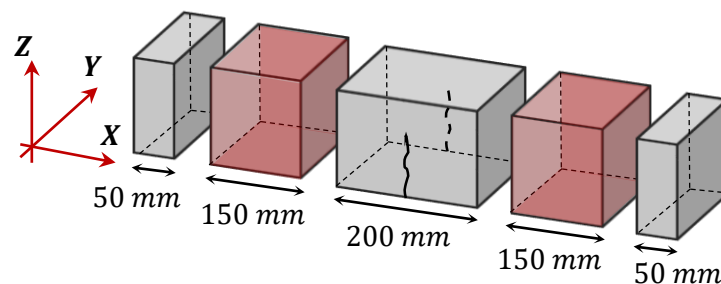


Figure 7.6 Cubic specimens cut from the beams.

After that, the inductive test (Torrents et al. 2012; Cavalaro et al. 2015) was conducted in moulded and cubic specimens with included steel fibres. In this test, a coil is used to measure the content and preferential orientation of the fibres in the axes perpendicular to the faces of the specimens. The convention from Figure 7.6 was adopted. According to this convention, the Z-direction is always parallel to the concrete casting direction. In the cut specimens, the X-direction is parallel to the length of the beam. In moulded specimens, the directions X and Y are defined indistinctly since, in principle, no in-plane preferential direction is evident. Finally, the BCN (Figure 7.4) was performed as described in this section

in all cubic specimens. The direction of loading was parallel to the casting direction (Z). The force measured during the test was converted into stress following the equations proposed in UNE 83515:2010.

7.4 ANALYSIS AND COMPARISON OF THE RESULTS

A preliminary analysis of the results is conducted to evaluate the influence of the variables from the study and the need to include them in the correlation. Even though other variables were also analysed, this section only describes the influence of the content of fibres, the rheology (conventional or self-compacting) and the type of cubic specimen (moulded or cut).

7.4.1 Influence of the fibre type

The differences between steel and plastic fibres in the mechanical response of FRC have been extensively described in literature (Barros et al. 2005; Sivakumar & Santhanam 2007; Buratti et al. 2011; Soutsos et al. 2012; Alberti et al. 2014) and are not the objective of this paper. Rather than that, the results of the 3PBT and the BCN for different contents of SF are compared. The influence of the contents is depicted in Figure 7.7 in a plot load-CMOD for the 3PBT and load-axial displacement for the BCN results.

The results from the 3PBT and BCN show a similar variation with the fibre content. In other words, higher stresses are resisted as the fibre content increases. The strength obtained in the BCN is in general lower than the strength observed in the 3PBT. This was more remarkable in dosage SCC_H60_SF_60 with 60 kg/m^3 of fibres, which was the only one to present hardening in the 3PBT after the first crack appeared. Conversely, none of the dosages presented hardening behaviour in the BCN.

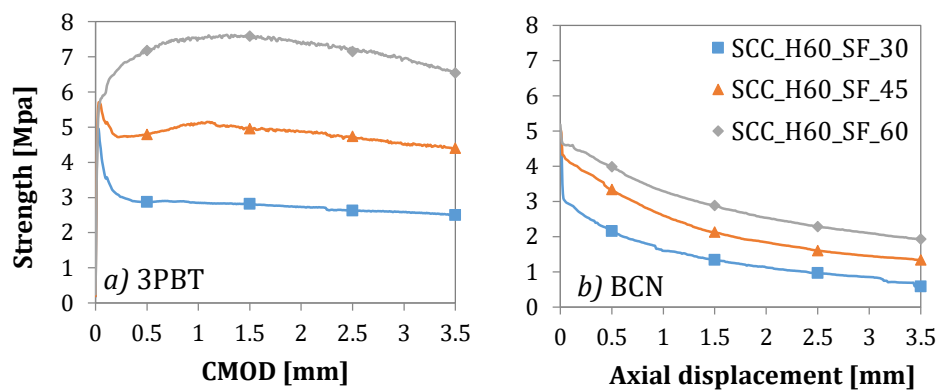


Figure 7.7 Residual strength in a) 3PBT and b) BCN.

This outcome may be attributed to the differences between the cracking mechanisms in each test. Previous studies showed that the same FRC may present hardening in bending tests and softening in direct tension tests (Wille et al. 2014a). In the former, the crack length increases gradually due to the formation of a pair with compression stresses provided by the unaffected concrete matrix and tensile stresses provided by the fibre bridging the cracks. Conversely, in the direct tension tests, the cracks tend to form abruptly, almost eliminating the contribution of the concrete matrix that has to be resisted by the fibres at this moment. In this context, a change of stiffness is more likely to occur, being observed as a drop in the

stresses resisted just after cracking. Notice that the mechanism developed in the BCN is closer to that found in the direct tension test than in the bending test since cracks appear abruptly and the contribution of concrete is hindered.

Another factor that could explain the lower stresses found in the BCN in comparison with the 3PBT is the effective number and orientation of fibres bridging the cracks. In the BCN, between 2 and 4 cracks are formed during the test. Usually the cracks with lower contribution of fibre tend to open more than others with higher fibre contribution. Therefore, the stresses measured become influenced by the overall in-plane fibre orientation instead of being a result of a single cracking plane that tend to be perpendicular to the direction with higher contribution, such as in the 3PBT.

7.4.2 Influence of the rheology

Figure 7.8 shows the average residual strengths measured with 13 specimens tested under the BCN and 3 specimens tested by means of the 3PBT for each of the two equivalent mixes of conventional and self-compacting concrete: CC_H60_SF_45 and SCC_H60_SF_45, respectively. The scatter of the results is also shown using the coefficient of variation (CV) represented at the right vertical axis. Notice that both mixes present the identical nominal fibre type and content, as well as similar average compressive strength.

Immediately after cracking occurs in the 3PBT, the average residual strength of CC_H60_SF_45 is higher than that of SCC_H60_SF_45. As the crack opening grows, the trend is inverted and the performance of SCC_H60_SF_45 is greater than CC_H60_SF_45. By the typical scatter of the 3PBT, the results of the flexural test may be considered approximately the same. This conclusion is also derived from the analysis of the results from the BCN, which shows approximately the same residual strength for SCC_H60_SF_45 and SCC_H60_SF_45 throughout the test.

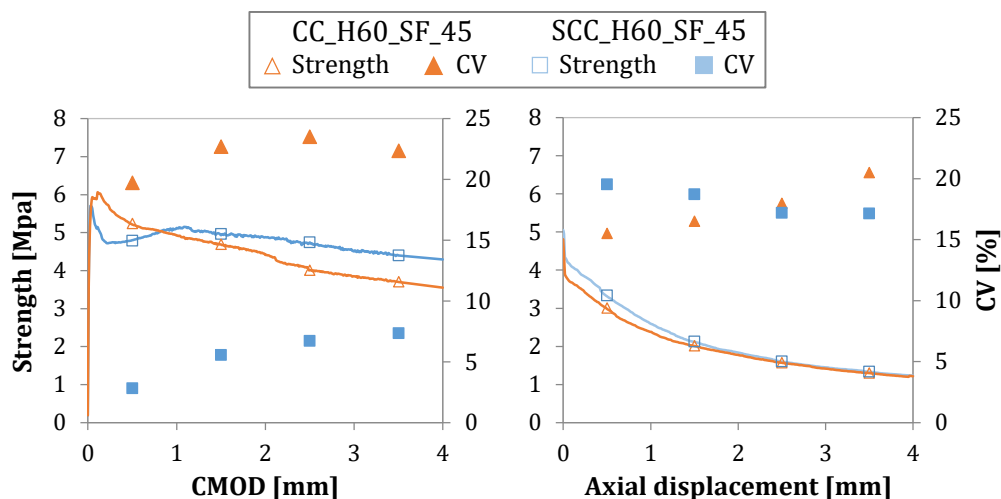


Figure 7.8 Influence of the rheology in the results of the a) 3PBT and the b) BCN.

The similarities of the residual response of both types of concrete may be explained by the fibre orientation. In the specimens cut from the beams tested with the 3PBT, the contribution of fibres in the X-direction is 41.5% for conventional concrete and 43.2% for self-compacting concrete. It is evident that, in spite of the change in rheology, small variations in terms of fibre orientation are observed in the main direction characterized in

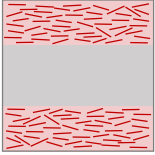
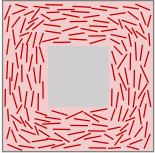
this 3PBT. Likewise, the contribution of fibres in the plane XY in moulded specimens tested with the BCN is approximately 80% regardless of the type of concrete. All these results justify the similarities between conventional and self-compacting concrete assessed in this study.

7.4.3 Influence of the type of cubic specimen

The manufacturing procedure of the two types of cubic specimen (cast and cut from the beam) may affect both the orientation and the mechanical performance. For this reason, the fibre orientation and the mechanical performance of both types of specimen is assessed and compared in order to know whether they may be used indistinctly for the assessment of the correlation. Table 7.5 shows the average orientation measured with the inductive test and the corresponding coefficient of variation (CV) in both types of specimen calculated for the 10 dosages with different contents of steel fibres. Illustrative schemes of the preferential orientation measured are also presented.

Approximately 80% of the contribution of the fibres is concentrated in the plane perpendicular to the casting direction in both types of specimens. This may be explained by the flow and the external vibration applied in some of them during the production, which favour a fibre alignment parallel to the XY plane (Stähli et al. 2008; Boulekbache et al. 2010; Edgington & Hannant 1972; Martinie & Roussel 2011; Wille et al. 2014b).

Table 7.5 Average values and CV of the fibre contribution for cut and moulded specimens.

Type of specimen	X-axis		Y-axis		Z-axis		Scheme of orientation
	Orientation	CV	Orientation	CV	Orientation	CV	
Cut	46.5%	5.6%	33.1%	7.0%	20.4%	6.9%	
Moulded	38.9%	3.5%	38.9%	3.0%	22.2%	8.6%	

In cut specimens, 46.5% of the contribution of the fibres is concentrated in X while only 33.1% of the contribution is observed in Y. This contrasts with the results from the moulded specimens, which display almost the same contribution of fibres in X and in Y. Interestingly, the scatter for the measurements in both directions for cut specimens is around twice as high as the calculated for moulded specimens (see CV in Table 7.5).

All these differences may be attributed to the influence of the shape of the specimens, the wall-effect and the flow of concrete during the production process. In the case of the cut specimens, the predominant wall effect is observed along the X-direction of the beam. This is also the main flowing direction, favouring a higher fibre contribution in this direction. Nevertheless, in the case of moulded specimens, the wall-effect imposed by the formwork and the distance of flow in X and in Y should be practically identical. Consequently, similar contributions are observed.

The influence of the content of SF on the orientation of each type of specimen is exhibited in Figure 7.9. As expected, the content of fibres showed no significant influence on the orientation. This is reasonable since the same mixing and casting process was used. Moreover, the trend in the orientation is similar to the previously described in Table 7.5.

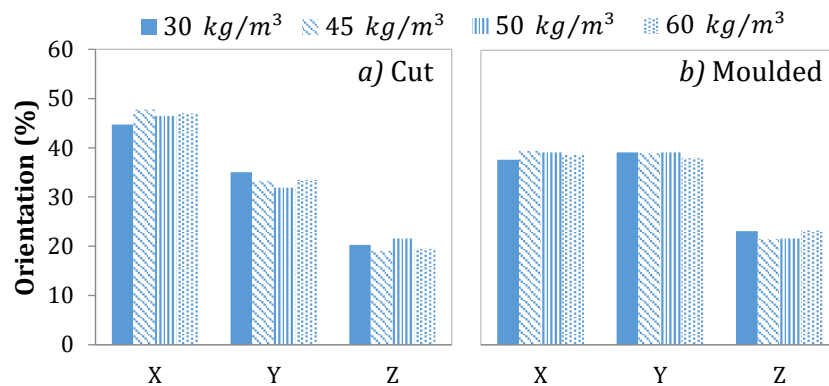


Figure 7.9 Orientation of fibres according to the content in a) cut and b) moulded specimens.

Figure 7.10a and 10.b show the average residual strength for the dosages with 50 kg/m^3 of steel fibres (SCC_L60_SF_50A, SCC_L60_SF_50B, SCC_L60_SF_50C and SCC_H60_SF_50) and 3.5 kg/m^3 of plastic fibres (SCC_L60_PF1_3.5A and SCC_L60_PF1_3.5B), respectively. Other mixes present similar results. The grey curves show the average strength of each dosage depending on the type of specimen. The red curves represent the average strength of all dosages separated by cut or moulded samples.

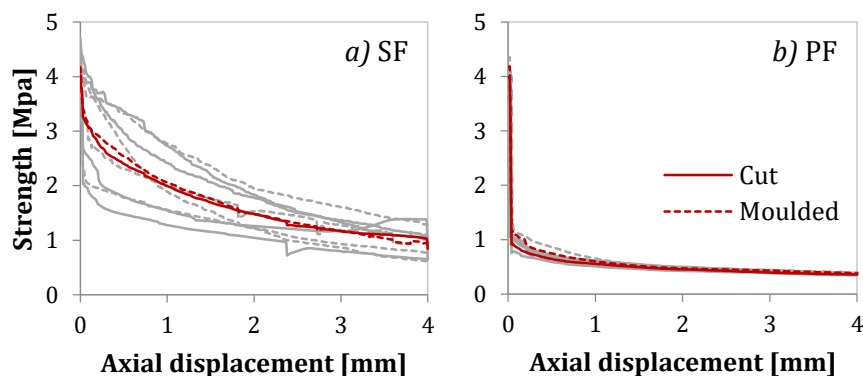


Figure 7.10 Residual strength with the BCN in cut and moulded specimens with a) SF and b) PF.

No significant difference between the moulded and cut specimens was expected in the mechanical results since in both cases approximately 80% of the fibres are aligned in the XY plane. The curves confirm the small differences in terms of the average residual strength regardless of the type of fibre used. A slightly bigger scatter is observed in the cut specimens, which is in line with the higher CV found in the fibre contribution for the latter in Figure 7.5. The results suggest that the average mechanical results obtained between moulded and cut samples are similar enough to use both types of specimens in the correlation analysis.

7.5 CORRELATIONS

7.5.1 Correlation depending on variables and test parameters

In this section a linear regression is performed between different parameters from the tests to identify those that provide the highest correlation degrees. Besides identifying the parameters that provide the best correlation, the aim is to determine whether a general correlation is possible or if it is necessary to derive specific formulations depending on the type of concrete or of fibre used.

The average stress and the average tenacity of each concrete mix were calculated for reference displacement values. For the 3PBT, the CMOD of 0.5, 1.5, 2.5 and 3.5 *mm* were taken as a reference. In the case of the BCN, the axial displacements of 0.5, 1.5, 2.5 and 3.5 *mm* from the beginning of the test and also after cracking were taken as a reference. The nomenclature used to refer to each parameter starts with the letter *F* for forces and *E* for energy values. Then, either *bcn* or *3pbt* is appended as a subscript depending on the test. The corresponding CMOD or axial displacement is placed at the end as a subscript. For example, $E_{bcn,1.5}$ represents the energy estimated in the BCN for an axial displacement up to 1.5 *mm* after cracking.

Correlations were performed with every possible combination of one parameter of the 3PBT and one parameter of the BCN. This procedure was repeated considering all data from the experimental programme or by grouping the data by rheology (conventional or self-compacting concrete), by strength class (smaller than 60 *MPa* or bigger than 60) and type or content of fibre. To simplify the analysis of the results, the minimum, the maximum and the average correlation degrees were calculated for all possible combinations with each parameter of the BCN. Figure 7.11 shows a summary of the coefficients of determination (R^2) obtained for $F_{bcn,0.5}$, $F_{bcn,1.5}$ and $E_{bcn,1.5}$, which were the parameters that showed the highest correlation degree in the linear correlation among all the analysed parameters. These represent the load and the energy obtained in the BCN for axial displacements of 0.5 and 1.5 *mm* measured after cracking.

The analysis shows a significant variability in R^2 . When all data are considered, the average R^2 is approximately 0.60, represented in a dashed line in Figure 7.11. This is also true for all correlations performed when the results are grouped by rheology. Notice that the average calculated for conventional concrete is the same as that for self-compacting concrete. This suggests that the results from both concrete types may be considered indistinctly in the same formulation without compromising R^2 . Despite that, it is noteworthy that the scatter in R^2 is twice as high in the conventional concrete than in self-compacting concrete.

Significant differences are observed when the data is grouped by strength class. In the case of mixes with compressive strength below 60 *MPa*, average R^2 values close to 0.90 are obtained. This improvement with regards to the general correlation is compensated by a smaller average R^2 in the mixes with compressive strength above 60 *MPa*. Moreover, a higher variability is observed in this last group. Based on these results, the definition of separate correlations is not justified since the improvement observed would be minor.

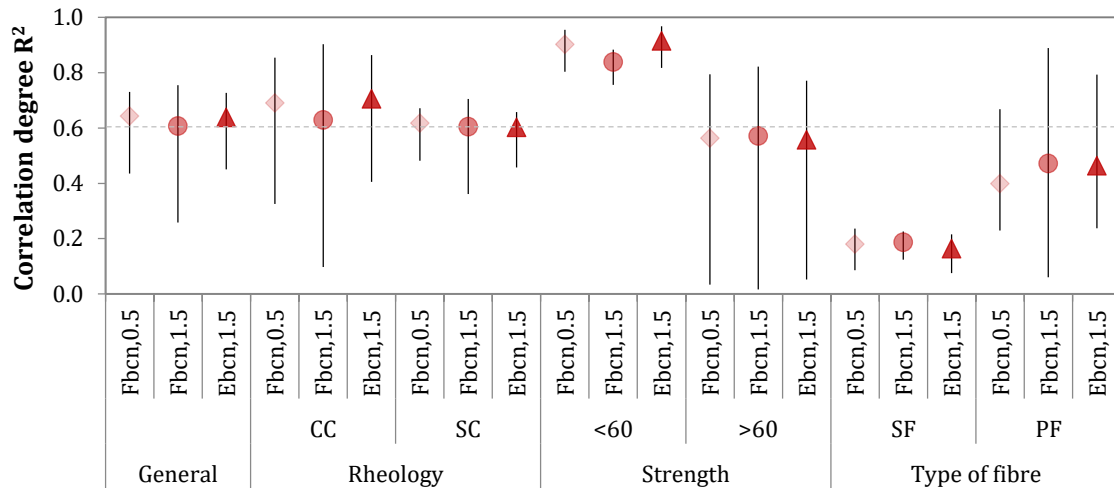


Figure 7.11 Results of linear correlation analysis.

The grouping by fibre type shows lower average values of R^2 for steel fibre than for plastic fibre. Such outcome may be attributed to the wider range of contents tested in the former, which varies from 3.5 kg/m^3 to 25 kg/m^3 . This contrasts with the range of steel fibres that goes from 30 kg/m^3 to 60 kg/m^3 . Despite the difference in terms of average values, the variability in the results of the R^2 calculated in plastic fibre is several times bigger, presenting values that are close to those of steel fibre.

It is important to remark that the average R^2 obtained after grouping the fibres by type is smaller than that of the general correlation. Again, this indicates that the separate consideration is not justified since it would not contribute to a better correlation in the case of the present experimental programme. Therefore, a general correlation applicable to all types of concrete, types and contents of fibre is proposed in the next section.

7.5.2 Proposal of correlation

An in-depth analysis was performed to identify the equation that provides the best correlations between the BCN and the 3PBT. In order to increase R^2 values, a multivariable regression was performed. The outcome of the equation should be a parameter of the 3PBT, whereas the input should consist of parameters of the BCN or other characteristics of the concrete. After several regressions, it was found that the best correlations relate the force measured for a certain value of CMOD in the 3PBT with the force and the energy for the same axial displacement measured in the BCN. Eq. 7.1 shows the equation proposed as a result of the regression study.

$$F_{3PBT,i} = a \cdot F_{BCN,i} + b \cdot E_{BCN,i}^2 \quad (7.1)$$

In this equation, the terms a and b are constants obtained in the regression for a CMOD and an axial displacement of i . The values of both constants and of the R^2 are presented in Table 7.6. The i corresponding to 0.5 mm is not included in the table since in this case it was not possible to identify an acceptable correlation between tests. This may be attributed to the differences in terms of crack formation in both tests, whose influence is evident for low displacements. This issue was also described by Bernard (Bernard 2002), who did not find good correlations between tests at low levels of deformation.

Table 7.6 Constants and confidence interval of Eq. 7.1.

i (mm)	a	b	$CI_{99\%}$ (kN)	R	R^2
1.5	1.76E-01	-3.29E-04	2.00	0.86	0.74
2.5	1.45E-01	4.70E-06	1.67	0.89	0.79
3.5	1.52E-01	1.46E-05	1.65	0.87	0.76

Figure 7.12 shows the comparison between the results obtained from 3PBT and the corresponding result estimated for the same mix with Eq. 7.1 from the results of the BCN for the displacements i of 1.5, 2.5 and 3.5 mm. The straight line indicates the equivalence line. The predictions made with Eq. 7.1 approaches the results from the 3PBT despite the wide variety of compositions and fibre types used. As the displacement increases, so does the goodness of the predictions made with the correlation.

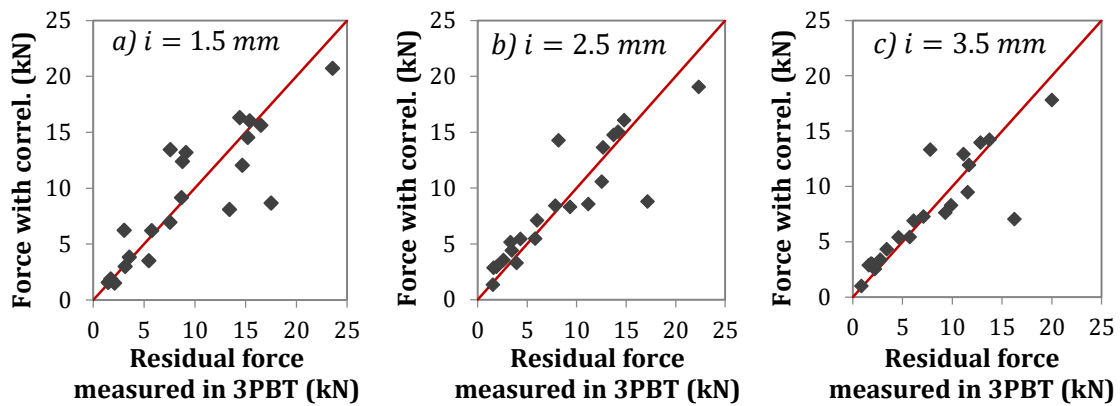


Figure 7.12 Force measured in the 3PBT and estimated from the BCN with the correlation.

7.5.3 Confidence intervals

A natural variability of results should be expected when applying either the 3PBT or the BCN. This variability should also affect the correlations obtained. In certain practical situations, it might be interesting to consider a safety margin capable of compensating at least part of the uncertainty in the prediction of the results of one test. A statistical analysis of the results from Figure 7.12 was conducted with the aim of assessing confidence intervals for the correlation proposed.

First, the Kolmogorov-Smirnov test was applied to determine whether the error in the predictions from Eq. 7.2 with regards to the experimental results follow a normal distribution. Once the normality was verified, the confidence interval of 99% ($CI_{99\%}$) presented in Table 7.6 were calculated for the displacements i of 1.5, 2.5 and 3.5 mm. The predicted value of the 3PBT considering the safety margin should be calculated according with Eq. 7.2.

$$F_{3PBT,i} = a \cdot F_{BCN,i} + b \cdot E_{BCN,i}^2 - CI_{99\%,i} \quad (7.2)$$

7.5.4 Verification of the results

The formulation obtained in the parametric study is here compared with the experimental results of the 3PBT for all dosages. Figure 7.13 shows several results of the load-CMOD for

both the experimental data (3PBT) in a solid line and the results calculated by means of the correlation proposed in a dashed line. The points of the predicted results are shown as a continuous plot load-CMOD in combination with the lower confidence interval corresponding to each CMOD.

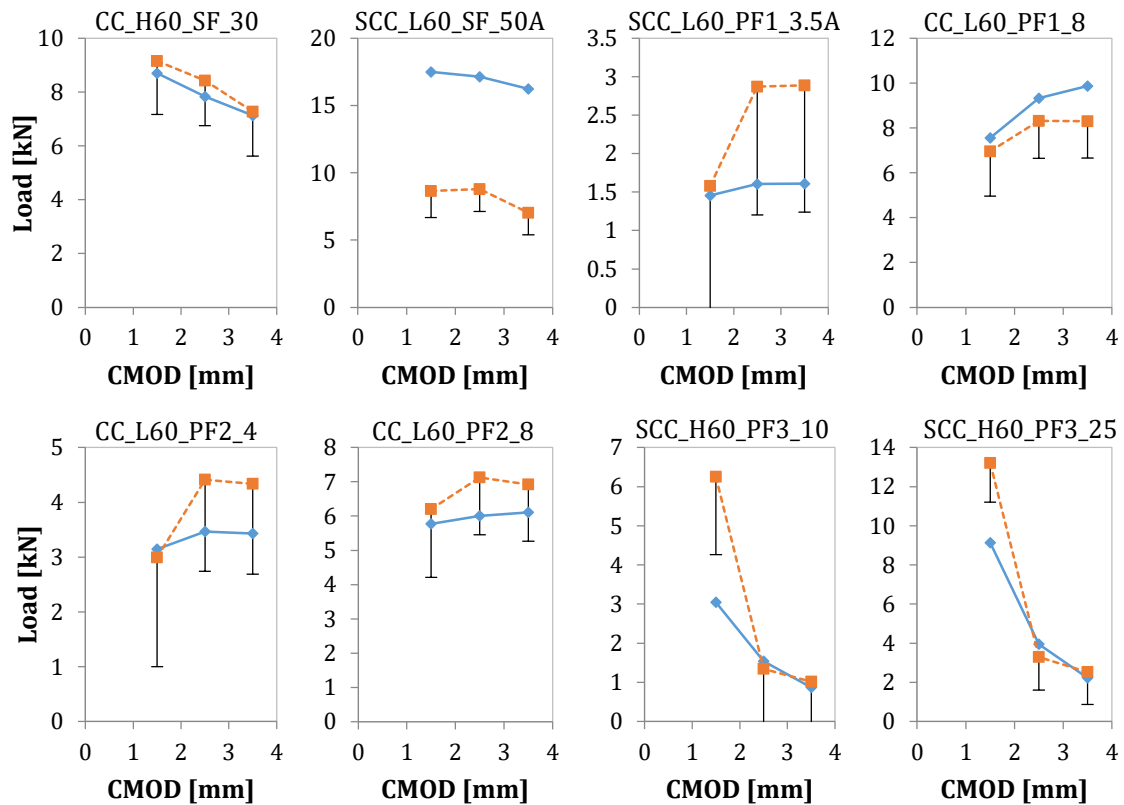


Figure 7.13 Real and predicted curves of 3PBT with confidence intervals.

A general overview of the results shows that the calculated curves follow similar trends to those obtained directly from the 3PBT. In the great majority of cases the values measured during the 3PBT are found above the limit defined by the confidence intervals. The only composition in which this is not fulfilled for all displacements is the SCC_H60_SF_60. This confirms that the safety margin introduced is capable of compensating the errors of the predictions.

The accuracy of the prediction decreases with the load level. In certain cases, negative values of the confidence lower limit are obtained. This should be expected when the force measured during the 3PBT are below 5 kN, being especially evident in some of the mixes with plastic fibres.

7.6 REAL CASE IMPLEMENTATION

The use of the correlations between the 3PBT and the Barcelona test is particularly interesting to reduce the scatter and, consequently, the likelihood of rejecting uncomplying batches. For this reason, the correlations are particularly addressed to large scale works in which high amounts of concrete need to be produced. In case that project management decides to use the BCN instead of the 3PBT, the correlations need to be calibrated and adapted to the particular case of the work concerned.

A real case of application is here presented. In this case, only the results of three concrete batches were provided and preliminary results of the correlation were calculated. It is necessary to count with results of both the bending and the Barcelona test. Notice that when further results are provided, both the robustness and the accuracy of the correlation improve given the increased reliability of the calibrated parameters.

7.6.1 Post-cracking strength

The average results of the three-point bending tests conducted on the three batches (B1, B2 and B3) are presented in Table 7.7. The residual strengths at crack openings of 0.5, 1.5, 2.5 and 3.5 mm (f_{R1} , f_{R2} , f_{R3} and f_{R4} , respectively) are shown, along with the coefficient of variation of each parameter. The results of the cubic specimens tested under the Barcelona test are presented in Table 7.8. The results show the average residual strength for vertical displacements of 0.5, 1.5, 2.5 and 3.5 mm ($f_{R0.5}$, $f_{R1.5}$, $f_{R2.5}$ and $f_{R3.5}$, respectively), as well as the scatter associated to each strength.

Table 7.7 Bending test results of B1, B2 and B3.

Param. [MPa]	B1		B2		B3		B1-B2-B3	
	Average	CV %	Average	CV %	Average	CV %	Average	CV %
f_{R1}	2.36	22.2%	3.10	23.6%	3.02	23.9%	2.83	14.4 %
f_{R2}	2.49	26.1%	3.06	24.8%	3.17	25.6%	2.91	12.7 %
f_{R3}	2.39	26.9%	2.83	22.1%	3.03	23.8%	2.75	11.8 %
f_{R4}	2.27	27.5%	2.60	23.5%	2.80	23.2%	2.56	10.4 %

Table 7.8 Barcelona test result of B1, B2 and B3.

Param. [MPa]	B1		B2		B3		B1-B2-B3	
	Average	CV %	Average	CV %	Average	CV %	Average	CV %
$f_{R0.5}$	1.48	14.0%	1.54	9.1%	1.47	23.3%	1.50	2.5 %
$f_{R1.5}$	1.05	17.7%	1.02	12.0%	0.98	22.6%	1.02	3.5 %
$f_{R2.5}$	0.86	19.0%	0.75	19.0%	0.80	20.8%	0.80	6.9 %
$f_{R3.5}$	0.74	21.2%	0.60	24.6%	0.68	21.3%	0.67	10.4 %

The results show that Batch 1 presented the lowest residual strengths when conducting the three-point bending test. With the exception of f_{R1} , B1 also presented the highest scatter among the three batches, even though the dispersion was also similarly high in B2 and B3 with CV around 23% and 25%. Conversely, the results of the Barcelona test present the highest residual strengths in B1, with the exception of $f_{R0.5}$. Notice that lower residual strengths when compared to the three-point bending test are achieved, which is mainly attributed to the different cracking mechanism and the higher cracking surface area.

Regardless of the different results among batches, the average strengths (B1-B2-B3) in both the bending and the Barcelona test present a more reduced scatter. In the bending test the CV is reduced to a value around 12%, whereas in the Barcelona test the average scatter is 5.8%. Such a reduced variability in the results of different batches indicates the similarity between them and the homogeneity of the material, thus revealing an appropriate manufacturing procedure.

7.6.2 Correlation between tests

To achieve the correlation between the mechanical parameters of both tests, the parameters a and b of Eq. 7.1 need to be calibrated. As described in Section 7.5, using the load and the energy of the Barcelona test at displacements of 0.5, 1.5, 2.5 and 3.5 mm it is possible to obtain a correlated value of the load of the bending test at crack openings of 0.5, 1.5, 2.5 and 3.5 mm. Each crack opening of the bending test is correlated with the displacement counterpart of the Barcelona test in Eq. 7.1. In other words, to obtain the estimated flexural load at a CMOD of 0.5 mm ($F_{3PBT,0.5}$), the load and the energy of the Barcelona test at displacements 0.5 mm ($F_{BCN,0.5}$ and $E_{BCN,0.5}$) needs to be used.

The experimental results of B1 and B2 were used for the calibration, while B3 was used to verify the results. Given the reduced availability of batches, the results of all the specimens tested were used in order to have a higher amount of data and increase the reliability of the correlation with more accurate results of a and b . Batch B1 presented 10 specimens for the three-point bending test and 20 for the Barcelona test. The results of the Barcelona test were therefore averaged by pairs, thus obtaining 10 results to be correlated with the 10 results of the bending test. The same procedure was followed for B2, which presented 6 specimens for bending and 12 for the Barcelona test. The parameters a and b after the calibration are shown in Table 7.9 for each crack opening.

Table 7.9 Calibrated parameters of correlation.

CMOD [mm]	a	b
0.5	$1.19 \cdot 10^{-1}$	$7.11 \cdot 10^{-4}$
1.5	$1.76 \cdot 10^{-1}$	$1.80 \cdot 10^{-4}$
2.5	$1.76 \cdot 10^{-1}$	$1.53 \cdot 10^{-4}$
3.5	$1.95 \cdot 10^{-1}$	$8.94 \cdot 10^{-5}$

A schematic representation of how to obtain the load and the energy parameters of the bending and the Barcelona test is shown in Figure 7.14. The energy of the Barcelona test is calculated as the area under the load-displacement curve up to the selected displacement. The example represents the parameters for a CMOD or a vertical displacement of 0.5 mm, even though the rest of parameters are calculated similarly.

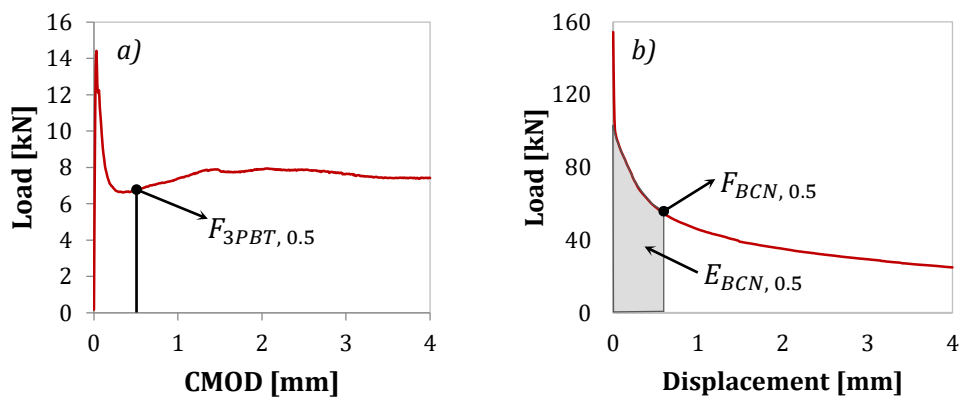


Figure 7.14 a) Three-point bending test and b) Barcelona test curve.

The values in Figure 7.10 show the experimental results of the bending test compared to the results of the correlation calculated with the parameters in Figure 7.9 and the experimental results of the Barcelona test for B3. A confidence interval of 99% for each load and crack opening is also presented according to the results of the calibration.

Table 7.10 Experimental and correlated results.

CMOD [mm]	F_{3PBT}^{exp} [kN]	F_{3PBT}^{corr} [kN]	$CI_{99\%}$ [kN]
0.5	9.14	8.24	1.33
1.5	8.85	8.53	1.51
2.5	8.26	7.64	1.54
3.5	7.55	6.84	1.45

A general overview of the results shows similar trends of both the experimental results and the correlated values. It is noteworthy that the average experimental results of the three-point bending test are slightly higher than the average results obtained by the correlation. The lowest value of the confidence interval corresponds to a safety margin that reduces the value of the experimental result to remain on the conservative side.

7.7 CONCLUDING REMARKS

The approach proposed in this study showed that it is possible to predict the 3PBT based on the results of the BCN with a confidence margin, despite the wide variety of fibre type, fibre content and rheology. The following conclusions may be derived based on the results and the analysis presented here.

- The amount of accepted batches during quality control increases for tests with lower CV. In this regard, it is suggested to use alternative testing methodologies with the aim of reducing the variability of the results. The use of the BCN with respect to the 3PBT verifies this recommendation and makes it more suitable for quality control.
- The same FRC mix may present hardening in the 3PBT and softening in the BCN. This difference is mainly attributed to the cracking mechanism that takes place in each test. In the BCN, the cracks form abruptly. The load resisted by the cementitious matrix is almost instantaneously transferred to the fibre. Conversely, in the 3PBT the crack height tends to increase progressively, yielding a more gradual load transfer from the matrix to the fibres in the area subjected to tension.
- The correlation between the 3PBT and the BCN considering only one parameter of each test did not provide acceptable results. In order to improve the correlation degree, it is advisable to include more than one parameter in the regression. In the present study, the parameters that yielded the best fits were the force and the energy measured for a

certain axial displacement in the BCN, which are related with the force measured in the 3PBT.

- Only one equation (Eq. 7.2) is needed to correlate the 3PBT and the BCN, regardless of the type of fibre, the content of fibre or the rheology of concrete. The correlation degrees (R^2) achieved range from 0.70 and 0.75 depending on the CMOD. It is important to remark that for low CMOD values, the correlation with the BCN may not be possible due to the differences in terms of the crack formation in both tests.
- Almost all experimental measurements with the 3PBT remain above the prediction with the confidence interval using the results from the BCN. This confirms that the use of confidence intervals is an interesting approach to obtain predictions on the safe side for a material subjected to significant scatter, such as FRC.

Notice that the influence on the results of the correlation of different variables such as the type of concrete, type of fibre or content of fibres was analysed. From the results, it was concluded that the correlation did not improve significantly when the analysis was conducted separately with these parameters. According to this, the equation to correlate the BCN and the 3PBT may be used in any situation, however, the calibration of the parameters needs to be conducted in all cases.

The geometry, mode of fracture and test setup of the beams used for the three-point bending are more representative of the real behaviour of a structural element. For this reason, the use of the bending test is more suitable than the BCN at the design stage. The optimization of the quality control needs an approach oriented to simplification and minimization of resources. In this regard, the specific conclusions here derived open up the possibility of using the BCN as a complementary test for the systematic quality control of FRC. The same approach may be applied to correlate other tests or to obtain better correlations for specific types of FRC.

8 CONCLUSIONS

8.1 GENERAL CONCLUSIONS

FRC is currently being used in many different applications and has turned into a real alternative to traditional reinforced concrete. With a demand expected to keep growing, design procedures of FRC require to be updated to enhance the structural safety and optimize the performance of FRC structures. In this line, the main topics herein developed have analysed and discussed the suitability of the constitutive model for FRC based on the specifications of the MC2010, the influence of the orientation of the fibres and the optimization of quality control procedures. In response to the general objectives defined in Chapter 1, the general conclusions and the implications of the issues addressed in this thesis are presented.

The influence of the size effect on the parameters defining the FRC constitutive model of the MC2010 was analysed using smaller beams than the standard dimension ($150 \times 150 \times 600 \text{ mm}$) to simplify the test procedure. The MC2010 states that the residual strengths defining the constitutive model are associated to specific CMODs, although the results of the study revealed that using the rotation of the specimen leads to more accurate results than the crack opening, especially in small beams. The reason for this is that a certain crack opening in a standard specimen is proportionally smaller than the same crack opening in a smaller sample for achieving an equivalent damage level in both specimens. Accordingly, using the rotation of the specimen in lieu of the CMOD to determine the residual parameters of the constitutive law entails equivalent crack openings and strains between different sized specimens.

The most relevant contribution of the model to predict the residual strength of FRC based on fibre orientation and fibre pull-out is that it is possible to take into account the variability of the orientation of the fibres and the influence of the cross-sectional dimensions. It also

determines the number of fibres at the cracked surface and shows their distribution at the cross-section. The model is also flexible to be applied with fibres of different geometries and lengths if the appropriate pull-out laws are implemented.

The repercussions of using different reinforcement configurations—rebars and different fibre contents and geometries—was assessed by testing real-scale slabs. This study proves that, in presence of rebars, fibres activate secondary cracks and increase the load-bearing capacity of slabs. Additionally, in some cases, the ductility requirements of the MC2010 are too conservative and the reinforcement ratio can, therefore, be reduced.

Analytical methods and numerical simulations (FEM) of the slabs confirmed that the FRC constitutive model of the MC2010 significantly overestimates their response. Constitutive models are often simplified for practical convenience, ignoring multiple factors affecting the residual strength of FRC such as the geometry of the element and the fibre orientation.

Quality control was addressed proposing a correlation between the Barcelona test (BCN) and the 3PBT to simplify and make more accessible testing procedures for FRC. The BCN is conducted in a conventional hydraulic press and is more affordable than a 3PBT, which requires a closed-loop testing machine difficult to find in laboratories given its high cost. The BCN is also less time-consuming than a 3PBT and since specimens are also smaller, a higher number of tests can be performed to increase the reliability of the results.

8.2 SPECIFIC CONCLUSIONS

In response to the specific objectives proposed in Chapter 1, a summary of the specific conclusions obtained in the different chapters is presented as follows.

Size effect

- Smaller specimens generally exhibited higher strengths than larger elements, especially as a result of the higher number of fibres oriented perpendicularly to the cracked surface when reducing the cross-section.
- The Equivalent Crack Opening method (ECO) is proposed to calculate the values of f_{R1} and f_{R3} using the rotation of the specimen in case of testing small specimens to determine the parameters of the constitutive law. According to this approach, the absolute value of the crack opening is smaller as the dimension of the specimen decreases although it remains proportional with the specimen size if compared to larger samples.
- The cross-sectional analyses conducted with the constitutive law calculated through the ECO presented accurate results for the three specimen dimensions and the two contents of fibres of the study. The Full Crack Opening method (FCO) underestimated the results at small crack widths while these are overestimated at high crack openings.
- The ultimate strain of 3.5‰ in compression was extended beyond this value in the FRC mixes analysed to achieve the equilibrium between tensile stress and compression. This is attributed to the remaining strength after cracking under compression due to the presence of fibres.

Distribution and orientation of fibres

- The number of fibres crossing the cracked section estimated by the isotropy-based model agrees with results reported in the literature. The average orientation number of the fibres is higher when close to the boundaries due to the wall-effect. In this line, reducing the dimension of the specimen and the area of the cross-section increases the influence of the wall-effect and leads to a higher average orientation number of fibres in a perpendicular direction to the cracked surface.
- According to the results of the model, fibres tend to present a higher pull-out during fibre removal when the inclination angle increases. This is a result of the increasing bridging capacity of fibres with a higher inclination with respect to the pull-out load.
- The results of the model allow estimating the post-cracking strength of FRC considering the influence of the fibre content and the size of the specimen. Different types of fibres can be used according to the pull-out law implemented in the model.

Characterization of slabs

- Double hooked-end fibres (2HE) lead to lower compressive strengths when compared to FRC with conventional hooked-end fibres (1HE). This is attributed to a reduction of the packing density of concrete given the higher air content introduced by mixing fibres with double hook. Conversely, the tensile strength of FRC increased as a result of the enhanced anchorage provided by the double hooks.
- Slabs with fibres exhibited a higher number of cracks, thus reducing the average crack width while reducing the distance between them. Fibres 2HE provided greater strengths at higher crack widths and their use resulted in a higher number of cracks if compared to slabs reinforced with fibres 1HE.
- Slabs reinforced only with fibres did not meet the minimum ductility requirements of the MC2010. Slabs reinforced with a combination of fibres and traditional reinforcement presented a critical or supracritical behaviour. Slabs reinforced with fibres 2HE exhibited a higher ductility than those reinforced with fibres 1HE.
- The analysis of the cores revealed a higher anisotropy of the orientation of the fibres when closer to the edges of the slabs, with fibres presenting a preferential orientation in a direction parallel to the wall. Additionally, the two layers of cores reveal a different orientation of the fibres according to the depth of the slab.

Modelling of slabs

- The results of AES indicate that fibres present a higher contribution in SLS than in ULS. This could be particularly appreciated in fibres 1HE, whose contribution did not exceed strains beyond 4.0‰. Instead, fibres 2HE were able to resist higher strengths at strains greater than 4.0‰, although their contribution at SLS was lower when compared to fibres 1HE.
- A clear size effect on FRCS and HRCS could be appreciated when conducting the AES. The parameters of the constitutive law obtained with a 150x150x600 mm had to be considerably reduced to fit the experimental results of FRCS and HRCS, this indicating the higher strength of the small specimen with respect to the real-scale slab.

- The results of the AES suggest that the combination of fibres with traditional reinforcement leads to reduce the reinforcing contribution of the fibres. This effect could not be appreciated in the FEM analysis given that the same calibration used for FRCS and HRCS provided a good approximation between the simulation and the experimental values.

Correlation between the BCN and the 3PBT

- The smaller dimensions and the more reduced time to conduct the BCN simplifies the testing procedure with respect to 3PBT. In terms of quality control, these assets entail the possibility of conducting a higher number of tests and reduce the uncertainty associated to the scatter of FRC results.
- At least two parameters of the BCN test in the correlation are required to achieve one equation providing acceptable results of the 3PBT based on the former. However, the correlation presents some limitations for low CMODs values given the differences in terms of crack formation between tests.
- Most of the estimations of the 3PBT calculated through the parameters of the BCN show results above the experimental 3PBT values. The use of confidence intervals also provides a tool to obtain predictions on the safe side given the high scatter of FRC.

8.3 FUTURE PERSPECTIVES

Based on the findings of this doctoral thesis, several suggestions on future works are presented. Given that the topics herein addressed still need further research, these suggestions aim to shed light on unsolved problems and help to improve the knowledge about the reinforcing mechanisms of fibres.

Size effect

- Analyse whether the proposed approach based on the rotation of the sample can be applied to specimens and elements of other dimensions. Conduct an experimental programme involving larger and smaller samples with proportional and non-proportional dimensions with the aim of determining which parameter—depth, width or length—plays the most important role.
- Extend the study to additional types and contents of fibres. Conduct parametric analyses to identify up to which extent the content of fibres is responsible for the size effect.
- Propose new parameters and alternative approaches to account for the size effect in the FRC constitutive model to increase the reliability of the analyses and designs.

Distribution and orientation of fibres

- Verify the influence of other types and contents of fibres on the estimations of the residual strength implementing the required pull-out laws. Perform a parametric analysis of the model to enhance the accuracy of the results and improve the model to obtain more accurate predictions of the flexural behaviour of FRC based on the orientation of fibres.

- Analyse and determine experimentally the orientation number of the fibres in the three regions—bulk, boundaries and corners—at the cross-section. Improve the model by dividing the cross-section into the three regions specified to introduce different orientation numbers.
- Verify the model with concrete mixes presenting different rheologies given the influence of the flowability and vibration on the orientation and distribution of fibres.

Characterization and modelling of slabs

- Conduct additional experimental programmes involving the analysis of real-scale elements to study the reinforcing effect of fibres as well as their distribution and orientation within the elements. Determine the optimum contents of fibres to replace totally or partially the traditional reinforcement.
- Analyse the specific cases under which the constitutive law for FRC of the MC2010 overestimates the results of large structural elements. Analyse which part of these overestimations are due to the orientation of the fibres and which are a result of the change of the dimensions. Propose specific parameters to adjust the results of the 3PBT according to the dimensions of the structural element in line with the solution proposed by RILEM and the German DBV.
- Determine the influence of the testing configuration and analyse the effect of testing real-scale elements under isostatic or hyperstatic configurations. Increase the content of fibres, given the relatively low content used in the slabs for the study herein presented.

Correlation between the BCN and the 3PBT

- Provide specific recommendations on how to determine and conduct the correlations to obtain more accurate results. Extend the study to additional types, geometries and contents of fibres to account for the particularities of each case.
- Conduct statistical analyses of the results beyond the normal distribution to define more precise confidence intervals.

REFERENCES

- Abdallah, S., Fan, M., Zhou, X., et al., 2016a. Anchorage Effects of Various Steel Fibre Architectures for Concrete Reinforcement. *International Journal of Concrete Structures and Materials*, 10(3), pp.325–335.
- Abdallah, S. & Fan, M., 2017a. Anchorage mechanisms of novel geometrical hooked-end steel fibres. *Materials and Structures*, 50(2), p.139.
- Abdallah, S., Fan, M. & Rees, D.W.A., 2016b. Analysis and modelling of mechanical anchorage of 4D/5D hooked end steel fibres. *Materials & Design*, 112, pp.539–552.
- Abdallah, S., Fan, M. & Zhou, X., 2017b. Pull-Out Behaviour of Hooked End Steel Fibres Embedded in Ultra-high Performance Mortar with Various W/B Ratios. *International Journal of Concrete Structures and Materials*, 11(2), pp.301–313.
- Abrishambaf, A., Barros, J. & Cunha, F.N.M., 2012. Assessment of Fibre Orientation and Distribution in Steel Fibre Reinforced Self-Compacting Concrete Panels. In *8th RILEM International Symposium on Fibre Reinforced Concrete. BEFIB 2012*. pp. 1–12.
- Abrishambaf, A., Barros, J.A.O. & Cunha, V.M.C.F., 2013. Relation between fibre distribution and post-cracking behaviour in steel fibre reinforced self-compacting concrete panels. *Cement and Concrete Research*, 51, pp.57–66.
- Abrishambaf, A., Barros, J.A.O. & Cunha, V.M.C.F., 2015. Tensile stress–crack width law for steel fibre reinforced self-compacting concrete obtained from indirect (splitting) tensile tests. *Cement and Concrete Composites*, 57, pp.153–165.
- Abrishambaf, A., Pimentel, M. & Nunes, S., 2017. Influence of fibre orientation on the tensile behaviour of ultra-high performance fibre reinforced cementitious composites. *Cement and Concrete Research*, 97, pp.28–40.

- Abu-Lebdeh, T. et al., 2011. Effect of matrix strength on pullout behavior of steel fiber reinforced very-high strength concrete composites. *Construction and Building Materials*, 25(1), pp.39–46.
- AENOR (Asociación Española de Normalización y Certificación), 2010. UNE 83515. Fibre reinforced concrete. Determination of cracking strength, ductility and residual tensile strength. Barcelona test.
- AFGC, 2013. *Ultra high performance fibre-reinforced concrete. Recommendations*, Association Française de Génie Civil.
- Akçay, B. & Tasdemir, M.A., 2012. Mechanical behaviour and fibre dispersion of hybrid steel fibre reinforced self-compacting concrete. *Construction and Building Materials*, 28(1), pp.287–293.
- Alberti, M.G., Enfedaque, A., et al., 2016a. Fibre distribution and orientation of macro-synthetic polyolefin fibre reinforced concrete elements. *Construction and Building Materials*, 122, pp.505–517.
- Alberti, M.G., Enfedaque, A., Gálvez, J.C., et al., 2016b. Reliability of polyolefin fibre reinforced concrete beyond laboratory sizes and construction procedures. *Composite Structures*, 140, pp.506–524.
- Alberti, M.G., Enfedaque, A. & Gálvez, J.C., 2016c. Fracture mechanics of polyolefin fibre reinforced concrete: Study of the influence of the concrete properties, casting procedures, the fibre length and specimen size. *Engineering Fracture Mechanics*, 154, pp.225–244.
- Alberti, M.G., Enfedaque, A. & Gálvez, J.C., 2014. On the mechanical properties and fracture behavior of polyolefin fiber-reinforced self-compacting concrete. *Construction and Building Materials*, 55, pp.274–288.
- Alberti, M.G., Enfedaque, A. & Gálvez, J.C., 2017. On the prediction of the orientation factor and fibre distribution of steel and macro-synthetic fibres for fibre-reinforced concrete. *Cement and Concrete Composites*, 77, pp.29–48.
- Alfarah, B., López-Almansa, F. & Oller, S., 2017. New methodology for calculating damage variables evolution in Plastic Damage Model for RC structures. *Engineering Structures*, 132, pp.70–86.
- Awinda, K., Chen, J. & Barnett, S.J., 2016. Investigating geometrical size effect on the flexural strength of the ultra high performance fibre reinforced concrete using the cohesive crack model. *Construction and Building Materials*, 105, pp.123–131.
- Balázs, G.L. et al., 2017. Observation of steel fibres in concrete with Computed Tomography. *Construction and Building Materials*, 140, pp.534–541.
- Banthia, N. et al., 2012. Fiber-reinforced concrete in precast concrete applications: Research leads to innovative products. *PCI Journal*, 57(3), pp.33–46.
- Barnett, S.J. et al., 2010. Assessment of fibre orientation in ultra high performance fibre reinforced concrete and its effect on flexural strength. *Materials and Structures*, 43(7), pp.1009–1023.
- Barr, B.I.G., Lee, M.K., de Place Hansen, E.J., et al., 2003a. Round-robin analysis of the RILEM TC 162-TDF beam-bending test: Part 3—Fibre distribution. *Materials and Structures*, 36(9), pp.631–635.

- Barr, B.I.G., Lee, M.K., Barragán, B., et al., 2003b. Round-robin analysis of the RILEM TC 162-TDF uni-axial tensile test: Part 1. *Materials and Structures*, 36(4), pp.265–274.
- Barros, J.A.O. et al., 2005. Post-cracking behaviour of steel fibre reinforced concrete. *Materials and Structures*, 38(1), pp.47–56.
- Bastien-Masse, M., Denarié, E. & Brühwiler, E., 2016. Effect of fiber orientation on the in-plane tensile response of UHPFRC reinforcement layers. *Cement and Concrete Composites*, 67, pp.111–125.
- Bažant, Z.P., 2002. Concrete fracture models: testing and practice. *Engineering Fracture Mechanics*, 69(2), pp.165–205.
- Bernard, E.S., 2002. Correlations in the behaviour of fibre reinforced shotcrete beam and panel specimens. *Materials and Structures*, 35(3), pp.156–164.
- Bernardi, P. et al., 2016. Experimental and numerical study on cracking process in RC and R/FRC ties. *Materials and Structures*, 49(1–2), pp.261–277.
- Bischoff, P.H., 2003. Tension Stiffening and Cracking of Steel Fiber-Reinforced Concrete. *Journal of Materials in Civil Engineering*, 15(2), pp.174–182.
- Blanco, A. et al., 2013. Application of constitutive models in European codes to RC–FRC. *Construction and Building Materials*, 40, pp.246–259.
- Blanco, A. et al., 2015a. Application of FRC constitutive models to modelling of slabs. *Materials and Structures*, 48(9), pp.2943–2959.
- Blanco, A. et al., 2015b. Assessment of the fibre orientation factor in SFRC slabs. *Composites Part B: Engineering*, 68, pp.343–354.
- Blanco, A., 2013. *Characterization and modelling of SFRC elements*. PhD Thesis, Universitat Politècnica de Catalunya.
- Blanco, A. et al., 2014. Constitutive model for fibre reinforced concrete based on the Barcelona test. *Cement and Concrete Composites*, 53, pp.327–340.
- Boulekbache, B. et al., 2010. Flowability of fibre-reinforced concrete and its effect on the mechanical properties of the material. *Construction and Building Materials*, 24(9), pp.1664–1671.
- Buratti, N., Ferracuti, B. & Savoia, M., 2013. Concrete crack reduction in tunnel linings by steel fibre-reinforced concretes. *Construction and Building Materials*, 44, pp.249–259.
- Buratti, N., Mazzotti, C. & Savoia, M., 2011. Post-cracking behaviour of steel and macro-synthetic fibre-reinforced concretes. *Construction and Building Materials*, 25(5), pp.2713–2722.
- Caratelli, A. et al., 2011. Structural behaviour of precast tunnel segments in fiber reinforced concrete. *Tunnelling and Underground Space Technology*, 26(2), pp.284–291.
- Caratelli, A., Meda, A. & Rinaldi, Z., 2012. Design according to MC2010 of a fibre-reinforced concrete tunnel in Monte Lirio, Panama. *Structural Concrete*, 13(3), pp.166–173.
- di Carlo, F., Meda, A. & Rinaldi, Z., 2016. Design procedure for precast fibre-reinforced concrete segments in tunnel lining construction. *Structural Concrete*, 17(5), pp.747–759.
- Carmona, S. et al., 2016. Distribution of fibers in SFRC segments for tunnel linings. *Tunnelling and Underground Space Technology*, 51, pp.238–249.

- Cavalaro, S.H.P. et al., 2016. Assessment of fibre content and 3D profile in cylindrical SFRC specimens. *Materials and Structures*, 49(1-2), pp.577-595.
- Cavalaro, S.H.P. et al., 2015. Improved assessment of fibre content and orientation with inductive method in SFRC. *Materials and Structures*, 48(6), pp.1859-1873.
- Cavalaro, S.H.P. & Aguado, A., 2015. Intrinsic scatter of FRC: an alternative philosophy to estimate characteristic values. *Materials and Structures*, 48(11), pp.3537-3555.
- CEN, 2014. EN 12390-13:2014. Testing hardened concrete – Part 13: Determination of secant modulus of elasticity in compression.
- CEN, 2009. EN 12390-3. Testing hardened concrete. Part 3: Compressive strength of test specimens.
- CEN, 2007. EN 14651:2007. Test method for metallic fibre concrete. Measuring the flexural tensile strength (limit of proportionality (LOP), residual).
- Chiaia, B., Fantilli, A.P. & Vallini, P., 2009a. Combining fiber-reinforced concrete with traditional reinforcement in tunnel linings. *Engineering Structures*, 31(7), pp.1600-1606.
- Chiaia, B., Fantilli, A.P. & Vallini, P., 2009b. Evaluation of crack width in FRC structures and application to tunnel linings. *Materials and Structures*, 42(3), pp.339-351.
- Conforti, A. et al., 2018. Comparing test methods for the mechanical characterization of fiber reinforced concrete. *Structural Concrete*, 19(3), pp.656-669.
- Cunha, V.M.C.F., Barros, J.A.O. & Sena-Cruz, J.M., 2012. Numerical simulation of three-point bending tests: two distinct approaches. In *BEFIB2012*. Guimaraes.
- Cunha, V.M.C.F., Barros, J.A.O. & Sena-Cruz, J.M., 2010. Pullout Behavior of Steel Fibers in Self-Compacting Concrete. *Journal of Materials in Civil Engineering*, 22(1), pp.1-9.
- Dupont, D. & Vandewalle, L., 2005. Distribution of steel fibres in rectangular sections. *Cement and Concrete Composites*, 27(3), pp.391-398.
- Edgington, J. & Hannant, D.J., 1972. Steel fibre reinforced concrete. The effect on fibre orientation of compaction by vibration. *Materials and Structures*, 5(1), pp.41-44.
- EHE, 2008. *EHE-08 Instrucción de hormigón estructural*.
- Ferrara, L., Faifer, M. & Toscani, S., 2012. A magnetic method for non destructive monitoring of fiber dispersion and orientation in steel fiber reinforced cementitious composites—part 1: method calibration. *Materials and Structures*, 45(4), pp.575-589.
- Ferrara, L. & Meda, A., 2007. Relationships between fibre distribution, workability and the mechanical properties of SFRC applied to precast roof elements. *Materials and Structures*, 39(4), pp.411-420.
- Ferrara, L., Ozyurt, N. & di Prisco, M., 2011. High mechanical performance of fibre reinforced cementitious composites: the role of “casting-flow induced” fibre orientation. *Materials and Structures*, 44(1), pp.109-128.
- Ferrara, L., Park, Y.-D. & Shah, S.P., 2008. Correlation among Fresh State Behavior, Fiber Dispersion, and Toughness Properties of SFRCs. *Journal of Materials in Civil Engineering*, 20(7), pp.493-501.
- fib, 2010. *fib Model Code for Concrete Structures 2010*.

- Genikomsou, A.S. & Polak, M.A., 2015. Finite element analysis of punching shear of concrete slabs using damaged plasticity model in ABAQUS. *Engineering Structures*, 98, pp.38–48.
- Ghafari, E. et al., 2014. The effect of nanosilica addition on flowability, strength and transport properties of ultra high performance concrete. *Materials & Design*, 59, pp.1–9.
- Giaccio, G., Tobes, J.M. & Zerbino, R., 2008. Use of small beams to obtain design parameters of fibre reinforced concrete. *Cement and Concrete Composites*, 30(4), pp.297–306.
- Gonzalez-Corominas, A., Etxeberria, M. & Poon, C.S., 2016. Influence of steam curing on the pore structures and mechanical properties of fly-ash high performance concrete prepared with recycled aggregates. *Cement and Concrete Composites*, 71, pp.77–84.
- Grünewald, S., 2004. *Performance-based design of self-compacting fibre reinforced concrete*. PhD Thesis, Delft University of Technology.
- Holschemacher, K., Mueller, T. & Ribakov, Y., 2010. Effect of steel fibres on mechanical properties of high-strength concrete. *Materials & Design (1980-2015)*, 31(5), pp.2604–2615.
- Hoover, C.G. & Bažant, Z.P., 2014. Cohesive crack, size effect, crack band and work-of-fracture models compared to comprehensive concrete fracture tests. *International Journal of Fracture*, 187(1), pp.133–143.
- Jamshidi Avanaki, M. et al., 2018. Numerical-aided design of fiber reinforced concrete tunnel segment joints subjected to seismic loads. *Construction and Building Materials*, 170, pp.40–54.
- Jones, P.A., Austin, S.A. & Robins, P.J., 2008. Predicting the flexural load–deflection response of steel fibre reinforced concrete from strain, crack-width, fibre pull-out and distribution data. *Materials and Structures*, 41(3), pp.449–463.
- Kang, S.-T. & Kim, J.-K., 2012. Numerical simulation of the variation of fiber orientation distribution during flow molding of Ultra High Performance Cementitious Composites (UHPCC). *Cement and Concrete Composites*, 34(2), pp.208–217.
- Kang, S.-T. & Kim, J.-K., 2011. The relation between fiber orientation and tensile behavior in an Ultra High Performance Fiber Reinforced Cementitious Composites (UHPFRCC). *Cement and Concrete Research*, 41(10), pp.1001–1014.
- Kang, S.T. et al., 2011. The effect of fibre distribution characteristics on the flexural strength of steel fibre-reinforced ultra high strength concrete. *Construction and Building Materials*, 25(5), pp.2450–2457.
- Karihaloo, B.L., Murthy, A.R. & Iyer, N.R., 2013. Determination of size-independent specific fracture energy of concrete mixes by the tri-linear model. *Cement and Concrete Research*, 49, pp.82–88.
- Kasper, T. et al., 2008. Lining design for the district heating tunnel in Copenhagen with steel fibre reinforced concrete segments. *Tunnelling and Underground Space Technology*, 23(5), pp.574–587.
- Kim, D.J., Naaman, A.E. & El-Tawil, S., 2008. Comparative flexural behavior of four fiber reinforced cementitious composites. *Cement and Concrete Composites*, 30(10), pp.917–928.

- Kim, H.K., Jeon, J.H. & Lee, H.K., 2012. Workability, and mechanical, acoustic and thermal properties of lightweight aggregate concrete with a high volume of entrained air. *Construction and Building Materials*, 29, pp.193–200.
- Krenchel, H., 1975. *Fibre spacing and specific fibre surface*.
- de la Fuente, A., Escariz, R.C., et al., 2012a. A new design method for steel fibre reinforced concrete pipes. *Construction and Building Materials*, 30, pp.547–555.
- de la Fuente, A. et al., 2014. Diseño óptimo de dovelas de hormigón reforzado con fibras para el revestimiento de túneles. *Hormigón y Acero*, 65(274), pp.267–279.
- de la Fuente, A., Pujadas, P., et al., 2012b. Experiences in Barcelona with the use of fibres in segmental linings. *Tunnelling and Underground Space Technology*, 27(1), pp.60–71.
- de la Fuente, A. et al., 2011. Experimentación y simulación numérica de tubos de hormigón con fibras. *Materiales de Construcción*, 61(302), pp.275–288.
- de la Fuente, A., Aguado, A., et al., 2012c. Numerical model for the analysis up to failure of precast concrete sections. *Computers & Structures*, 106–107, pp.105–114.
- de la Fuente, A. et al., 2018. Partial Safety Factor for the Residual Flexural Strength of FRC Precast Concrete Segments. In *High Tech Concrete: Where Technology and Engineering Meet*. Springer International Publishing, pp. 1768–1775.
- de la Fuente, A. et al., 2017. Sustainability based-approach to determine the concrete type and reinforcement configuration of TBM tunnels linings. Case study: Extension line to Barcelona Airport T1. *Tunnelling and Underground Space Technology*, 61, pp.179–188.
- Lameiras, R., Barros, J.A.O. & Azenha, M., 2015. Influence of casting condition on the anisotropy of the fracture properties of Steel Fibre Reinforced Self-Compacting Concrete (SFRSCC). *Cement and Concrete Composites*, 59, pp.60–76.
- Laranjeira, F. et al., 2011. Characterization of the orientation profile of steel fiber reinforced concrete. *Materials and Structures*, 44(6), pp.1093–1111.
- Laranjeira, F., 2010. *Design-oriented constitutive model for steel fiber reinforced concrete*. PhD Thesis, Universitat Politècnica de Catalunya.
- Laranjeira, F. et al., 2012. Framework to predict the orientation of fibers in FRC: A novel philosophy. *Cement and Concrete Research*, 42(6), pp.752–768.
- Laranjeira, F., Aguado, A. & Molins, C., 2010a. Predicting the pullout response of inclined straight steel fibers. *Materials and Structures*, 43(6), pp.875–895.
- Laranjeira, F., Molins, C. & Aguado, A., 2010b. Predicting the pullout response of inclined hooked steel fibers. *Cement and Concrete Research*, 40(10), pp.1471–1487.
- Lataste, J.F. et al., 2009. Determination of fibres orientation in UHPFRC and evaluation of their effect on mechanical properties. In *7th International Symposium on Nondestructive Testing in Civil Engineering*. Nantes (France).
- Lataste, J.F., Behloul, M. & Breysse, D., 2008. Characterisation of fibres distribution in a steel fibre reinforced concrete with electrical resistivity measurements. *NDT & E International*, 41(8), pp.638–647.
- Lawler, J.S., Zampini, D. & Shah, S.P., 2005. Microfiber and Macrofiber Hybrid Fiber-Reinforced Concrete. *Journal of Materials in Civil Engineering*, 17(5), pp.595–604.

- Lee, Y., Kang, S.-T. & Kim, J.-K., 2010. Pullout behavior of inclined steel fiber in an ultra-high strength cementitious matrix. *Construction and Building Materials*, 24(10), pp.2030–2041.
- Liao, L. et al., 2015. Design of FRC tunnel segments considering the ductility requirements of the Model Code 2010. *Tunnelling and Underground Space Technology*, 47, pp.200–210.
- Liao, L. et al., 2016. Design procedure and experimental study on fibre reinforced concrete segmental rings for vertical shafts. *Materials & Design*, 92, pp.590–601.
- Lim, S. et al., 2018. Structural behavior prediction of SFRC beams by a novel integrated approach of X-ray imaging and finite element method. *Construction and Building Materials*, 170, pp.347–365.
- Löfgren, I., Stang, H. & Olesen, J.F., 2005. Fracture Properties of FRC Determined through Inverse Analysis of Wedge Splitting and Three-Point Bending Tests. *Journal of Advanced Concrete Technology*, 3(3), pp.423–434.
- López, J.Á. et al., 2016. A simplified five-point inverse analysis method to determine the tensile properties of UHPFRC from unnotched four-point bending tests. *Composites Part B: Engineering*, 91, pp.189–204.
- López, J.Á. et al., 2015. An inverse analysis method based on deflection to curvature transformation to determine the tensile properties of UHPFRC. *Materials and Structures*, 48(11), pp.3703–3718.
- Mahmud, G.H., Yang, Z. & Hassan, A.M.T., 2013. Experimental and numerical studies of size effects of Ultra High Performance Steel Fibre Reinforced Concrete (UHPFRC) beams. *Construction and Building Materials*, 48, pp.1027–1034.
- Maluk, C., Bisby, L. & Terrasi, G.P., 2017. Effects of polypropylene fibre type and dose on the propensity for heat-induced concrete spalling. *Engineering Structures*, 141, pp.584–595.
- Martinie, L. & Roussel, N., 2011. Simple tools for fiber orientation prediction in industrial practice. *Cement and Concrete Research*, 41(10), pp.993–1000.
- Matthews, S. et al., 2018. fib Model Code 2020: Towards a general code for both new and existing concrete structures. *Structural Concrete*, 19(4), pp.969–979.
- Meda, A., Minelli, F. & Plizzari, G.A., 2012. Flexural behaviour of RC beams in fibre reinforced concrete. *Composites Part B: Engineering*, 43(8), pp.2930–2937.
- Mehta, P. & Monteiro, P.J.M., 2006. *Concrete: Microstructure, Properties, and Materials*, McGraw-Hill Education.
- Meng, G. et al., 2016. Experimental investigation of the mechanical behavior of the steel fiber reinforced concrete tunnel segment. *Construction and Building Materials*, 126(4), pp.98–107.
- Meng, W. & Khayat, K.H., 2017. Improving flexural performance of ultra-high-performance concrete by rheology control of suspending mortar. *Composites Part B: Engineering*, 117, pp.26–34.
- Minelli, F. et al., 2014. Are steel fibres able to mitigate or eliminate size effect in shear? *Materials and Structures*, 47(3), pp.459–473.

- Minelli, F. & Plizzari, G., 2015. Derivation of a simplified stress–crack width law for Fiber Reinforced Concrete through a revised round panel test. *Cement and Concrete Composites*, 58, pp.95–104.
- Minelli, F. & Plizzari, G., 2010. Fiber reinforced concrete characterization through round panel test-Part I: experimental study. In *FraMCoS-7*. Jeju, South Korea.
- Mínguez, J., González, D.C. & Vicente, M.A., 2018. Fiber geometrical parameters of fiber-reinforced high strength concrete and their influence on the residual post-peak flexural tensile strength. *Construction and Building Materials*, 168, pp.906–922.
- Mobasher, B., Bakhshi, M. & Barsby, C., 2014. Backcalculation of residual tensile strength of regular and high performance fiber reinforced concrete from flexural tests. *Construction and Building Materials*, 70, pp.243–253.
- Mobasher, B., Yao, Y. & Soranakom, C., 2015. Analytical solutions for flexural design of hybrid steel fiber reinforced concrete beams. *Engineering Structures*, 100, pp.164–177.
- Molins, C., Aguado, A. & Saludes, S., 2009. Double Punch Test to control the energy dissipation in tension of FRC (Barcelona test). *Materials and Structures*, 42(4), pp.415–425.
- de Montaignac, R., Massicotte, B. & Charron, J.-P., 2012. Design of SFRC structural elements: flexural behaviour prediction. *Materials and Structures*, 45(4), pp.623–636.
- Naaman, A.E., 2003. Engineered Steel Fibers with Optimal Properties for Reinforcement of Cement Composites. *Journal of Advanced Concrete Technology*, 1(3), pp.241–252.
- NBN (Bureau de Normalisation), 1992. B 15-238. Test on fibre reinforced concrete—bending test on prismatic samples.
- Neville, A.M., 1996. *Properties of concrete*. John Wiley & Sons.
- Nguyen, D.L. et al., 2014. Size and geometry dependent tensile behavior of ultra-high-performance fiber-reinforced concrete. *Composites Part B: Engineering*, 58, pp.279–292.
- Nguyen, D.L. et al., 2013. Size effect on flexural behavior of ultra-high-performance hybrid fiber-reinforced concrete. *Composites Part B: Engineering*, 45(1), pp.1104–1116.
- Nili, M. & Ehsani, A., 2015. Investigating the effect of the cement paste and transition zone on strength development of concrete containing nanosilica and silica fume. *Materials & Design*, 75, pp.174–183.
- Nunes, S. et al., 2017. Estimation of the tensile strength of UHPFRC layers based on non-destructive assessment of the fibre content and orientation. *Cement and Concrete Composites*, 83, pp.222–238.
- Nunes, S., Pimentel, M. & Carvalho, A., 2016. Non-destructive assessment of fibre content and orientation in UHPFRC layers based on a magnetic method. *Cement and Concrete Composites*, 72, pp.66–79.
- Ozyurt, N., Mason, T.O. & Shah, S.P., 2006. Non-destructive monitoring of fiber orientation using AC-IS: An industrial-scale application. *Cement and Concrete Research*, 36(9), pp.1653–1660.
- Pająk, M. & Ponikiewski, T., 2013. Flexural behavior of self-compacting concrete reinforced with different types of steel fibers. *Construction and Building Materials*, 47, pp.397–408.

- Park, S.H. et al., 2014. Effect of shrinkage reducing agent on pullout resistance of high-strength steel fibers embedded in ultra-high-performance concrete. *Cement and Concrete Composites*, 49, pp.59–69.
- Parmentier, B. et al., 2008. Dispersion of the mechanical properties of FRC investigated by different bending tests. In *Tailor Made Concrete Structures: New Solutions for our Society*. CRC Press, pp. 507–512.
- Perumal, R., 2015. Correlation of Compressive Strength and Other Engineering Properties of High-Performance Steel Fiber-Reinforced Concrete. *Journal of Materials in Civil Engineering*, 27(1), p.04014114.
- Pichler, C., Lackner, R. & Mang, H.A., 2006. Safety Assessment of Concrete Tunnel Linings under Fire Load. *Journal of Structural Engineering*, 132(6), pp.961–969.
- Plizzari, G. & Tiberti, G., 2007. Structural behavior of SFRC tunnel segments. In *FraMCoS-6*. Catania, Italy, pp. 1577–1584.
- Ponikiewski, T. et al., 2015. X-ray computed tomography harnessed to determine 3D spacing of steel fibres in self compacting concrete (SCC) slabs. *Construction and Building Materials*, 74, pp.102–108.
- di Prisco, M. et al., 2004. On size effect in tension of SFRC thin plates. In *FraMCoS-5*. Vail, USA, pp. 1075–1082.
- di Prisco, M., Colombo, M. & Dozio, D., 2013. Fibre-reinforced concrete in fib Model Code 2010: principles, models and test validation. *Structural Concrete*, 14(4), pp.342–361.
- di Prisco, M., Ferrara, L. & Lamperti, M.G.L., 2013. Double edge wedge splitting (DEWS): an indirect tension test to identify post-cracking behaviour of fibre reinforced cementitious composites. *Materials and Structures*, 46(11), pp.1893–1918.
- di Prisco, M., Lamperti, M.G.L. & Lapolla, S., 2010. Double-edge wedge splitting test: preliminary results. In *FraMCoS-7*. Jeju, South Korea, pp. 1579–1586.
- di Prisco, M., Plizzari, G. & Vandewalle, L., 2009. Fibre reinforced concrete: new design perspectives. *Materials and Structures*, 42(9), pp.1261–1281.
- Prudencio, L. et al., 2007. Prediction of steel fibre reinforced concrete under flexure from an inferred fibre pull-out response. *Materials and Structures*, 39(6), pp.601–610.
- Pujadas, P., 2013. *Caracterización y diseño del hormigón reforzado con fibras plásticas*. PhD Thesis, Universitat Politècnica de Catalunya.
- Pujadas, P. et al., 2012. Cracking behavior of FRC slabs with traditional reinforcement. *Materials and Structures*, 45(5), pp.707–725.
- Pujadas, P., Blanco, A., Cavalaro, S., de la Fuente, A., et al., 2014a. Fibre distribution in macro-plastic fibre reinforced concrete slab-panels. *Construction and Building Materials*, 64, pp.496–503.
- Pujadas, P., Blanco, A., Cavalaro, S.H.P., de la Fuente, A., et al., 2014b. Multidirectional double punch test to assess the post-cracking behaviour and fibre orientation of FRC. *Construction and Building Materials*, 58, pp.214–224.
- Pujadas, P. et al., 2013. New analytical model to generalize the Barcelona test using axial displacement. *Journal of Civil Engineering and Management*, 19(2), pp.259–271.

- Pujadas, P., Blanco, A., Cavalaro, S. & Aguado, A., 2014c. Plastic fibres as the only reinforcement for flat suspended slabs: Experimental investigation and numerical simulation. *Construction and Building Materials*, 57, pp.92–104.
- Pujadas, P., Blanco, A., Cavalaro, S.H.P., Aguado, A., et al., 2014d. Plastic fibres as the only reinforcement for flat suspended slabs: Parametric study and design considerations. *Construction and Building Materials*, 70, pp.88–96.
- Ramezaniapour, A.A., Khazali, M.H. & Vosoughi, P., 2013. Effect of steam curing cycles on strength and durability of SCC: A case study in precast concrete. *Construction and Building Materials*, 49, pp.807–813.
- Ramezaniapour, A.M. et al., 2014. Influence of initial steam curing and different types of mineral additives on mechanical and durability properties of self-compacting concrete. *Construction and Building Materials*, 73, pp.187–194.
- RILEM TC 162-TDF, 2003. Final recommendation of RILEM TC 162-TDF: Test and design methods for steel fibre reinforced concrete sigma-epsilon-design method. *Materials and Structures*, 36(262), pp.560–567.
- Robins, P. et al., 2001. Flexural strain and crack width measurement of steel-fibre-reinforced concrete by optical grid and electrical gauge methods. *Cement and Concrete Research*, 31(5), pp.719–729.
- Robins, P., Austin, S. & Jones, P., 2002. Pull-out behaviour of hooked steel fibres. *Materials and Structures*, 35(7), pp.434–442.
- Robins, P.J., Austin, S.A. & Jones, P.A., 2003. Spatial distribution of steel fibres in sprayed and cast concrete. *Magazine of Concrete Research*, 55(3), pp.225–235.
- Segura-Castillo, L., Cavalaro, S.H.P., et al., 2018a. Fibre distribution and tensile response anisotropy in sprayed fibre reinforced concrete. *Materials and Structures*, 51(1), p.29.
- Segura-Castillo, L., Monte, R. & de Figueiredo, A.D., 2018b. New Test for the Characterization of the Tensile Constitutive Behaviour of FRC. In *High Tech Concrete: Where Technology and Engineering Meet*. Springer International Publishing, pp. 382–389.
- Serna, P. et al., 2009. Structural cast-in-place SFRC: technology, control criteria and recent applications in Spain. *Materials and Structures*, 42(9), pp.1233–1246.
- Shah, A.A. & Ribakov, Y., 2011. Recent trends in steel fibered high-strength concrete. *Materials & Design*, 32(8–9), pp.4122–4151.
- Sivakumar, A. & Santhanam, M., 2007. Mechanical properties of high strength concrete reinforced with metallic and non-metallic fibres. *Cement and Concrete Composites*, 29(8), pp.603–608.
- Sorelli, L.G., Meda, A. & Plizzari, G.A., 2005. Bending and Uniaxial Tensile Tests on Concrete Reinforced with Hybrid Steel Fibers. *Journal of Materials in Civil Engineering*, 17(5), pp.519–527.
- Soutsos, M.N., Le, T.T. & Lampropoulos, A.P., 2012. Flexural performance of fibre reinforced concrete made with steel and synthetic fibres. *Construction and Building Materials*, 36, pp.704–710.
- Söylev, T.A. & Özturan, T., 2014. Durability, physical and mechanical properties of fiber-reinforced concretes at low-volume fraction. *Construction and Building Materials*, 73, pp.67–75.

- Spasojevic, A. et al., 2008. Influence of tensile properties of UHPFRC on size effect in bending. In *Ultra High Performance Concrete (UHPC), Second International Symposium on Ultra High Performance Concrete*. Kassel, Germany, pp. 303–310.
- Stähli, P., Custer, R. & van Mier, J.G.M., 2008. On flow properties, fibre distribution, fibre orientation and flexural behaviour of FRC. *Materials and Structures*, 41(1), pp.189–196.
- Stroeven, P. & Hu, J., 2006. Effectiveness Near Boundaries of Fibre Reinforcement in Concrete. *Materials and Structures*, 39(10), pp.1001–1013.
- Švec, O. et al., 2014. Influence of formwork surface on the orientation of steel fibres within self-compacting concrete and on the mechanical properties of cast structural elements. *Cement and Concrete Composites*, 50, pp.60–72.
- Thienel, K., 2018. Verification of Conversion Factors Used for Compressive Strength Values Obtained for Structural Lightweight Concrete. In D. A. Hordijk & M. Luković, eds. *High Tech Concrete: Where Technology and Engineering Meet*. Springer International Publishing, pp. 1636–1644.
- Tiberti, G. et al., 2017. Crack control in concrete members reinforced by conventional rebars and steel fibers. *IOP Conference Series: Materials Science and Engineering*, 246(1), p.012008.
- Tiberti, G., Minelli, F. & Plizzari, G., 2015. Cracking behavior in reinforced concrete members with steel fibers: A comprehensive experimental study. *Cement and Concrete Research*, 68, pp.24–34.
- Tiberti, G., Minelli, F. & Plizzari, G., 2014. Reinforcement optimization of fiber reinforced concrete linings for conventional tunnels. *Composites Part B: Engineering*, 58, pp.199–207.
- Torrents, J.M. et al., 2012. Inductive method for assessing the amount and orientation of steel fibers in concrete. *Materials and Structures*, 45(10), pp.1577–1592.
- Vandewalle, L., 2006. Hybrid fiber reinforced concrete. In *Measuring, Monitoring and Modeling Concrete Properties*. Springer Netherlands, pp. 77–82.
- Vandewalle, L. et al., 2003. RILEM TC 162-TDF: “Test and design methods for steel fibre reinforced concrete” - sigma-epsilon-design method - Final recommendation. *Materials and Structures*, 36, pp.560–567.
- Vasanelli, E. et al., 2014. Crack width prediction of FRC beams in short and long term bending condition. *Materials and Structures*, 47(1–2), pp.39–54.
- Venkateshwaran, A., Tan, K.H. & Li, Y., 2018. Residual flexural strengths of steel fiber reinforced concrete with multiple hooked-end fibers. *Structural Concrete*, 19(2), pp.352–365.
- Walraven, J., 2013. fib Model Code for Concrete Structures 2010: mastering challenges and encountering new ones. *Structural Concrete*, 14(1), pp.3–9.
- Wille, K., El-Tawil, S. & Naaman, A.E., 2014a. Properties of strain hardening ultra high performance fiber reinforced concrete (UHP-FRC) under direct tensile loading. *Cement and Concrete Composites*, 48, pp.53–66.
- Wille, K., Tue, N.V. & Parra-Montesinos, G.J., 2014b. Fiber distribution and orientation in UHP-FRC beams and their effect on backward analysis. *Materials and Structures*, 47(11), pp.1825–1838.

- Wong, H.S. et al., 2011. Effect of entrained air voids on the microstructure and mass transport properties of concrete. *Cement and Concrete Research*, 41(10), pp.1067–1077.
- Woo, L.Y. et al., 2005. Characterizing fiber dispersion in cement composites using AC-Impedance Spectroscopy. *Cement and Concrete Composites*, 27(6), pp.627–636.
- Wu, Z., Shi, C., He, W., et al., 2016. Effects of steel fiber content and shape on mechanical properties of ultra high performance concrete. *Construction and Building Materials*, 103, pp.8–14.
- Wu, Z., Shi, C. & Khayat, K.H., 2016. Influence of silica fume content on microstructure development and bond to steel fiber in ultra-high strength cement-based materials (UHSC). *Cement and Concrete Composites*, 71, pp.97–109.
- Yazıcı, Ş. & İnan Sezer, G., 2007. The effect of cylindrical specimen size on the compressive strength of concrete. *Building and Environment*, 42(6), pp.2417–2420.
- Yermak, N. et al., 2017. Influence of steel and/or polypropylene fibres on the behaviour of concrete at high temperature: Spalling, transfer and mechanical properties. *Construction and Building Materials*, 132, pp.240–250.
- Yi, S.-T., Yang, E.-I. & Choi, J.-C., 2006. Effect of specimen sizes, specimen shapes, and placement directions on compressive strength of concrete. *Nuclear Engineering and Design*, 236(2), pp.115–127.
- Yoo, D.-Y., Kim, S., et al., 2017a. Effects of fiber shape, aspect ratio, and volume fraction on flexural behavior of ultra-high-performance fiber-reinforced cement composites. *Composite Structures*, 174, pp.375–388.
- Yoo, D.-Y. et al., 2014. Material and bond properties of ultra high performance fiber reinforced concrete with micro steel fibers. *Composites Part B: Engineering*, 58, pp.122–133.
- Yoo, D.-Y., Banthia, N., Yang, J.-M., et al., 2016a. Size effect in normal- and high-strength amorphous metallic and steel fiber reinforced concrete beams. *Construction and Building Materials*, 121, pp.676–685.
- Yoo, D.-Y., Banthia, N., Kang, S.-T., et al., 2016b. Size effect in ultra-high-performance concrete beams. *Engineering Fracture Mechanics*, 157, pp.86–106.
- Yoo, D.-Y., Park, J.-J. & Kim, S.-W., 2017b. Fiber pullout behavior of HRPFRCC: Effects of matrix strength and fiber type. *Composite Structures*, 174, pp.263–276.
- Yoo, D.-Y. & Yoon, Y.-S., 2015a. Structural performance of ultra-high-performance concrete beams with different steel fibers. *Engineering Structures*, 102, pp.409–423.
- Yoo, D.-Y., Yoon, Y.-S. & Banthia, N., 2015b. Predicting the post-cracking behavior of normal- and high-strength steel-fiber-reinforced concrete beams. *Construction and Building Materials*, 93, pp.477–485.
- Yu, R., Spiesz, P. & Brouwers, H.J.H., 2014. Mix design and properties assessment of Ultra-High Performance Fibre Reinforced Concrete (UHPFRC). *Cement and Concrete Research*, 56, pp.29–39.
- Zerbino, R. et al., 2012. On the orientation of fibres in structural members fabricated with self compacting fibre reinforced concrete. *Cement and Concrete Composites*, 34(2), pp.191–200.

- Zhan, Y. & Meschke, G., 2014. Analytical Model for the Pullout Behavior of Straight and Hooked-End Steel Fibers. *Journal of Engineering Mechanics*, 140(12), p.04014091.
- Zhang, S. et al., 2018. Experimental and analytical study of the fibre distribution in SFRC: A comparison between image processing and the inductive test. *Composite Structures*, 188(December 2017), pp.78–88.
- Zhou, B. & Uchida, Y., 2017a. Influence of flowability, casting time and formwork geometry on fiber orientation and mechanical properties of UHPFRC. *Cement and Concrete Research*, 95, pp.164–177.
- Zhou, B. & Uchida, Y., 2017b. Relationship between fiber orientation/distribution and post-cracking behaviour in ultra-high-performance fiber-reinforced concrete (UHPFRC). *Cement and Concrete Composites*, 83, pp.66–75.
- Žirgulis, G. et al., 2016. Influence of reinforcing bar layout on fibre orientation and distribution in slabs cast from fibre-reinforced self-compacting concrete (FRSCC). *Structural Concrete*, 17(2), pp.245–256.

PUBLICATIONS

The publications developed during the PhD thesis are presented subsequently:

Galeote, E., Blanco, A., Cavalaro, S.H.P., de la Fuente, A. Correlation between the Barcelona test and the bending test in fibre reinforced concrete. *Construction and Building Materials*, 2017, vol. 152, p. 529-538.

Galeote, E., Blanco, A., Cavalaro, S.H.P., de la Fuente, A. Influence of the beam size on the residual strength of fibre-reinforced concrete. In *Proceedings of the 3rd FRC International Workshop Fibre Reinforced Concrete*, Desenzano (Italy), 2018.

Galeote, E., Blanco, A., Cavalaro, S.H.P., de la Fuente, A. Optimized quality control procedure with the Barcelona test and the inductive method for FRC. In *Proceedings of the 3rd FRC International Workshop Fibre Reinforced Concrete*, Desenzano (Italy), 2018.

Galeote, E., Blanco, A., de la Fuente, A. Effect of reinforcement configuration on the ductility requirements of real-scale slabs. In *Proceedings of the 3rd FRC International Workshop Fibre Reinforced Concrete*, Desenzano (Italy), 2018.

Galeote, E., García, Y., Blanco, A., de la Fuente, A. Caracterización de hormigón de alta resistencia reforzado con microfibras metálicas. In *Proceedings of the VII Congreso Internacional de Estructuras de ACHE*, A Coruña (Spain), 2017.

Galeote, E., Quijano, N., Blanco, A., Pinillos, L. M., de la Fuente, A. Cuantías mínimas de refuerzo para dovelas de hormigón reforzado con fibras para anillos de túnel. Campaña experimental. In *Proceedings of the VII Congreso Internacional de Estructuras de ACHE*, A Coruña (Spain), 2017.

Galeote, E., Blanco, A., de la Fuente, A., Goodier, C., Austin, S. Size effect on post-cracking strength of high performance fibre-reinforced concrete. In *Proceedings of the fib Symposium 2017*, Maastricht (the Netherlands), 2017.

Galeote, E., Blanco, A., de la Fuente, A., Cavalaro, S.H.P. Creep behaviour of cracked high performance fibre reinforced concrete beams under flexural load. In *Proceedings of the International RILEM Workshop on Creep Behaviour in Cracked Sections of Fiber Reinforced Concrete 2016*, Valencia (Spain), 2016.

Galeote, E., Cavalaro, S.H.P., de la Fuente, A., Blanco, A. Correlation between the Barcelona test and the three-point bending test for the characterization of SCFRC. In *Proceedings of the IV Congresso Ibero-americano sobre Betão Auto-compactável*, Oporto (Portugal), 2015.

Blanco, A., Cavalaro, S.H.P., Galeote, E., Aguado, A. Assessment of constitutive model for ultra-high performance fiber reinforced cement composites using the Barcelona test. In *Proceedings of the 7th International RILEM Workshop On High Performance Fiber Reinforced Cement Composites*, Stuttgart (Germany), 2015.

